Development of Cryogenic Detection Systems for a Search of the Neutron Electric Dipole Moment

by

Robert Dipert

A Dissertation Presented in Partial Fulfillment
of the Requirements for the Degree
Doctor of Philosophy

Approved April 2019 by the
Graduate Supervisory Committee:

Ricardo Alarcon, Chair
Ralph Chamberlin
Robert Golub
Tingyong Chen
Kevin Schmidt

ARIZONA STATE UNIVERSITY

May 2019

ABSTRACT

Seeking an upper limit of the Neutron Electric Dipole Moment (nEDM) is a test of charge-parity (CP) violation beyond the Standard Model. The present experimentally tested nEDM upper limit is $3x10^{-26}$ e cm. An experiment to be performed at the Oak Ridge National Lab Spallation Neutron Source (SNS) facility seeks to reach the 3×10^{-28} e cm limit. The experiment is designed to probe for a dependence of the neutron's Larmor precession frequency on an applied electric field. The experiment will use polarized helium-3 (^{3}He) as a comagnetometer, polarization analyzer, and detector.

Systematic influences on the nEDM measurement investigated in this thesis include (a) room temperature measurements on polarized ^{3}He in a measurement cell made from the same materials as the nEDM experiment, (b) research and development of the Superconducting QUantum Interference Devices (SQUID) which will be used in the nEDM experiment, (c) design contributions for an experiment with nearly all the same conditions as will be present in the nEDM experiment, and (d) scintillation studies in superfluid helium II generated from alpha particles which are fundamentally similar to the nEDM scintillation process. The result of this work are steps toward achievement of a new upper limit for the nEDM experiment at the SNS facility.

ACKNOWLEDGMENTS

I would like to thank Ricardo Alarcon, my adviser, who has patiently worked through my academic and personal challenges over these many years. His patience and availability were vital qualities resulting in the success of this research.

Many thanks to Austin Reid, NCSU graduate student and now Indiana University post-doc. There is a unique bond which forms between those whom have experienced such a roller coaster as graduate school together. We have grown in many ways since the beginning of this journey and I look forward to seeing whom we will grow into in the future.

A special place in my heart and career exist for Chris Swank, whom had graduated from NCSU a few months prior to me arriving there. He provided invaluable guidance, support, encouragement, friendship, and levity. The year we spent together at TUNL, prior to his work at CalTech, set the tone for the rest of my graduate experience and I will always look upon that year with appreciation and thankfulness.

I have great appreciation for the knowledge, determination, skills, and research experience offered to me by Bob Golub. He is truly a unique man and I am honored to have spent so much time with him and have had the opportunity to learn so much from him. His passion for science and never ending curiosity are beyond the scope of my comprehension.

My deepest gratitude and thanks go to Toni Craige who has weathered the storm of graduate school at my side. My love has been supportive and encouraging and helped to smooth many tumultuous moments.

This work would not have been possible without the efforts of many people. A short and incomplete list of people I would like to thank includes: Ekaterina Korobkina, Igor Berkutov, Larry Bartoszek, Weijun Yao, Bastiaan Driehuys, Geoff Schrank, Chris Westerfeldt, Robin Cantor, Steven Clayton, Richard Nappi, Takeyasu Ito, Nguyen Phan, Kent Leung, Qiang (Alan) Ye, Bret Carlin, Richard O'Quinn, Gary Cofer, Jerry Dahlke, David Kendellen, Srun (Jump) Sosothikul, Paul Huffman, Albert Young, Vince Cianciolo, Matt Freeman, Mike Gnann, Leah Broussard, David Haase, and Zhiwen Zhao.

TABLE OF CONTENTS

Page

LIST OF TABLES vii

LIST OF FIGURES ix

CHAPTER

1 NEUTRON ELECTRIC DIPOLE MOMENT OVERVIEW 1

1.1 Physics Motivation 1

1.1.1 Magnetic Monopoles 1

1.1.2 Neutron Electric Dipole Moment (nEDM) Introduction 3

1.1.3 Symmetry Violation 4

1.2 Baryon Asymmetry 5

1.3 History of nEDM Experiments 8

1.4 Structure of This Thesis 10

2 EXPERIMENTAL CONSIDERATIONS FOR THE SEARCH OF THE nEDM 13

2.1 SNS-nEDM Overview 13

2.2 Production of UCN 19

2.3 ^{3}He as Comagnetometer, Polarization Analyzer, and Detector 20

2.4 Scintillation Detection in Superfluid Liquid Helium 21

3 ROOM TEMPERATURE AND CRYOGENIC MEASUREMENTS ON POLARIZED HELIUM-3 23

3.1 Common Experimental Apparatus 25

3.1.1 Cryostat 25

3.1.2 Common Magnetic Coil Systems 27

3.2 Design and Construction of a ^{3}He Measurement Cell 29

3.2.1 Cell Designs 30

3.2.2 Measurement Cell Geometry and Coating 37

3.3 Spin Exchange Optical Pumping Technique 39

3.4 Nuclear Magnetic Resonance Technique 43

CHAPTER Page

3.5 Room Temperature Measurements 47
3.5.1 Calibrating Tip Angle 50
3.5.2 Calculation of the Longitudinal Relaxation Rate T_1 54
3.5.3 Room Temperature Results 59
3.6 SQUID Overview and Motivation 61
3.6.1 SQUID Principles of Operation 61
3.6.2 SQUIDs: A Practical Approach 64
3.6.3 SQUID System Design and Construction 68
3.6.4 Cryoswitch Simulation 71
3.6.5 Cryoswitch Resistance Measurement 78
3.7 SQUID Measurements at 4 K 79
3.7.1 SQUID Experimental Setup 79
3.7.2 Noise Spectrum 81
3.8 Conclusions 85
4 SYSTEMATIC AND OPERATIONAL STUDIES APPARATUS 86
4.1 PULSTAR Measurement Overview 87
4.2 COMSOL Simulations and Physics 91
4.2.1 Conductivity 92
4.2.2 Black-Body Radiation 94
4.3 COMSOL Simulation Models 96
4.3.1 Actuator Arm 97
4.3.2 Neutron Guide 101
4.3.3 Heat Shields 108
4.4 SQUID System Design 111
4.4.1 Overview 113
4.4.2 SQUID and Cryoswitch Control Techniques 113

CHAPTER Page

4.4.3 Room Temperature Control Structure 117
4.4.4 SQUID Mounting Location and Thermal Anchoring 118
4.4.5 SQUIDs in the SOS Experiment 125
4.4.6 Pick Up Coil Arrays 128
4.5 Conclusions and Future Work 130
5 LIQUID HELIUM SCINTILLATION 132
5.1 LHe Scintillation Theory 133
5.2 Overview of the Experiment 134
5.2.1 Experimental Setup 135
5.2.2 Experimental Procedure 142
5.3 Problems and Solutions 142
5.3.1 PMT Heat Sink to IVC 144
5.3.2 Less Scintillation Light Than Expected 148
5.4 Data Analysis 151
5.5 Results 156
5.5.1 Results For Temperature Range 0.61 K to 2.42 K 156
5.5.2 Results For Measurements at 0.61 K 158
5.5.3 Results For Temperatures Between 2.03 to 3.06 K Data 160
5.6 Conclusions and Future Work 162
6 Conclusions and Future Work 164
REFERENCES 168
APPENDIX
Appendix A CALCULATION OF HEAT TRANSFER BETWEEN LIQUID HELIUM AND METAL SURFACES 176
A.1 Snell's Law 177
A.2 Acoustic Impedance 179

APPENDIX Page

A.3 Transmission 182

Appendix B SPIN EXCHANGE OPTICAL PUMPING (SEOP) CELL PRODUCTION 183

Appendix C ROOM TEMPERATURE T_1 DETAILS 188

C.1 Calculationn of Longitudinal Rexlation Rate 189

C.2 Table of Room Temperature Results 191

C.3 Tip Angle and T_1 Data Analysis 191

C.4 Tipping Angle and T1 Measurement Code 193

Appendix D EXPECTED SQUID OUTPUT 210

D.1 Flux Into Gradiometer From Polarized Source 211

Appendix E LIQUID HELIUM SCINTILLATION DATA AND CODE 214

E.1 Results - LHe Scintillation Data Tables 215

E.1.1 General Outline of Data Sets 215

E.1.2 Results Data Table For 0.61 K to 2.42 K 217

E.1.3 Results Data Table For 0.61 K 218

E.1.4 Results Data Tables For 2.03 to 3.06 K 219

E.2 LHe Scintillation Code 221

E.2.1 Command File 222

E.2.2 LANL Data Analysis Code 222

LIST OF TABLES

Table Page

1.1 The Effects of Applying Transformations in Parity and Time-reversal to the Components of Maxwell's Equations. Taken From C. Swank Thesis [1]. 2

3.1 Parameters Used in Room Temperature T_1 Measurements. 60

4.1 Maximum Window Temperatures Observed When Varying Window Layer Thicknesses for IVC Neutron Guide Window. 107

4.2 Heat Loads From Each Source Simulated in COMSOL and Fed Into the Appropriate Heat Shield Simulation. The Last Line of the Table Also Lists the Highest Temperature Simulated on Each Heat Shield. 110

4.3 Heat Loads Through 36 AWG Wires and SS Braid for One Cryocable. For Each Cryocable, There Are Six Ph Br and Two Cu Leads. Lengths and Cross Sectional Areas of the Leads and Braid Are Discussed in This Section's Text. The Columns Labeled "wire" and "cryocable" Give the Heat Load Through a Single 36 AWG Wire and a Single Cryocable, Respectively. 120

4.4 Heat Loads Through Cu Braid from SQUID Mount to Heat Sink Location. . . 125

5.1 Radioactive Source Data 135

C.1 Measured T_1 Values for Measurement Cell at Room Temperature As Reported in Section 3.5.3. 191

D.1 Parameters Put Into Simulation Discussed in This Appendix. 211

D.2 Flux Through Gradiometer in Units of Φ_0 for Various Concentrations and Fractions of Polarization. 212

E.1 Outline of Data Sets Collected at LANL. 215

E.2 Measured Temperatures for Temperature Dependent Data Set With No Electric Field. These Values Were Measured Using a ROx Resistor Inside of the Central Volume. 216

Table Page

E.3 Mean Number of Photoelectrons (PE's) and Mean Number of After Pulses Per Prompt Pulse Vs Temperature. More Details About These Results Discussed in Section 5.5.1. 217
E.4 Mean Number of Photoelectrons (PE's) and Mean Number of After Pulses Per Prompt Pulse Vs Voltage at Two Pressures. More Details About These Results Discussed in Section 5.5.2. 218
E.5 Mean Number of PEs Vs Voltage Between 2.03 to 3.06 K. 219
E.6 Num of After Pulses 219
E.7 Pedestal Offset 220
E.8 Sigma PMT Calibration 220
E.9 Single PE Calibration 221
E.10 Total Number of After Pulses Counted Per Voltage (in thousands). 221

LIST OF FIGURES

Figure Page

1.1 Publications of nEDM Upper Limit Measurements As a Function of Year Published. All Experiments Published Before 1980 Used Neutron Beams. All Experiments After 1980 Use Ultra-Cold Neutrons (UCN). The Predicted Sensitivity of the Sns-nedm Experiment Is Shown As Well. 9

2.1 Photograph of Full Sized Cell for SNS-nEDM Showing dTPB-dPS Illuminated Under UV Light. Photo Taken by Kent Leung. 16

2.2 Free Neutron and Helium-II Dispersion Curves. The Neutron Can Be Downscattered Via Coherent Single-photon Scattering, Resulting in the Neutron Being at Rest. 19

3.1 The Holding Field Coils Surround the Entire Cryostat and Transport Cell. (a) Photograph of Coils and Cryostat. (b) Schematic of Holding Field Coil Labels As Referenced in the Text. 28

3.2 Reproduction of Fig. 3.33 From Q. Ye's Thesis on the Holding Field Coils. In His Setup, He Used 8 Coils, in This Work Only 7 Coils Were Used. The Magnetic Field, Even at This Low Field Strength, Has Very Small Fluctuations From the Desired Field. 29

3.3 NMR Coils Used in the Room Temperature Experiment. 30

3.4 Left: Previous Experimental Setup From C. Swank's Thesis Work [1]. Right: Assembly of Measurement Cell Geometry Used in Present Work. 31

3.5 Schematic of New Support and Cell Design. From Top to Bottom: Buffer Cell, Sintered Volume, PEEK Tube, Experimental Cell. The Mixing Chamber of the Dilution Refrigerator Was Misaligned Due to Damage Acquired During Shipping. To Account for This, the Center Bore Between Cu Volume and PEEK Tube Was Cut at an Angle and Results in the Experimental Cell Being Directly Below the Center of the Dilution Refrigerator. Illustrated by A. Reid. 32

3.6 The Measurement Cell Before Being Attached to the PEEK Tube. (a) the 5 mil Kapton Film on the Interior Top of the Cell Is Yellow. (b) the Central Hole in This Design Is for Filling the ^{3}He From the Glass Tube. The Smaller Hole Below and to the Right Is a Threaded Blank for a Temperature Sensitive Resistor. (c) Top View of Cell: The Kapton Capillary Is Visible As Well As the Acrylic Ring Supporting the Capillary on the Film. 38

3.7 Spin Exchange Optical Pumping of Rb Valence Electron. 40

3.8 The NMR Process. (a) Magnetic Moment $\overrightarrow{\mu}$ Aligned with Magnetic Holding Field $\overrightarrow{B_0}$. (b) Apply a Transverse Oscillating Magnetic Field $\overrightarrow{B_1}$ to Cause Tilt of $\overrightarrow{\mu}$ by Angle θ. (c) Torque Between Holding Field and Magnetic Moment Causes Larmor Precession of $\overrightarrow{\mu}$. 44

3.9 NMR Dephasing Viewed in Rotating Reference Frame While Moving With a Central Frequency ω_l. This Process Is the Source of T_2. (a) In a Reference Frame Rotating With a Magnetic Moment at $\omega_l = -\gamma B_0$. When the Atoms Are First Tipped, All the Magnetic Moments Are Lined Up. (b) As Time Progresses, Different Regions Are Exposed to Slightly Different Magnetic Holding Fields, Resulting in Slightly Different Angular Velocities Causing the Moments to Spread. (c) When Enough Time Has Passed, the Magnetic Moments Throughout the Material Are Randomized. The Sum of All Magnetic Moments Becomes Zero in the Transverse Direction. 45

3.10 Data Collected Plotted Vs Time. Exponential Curve Fit to Dataset With $T_2 = 19.23\ sec.$ 46

3.11 Two Design Schematics for First-order Gradiometers. (a) Axial First-order Gradiometer. This Type of Gradiometer Is Used in the Present Work. (b) Series Planar First-order Gradiometer. This Type of Gradiometer or the Parallel Version Will Used in the PULSRAT-SOS and SNS-nEDM Experiments. 48

3.12 The FFT of a Signal From Two Measurements on the Same Polarized ^{3}He Filled Cell Are Shown. The Horizontal Axis Is Centered at the Larmor Frequncy in Units of Hz. The Vertical Axis Is in Arbitrary Unit. (a) the FFT of the Signal Taken by Using a Common Set of Coils Where Two Loops of Wound Coil Surrounding the Sample Were Wound in the Same Direction. The Large Gaussian Curve Is the Background Noise. The Small Bump, Circled in Red, Is the Signal. (b) The FFT of the Signal Taken Using an Axial First-order Gradiometer. The Clarity of the Signal Is Extremely Pronounced When Compared to the FFT From (a). 49

3.13 NMR Tipping Technique Described Theoretically and Expressed As Data From a Measurement. (a) When Tipping the Magnetic Moments of a Sample With Initial Polarization P_0. The Transverse Magnitude After the Tip S_0 Is Then Measured by the NMR Pick up Coils. This Figure Was Originally Drawn by Austin Reid. (b) FFT of Data Collected While Calibrating Tip Angle Showing Results of Tipping. The Plot Is Centered Around the NMR Frequency ω_l..... 51

3.14 Calibration of Tip Angle As a Function of Magnetic Field Strength..... 53

3.15 Results of Measurments of Tip Angle As a Function of NMR Pulse Duration. 54

3.16 Energy Levels in Two State Fermion System for ^{3}He. 55

3.17 The Results of the Room Temperature Measurements Are Shown. These Data Points Are Also Reported in Table C.1. 59

3.18 Simple Schematic of SQUID. Josephson Junctions Are Marked With 'x'. I_b Is the Bias Current and 'V' Leads Are Where the Voltage Is Measured. 63

3.19 Current Vs Voltage Curve Across Josephson Junctions. These Curves Are Used to Tune the SQUID for Operation. 63

3.20 Voltage Vs Flux Curve for DC SQUID. The Horizontal Units Are the Ratio of the Flux Through the SQUID Divided by the Flux Quantum. 64

3.21 Plot Measured on an Oscilloscope of Voltage Output While Tuning SQUID. During This Process, the Flux Entering the SQUID Sweeps Between Two Values, Such As the Dots Shown on Fig. 3.20 64

3.22 Schematic of CE2SBlue SQUID Chip. The I_b Leads Are for the Bias Current Running Across the SQUID Loop, the *Mod* Leads Control the Modulation and Feedback, the *Heater* Leads Control a Resistor As Either a *Heater* or *Cryoswitch*, and the *Input* Circuit Connects to the Pick up Coils and Couples to the SQUID Loop. The *Heater* in the Schematic Is Drawn As a Resistor in a Usual Circuit Diagram. The *H* Label Shows That When Used As a *Heater*, Both the SQUID Loop and Input Circuit Are Heated. The *CS* Label Shows That When Used As a *Cryoswitch*, Only the Input Circuit Is Brought Above the Superconducting Temperature Threshold. 66

3.23 Photo of SQUID Installation. In the Final State, the SQUID Is Placed Inside the Pb Enclosure and the Enclosure Is Soldered Shut With Another Sleet of Pb. This Assembly Is Attached to the LHe Bath. 70

3.24 Overview of Electronics Control Structure of Cryostat. 71

3.25 Surface Representation of COMSOL Model of CE2SBlue SQUID Chip. 73

3.26 Surface Temperature of COMSOL Model of CE2SBlue SQUID Chip With Wire Heat Loads From SQUID Cable. 73

3.27 Heat Flow Through SQUID Chip From Cu Leads of CE2SBlue Simulated In COMSOL. 74

3.28 Location of Resistor Placed in CE2SBluE COMSOL Model. 75

3.29 Result of COMSOL Simulation Showing Region Warmed by Heating of Cryoswitch Using 10 mA Current. 76

Figure Page

3.30 Time Dependent Results When Applying Current to Resistor Shown in Fig. 3.28. 77
3.31 Resistance in Supracon SW1 Cyroswitch Input Circuit As a Function of Applied Current. 79
3.32 PSD Flux Through the Pick up Coils Which Measure the Background Noise. 83
4.1 Photo of PULSTAR-SOS Cryostat As Currently Assembled in TUNL. 88
4.2 Basic Schematic of Pulstar Cryostat Concept. 89
4.3 Autodesk Inventor Model Created by Larry Bartoszek Showing IVC Internal Components for PULSTAR-SOS Experiment. This View Is From the Bottom of the Cryostat. The Measurement Cell Is Centrally Located in the IVC. The Green Fiber Optic Cable Array on the Right of the Figure Covers That Entire Side of the Measurement Cell. The Vestibule Has Ports for UCN, ^{3}He, and ^{4}He. Between the Vestibule and Measurement Cell Is a Φ 1 cm Hole With a Plug. The Plug Is Moved Into and Out of the Hole Via Operation of the Actuator Arm. 90
4.4 Cutaway of PULSTAR Cryostat. The Measurement Cell, Shown in Fig. 4.3, Is Located Centrally in the Lower Section of the Inner Vacuum Chamber (IVC). 96
4.5 Cross Section of Autodesk Inventor Actuator Arm Model. Lower Labels on the Model Mark General Components. Upper Labels Mark Specific Components Discussed in Detail in Section 4.3.1. 97

4.6 Heat Flow Simulation in IVC Actuator Arm Flange Created in COMSOL. The Arrows Represent the Heat Flow Direction. The Size of the Arrows Is Normalized Due to the Many Orders of Magnitude Spanned by the Heat Flow Magnitude in Different Regions. The Left Side of the Image Comes From Room Temperature. The Curved Band Running Top to Bottom in the Middle of the Figure Represents the Cu Braids. The Large Volumes on the Right Are the IVC Flange. The Extremely Small Heat Flow Through the Bellows Is Observable Between the Braids and Flange. 100

4.7 Cross Section of Autodesk Inventor Neutron Guide Model. 103

4.8 Diagram of Geometry of Circular Neutron Window. (a) View of Window on Circular Face. (b) Cross Section of Window Showing Radiative Heat Load $\dot{q}_{rad,in}$, Conductive Heat Load From Warmer Middle Section of Window $\dot{q}_{con,in}$, and Conductive Heat Load $\dot{q}_{con,out}$ Leaving the Infinitesimal Volume in Question. 104

4.9 Temperature Distribution on IVC Neutron Guide Window Simulated in COMSOL. Shown in Same Reference Frame As Eq. 4.18. 106

4.10 Temperature Plots of Nitrogen Jacket Simulations Made in COMSOL. The Central Port Shown in the Figures Is the Connection Point for the Neutron Guide and the Heat Load From It Was Applied at This Location. The Closed Port on the Right Side of the Figures Is the Location for the Actuator Arm and Its Heat Load Is Applied at That Location. The Top Surface of the Model Was Set to 77 K, As It Simulates Thermal Anchoring to the Liquid Nitrogen Bath. (a) Temperature Boundary Plot. (b) Temperature Contour Plot. 109

4.11 Temperature Plots of IVC Simulations Made in COMSOL With Radiation Incident on the Outer Surface. The Top Surface of the Model Was Set to 4.2 K, As It Simulates Thermal Anchoring to the Liquid Helium Bath. (a) Temperature Boundary Plot. (b) Temperature Contour Plot. 111

4.12 Overview of SQUID System for SOS Experiment. This Is the Initial Setup with Four SQUIDs. It Will Be Possible to Include Eight SQUIDs Later. 114

4.13 Cryoswitch Operation. Top Trace Is Potential Across Cryoswitch. Bottom Trace Is Read Out From SQUID Electronics. The Offset Seen on the Right Side of the Flat Region in the Middle Is Discussed in the Text. 116

4.14 Cutaway of Experimental Region in SOS Experiment. For Scale, the Outer Most Vacuum Chamber Has OD Φ 44 Inches. This Viewing Angle Faces Down the Length of the Actuator Arm. 119

4.15 Autodesk Inventor Models of Measurement Cells to Be Used in PULSTAR-SOS Experiment. This Model Was Created by L. Bartoszek. The Green Cylinders Are Positions Where Circular Pick Up Coils Will Be Placed. (a) Shows the Short Cell Which Will Be Used First for Intial Tests. (b) Shows the Full Sized Measurement Cell. 127

4.16 Magnetic Field Generated by Oscillating Polarized ^{3}He Atoms. This View Is From the End of the Measurement Cell. The Magnetic Holding Field Runs Left to Right. The Atoms Will Precessing in the Plane Perpendicular to the Holding Field. The Planned Location of the Pick Up Coils Near the Top and Bottom of the Cell Are Shown As Well As the Possible Location of the Gradiometer. These Are Not Necessarily to Scale, As the Final Pick Up Coil Sizes Have Not Been Selected. This Image Was Taken From S. Clayton's Paper [2] and Generated Using the Mathematica Code Described in That Paper. 129

5.1 Schematic of Central Volume and Important Plumbing Paths. During the Initial Run, the Dashed Line Was Not Present. This Was Added to Allow the Central Volume to Be Filled by Condensing Helium Gas From the Lhe Storage Dewar. 137
5.2 Data Acquisition (DAQ) System. The Digitizer Was a Skutek DDC10 Digitizer.137
5.3 Cutaway View of Central Volume From Autodesk Inventor Model Created by J. Ramsey (ORNL). All Components Shown Are Inside the IVC. 140
5.4 Photographs of Electrode Support Held by Bottom of Central Volume. Top Image Shows Green Fiber Optic Cables. This Is a View From Left Side of Fig. 5.3. Bottom Image Shows Hv Connector and G-10 Support Structure. Viewing From Right Side of Fig. 5.3. Both Photos Taken by N. Phan. 141
5.5 Plot of Temperature Measured on Inside of Central Volume Using ROx Resistor. “1st Run” - the PMT Was Not Heat Sunk to IVC Causing a Heat Load of About 10 MW Into the Central Volume. “2nd Run” - the PMT Was Heat Sunk to 4 K on IVC Increasing the Cooling Power of the System. 143
5.6 Geometry Used in COMSOL Simulation. Axis Units Are Centimeters. Material Identification: Pink: Borosilicate Glass. Light Blue: Plastic Simulated With Epoxy Thermal Conductivity and Specific Heat in Middle of Plastics Range. Dark Blue: Copper Wires. Green: G-10. Grey: SS304. 145
5.7 Heat Load Into Central Volume From PMT As a Function of Time. The Temperature in the Beginning of the Names of the Plot Labels Refers to the Temperature of the Central Volume in the Model. The “no Heatsink” and “heatsink” Label Indicates Whether or Not the Bottom of the PMT Shield Was Thermally Connected to the IVC. The Thermal Connection to the IVC Was Always Set to 4 K. 147
5.8 Average Temperature of PMT Glass in COMSOL Simulation. 147

5.9 Temperature Distribution on PMT and Support Structure in Stationary Simulation. 148

5.10 Waveform Output Types. In These Waveforms, the Pedestal Offset Has Not Been Adjusted. However, All Analyzed Data Was Performed on Waveforms After the Pedestal Had Been Calculated and Added to the Waveforms. (a) Waveform Which Has No After Pulses and Thus Is From β or Dark Counts. (b) Waveform From α Scintillation Showing After Pulses Marked With Red X's. 152

5.11 Pedestal Offset and Standard Deviations Measured During 2.03 - 3.06 K Measurements. The Values Plotted Here Can Be Found in Table E.7 153

5.12 Histogram of After Pulse Peak Values for 2.22 K Data Set. This Plot Clearly Shows the Dependence of the Number of After Pulses on Electric Field Strength. This Type of Trend Was Observable Across All Data Sets. 154

5.13 Fit of Convoluted Poisson-gaussian to Histogram Data From Eq. 5.2. The Mean and Standard Deviation of the Fit Are Then Taken and Reported in the Results. 155

5.14 Mean Number of PE's Observed in the Prompt Pulse Vs Temperature. The Values Recorded At .61 and 2.42 K Had Pressure $\sim$750 mbar. The Values Recorded in Between Had Pressure $\sim$890 mbar. A Table of This Data Can Be Found in Table E.3. 157

5.15 Mean Number of After Pulses Observed Per Prompt Pulse. A Table of This Data Can Be Found in Table E.3. 158

5.16 Mean Number of Photoelectrons From 0.61 K Dataset at Range of Voltages. The Standard Deviation of Each Result Is Plotted Above but the Values Were so Small, They Are Difficult to See in the Figure. The Values Plotted Here Can Be Found in Table E.4. 159

Figure Page

5.17 Mean Number of After Pulses For 0.61 K Data Sets. At Each Electric Field Value, the Mean Number of After Pulses for the 28 mbar Data Set Is Slightly Smaller Than the 750 mbar Data Set, Though the Stand Deviations for Each Are Quite Large. The Values Plotted Here Can Be Found in Table E.4. 160

5.18 Mean Number of PE's Observed in Prompt Pulse at Temperatures Between 2.03 to 3.06 K Vs Electric Field. The Values Plotted Here Are Also Found in Table E.5. 161

5.19 Mean Number of After Pulses Observed Per Prompt Pulse at Temperatures Between 2.03 - 3.06 K Vs Electric Field..... 162

A.1 Graphic Depiction of Snell's Law. The Incident and Refracted Angles Are θ_1 and θ_2, Respectively. The Index of Refraction of Each Material Are n_1 and n_2. The Velocity of the Wave in Each Material Are v_1 and v_2. 177

B.1 Photo of Glass Manifold Wrapped in Heater Tape. 186

D.1 Geometry Used in Mathematica Simulation. Dimensions Are mm. 212

D.2 Flux Through Gradiometer in Units of Φ_0. This Is the Same Data As Table D.2. 213

Chapter 1

NEUTRON ELECTRIC DIPOLE MOMENT OVERVIEW

1.1 Physics Motivation

The fundamental questions being investigated in relation to this work are the charge-parity (CP) and time-reversal (T) symmetries. These symmetries underlie our basic concepts about the universe and its evolution through time. The symmetries are known to not to be conserved to some extent and further investigation into them can assist greatly in refining the standard model, offer further explanation for the baryon asymmetry, and help to discover which additional *beyond the standard model* theories rest on solid foundations and might usefully be employed for predictions about our universe.

This chapter gives an overview of the history of the fundamental symmetries and neutron electric dipole moment (nEDM), theory, and current status. In section 1.1.1, the first theoretical suggestion of the violation of the symmetries by Dirac is discussed. Section 1.1.2 introduces the theoretical basis for how an nEDM measurement could be performed. The *Big Bang* history of the universe and *Baryon asymmetry* are discussed in section 1.2. A short history of symmetry violation is given in section 1.1.3. The chapter ends with section 1.3 offering the history of nEDM measurements to the present day. The chapter ends with section 1.4 giving an overview of the structure of this thesis.

1.1.1 Magnetic Monopoles

Among the many significant contributions to physics by Paul Dirac was the idea that a free magnetic charge or "magnetic monopole" may exist in nature [3, 4]. Although no evidence for a magnetic monopole seemed to exist. Magnetic monopoles are aesthetically pleasing because they would cause Maxwell's equations to be nearly symmetric in the interchange of electric and magnetic fields. The form of Maxwell's equations are then1

$$\nabla \cdot \boldsymbol{B} = \rho_M \tag{1.1}$$

$$\nabla \cdot \boldsymbol{E} = \rho_E \tag{1.2}$$

$$\nabla \times \boldsymbol{B} - \frac{\delta \boldsymbol{E}}{\delta t} = \boldsymbol{J}_E \tag{1.3}$$

$$\nabla \times \boldsymbol{E} + \frac{\delta \boldsymbol{B}}{\delta t} = \boldsymbol{J}_M \tag{1.4}$$

where $\boldsymbol{B}$ is the magnetic field, $\boldsymbol{E}$ is the electric field, ρ is a charge density, and $\boldsymbol{J}$ is a current. The subscripts M and E refer to the magnetic and electric charges, respectively. Lacking a magnetic charge means $\rho_M = 0$ and thus there is no magnetic current, so $\boldsymbol{J}_M = 0$.

Table 1.1: *The Effects of Applying Transformations in Parity and Time-reversal to the Components of Maxwell's Equations. Taken From C. Swank Thesis [1].*

Variable	P	T
t	+	-
∇	-	+
$\boldsymbol{B}$	+	-
$\boldsymbol{E}$	-	+
ρ_M	-	-
ρ_E	+	+
$\boldsymbol{J}_E$	-	-
$\boldsymbol{J}_M$	+	-
$\boldsymbol{s}$	+	-

If magnetic monopoles do exist, the P and T symmetries, discussed further in the following sections, would be violated. Table 1.1 shows the sign changes which result from application of P and T operations for each components of Eqns. 1.1 - 1.4. At that time, there had been no observation of violation of these symmetries. Dirac was able to demonstrate in 1948 [5] and 1949 [4] however, that magnetic monopoles could be used to explain

the quantization of electric charge. Obviously, that is a valuable logic and violation of the symmetries have been under investigation ever since. To date, no magnetic monopoles have been observed.

1.1.2 Neutron Electric Dipole Moment (nEDM) Introduction

The neutron is a fermion and thus follows Fermi statistics. Having spin $I = 1/2$, the neutron ground state can be characterized by the quantum number $m_l = \pm 1/2$. When placed in external electric $\boldsymbol{E}$ and magnetic $\boldsymbol{B}$ fields, the spin Hamiltonian can be written

$$H = -\left(d_n \boldsymbol{s} \cdot \boldsymbol{E} + \mu_n \boldsymbol{s} \cdot \boldsymbol{B}\right) \tag{1.5}$$

where d_n and μ_n are the electric and magnetic dipole moments, respectively, and $\boldsymbol{s}$ is the spin direction [6].

Referencing the transformations shown in Table 1.1, we see that under P, the term $\boldsymbol{s} \cdot \boldsymbol{E} \rightarrow \boldsymbol{s} \cdot (-\boldsymbol{E}) = -\boldsymbol{s} \cdot \boldsymbol{E}$. However, the $\boldsymbol{s} \cdot \boldsymbol{B}$ term does not change signs when applying the P operation. This means that reflecting the observer's coordinate system in all three dimensions, changes the Hamiltonian in a significant and non-symmetric way. Notice as well, that because $\boldsymbol{s} \rightarrow -\boldsymbol{s}$ under the time reversal operation, the term $\boldsymbol{s} \cdot \boldsymbol{E} \rightarrow -\boldsymbol{s} \cdot \boldsymbol{E}$. Again the $\boldsymbol{s} \cdot \boldsymbol{B}$ term does not change signs and the time reversal operation changes the Hamiltonian in a non-symmetric manner. These two types of calculations are what is meant by P and T violation.

In 1950, Purcell and Ramsey suggested that experimental evidence should be collected to consider the possibility of parity violation [7]. They proposed that the magnetic monopole could be a physical mechanism resulting in an elementary particle having and electric dipole moment (EDM). Additionally, Purcell and Ramsey argued that the possibility of elementary particles having non-zero EDMs could explain the quite notable asymmetry in relative amounts of matter and anti-matter observed in the universe. They acted on these statements by performing a magnetic resonance experiment on a neutron beam at Oak Ridge National

Laboratory in 1951 [8]. The results were considered quite controversial and publication did not occur until 1957 [9]. In that first published paper, an upper limit of $d_n \leq -(0.1 \pm 2.4) \times 10^{-20}\ e \cdot cm$ was reported.

1.1.3 Symmetry Violation

Following the developments above, in 1956, Lee and Yang then proposed a number of experiments to test parity violation in beta, meson, and hyperon decays [10]. They suggested this hoping to offer an explanation for the τ-θ puzzle. At the time, observations were made on τ^+ and θ^+ particles which decayed into states with opposite parity, even though the particles had the same mass, production rates, and lifetimes. This resulted in observations suggesting that these particles were actually the same particle but different decay modes were being observed. At that time, it was thought that a neutron EDM would be the most sensitive test for parity violation though they were not considering that an EDM would also result in time-reversal violation.

Lee and Yang suggested measuring the angular distribution of the average value of $A = \boldsymbol{s} \cdot \boldsymbol{p}_e$ in β-decays, where $\boldsymbol{s}$ is the nuclear angular momentum and $\boldsymbol{p}_e$ is the momentum of the emitted electron. When applying the parity operation, $\boldsymbol{s}$ keeps the same sign, while $\boldsymbol{p}_e \rightarrow -\boldsymbol{p}_e$. If the average value of A is non-zero, the electrons have an inclination to be emitted along a particular axis relative to $\boldsymbol{s}$ and parity will be violated. The first experimental evidence of this type of parity violation was published in 1957 on the β-decay of cobalt-60 [11].

In 1957, Landau published a paper on conservation laws for weak interactions [12]. He considered situations where the operations of charge conjugation and parity are applied together, called "CP". When CP is conserved, he established the argument that the general symmetry of space would be preserved. A few years later, in 1964, experiments performed on K^0 meson decay demonstrated that CP is not a viable conservation law either [13]. Since that time, additional measurements on the B meson [14, 15] have revealed more information on CP violating processes.

At the time of this writing, no experimental evidence of the combined symmetry of CPT being violated has been observed [16, 17]. Logic then dictates that violation of the CP symmetry therefore must be accompanied by violation of the T symmetry.

These violating processes are incorporated into the standard model via the Cabibbo-Kobayashi-Maskawa (CKM) quark mixing matrix [18]. The 3×3 CKM matrix describes flavour-change strengths for weak interactions. More specifically, the quantum state mismatch between quarks is calculable through this matrix when they propagate freely and when they are engaged in a weak interaction.

1.2 Baryon Asymmetry

Presently, in the early 21st century, it seems nearly canon that the Big Bang was an event that occurred. Most individuals however could not give a clear account as to why it is a convincing model for the beginning of our universe. In this section, some details about why the Big Bang is a convincing model will be given and why some unresolved issues with it make a search for the nEDM so compelling.

The Big Bang model offers explanations for some important observations which have been made about our universe. Some of these observations are (a) the *cosmic microwave background radiation* (CMB), (b) the red shift observed from Earth of many distant galaxies (also known as *Hubble's Law*), and (c) the relative ratios of light elements which were formed in the early universe and persist today. Implicit in the theory, is the idea that our position in the universe is not unique. We have had to deal with this ego crushing realization globally on a number of occasions. Although we have spent most of history thinking we are special, evidence suggests that the Earth is not the center of the universe, human's have evolved from animals, and other animals have languages. However, some interpretations of the Big Bang theory suggest that the universe may actually be infinite [19]. A side effect of such a universe is that no matter where you are situated, your vantage point is the *center of the universe* because all views in every direction from every location are the same.

The Big Bang models begin with the entire universe as a very small, high energy density, opaque plasma with extremely high pressures and temperatures. The universe then began to expand, cooling as it expanded, and all the stuff we can talk about happened after that. When the expansion happened, the photons from the early universe began to spread in every direction and the cooling which occurred allowed atoms to begin to form.

Here is a summary of a few observations: (a) We cannot see an edge to the universe. (b) The size of the universe has been calculated to be at least 100 times larger than the part of the universe we are capable of observing [19]. (c) The age of the universe appears to be 13.799 $\pm$ 0.021 billion years [20]. (d) We are receiving light from the CMB in all directions. (e) The CMB has a measured temperature, using the WMAP data, of 2.7260 $\pm$ 0.0013 K, which shows extremely high uniformity across a huge span of space [21]. (f) General relativity sets an upper limit on the rate at which information can be carried from one point in space to another. Thus if space were always as large as it is now, how is there such uniformity between point which never could have communicated with each other in the past? The Big Bang models say "because it wasn't always this size." It started out small and all the points in space could communicate with each other allowing a type of equilibrium which gave uniformity throughout... then it began to expand.

Another important observation is that we are receiving light from a significant number of distant galaxies and nebulae which are not within the visible spectrum [22]. In addition, light from galaxies further away have longer wavelengths than light coming from nearer galaxies. We do still believe however, that their stars are made of the same atoms our stars are made of. This is explained by incorporating *Hubble's Law* into the Big Bang models. This law describes that space itself is expanding and that the light is being stretched due to the Doppler effect. The law can be written simply as $v = H_0\ D$ where $H_0 \approx 70(km/s)/Mpc$ is Hubble's constant, D is the *proper distance* to the light source, and v is its velocity relative to the proper distance and cosmological time coordinate.

The third argument mentioned at the beginning of this section was that the relative ratios of light elements observed throughout the universe are consistent with cosmological theories developed from the Standard Model. This is known as the *Big Bang Nucleosynthesis*. The Big Bang model suggest that after the first three minutes of the existence of our universe, the universe expanded to a point when atomic matter could congeal out of that energy. In the process, predictable amounts of the smallest atoms, H, D, ^{3}He, ^{4}He, and ^{7}Li, were synthesized. Predictions from the model are in good agreement with the abundances of these atoms observed in our universe [23].

What isn't in good agreement between the models and observations is the ratio of matter to anti-matter [24]. If the Big Bang occurred while undergoing perfectly symmetric laws of physics, equal amounts of matter and anit-matter would have been produced. Our observations of the universe however, do not reveal equal amounts of matter and anti-matter but instead show us a universe mostly filled with matter. This unresolved observation is known as the *Baryon Asymmetry*. CP violation may offer insight into a mechanism by which the baryon asymmetry could have arisen.

Since CP violation has been observed directly, as mentioned in the sections above, it's worth taking a moment to consider if the baryon asymmetry could be explained by CP violation alone [25]. Known sources of CP violation are the K^0, D^0, B^0, and B_s (strange) meson decay processes. The most precise measurement performed has been the $K \to \pi\pi$ decay mode, which shows an asymmetry of $\mathcal{R}(\varepsilon`/\varepsilon) = (1.655 \pm 0.013) \times 10^{-3}$ [26]. The total amount of asymmetry in the universe can't be explained by this small of a violation [24]. Therefore, a significant source of CP or T violation needs to be discovered and measured. The existence of a neutron electric dipole moment could provide such evidence.

An analysis of the situation was given by Ellis *et al* [25] in 1981 which offers an upper limit to the nEDM while including the measured values regarding CP violation. In their paper, they calculate that the nEDM $d_n \geq 3 \times 10^{-28}$ $e\ cm$. They came to this conclusion by including X-ray emission observations from galactic clusters to infer the apparent baryon-

to-photon ratio. Advancements in the measurement of the CMB since 1981 continued to increase precision of our understanding of the baryon-to-photon ratio. More recent papers from 2009 [27] and 2010 [28] include the baryon-to-photon ratio observed in the more recent CMB measurements as well as minimal supersymmetric extensions to the standard model using electro-weak baryogenesis mechanisms. They also come to the conclusion that $d_n > \mathcal{O}(10^{-28})$ $e\ cm$. The standard model on the other hand implies the nEDM may reside in the range $10^{-33} < d_n < 10^{-31}$ $e\ cm$ [29]. For these reasons, probing for the nEDM at the resolution described by these papers is of great significance.

1.3 History of nEDM Experiments

Attempts to measure the nEDM have been underway since 1950. Fig. 1.1 shows each of the previously published results and the predicted sensitivity of the current research discussed in this thesis. The increase in sensitivity during the early beam experiments was seven orders of magnitude. Since moving to Ultra-Cold Neutron (UCN) detection techniques in 1980, the sensitivity has increased by another two orders of magnitude. These later experiments also used co-habiting magnetometer species (co-magnetometers) which help to identify and correct for inhomogeneities in the magnetic fields. Using this technique, the present upper limit of $d_n < 3 \times 10^{-26}$ $e\ cm$ was set in 2006 [30]. The nEDM experiment at the Spallation Neutron Source (SNS) intends to again increase the sensitivity by two orders of magnitude [31].

Currently, investigations into the nEDM are underway at

(a) the SNS facility at Oak Ridge National Laboratory (ORNL) in Tennessee USA

(b) Los Alamos National Laboratory (LANL)

(c) Petersburg Nuclear Physics Institute (PNPI) in Russia

(d) European Spallation Source (ESS) in Sweden

(e) Instiut Laue-Langevin (ILL) in Grenoble France called CryoEDM

(f) the Paul Scherrer Institute (PSI) in Villigen Switzerland

(g) TRIUMF in Canada

(h) FRM-II in Munich Germany

(i) the Research Center for Nuclear Physics (RCNP) in Japan [32]

These experiments operate under many experimental conditions and will provide varying levels of confidence and nEDM upper limits. All of them are performing the measurements using UCN. Obviously, reading this list of parties interested in such a challenging fundamental physics experiment demonstrates the general enthusiasm and necessity for making progress on this topic.



Figure 1.1: *Publications of nEDM Upper Limit Measurements As a Function of Year Published. All Experiments Published Before 1980 Used Neutron Beams. All Experiments After 1980 Use Ultra-Cold Neutrons (UCN). The Predicted Sensitivity of the Sns-nedm Experiment Is Shown As Well.*

1.4 Structure of This Thesis

As you have already read, Ch. 1 describes the history of the nEDM and our motivation in pursuing further analysis of it.

Ch. 2 describes an experiment being designed for the SNS facility at Oak Ridge National Laboratory. This is referred to as the SNS-nEDM experiment. This new experiment will be capable of pushing the nEDM upper limit down to $d_n \geq 3 \times 10^{-28}$ $e\ cm$, assuming an nEDM is not measured between the current experimental limit and this lower value.

The experiment is based on the measurement of the spin dependent interaction between polarized UCN and polarized ^{3}He. Two measurement cells will be exposed to magnetic and electric fields, filled with superfluid helium-II, and be cooled to 0.4 K. In one cell, the fields will be parallel. In the other cell, the fields will be anti-parallel. If an nEDM exists within the regime specified above, a difference in the frequencies at which the UCN rotate will be revealed by the rate of interaction with the ^{3}He. Superconducting QUantum Interference Devices (SQUID) will be used to monitor the uniformity of the magnetic holding field in the cells. The SQUIDs will monitor the field generated by the polarized ^{3}He as it oscillates in the measurement cells and analysis of the signal will allow for highly accurate field mapping.

I conducted measurements on polarized ^{3}He in the type of cells to be used in the SNS-nEDM experiment. Additionally, I conducted some measurements using SQUIDs to develop an understanding of their operation and what is needed to minimize environmental noise sources. These measurements are outlined in Ch. 3 along with descriptions of a ^{3}He polarization technique, Nuclear Magnetic Resonance (NMR) and SQUID operation.

The SNS-nEDM experiment is a monumental undertaking. It is estimated that nearly 6 months will be required for a single cooling and warming cycle, assuming no experimentation is performed while cold. In Ch. 4, an experiment called PULSTAR-SOS, which is being built as test bed for the SNS-nEDM, is described. The PULSTAR-SOS uses many of the same operational parameters as the SNS-nEDM. The primary differences are that PULSTAR-SOS will use a single cell and not include an electric field. It is being built and partially

commissioned at the Triangle Universities Nuclear Laboratory (TUNL) on Duke campus in Durham NC and will be operated in the PULSTAR reactor on NC State University campus in Raleigh NC.

Superfluid helium-II produces scintillation when exposed to some particles and atoms, such as the protons and tritons produced by the UCN and ^{3}He interaction. The collection of that scintillation light is a very important experimental technique for the SNS-nEDM. When helium-II is exposed to a 5.5 MeV α particle source, it also produces scintillation in a high energy density manner similar to the UCN and ^{3}He reaction products. I performed measurements at Los Alamos National Laboratory on this scintillation process. Ch. 5 discusses these measurements.

The last chapter of the thesis is Ch. 6 offering an overview of what has been discussed and how the content of the thesis is related to future work by the SNS-nEDM collaboration. This chapter also describes the current state of experiments being developed throughout the thesis.

The appendices attempt to give more detailed information on the background of some topics discussed in the thesis. Topics which may be considered tangential to the physics content of the thesis are found here in order to avoid drawing the reader's mind adrift.

At this point, it may be useful to define a use of language about helium which can be confusing. What most people would refer to as *regular* helium is also called "helium four" or ^{4}He because there are four nucleons in its nucleus, specifically two protons and one neutron. That type of helium was used very often during this work. When helium is cooled until it condenses into a liquid, it can be referred to as "liquid helium", LHe, "helium-I", or "helium one". When it is cooled even further, past the *lambda point* T_λ, it becomes a superfluid which has a lot of special properties. When it becomes a superfluid, it can be called "helium-II" or "helium two".

There is another type of helium that's a bit less common but still extremely common called "helium three" or ^{3}He. It's called that because it has three nucleons, specifically two

protons and one neutron. Sometimes, in this text, LHe is referred to as ^{4}He because the nature of its nuclear properties is relevant to the context of this work. For example, at atmospheric pressure, which is ∼1013 mbar, ^{4}He becomes a liquid at 4.2 K. At that same pressure, ^{3}He becomes a liquid at 3.2 K. Also, the superfluid transition temperature of ^{4}He is ∼2.17 K, while the transition occurs much closer to 1 mK for ^{3}He. If you'd like to learn more helium, there is an excellent book by J. Wilks called *The Properties of Liquid and Solid Helium* [33] which goes into amazing detail regarding these topics.

I hope this thesis is an asset to your work or interests.

Chapter 2

EXPERIMENTAL CONSIDERATIONS FOR THE SEARCH OF THE nEDM

This chapter gives a brief description of the neutron electric dipole moment (nEDM) experiment being developed for the Spallation Neutron Source (SNS) at Oak Ridge National Laboratory (ORNL). Throughout this document, this experiment will be referred to as the SNS-nEDM. The experimental sensitivity is planned to detect or set an upper limit of the nEDM to $d_n < 3 \times 10^{-28}$ $e\ cm$ [31] which would be an improvement on the current limit by two orders magnitude.

The theory underlying the use of electric fields to manipulate a possible nEDM are discussed in section 2.1. In that section, geometric details about the experimental apparatus are discussed including the measurement cells and field orientations. The calculated *bottle* lifetime of the UCN are outlined there as well. Some detail is given about the UCN and ^{3}He interaction, which results in the production of a proton and triton. Scintillation in the helium-II then produces extreme ultra violet (EUV) light as a result of interactions with these reaction products. The reader will also find a description of the critical spin dressing technique. Additional subsections have been added which attempt to explain how the UCN are produced in the measurement cells, previous analysis of systematic effects arising from the ^{3}He, and how the wavelength of the EUV light will be shifted to be made detectable.

2.1 SNS-nEDM Overview

When a magnetic moment $\boldsymbol{\mu}$ is placed in a magnetic field $\boldsymbol{B}$, the magnetic moment attempts to align with the field. If the moment is not aligned with the field, the component of the moment which is at a right angle to the field will exert a torque on the moment, $\boldsymbol{\tau} = \boldsymbol{\mu} \cdot \boldsymbol{B}$. This torque causes precession in the plane perpendicular to the field which is called *Larmor Precession*.

The neutron is a spin 1/2 particle with magnetic dipole moment $\boldsymbol{\mu}_n = \mu_n \boldsymbol{s}$, where $\boldsymbol{s}$ is the spin direction. The Larmor precession frequency from the magnetic dipole moment is $\nu = 2\mu B/h$. If the neutron possesses a non-zero electric dipole moment then $\boldsymbol{d}_n = d_n \boldsymbol{s}$. If it is then exposed to an external electric field, the Larmor precession frequency due to the electric dipole moment is $\nu = 2dE/h$.

The SNS-nEDM experiment will place neutrons in parallel and anti-parallel magnetic $\boldsymbol{B}$ and electric $\boldsymbol{E}$ fields. Referring back to Eq. 1.5, the spin Hamiltonian of the system can then be written as

$$H = -\left(d_n \boldsymbol{s} \cdot \boldsymbol{E} + \mu_n \boldsymbol{s} \cdot \boldsymbol{B}\right)$$

Following the previous statements, we can see that the Larmor frequency is

$$\nu = -2(\mu_n B + d_n E)/h \tag{2.1}$$

If the electric field is reversed $\boldsymbol{E} \rightarrow -\boldsymbol{E}$ and anti-parallel to the magnetic field, the Larmor frequency will be

$$\nu = -2(\mu_n B - d_n E)/h \tag{2.2}$$

Taking the difference between Eqs. 2.1 and 2.2, it can be seen

$$\Delta\nu = 4dE/h \tag{2.3}$$

From Eq. 2.3, the Larmor precssion frequency shift from the presence of a neutron EDM is seen to be linear in $\boldsymbol{E}$. This linear relationship is the most basic description of how the SNS-nEDM experiment is going to test the upper limit of a possible nEDM. The upper bound on this difference in frequency which can be investigated by the nEDM experiment is 3×10^{-28} $e\ cm$ [31].

The experimental region will be made of two rectangular PolyMethyl MethAcrylate (PMMA) cells with internal dimensions of 40 cm $\times$ 7.5 cm $\times$ 10 cm. Some discussion is

presently underway about changing these dimensions by a few centimeters. Fig. 2.1 shows a photograph of one of the cells.

The cells will be filled with isotopically pure superfluid ^{4}He and cooled to 0.4 K.

They will be placed near each other separated only by a high voltage (HV) electrode along one of their long sides. They will be exposed to a magnetic field with strength 30 mG, which will be uniform in both measurement cells and perpendicular to their longest axis. Ground electrodes will be placed on the far sides of each cell. This will create electric fields in each cell which are opposite in direction but equal in magnitude. This arrangement will result in one cell having an electric field parallel to the magnetic field while the other cell will have an electric field anti-parallel to the magnetic field. The electrodes will be capable of producing electric fields with $|E| \gtrsim 75$ kV cm^{-1} [34]. An electric field of this magnitude is possible because of the high dielectric breakdown strength of superfluid helium. Thus, Eq. 2.3 can be tested directly.

The cells will be filled with polarized ^{3}He from an atomic beam source to a [^{3}He:^{4}He] concentration of 10^{-10}. The ^{3}He will act as a comagnetometer, polarization analyzer, and detector. The polarization of the ^{3}He from the atomic bean source is expected to be $\sim$99.5% [35]. In this situation, the ^{3}He moves through the superfluid in a manner referred to as a *mechanical vacuum*. The ^{3}He lightly bonds with the surrounding ^{4}He atoms and moves as if it's mass were 2.3 $\times$ $m_{^3He}$. The superfluid still mostly allows the ^{3}He to move through it without viscosity, as superfluids are commonly described. The reader is referred to *The Properties of Liquid and Solid Helium* by Wilks [33] for more details about how superfluids behave. More discussion about polarized ^{3}He is offered in section 2.3.

Systematic effects in the magnetic fields within the measurement cells are of great interest because small deviations from the expected behavior could result in the measurement of a false EDM. For example, current leakage in the magnetic array could lead to mimicking of a false EDM [32]. Using magnetically susceptible atoms, such as ^{3}He, in the measurement cells with the UCN will help to identify field drifts as they occur. Thus the polarized ^{3}He

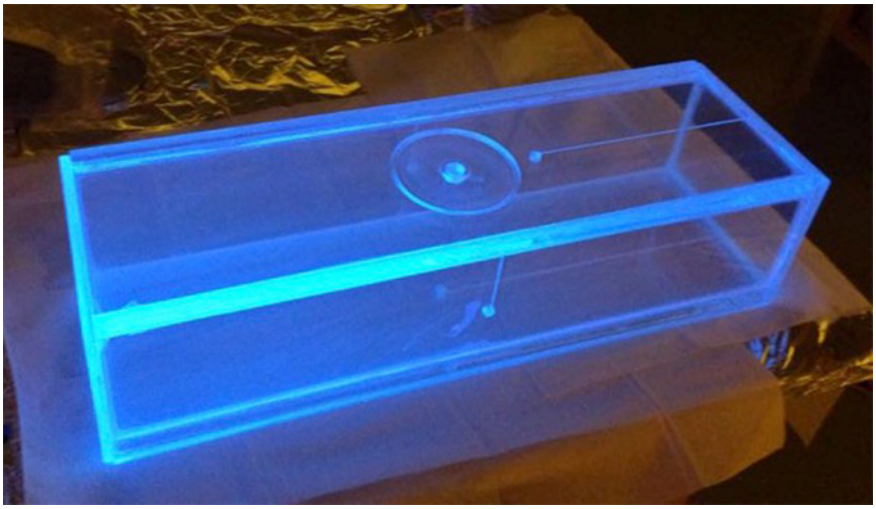


Figure 2.1: *Photograph of Full Sized Cell for SNS-nEDM Showing dTPB-dPS Illuminated Under UV Light. Photo Taken by Kent Leung.*

will be used to map the magnetic field strength throughout the cells to ensure uniformity in the field is maintained. The neutron number density will be described later in this section and will be less than 10^3 UCN cm^{-3}. The ^{3}He number density will be $\sim 10^{12}$ cm^{-3}, resulting in oscillating magnetic strengths on the order of a few fT. An array of Superconducting QUantum Interference Devices (SQUID) will be placed near the cells to monitor the ^{3}He oscillating fields. Section 3.4 goes into significantly more detail about how magnetic field non-uniformities influence the precession of the spins.

The neutrons will then be introduced to the measurement cells. The neutrons are provided by the Spallation Neutron Source (SNS) at Oak Ridge National Laboratory [36]. As of this writing, the SNS is in the Guinness Book of World Records as the "Most powerful pulsed spallation neutron source" producing an energy of 300 Kilowatt [37]. An accelerator sends pulses (microsecond duration) of protons onto a steel target filled with flowing liquid mercury, from there neutrons are emitted, and guided to the many experiments in the research bay.

The neutrons for the SNS-nEDM experiment are guided to a room on the side of the main research bay. This room was specifically built to house the SNS-nEDM experiment. The FNPB cold neutron beam will provide cold neutrons which are sent into the measurement

cell [38]. This is called "*in-situ* UCN production". A super-mirror and chopper will restrict the neutrons entering the cells to only neutrons with 8.9Å± 1% [39]. The production of the UCN comes from downscattering of the neutrons on the superfluid helium. Section 2.2 discusses the downscattering process. The volumetric production rate of polarized UCN is expected to be 0.31 UCN cm^{-3} s^{-1} [39].

The UCN will remain in the cell with a lifetime τ given by

$$\frac{1}{\tau} = \frac{1}{\tau_\beta} + \frac{1}{\tau_{up}} + \frac{1}{\tau_{^3He}} + \frac{1}{\tau_{walls}} \tag{2.4}$$

where $\tau_\beta \approx 879.3 \pm 0.75$ s is the beta decay lifetime for neutrons in a bottle (different than the current measurement from neutron beam measurements) [40], $\tau_{up} \approx 7 \times 10^4$ s is the lifetime for the neutrons to be upscattered by the superfluid helium [41], and $\tau_{^3He} \gtrsim 10^4$ s is the neutron and ^{3}He capture lifetime. The value for τ_{walls} is not a value which can be measured but must be calculated using the formula above. The value for τ for a cell can be measured. The design goal is to have $\tau_{walls} >$ 2,000 s [39]. Using these parameters, it is expected that the UCN density in the cell will be $\approx$ 170 UCN cm^{-3}.

The ^{3}He and neutron interaction produces an oppositely directed pair of protons and tritons, as described here

$$n +^3 He \rightarrow p + t + 764\ keV \tag{2.5}$$

The absorption cross section for the interaction between the neutron and ^{3}He is highly spin dependent. The following equation describes rate of absorption [29]

$$S(t) = \frac{\rho_{UCN}\ V}{\tau_{^3He}} \left(1 - P_n\ P_{^3He} \cdot cos(\theta_{n-^3He}\ t)\right) \tag{2.6}$$

where P_n and $P_{^3He}$ are the neutron and ^{3}He polarizations, respectively, ρ_{UCN} is the UCN density, V is the volume, and $(\tau_{^3He})^{-1}$ is the rate of absorption in the unpolarized configuration.

The initial preparation will polarize the ^{3}He and neutrons into the same spin state, minimizing the probability of a capture. They are then tipped by an angle of $\pi/2$, so that they are perpendicular to the magnetic field. The Larmor precession frequency is then guided by the Hamiltonian. The ^{3}He EDM is shielded by its electron cloud and will have no influence on its precession. Thus, the angle between the ^{3}He and neutrons θ_{n-^3He} will change in relation to $d_n \boldsymbol{s} \cdot \boldsymbol{E}$.

The rate at which particles precess is $\omega = \gamma\ B_0$, where γ is the gyromagnetic ratio and B_0 is the holding field strength. More details about this process are discussed in section 3.4. The relation between the ^{3}He and neutron gyromagnetic ratios is $\gamma_{^3He} \approx 1.112 \times \gamma_n$. Thus, the ^{3}He will spin faster than the neutron. Since they will be rotating at different rates, the angle θ_{n-^3He} from Eq. 2.6 will change allowing a sweep of values across that equation.

A technique called *critical spin dressing* is described by Golub and Lamoreaux [29] and will be used in this experiment. *Spin dressing* alters the precession frequency of a species by applying a non-resonant oscillating magnetic field. The technique wiggles the field perpendicular to the precession plane. This causes the precession in the plane to slow down and can be used to reach a specific desired frequency. The critical spin dressing will apply this technique to both species simultaneously. The intention is that the frequency of rotation can become equal allowing selection of the angle between the ^{3}He atoms and neutrons. With the angle selected, the ^{3}He acts as a polarization analyzer and detector.

When the neutron capture occurs, the reaction products found in Eq. 2.5 interact with the LHe bath and cause LHe scintillation in the extreme ultra-violet (EUV) [42]. The EUV light travels through the LHe in the measurement cell and reaches the cell wall. The cell walls are coated with Deuterated TetraPhenyl Butadiene-doped deuterated PolyStyrene (dTPB-dPS). The dTPB-dPS is a wavelength shifter which shifts the EUV light to blue light, detectable by silicon photomultipliers (SiPM) [43]. I performed research on a similar scintillation process at Los Alamos National Laboratory using α particles and those studies are discussed in Ch. 5. Further discussion of the dTPB-dPS coating can be found in section

2.4. The blue light enters the cell walls and is directed toward fiber optic cables which guide the light to SiPMs far from the strong electric fields around the measurement cells.

2.2 Production of UCN

Prior to the introduction of ^{3}He or neutrons to the measurement cells, the cells will be filled with superfliud liquid helium, in the helium-II phase. A cold neutron beam line will guide the neutrons into the experimental cells. The polarized cold neutron beam will penetrate the PMMA cell walls easily. Once in contact with helium-II, the cold neutrons will be downscattered to ultra-cold neutrons (UCN) by "Super-thermal" process [44] which is a coherent single-photon emission process. UCN are neutrons which are fully reflected at angle of incidence [45] and thus will be remain inside the measurement cell. The dispersion curves seen in Fig. 2.2 shows the wavenumber and energy of each species. The intersection is the energy at which the downscattering can occur and results in a neutron essentially at rest.

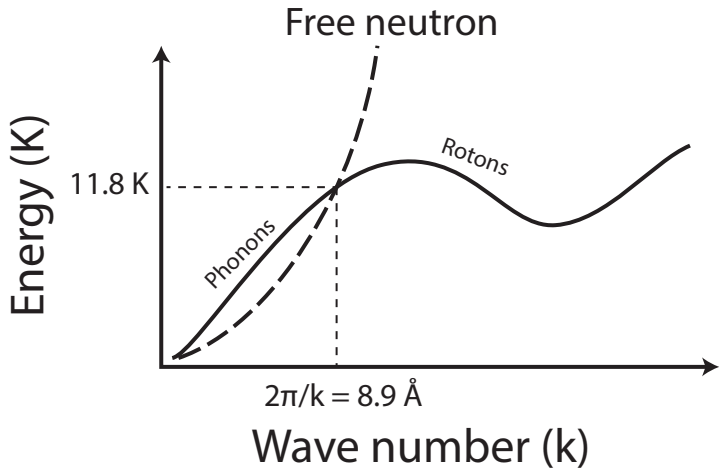


Figure 2.2: *Free Neutron and Helium-II Dispersion Curves. The Neutron Can Be Downscattered Via Coherent Single-photon Scattering, Resulting in the Neutron Being at Rest.*

2.3 ^{3}He as Comagnetometer, Polarization Analyzer, and Detector

As mentioned above, polarized ^{3}He will be used as a comagnetometer, polarization analyzer, and detector. Its service in these roles have been described in section 2.1. This section describes some of the systematic issues with using ^{3}He in the experiment and gives some report on what the collaboration has done to understand the possible influences it may have on operations and results.

As one would expect, there are systematic effects which can result from using a co-habiting species. Specifically, the Bloch-Siegert induced false EDM, commonly referred to as the *geometric phase frequency shift* is of concern [46, 47]. The effect is caused by the interaction of the motional magnetic field resulting from the interaction between the co-habiting atom's movement via $\boldsymbol{v} \times \boldsymbol{E}$. Thus, this effect is linear in electric field as is the possible EDM.

A general solution to the geometric phase has been developed using the density matrix [48]. Work by Barabanov, Golub, and Lamoreaux proposed a method to directly measure the geometric phase through the atom's velocity correlation function by measuring the longitudinal relaxation rate for the polarized ^{3}He atoms [49, 50]. Significant experimental progress was made on understating the effect by J. Yoder [51], Q. (Alan) Ye [52] and C. Swank [1]. In their studies, they investigated the systematic effect by measuring the longitudinal relaxation rate T_1 of polarized ^{3}He. The intricate details of the T_1 are not necessary at this point and are discussed in more detail in section 3.5.2. A simple explanation of the T_1 is that it's the relaxation time constant of an exponential function for the atoms which is caused by interactions with the environment (i.e. the measurement cell).

The study by J. Yoder [51] and Q. Ye [52] were conducted at the same time. These were the first investigations into the depolarization rate of ^{3}He on a dTPB-dPS surface at low temperature. In Ye's thesis, measurements performed at 1.9 K and $\sim$0.4 K are reported. He performed measurements on the ^{3}He depolarization rate in a small cylindrical measurement cell with length 2 inches and diameter 2 inches. Starting with data from the

small measurement cell used in his study and extrapolating to the full scale measurement cell planned for use in the SNS-nEDM, the T_1 relaxation time constant in the full scale cell is ∼4870 secs. The calculated holding time of neutrons in the SNS-nEDM measurement cell was reported in section 2.1 and is ≈ 600 secs. This demonstrates that the ^{3}He depolarization rate will not be the limiting factor in a successful measurement.

In his study, C. Swank examined the position-position correlation function of polarized ^{3}He within a similar experimental environment to what will be present in the SNS-nEDM experiment [1, 53]. Those conditions included a cell made of the same material and coated with the same wavelength shifting molecules dTPB-dPS. The measurement cell and dTPB-dPS will be discussed in section 2.4. Measurements were made in the transition region with [^{3}He:^{4}He] molar concentration ratio as low as 10^{-6}. Further study is needed because the SNS-nEDM will be operating with a concentration of 10^{-10}.

2.4 Scintillation Detection in Superfluid Liquid Helium

Extreme ultra-violet (EUV) photons with wavelength 80 nm are produced by LHe scintillation in response to the charged proton and tritons as they recoil from an interaction location between the neutron and polarized ^{3}He [54]. Presently, Hamamatsu SiPMs are being tested for light detection. They have a maximum photon detection efficiency between 400 to 500 nm [55].

To make the photons detectable, the interior surface of the measurement cell will be coated in *Deuterated TetraPhenyl Butadiene-doped deuterated PolyStyrene* (dTPB-dPS). When the EUV photons reach the dTPB-dPS coating they are wavelength shifted to blue light as it passes the interior wall and enters the PMMA volume. The blue light has a spectral peak at 440 nm with a width of 50 nm [56]. The light is then transported down the interior of the measurement cell walls to fiber optic cables which then transport it to SiPMs for detection. Low neutron absorption cross section and excellent wavelength shifting efficiency make dTPB-dPS an ideal choice for the role it plays.

As mentioned in section 2.3, the depolarization rate of ^{3}He on the dTPB-dPS surface has been studied by J. Yoder, Q. Ye and C. Swank. Those measurements confirmed that the T_1 depolarization rate is low enough for reliable use of ^{3}He in this future experiment.

Chapter 3

ROOM TEMPERATURE AND CRYOGENIC MEASUREMENTS ON POLARIZED HELIUM-3

In the nEDM experiment currently being built at the Oak Ridge National Laboratory SNS facility, the measurement cell will be constructed of a dTPB-dPS coated PMMA cell and polarized ^{3}He will be used as a polarization analyzer, comagnetometer, and detector [29]. In reference to the SNS-nEDM experiment, these topics are discussed in Ch. 2.

This chapter discusses polarized ^{3}He measurements performed under conditions similar to those which will be encountered in the SNS-nEDM experiment. The experiments were conducted in a cryostat located in the Triangle Universities Nuclear Laboratory (TUNL) on Duke University campus. The experimental apparatus used in these studies consists of a cryostat, systems of magnetic coils, vacuum systems, computer systems, and thermometry. One set of measurements reported was taken at room temperature to test the quality of the deuterated TetraPhenyl Butadiene-doped deuterated PolyStyrene (dTPB-dPS) coating technique using Nuclear Magnetic Resonance (NMR). A second set of measurements reported was conducted at 4 K to test the use of a Superconducting QUantum Interference Device (SQUID). Measurements were performed on the noise background and ability to operate a SQUID to detect the polarized ^{3}He precession. The experimental system which was present in both is described in section 3.1.

In the SNS-nEDM experiment, polarized UCN and ^{3}He need to be held in the measurement cell for as long as possible. The longitudinal relaxation rate T_1 is an exponential time constant which characterizes the depolarization rate of a sample of polarized atoms or molecules as they are affected by the container and magnetic field gradients. Measuring the time constant T_1 using ^{3}He at room temperature in a cell similar to that planned to be used in the SNS-nEDM gives insight into the characteristics which can be expected at

colder temperatures. Specifically, it is expected that the T_1 at low temperature will be about 3 times larger than the T_1 at room temperature [1, 52]. This is partially due to less frequent collisions with the walls because of the slower motion of the atoms. The influence of dTPB-dPS on the T_1 is therefore of great interest.

The reason the measurement cells are coated with dTPB-dPS is to cause EUV light from the n-^{3}He interaction to be wavelength shifted into the visible spectrum and to detect that light using silicon photomultipliers (SiPM) [57]. Building and coating the measurement cells requires special processing and techniques. Optimal techniques are still being investigated. A coating process had been tested in previous experiments [1, 52] and continued investigation of the process is of interest. For the research reported here, a new dTPB-dPS coated PMMA cell was constructed and room temperature measurements performed on it. Some modifications to the cell design were used to reduce noise in the system and these changes are outlined in section 3.2.1. The design and construction of the cell is discussed in section 3.2.2.

The Spin Exchange Optical Pumping (SEOP) technique was used to polarize ^{3}He gas for these experiments. The technique and physical processes for SEOP are outlined in section 3.3.

The SNS-nEDM experiment will use NMR to monitor the orientation of neutrons and ^{3}He in the measurement cell. This is a common technique with many applications, the most common being Magnetic Resonance Imaging (MRI) used in the medical field. In medical applications, images are generated from the collected data. Of greater use for our experiment is frequency analysis of the signal, since the shift in frequency is the targeted parameter in the SNS-nEDM measurement. Some aspects of how NMR was used during the room temperature measurements are reported in section 3.4.

There are many techniques used widely and commonly in NMR systems. Details about how the NMR process was employed and the room temperature measurements on the constructed cell are discussed in section 3.5. The results show that the depolarization rates on

the dTPB-dPS coated surfaces are adequate for use in the PULSTAR-SOS and SNS-nEDM experiments.

Polarized ^{3}He will be used in the SNS-nEDM experiment at very low concentrations [58], roughly 10^{-10} [^{3}He:^{4}He]. This will result in a small magnetic field from the ^{3}He and thus a small flux through the detection system coils. To detect the small signal, the team plans to use SQUIDs. The extremely high sensitivity of SQUIDs makes shielding and reduction of environmental electromagnetic noise a priority. The theory of SQUIDs is outlined in section 3.6. Implementation of SQUIDs to test the noise background as well as polarized ^{3}He NMR calculations in relationship to the noise measurements are reported in section 3.7.

3.1 Common Experimental Apparatus

This section outlines the experimental systems which were used in both the room temperature (section 3.5) and SQUID measurements (section 3.7). The cryostat, magnetic coils, and measurement cell are all described here.

3.1.1 Cryostat

The cryostat is a cylindrical dewar from International Cryogenics with four layers. The layers are the Outer Vacuum Chamber (OVC), liquid N_2 jacket, liquid helium bath, and the Inner Vacuum Chamber (IVC). A Leiden Cryogenics Minikelvin 126-TOF dilution refrigerator is inserted centrally. The measurement cell and pick up coils were hung from the bottom of the mixing chamber of the dilution refrigerator.

There were three separate vacuum volumes: (a) OVC, (b) IVC, and (c) measurement cell. Two pumping systems were used to create and maintain the three volumes. One pumping system maintained the vacuums in the IVC and OVC, and a second pumping system maintained the vacuum in the measurement cell.

The vacuum for the IVC and OVC was maintained by a scroll pump backing a turbomolecular pump. Using flex-hose and valves, these pumps were used to pump down the IVC and OVC.

The pumping system for the measurement cell had a Pfeiffer turbo backed by a Pfeiffer piston pump. It was connected to a system of flex-hoses. This system was kept as clean as possible. This section of plumbing also used liquid nitrogen and liquid helium traps.

Both systems could also be connected to a helium leak checker. We considered it a good vacuum if the helium leak rate was $\mathcal{O}(10^{-9})$ mbar L s $^{-1}$.

When polarized ^{3}He was needed, I would polarize it in another lab and bring it to the experimental hall. Polarized ^{3}He can be transported in a set of magnetic holding field coils (usually Helmholtz coils) or in the Earth's magnetic field. During transit, it is carried in a spherical glass cell called the *transport cell*. It mentioned here because it will be mentioned again later.

When I began working with this cryostat, all the volumes were pumped down and the nitrogen jacket was filled with liquid nitrogen. In that scenario, the dilution refrigerator would take about two weeks to cool to 77 K then liquid helium cooling could begin. I spent some time with W. Yao installing tubing from the liquid helium filling location to the bottom of the helium bath as well as some power heaters at the bottom of the helium bath. Using a different technique than previously mentioned, we would (a) pump down the OVC, (b) fill the IVC with nitrogen, neon, or helium gas to about 200 mbar, (c) then fill the helium bath with liquid nitrogen. The gas in the IVC is called an *exchange gas* and provides faster cooling of the components inside the IVC than a vacuum provides. This would cool the dilution refrigerator to 77 K within a few hours. The top of the new tubing could then be connected to the liquid nitrogen jacket, the helium bath would be sealed, and the heaters in the helium bath could be powered on. This would evaporate some of the liquid nitrogen and fill the helium bath with pressurized nitrogen gas to a few hundred mbar above atmospheric pressure. The liquid nitrogen would be pushed through the tube, out of the helium bath, and into the nitrogen jacket.

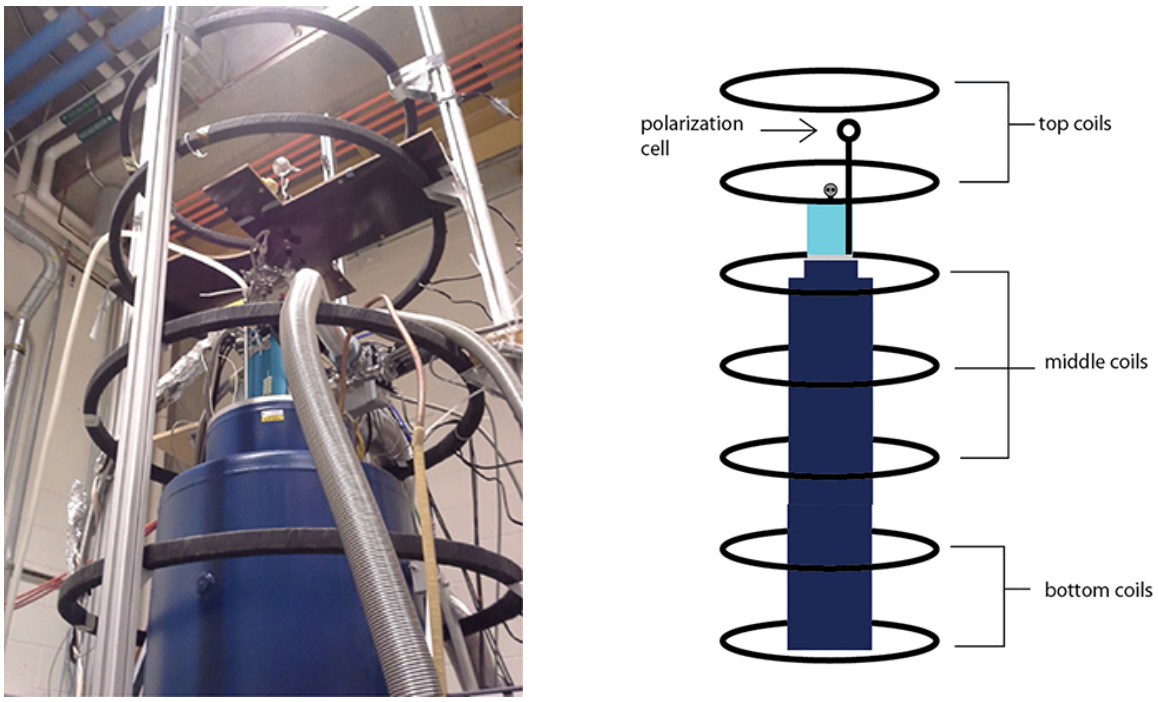
One technique at this point, is to start pumping on the helium bath. If the temperature drops then you know there is still liquid nitrogen in the bath. Liquid nitrogen become solid

nitrogen around 63 K, so if the temperature was getting close to that value, we were sure there was still liquid nitrogen in the helium bath. Another technique is to leave the heaters on until the temperature in the IVC reaches the mid 80s K. This technique ends up using slightly more liquid helium during the next phase of cooling. During my time in graduate school, I never once saw anyone feel confident about using the pumping technique, it was always a question about whether or not there may be some liquid nitrogen left in the bottom of the helium bath. If nitrogen had been left there and it became a solid, the cost in liquid helium would be significantly greater for cooling a volume of nitrogen than for just cooling the very thin metal sheets constructing the cryostat. For this reason, the second technique was always used for cooling later in our experiments.

At this point, we would begin to fill the helium bath with liquid helium. If nitrogen gas had been put into the IVC, it would be pumped out once the system reached 77 K. If neon gas had been put into the system, it would be pumped out as liquid helium was filling the helium bath and the system was reaching around 30 K. This is because it becomes a solid around 25 K. It wasn't an issue if some neon froze inside the IVC because the IVC contained a charcoal pump but evacuating it ensured that a random heat leak didn't develop. If helium gas was used, pumping would begin as the temperature reached 10 K or lower.

3.1.2 Common Magnetic Coil Systems

This section discusses the magnetics packages which were used in both the room temperature and SQUID measurements. The magnetics package for the experiments included holding field coils and NMR coils. Fig. 3.1 shows an image and schematic of the holding field coils and their positions. The holding field and NMR coils for the room temperature and SQUID measurements were the same. The pick up coils for the room temperature measurement and SQUID measurements were different and are discussed in sections 3.5 and 3.6.3, respectively. Additionally, the SQUID measurements had a superconducting Pb shielding which is discussed in section 3.6.3.



(a) **(b)**

Figure 3.1: *The Holding Field Coils Surround the Entire Cryostat and Transport Cell. (a) Photograph of Coils and Cryostat. (b) Schematic of Holding Field Coil Labels As Referenced in the Text.*

The holding field is generated by 7 coils surrounding the cryostat. The coils are 33 inches in diameter and separated by 16.5 - 17.5 in. There are three relevant groups of coils: top, middle, and bottom. All the coils maintain a vertical magnetic field to ensure the polarized atoms do not pass through a region of zero field, as this increases the likelihood of depolarization. The top two coils are a Helmholtz pair. They are centered around a location where the transport cell is placed and connected to the experimental system on top of the cryostat. The middle three coils hold the polarized atoms in a field during transportation to the measurement cell. The bottom two coils produce the field during the execution of the experiment.

Through a computer, the top and bottom sets of coils are controlled by Agilent 33120A WaveForm Generators and powered by the Kepco Power Sources. The middle group is controlled by the TekPower HY1803D DC Power Supply. The last full analysis of the field

produced by the coils was performed by Q. Ye and reported in his thesis [52]. Fig. 3.33 from that thesis is reproduced here as Fig. 3.2. In his work, eight coils were used, though only 7 coils were used in the current measurements.

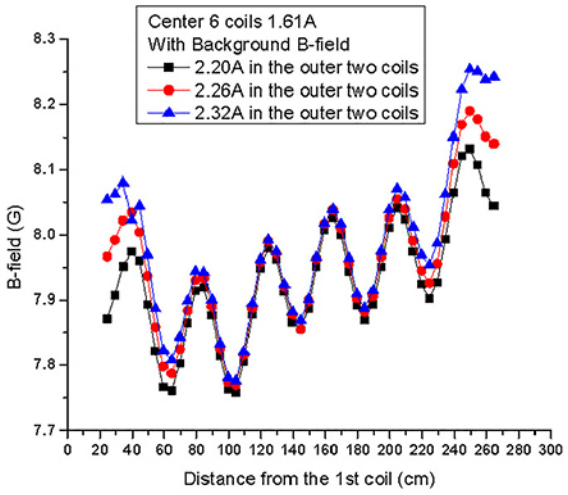


Figure 3.2: *Reproduction of Fig. 3.33 From Q. Ye's Thesis on the Holding Field Coils. In His Setup, He Used 8 Coils, in This Work Only 7 Coils Were Used. The Magnetic Field, Even at This Low Field Strength, Has Very Small Fluctuations From the Desired Field.*

The NMR tipping coils were rectangular and had been constructed by C. Swank for his thesis work [1]. The exact number of turns was not recorded but through calculation and visual attempts at counting, there seem to be about 15 turns per coil. They are composed of 22 gauge Cu wire, have inductance 106.3 μH, and resistance 0.7 Ω. Each coil is 5.5 inches wide and 7 inches tall. The coils are shown in Fig. 3.3. The NMR coils were controlled by the NMR control computer.

3.2 Design and Construction of a ^{3}He Measurement Cell

Experimental setups similar to the one being used in this work were previously built and used by C. Swank [1] and Q. Ye's work [52]. The previous design of this experimental apparatus [1] had a number of magnetized metals, likely to introduce additional electromagnetic noise which would compete with the desired signal. Upgrades were made to the buffer cell, support structure, measurement cell, pick up coils, and ^{3}He polarization system.

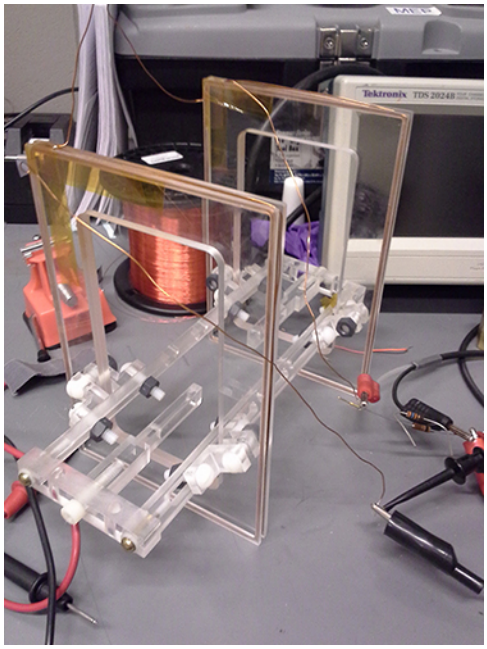


Figure 3.3: *NMR Coils Used in the Room Temperature Experiment.*

These upgrades (a) replaced magnetized metals with brass, (b) replaced indium seals with Kapton gaskets, and (c) improved thermal contact between the mixing chamber and the measurement cell. Many of the materials have changed but the measurement cell is still made of Poly Methyl MethAcrylate (PMMA). These changes are discussed in section 3.2.1.

Deuterated TetraPhenyl Butadiene-doped deuterated PolyStyrene (dTPB-dPS) was coated onto the interior of the measurement cell to test conditions similar to those planned for the PULSTAR-SOS and SNS-nEDM experiments. Section 3.2.2 discusses the process of designing and coating the PMMA measurement cell with dTPB-dPS.

3.2.1 Cell Designs

In the previous experiments using this apparatus [1, 52], the measurement cell was supported by 20 Cu wires attached to the mixing chamber and had a stainless steel (SS) capillary from the inside of the buffer cell to the measurement cell which allowed the transport of superfluid ^{4}He, see left side of Fig. 3.4. The Cu wires were used to support the cell and provide thermal connection between the measurement cell and mixing chamber.

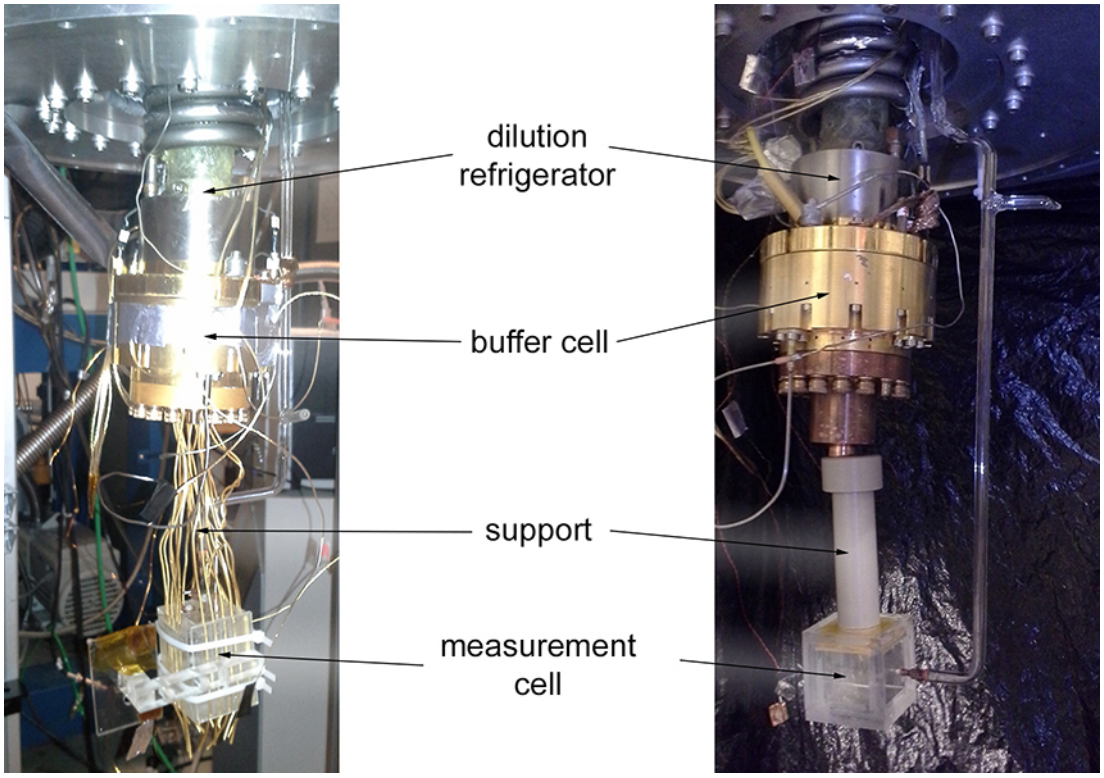


Figure 3.4: *Left: Previous Experimental Setup From C. Swank's Thesis Work [1]. Right: Assembly of Measurement Cell Geometry Used in Present Work.*

The wires were likely introducing Johnson-Nyquist noise to the system which may effect the signal when higher sensitivity is reached. The SS capillary would have had the same effect, although it's contribution would have been significantly less. These supports and transport line have been replaced by an extension to the buffer cell, a PEEK tube, and a Kapton capillary, see right side of Fig. 3.4.

The buffer cell extension is a sintered silver filled Cu housing, granting increased thermal contact between the LHe and buffer cell walls. It is sealed to the buffer cell with a Kapton gasket which was tested in the HMI cryostat to 1.5 K while immersed in LHe. The increase in the contact area between LHe and metal walls is very important. The velocity of sound in LHe and solid Cu are around 240 m/s and 4000 m/s, respectively. An analysis of Snell's Law for heat transfer from LHe to metal, shows that the fraction of phonons which are transmitted through the critical cone is about 1.8×10^{-3}. Analysis of the acoustic

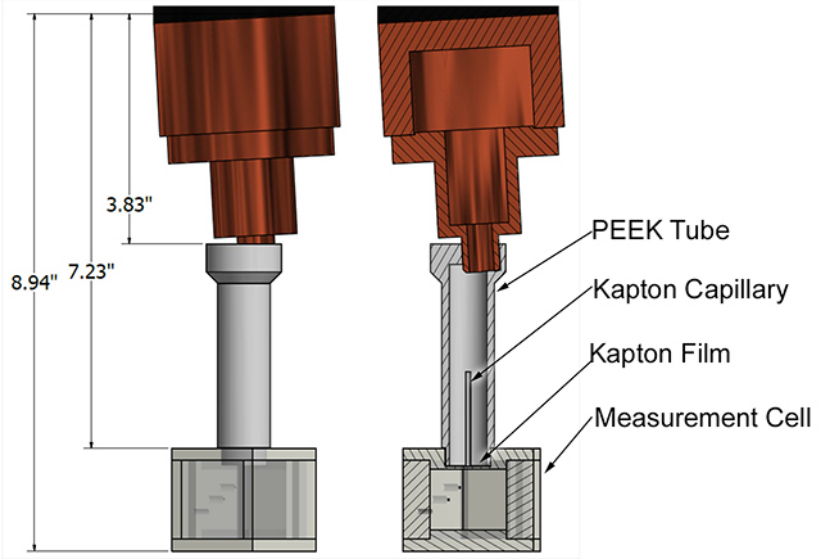


Figure 3.5: *Schematic of New Support and Cell Design. From Top to Bottom: Buffer Cell, Sintered Volume, PEEK Tube, Experimental Cell. The Mixing Chamber of the Dilution Refrigerator Was Misaligned Due to Damage Acquired During Shipping. To Account for This, the Center Bore Between Cu Volume and PEEK Tube Was Cut at an Angle and Results in the Experimental Cell Being Directly Below the Center of the Dilution Refrigerator. Illustrated by A. Reid.*

mismatch between the LHe and metal finds a transmission probability of 3.89x10 $^{-3}$. Taking the product of these values to find the actual likelihood of heat transfer from LHe to Cu by a phonon gives a probability of 10 $^{-5}$, showing that increasing the contact area as much as possible is very valuable and was implemented through the sintered volume. The calculations for this analysis are included in App. A.

The top of the measurement cell is no longer solid PMMA but instead has a hole in it with Φ 3/4 inch which is covered by a 5 mil Kapton film glued on from the inside during cell construction. The PEEK tube allows ^{4}He from the buffer cell to contact the top of the Kapton film. This should permit superior cooling of the contents of the cell when compared to the previous design using the Cu wires. A hole was then made in the Kapton film using a needle and a Kapton capillary was glued to one side of the film concentrically aligned with the hole. A small acrylic ring was placed near the base of the Kapton capillary for support. The capillary extends nearly to the bottom of the sintered volume and will allow superfluid ^{4}He to flow from the PEEK tube into the measurement cell. See Fig. 3.5.

We now wish to know how quickly polarized ^{3}He will flow through this orifice and into the PEEK tube. Two cases are of interest in regard to the experiments discussed in this thesis, either the measurement cell will be under vacuum when the polarized ^{3}He is introduced or it will be filled with superfluid ^{4}He. The following calculation assumes the first case, where the measurement cell is under vacuum.

The primary geometric parameter we are interested in is the conductance C_{total} from the measurement cell to the PEEK tube. First, we find the conductance through the orifice on the Kapton film [59].

$$C_{orifice} = A \cdot \frac{\bar{c}}{4} \tag{3.1}$$

$$= A \cdot \frac{1}{4} \cdot \sqrt{\frac{8kT}{\pi m}} \tag{3.2}$$

$$= A \cdot \sqrt{\frac{k_B T}{2\pi m}} \tag{3.3}$$

where A is the area of the orifice, $\bar{c}$ is the mean thermal velocity, k_B is Boltzmann's constant, and m is the (mean) molecular mass for the particular gas in the vacuum vessel. The orifice in the Kapton film had $d_{orifice} = \Phi 0.3\ mm$. ^{3}He has 3 nucleons and thus $m = 3 \cdot (1.66 \times 10^{-27}\ kg) = 4.98 \times 10^{-27}\ kg$. Thus

$$C_{orifice} = \pi \left(\frac{d_{orifice}}{2}\right)^2 \left(\frac{k_B T}{2\pi m}\right)^{1/2} \tag{3.4}$$

$$= 3.04 \times 10^{-6}\ m^3/s \tag{3.5}$$

Next, we would like to know the conductance through the Kapton capillary. This is most easily accomplished by looking in a reference figure, such as Fig. 3.16 in *Experimental Techniques for Low-Temperature Measurements* by J.W. Ekin [59]. The Kapton capillary has $ID = 0.3\ cm$ and length $L = 3\ in = 7.6 \times 10^{-2}\ m$. We find the conductance of the capillary is

$$C_{capillary} = 3 \times 10^{-4}\ m^3/s \tag{3.6}$$

We can then calculate the total conductance C_{total} from the measurement volume through the orifice and Kapton capillary to be

$$\frac{1}{C_{total}} = \frac{1}{C_{orifice}} + \frac{1}{C_{capillary}} \tag{3.7}$$

$$C_{total} = 3.01 \times 10^{-6}\ m^3/s \tag{3.8}$$

We are now going to need to know how many atoms are inside the measurement cell at the start of a measurement. First, we may calculate the number of moles which were in the transport cell n_t. Let's assume the transport cell, at room temperature, contained roughly $P_t = 1$ atm $= 10^5$ Pa $= 1013$ mbar of gaseous ^{3}He. The transport cell has volume is $V_t =$ 180 cc. The ideal gas law can be used to find the number of moles in the transport cell.

$$n_{total} = \frac{P_t\ V_t}{R\ T_t} \tag{3.9}$$

$$\approx\ 7.2 \times 10^{-3}\ mol \tag{3.10}$$

where $R = 8.31\ Pa\ m^3\ mol^{-1} K^{-1}$ is the gas constant and T_t is the temperature.

The volume of the measurement cell is V_m=16.4 cc. We can calculate the number of moles n_m of ^{3}He which move into the measurement cell by another application of the ideal gas law. The total number of moles of atoms in the system will now be distributed between the transport cell volume V_t and measurement volume V_m such that $n_{total} = n_m + n_t$. When the transport cell is opened to the measurement cell, equalization between the two volumes will occur until the pressures in each volume are equal.

$$P_t = P_m \tag{3.11}$$

$$\frac{n_m R T_m}{V_m} = \frac{n_t R T_t}{V_t} \tag{3.12}$$

$$\frac{n_m R T_m}{V_m} = (n_{total} - n_m)\frac{R T_t}{V_t} \tag{3.13}$$

$$n_m = n_{total}\left(\frac{T_m}{V_m}\frac{V_t}{T_t} + 1\right)^{1/2} \tag{3.14}$$

$$= 6.3 \times 10^{-3}\ mol \tag{3.15}$$

where the subscripts t and m represent quantities related to the *transport* and *measurement* cells, respectively. Once these atoms have entered the measurement cell, the valve between the measurement cell and transport cell is closed. From this point on, only n_m moles of ^{3}He are in the system. The system will now equalize the pressure between the measurement cell and PEEK volume through the orifice and Kapton capillary.

The gas volume flow rate Q is used to calculate how quickly the gas will flow.

$$Q = C_{total}(P_1 - P_2) \tag{3.16}$$

where P_1 is the ^{3}He gas pressure inside the sample and P_2 is the pressure inside the PEEK tube. The gas pressure inside the cold cell at this point is $P_1 \approx 133\ mbar = 13,300\ Pa$. The pressure in the PEEK tube is $P_2 \approx 10^{-4}\ mbar$ because it has been under vacuum until this moment. Since $P_1 \gg P_2$, we don't actually need to include P_2 in this initial calculation. Thus

$$Q = C_{total}\ P_1 \tag{3.17}$$

$$= 0.040\ Pa\ m^3/s \tag{3.18}$$

The relation between the gas volume flow rate Q and molar flow rate $\dot{n} = \delta n/\delta t$ is $Q = \dot{n}RT$ where $R = 8.31\ J/(mol\ K)$ is the gas constant and $T = 4.2\ K$ is the temperature.

$$\dot{n} = \frac{Q}{RT} \tag{3.19}$$

$$= 1.2 \times 10^{-3}\ mol/s \tag{3.20}$$

The flow of the atoms from the measurement cell to the PEEK tube follows an exponential curve of the form $n(t) = n_m\ EXP(-t/\tau) + n_{eq}$, where n_{eq} is the equilibrium number of atoms left in the measurement cell. The time constant τ is

$$\tau = \frac{n}{\dot{n}} \tag{3.21}$$

$$= \frac{6.3 \times 10^{-3}\ mol}{1.2 \times 10^{-3}\ mol/s} \tag{3.22}$$

$$= 5.25\ sec \tag{3.23}$$

After about 4 τ, the exponential has decayed to within $\sim 1.8\%$ of the systems equilibrium state and so we can say the system is fairly stable after about 20 secs. We assume all ^{3}He which enters the PEEK volume becomes depolarized, as they will bounce off the Cu volume at the top of the tube. Particle exchange between the PEEK tube and measurement volume decreases significantly at this point.

The dilution refrigerator had previously been used by Bob Golub while he worked in Germany. During transportation to the United States, the mixing chamber stage was damaged. A manual repair was performed leaving the mixing chamber at an angle, see the right side of Fig. 3.4. While using the Cu wires, the cell could easily be positioned in 3 dimensions at the desired location without much effort. The PEEK tube however is a rigid body and if it had been constructed with perfect symmetry relative to the mixing chamber, the measurement cell would have had 1 inch horizontal displacement from the center of the magnetics package. Care was taken to measure the angle of the mixing chamber relative to horizontal and the PEEK tube was designed to account for the angle. This knowledge was implemented by cutting a specialized access hole for the mixing chamber extension at an

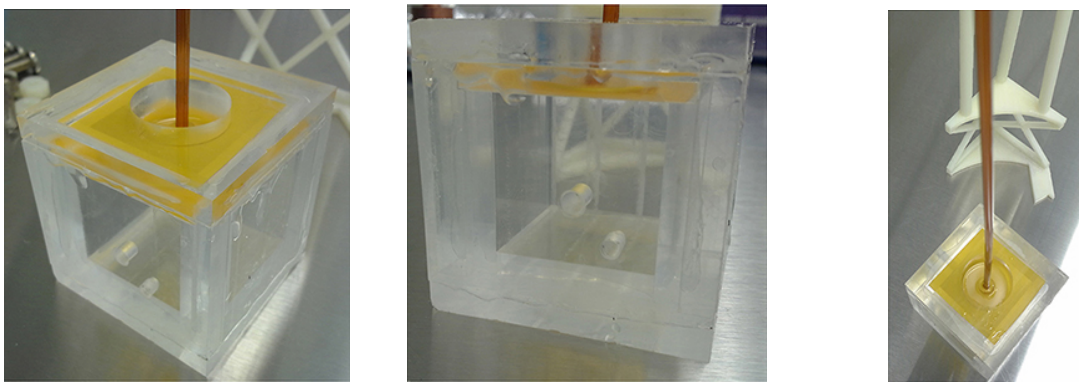
angle and supporting the cell and PEEK tube in a 3D printed fixture during the application and drying of Stycast 1266. The implementation was a success, the cell is less than 1^0 from horizontal and occupies a position central to the magnetics package.

The buffer cell has four seals on it. Three of the seals are small ports for transport of the ^{4}He into and out of the buffer cell. The large fourth seal previously held the flange to which the Cu support wires were attached but now is attached to the buffer cell extension containing sintered silver. Each of these had previously been sealed with a Φ 0.8 mm indium. Indium goes superconducting below 3.4 K however, which would add undesired and unpredictable magnetic fields around the sample. Simulations were run to estimate the influence of the seals on the magnetic fields near the sample. It was determined that the large seal could cause enough distortion in the fields to warrant investment of time to find a new solution. A 5 mil Kapton gasket was cut to seal this flange which was tested successfully to 1.5 K in the HMI cryostat while immersed in superfluid LHe. The small seals was successfully replaced with a Kapton gaskets.

3.2.2 Measurement Cell Geometry and Coating

The measurement cell is a hollow PMMA cube. It has exterior side length 1.702 inches and interior side length 1 inch. The volume is 1 in^3 (16.39 cc). It is glued together using Stycast 1266 from six sides custom designed and machined. The top of the cell has a 3/4 inch through hole which is covered on the inside with a 5 mil Kapton film. This allows thermal contact between ^{4}He in the buffer cell and the contents of the cell, see Fig. 3.6 (a) and (c).

When being used with superfluid ^{4}He, the ^{4}He can enter the cell from the top through the Kapton capillary. The Kapton film covering the top of the cell has a pin hole poked into it which will not allow much polarized ^{3}He to escape. The ^{3}He travels from the top of the cryostat down through a glass tube and will enter the cell from the side through the Cu to glass transition.



(a) **(b)** **(c)**

Figure 3.6: *The Measurement Cell Before Being Attached to the PEEK Tube. (a) the 5 mil Kapton Film on the Interior Top of the Cell Is Yellow. (b) the Central Hole in This Design Is for Filling the ^{3}He From the Glass Tube. The Smaller Hole Below and to the Right Is a Threaded Blank for a Temperature Sensitive Resistor. (c) Top View of Cell: The Kapton Capillary Is Visible As Well As the Acrylic Ring Supporting the Capillary on the Film.*

The interior faces of the PMMA and the Kapton surface were coated with dTPB-dPS. The SNS-nEDM experiment will also have its cell coated with this material to allow extreme ultra-violet (EUV) photons to wavelength shift to the visible spectrum for detection by SiPMs. The dTPB-dPS is not used here for that purpose but instead to match some of the experimental conditions of the SNS-nEDM experiment as closely as possible.

The dTPB-dPS is sensitive to UV light and deteriorates in it's presence. For this purpose a clean room with non-UV emitting lights was used to mix the solution and coat the interior surfaces. The dTPB-dPS was mixed beforehand and placed in a petri dish. A suction cup was attached to the outside of the cell wall and the interior surface carefully dipped horizontally a couple of mm into the solution for a few seconds. The wall was removed from the solution and the suction cup then held firmly by hand on the non-covered sides and force dried by waving the arm up and down. This technique was developed by the PULSTAR team and is found to result in the most uniform distribution of film on the surface of PMMA. Other techniques resulted in irregularities in the density of the film, or areas uncovered. When exposed to UV light, dTPB-dPS glows bright blue. Fig. 2.1 shows a photograph of the cell while being illuminated by a UV light. All interior surfaces of

the cell are glowing. Once all the walls were coated, the surfaces were checked using this technique and irregularities or imperfections were not visible to the naked eye.

Stycast 1266 is an epoxy composed of two solutions. When mixed in the proportion of 0.28:1 by weight, the solution begins to harden over the following 3-24 hrs depending upon the temperature. After mixing the solutions, the user stirs by hand for 5 min. It is ideal then to place the solution in a vacuum for 10 min to remove all bubbles. At this point it is ready for application and will be extremely viscous 60 min later. To reach the ideal viscosity, an unused cell was practiced upon while the Stycast cured. About 25 min after removing the solution from the vacuum chamber, when the viscosity was high enough to feel when manipulating with a glass pipette, the cell was carefully constructed by hand then placed inside of a system of three clamps. Ideally, the Stycast will fill the gaps and not enter into the interior region of the cell covered with dTPB-dPS. Visual inspection offered positive confirmation that the distribution of Stycast was in the appropriate locations through the cell. Leak checking with gaseous He after installation of the cell in the Cell Assembly confirms that no gaps exist in the joints of the cell.

3.3 Spin Exchange Optical Pumping Technique

This section explains the process of polarizing the ^{3}He. The process is called Spin Exchange Optical Pumping (SEOP) [60, 61, 62]. The basic idea is that one can polarize an electron on an alkali metal vapor atom and transfer the polarization to the nucleus of the ^{3}He atom.

The first step is to coat the interior of a glass cell with an alkali metal. This process is described very well by Jacob *et al* [63]. If you choose to follow the instructions in that paper, be sure to follow each instruction carefully. No steps should be omitted. For our setup, Rb was used to coat the cell. A summary of the technique I used to create SEOP cells is contained in App. B.

A gaseous mixture of ^{3}He and N_2 is then introduced to the cell. Usually, about 50-100 mbar of N_2 and 1 to 9 bar of ^{3}He are used. Our cells were kept pretty close to 1 bar. The

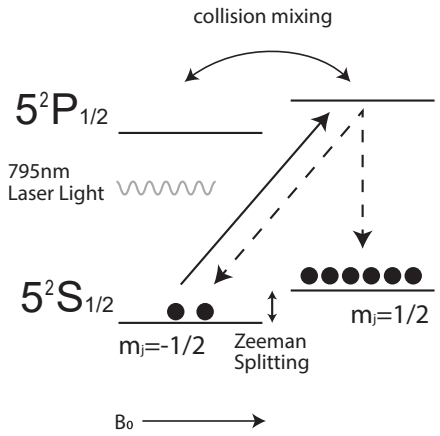


Figure 3.7: *Spin Exchange Optical Pumping of Rb Valence Electron.*

cell is placed inside an oven and heated to around 210^0 C. Note that Rb starts to become a vapor at 39^0 C. It is common for the heating to come from a flowing hot air system. The alkali metal vapor density should be on the order of 1×10^{14} cm $^{-3}$ to 1×10^{15} cm $^{-3}$ [64].

The cell is placed in a magnetic field with an orientation along the axis of the laser light. The cell is then exposed to right-handed circularly polarized laser light with a wavelength of 794.8 nm [65, 66]. This is resonant with the D_1 transition where $5^2S_{\frac{1}{2}} \rightarrow 5^2P_{\frac{1}{2}}$ transition for the Rb. The laser deposits angular momentum in the Rb valence electron [61] where $5^2S_{\frac{1}{2}}(m_j = -\frac{1}{2})$ state transitions to the $5^2P_{\frac{1}{2}}(m_j = \frac{1}{2})$ state coming from the $\Delta m = 1$ selection rule. Fig. 3.7 shows a diagram of the process.

The excited atoms then attempt to decay back to one of the Zeeman split ground states. The decay rates back to the $5^2S_{\pm 1/2}$ ground states are found in the Clebsch-Gordan coefficients [67]. The probability of decay to the $m_j = -1/2$ state is $\frac{2}{3}$. The probability of decay to the $m_j = +1/2$ state is $\frac{1}{3}$ [52]. In these conditions, the $m_j = +1/2$ state cannot be excited again but the $m_j = -1/2$ state can. If left pumping the $5^2S_{\frac{1}{2}}(m_j = -\frac{1}{2})$ state will be depopulated and eventually the $5^2S_{\frac{1}{2}}(m_j = +\frac{1}{2})$ will be occupied by all available electrons.

In the absence of a buffer gas, radiative decay results in fluorescent photons which are resonant with the optical pumping D_1 transition. The D_1 energy difference is the difference

between the fine structure energies in the $^2S_{\frac{1}{2}}$ and $^2P_{\frac{1}{2}}$ states [66]. These photons are not polarized and can result in depolarization of the spin population which we are trying to accumulate. The effect is mitigated by adding N_2, as a buffer gas, to the cell. The N_2 gas collisionally de-excites the electrons back to the ground states equally without photon emission. The N_2 also collisionally randomizes the P states which is called *collision mixing*. The N_2 relaxation process occurs in about 27 ns, which is approximately 10 times faster than the natural relaxation rate [61]. This results in the polarization of the Rb electrons approaching 100% and only about 5% of the excited electrons decay by emitting a photon [52]. The amount of N_2 should be orders of magnitude larger than the Rb density and orders of magnitude smaller than the ^{3}He density.

The polarization from the Rb electron is then collisionally transferred to the ^{3}He nucleus [62]. The spin angular momentum is transferred through a weak hyperfine-like coupling between the electron and nucleus. Although, polarization in ^{3}He increases through this process, it is again lost through wall relaxation, ^{3}He-^{3}He collisions, and magnetic field gradients. Approximately 3% of polarized Rb electrons exchange their angular momentum with ^{3}He nucleus during the picosecond interaction [52]. The process is extremely slow, taking about 12-15 hours to polarize a cell enough for functional use.

When the polarization cell returns to room temperature, the Rb solidifies onto the walls but the N_2 remains in a gaseous state in the cell with the ^{3}He. After this process the ^{3}He has an absolute polarization of 10-30%. This leaves many ^{3}He atoms in the cell which are not contributing the signal but are decreasing the mean free path of the particles leading to quicker depolarization of the sample.

While working on this process, I created a number of SEOP ready cells. Each cell takes about 8 days to process from cleaning the manifold [63] to first filling with ^{3}He. A description of the process I used is found in App. B. The development process is arduous and requires attention to each step. I successfully produced a few cells which were capable of polarizing ^{3}He. However, we were fortunate to have been working with the Duke Center for In Vivo

Microscopy (CIVM). We decided the most efficient use of our resources would be to use the ^{3}He polarization setup they already had in their lab. Their system had a polarization cell coated with Rb which lived inside an oven. It could be filled with a ^{3}He and N_2 mixture which would be polarized inside of it. Then a transportation cell, could be filled from the polarization cell and transported to the experiment. This significantly reduced the amount of wasted ^{3}He because the polarization cell would polarize ^{3}He at pressures between 1.5 to 9 bar, while we only needed 1 bar in our experiment. The polarization cell would be filled every 10 - 15 times a polarized ^{3}He measurement was performed. Most of the ^{3}He waste is the result of ^{3}He left in the fill lines between the ^{3}He cylinder and polarization cell. For the experiments discussed in this chapter, polarized ^{3}He was taken from CIVM. The transport cell was filled to pressures between 0.5 to 2 bar. The transport cell was then carried, by hand, to the experimental hall and placed on top of the cryostat.

It is worth noting that this SEOP process works equally well to polarize the nucleus of the Xenon atom [68]. This technique is presently being studied intensively by the CIVM group to produce the highest resolution images of lungs available to humanity at the current time.

Two additional polarization techniques may be of interest to the reader, should they be planning to polarize ^{3}He. The first technique adds potassium to the Rb cell which is then referred to as a *hybrid* cell [62]. The technique significantly reduces polarization time by first polarizing the Rb, which transfers polarization to the K, which then transfers the polarization to the ^{3}He with higher efficiency than Rb. A second technique called *Metability Exchange Optical Pumping* (MEOP) is a significantly faster technique, resulting in polarization in seconds [69]. This technique can result in polarization as high as 100% but can do so for only a few mbar of ^{3}He at a time.

3.4 Nuclear Magnetic Resonance Technique

This section outlines some useful details about the process of Nuclear Magnetic Resonance (NMR) and how it was used in the reported experiments. The NMR technique stimulates the rotation of the magnetic moment of a particle, atom, or molecule. As will be described, the rate of rotation is referred to as the Larmor frequency and is a function of the ambient magnetic field [70]. In the reported experiments, NMR was used to measure the behavior of polarized ^{3}He atoms. This is true for both the room temperature and SQUID measurements.

One first polarizes the nuclei by aligning their quantum mechanical spin states, as described in section 3.3. ^{3}He is an excellent candidate for this procedure due to having one unpaired neutron in its nucleus [71]. Protons and neutrons are fermions (spin 1/2), they obey the Pauli exclusion principle and reside in their own solitary energy states [67]. Within the atoms, two of these states are closely paired in energy being only differentiated by their hyperfine structure [71].

The two protons in the nucleus of ^{3}He are paired with each other. They are roughly in the same state but their spins orient in opposite directions, therefore, the magnetic field generated by them is not measurable at a distance. The neutron in the nucleus of ^{3}He has no such partner. Its magnetic moment vector $\overrightarrow{\mu_n}$ is not canceled by other phenomena within the atom.

When a reasonable portion of the atoms within the ^{3}He gas have spin states which are aligned, it creates a magnetic gas [72]. The gas is held in a magnetic holding field $\overrightarrow{B_0}$ and the spins $\overrightarrow{\mu}$ align with the holding field, as shown in Fig. 3.8a.

The bulk polarization as a function of time can be written as $P(t) = P_0\ exp(-t/T_1)$ where $P(t)$ is the polarization over time, P_0 is the initial polarization, T_1 is the spin lattice longitudinal relaxation time constant, and t is time [73]. As the equation describes, the polarization of the atoms will be exponentially lost over time. The polarization may be lost to many mechanisms including magnetic field gradients, bounces off the walls, interactions

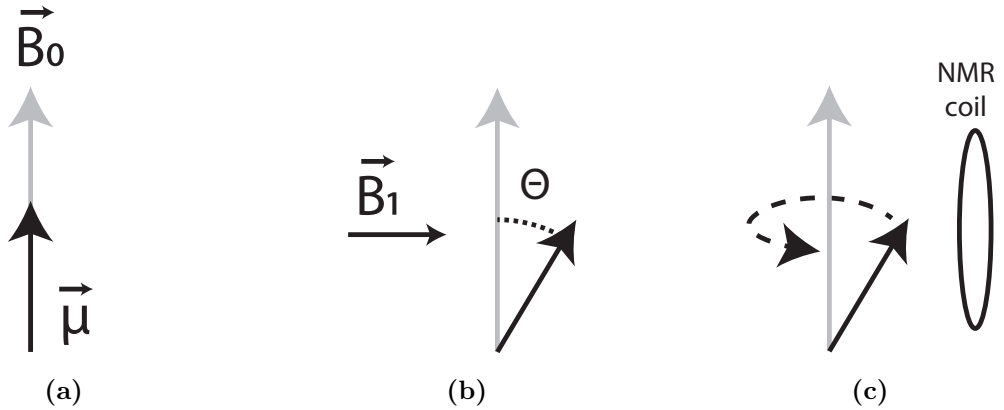


Figure 3.8: *The NMR Process. (a) Magnetic Moment $\overrightarrow{\mu}$ Aligned with Magnetic Holding Field $\overrightarrow{B_0}$. (b) Apply a Transverse Oscillating Magnetic Field $\overrightarrow{B_1}$ to Cause Tilt of $\overrightarrow{\mu}$ by Angle θ. (c) Torque Between Holding Field and Magnetic Moment Causes Larmor Precession of $\overrightarrow{\mu}$.*

between ^{3}He atoms, or application of external magnetic fields [1]. In this experiment, the primary depolarization mechanisms are bounces off the walls and interactions between ^{3}He atoms because the magnetic field is made mostly uniform by using Helmholtz coils [74]. Such that

$$\frac{1}{T_1} = \frac{1}{T_{1\ wall}} + \frac{1}{T_{1\ ^3He:^3He}} \tag{3.24}$$

Suppose we have some polarized atoms in a magnetic holding field. Considering viewing the spin system in a rotating frame which is resonant with the atom's Larmor frequency at a frequency ω_1. When an oscillating transverse magnetic field $\overrightarrow{B_1}(t)$ is applied to the gas, $\overrightarrow{\mu}$ tilts by an angle θ [75] as shown in Fig. 3.8b.

$$\theta = \frac{1}{2}\gamma\ |\overrightarrow{B_1}(t)|\ t \tag{3.25}$$

where θ is given in radians, t is the time over which $\overrightarrow{B_1}$ is applied, and γ is the moment's gyromagnetic ratio. For ^{3}He, the gyromagnetic ratio $\gamma_{^3He} = 3.243\ kHz/G$ [76]. After this tilt occurs, the total amount of possible magnetization left in the direction of the holding field (Fig. 3.8b), is $P_0\ cos(\theta)$. As the tipping processes are repeated, the total amount of magnetization decreases each time, $P_{i+1} = P_i\ cos(\theta)$.

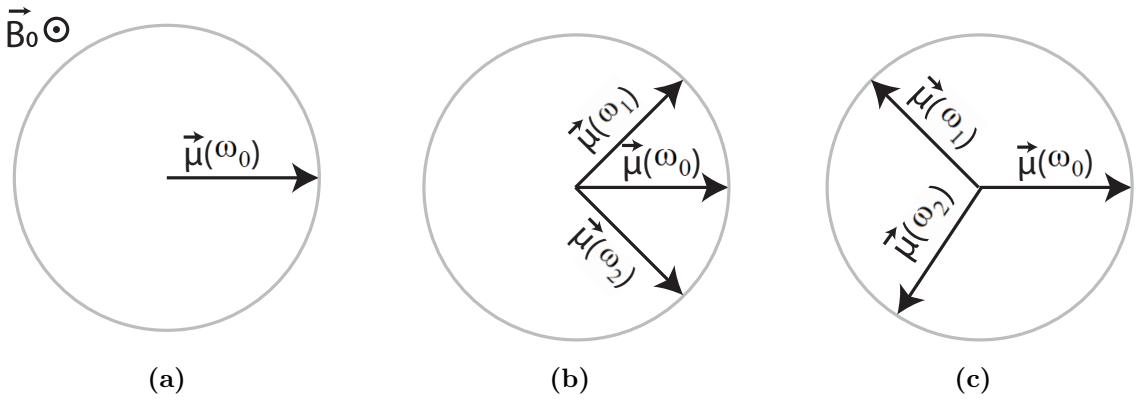


Figure 3.9: *NMR Dephasing Viewed in Rotating Reference Frame While Moving With a Central Frequency ω_l. This Process Is the Source of T_2. (a) In a Reference Frame Rotating With a Magnetic Moment at $\omega_l = -\gamma B_0$. When the Atoms Are First Tipped, All the Magnetic Moments Are Lined Up. (b) As Time Progresses, Different Regions Are Exposed to Slightly Different Magnetic Holding Fields, Resulting in Slightly Different Angular Velocities Causing the Moments to Spread. (c) When Enough Time Has Passed, the Magnetic Moments Throughout the Material Are Randomized. The Sum of All Magnetic Moments Becomes Zero in the Transverse Direction.*

Once the atoms are tilted, the magnetic holding field $\overrightarrow{B_0}$ will exert a torque $\overrightarrow{\tau}$ on the magnetic moment [70] as shown in Fig. 3.8c.

$$\overrightarrow{\tau} = \overrightarrow{\mu} \times \overrightarrow{B_0} \tag{3.26}$$

Under the influence of the holding field, the atoms will begin to rotate at their Larmor frequency [75].

$$\omega_L = -\gamma B_0 \tag{3.27}$$

If a conducting coil is placed near this system, the changing magnetic field will induce a current in the coil from the counter-electromotive force (back EMF) [77] as shown in Fig. 3.8c. The process described here is called Free Induction Decay (FID) [70].

In general, the magnitude and phase of $\overrightarrow{B_1}$ can be generated by many useful and sometimes complicated functions [78]. In the studies reported here, a simple sine wave was used. For a sine wave, the frequency should be selected to match ω_L, the Larmor frequency from Eq. 3.27. This results in driving the magnetic moments optimally.

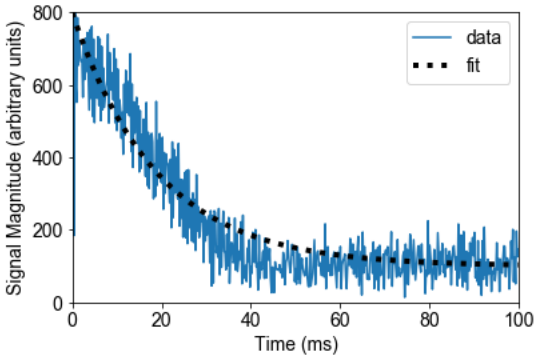


Figure 3.10: *Data Collected Plotted Vs Time. Exponential Curve Fit to Dataset With* $T_2 = 19.23$ *sec.*

At the instant the atoms are tilted, they are mostly pointing in the same direction meaning they are in phase. As they precess, they begin to dephase by pointing in slightly different directions. The dephasing occurs because there are inevitably non-uniformities in $\overrightarrow{B_0}$. This causes the cumulative magnetic field from the ensemble to decrease in magnitude and eventually dissipate as the atoms all point in random directions along the horizontal axis.

To understand this aspect of the signal decay process more clearly, consider entering a rotating reference frame moving along with $\overrightarrow{\mu}$ as in Fig. 3.9a. Let us now take a top down view staring down along the holding field vector lines.

Some magnetic moments in the volume will be exposed to the desired magnetic holding field resulting in rotation at a rate of ω_L. Non-uniformities in the field cause some atoms to rotate faster at ω_1 due to slightly larger magnetic holding field magnitudes and some atoms to rotate slower at ω_2 due to slightly smaller magnetic holding field values as in Fig. 3.9b [73]. As our reference frame rotates with ω_L, we would see a spreading out of the magnetic moments. In the transverse direction, this causes the total magnetic field generated by the collection of particles to decrease in magnitude. The decrease in magnitude can be described by an exponential decay with time constant T_2 as $M(t) = M_0\, exp\,(-\,t/T_2)$ where M_0 was the initial magnetization when the tip occured. A derivation of this logic from the Bloch Equations is thoroughly discussed in [70].

As time progresses, the many magnetic moments in the system begin to point in random directions. Once they are completely randomized, the total magnetic field from the system in the transverse direction returns to zero. A signal read out from the coupled pick up coil is shown in Fig. 3.10.

If the tipping of the atoms did not cause the magnetic moments to point perpendicular to the holding field $\overrightarrow{B_0}$, some magnetization along the direction of the holding field may still remain. Another tip may then be applied to perform another measurement.

3.5 Room Temperature Measurements

This section outlines ^{3}He NMR measurements conducted at room temperature. The longitudinal relaxation rate T_1 was measured to evaluate the quality of the dTPB-dPS coating on the PMMA measurement cell. Specifics about the nature of the time constant T_1 are covered in section 3.5.2. The previous cells used on this apparatus were of a slightly different geometry and used for a different measurement, though the basics of the cell design were similar. The results showed that the measurement cell which we had built had a T_1 on the same order of magnitude as the previous cells but was slightly shorter. The SEOP technique described in section 3.3 was used to polarize ^{3}He. Please recall that some aspects of the experimental setup are described in section 3.1.

Two computers were used in the lab for instrument control and data acquisition. The Gollum computer ran LabView VIs which control the holding field power sources. The Apollo computer had the TecMag TNMR program on it and ran all NMR controls and DAQ. The TNMR program was used to operate the experimental sequences. It controlled the NMR coils and collected data. The program was setup with sequential and parallel operations on time lines with resolution of a nanosecond. The program also performed Fast Fourier Transforms (FFT) on the data for analysis. Fig. 3.12 shows output from the FFT process.

A first-order gradiometer is made of two loops of connected conducting wire [74]. Each of the loops may have multiple turns of wire on it. There are two common constructions

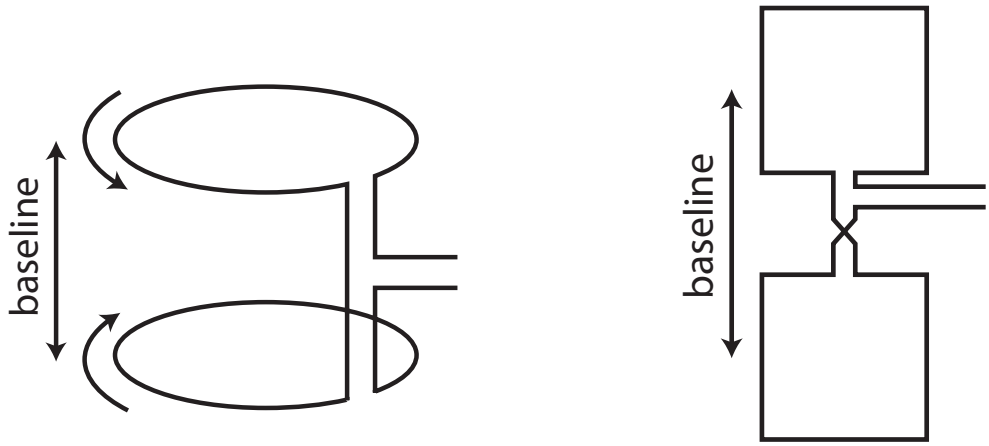
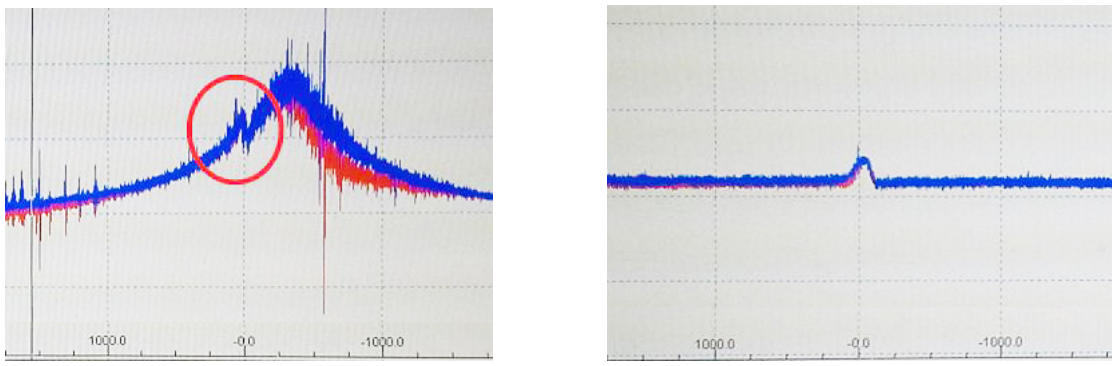


Figure 3.11: *Two Design Schematics for First-order Gradiometers. (a) Axial First-order Gradiometer. This Type of Gradiometer Is Used in the Present Work. (b) Series Planar First-order Gradiometer. This Type of Gradiometer or the Parallel Version Will Used in the PULSRAT-SOS and SNS-nEDM Experiments.*

for first-order gradiometers. One common type has the two loops sharing an axis and are facing each other. This is known as the *axial first-order gradiometer* and can be seen in Fig. 3.11a. Another common type places the loops on a plane together and is known as the *planar first-order gradiometer*. Fig. 3.11b shows a series planar gradiometer. For an in-depth view of gradiometers, please see the *SQUID Handbook* [74].

Similar to all other conducting loops, Farady's Law applies, namely $\varepsilon = |\frac{d\Phi}{dt}|$, where ε is the induced potential in the loop, Φ is the magnetic flux through the loop and t is time. This states that changing magnetic fields which penetrate the cross sectional area of the loop cause an induced EMF in the loop [77]. However, with gradiometers, each loop is wound in a different direction and the output from the circuit is the difference between the fluxes measured in each loop. The result is that time dependent flux which penetrates both loops is canceled in analog. The technique in using them is to place one loop close to the source of the signal one wishes to detect and the other loop some distance away from the source. As will be discussed in section 3.6, SQUIDs are extremely sensitive devices and protecting them from excessively large environmental noises is of necessity.



(a) **(b)**

Figure 3.12: *The FFT of a Signal From Two Measurements on the Same Polarized ^{3}He Filled Cell Are Shown. The Horizontal Axis Is Centered at the Larmor Frequncy in Units of Hz. The Vertical Axis Is in Arbitrary Unit. (a) the FFT of the Signal Taken by Using a Common Set of Coils Where Two Loops of Wound Coil Surrounding the Sample Were Wound in the Same Direction. The Large Gaussian Curve Is the Background Noise. The Small Bump, Circled in Red, Is the Signal. (b) The FFT of the Signal Taken Using an Axial First-order Gradiometer. The Clarity of the Signal Is Extremely Pronounced When Compared to the FFT From (a).*

For the room temperature mesaurement, a first-order gradiometer with 70 turns on each coil was placed adjacent to the measurement cell. The transport cell containing polarized ^{3}He was carried from the CIVM center and placed on top of the cryostat in a magnetic holding field. The TNMR program was started. The valve on the transport cell was opened. The ^{3}He was then transported down through a glass capillary ($\sim$ 2 m in length) to the measurement cell. The measurements are then performed in the measurement cell. When one measurement cycle is complete, the cell is evacuated using a vacuum pump, and the process is repeated.

The first step in preparing the system was to calibrate the tip angle initiated by the NMR pulse, Eq. 3.25. The tipping process results in some amount of depolarization as the vertical component of the gas's magnetization is reduced. The depolarization which results from performing the tipping must be taken into account when calculating T_1. Calculation of the tip angle is discussed in section 3.5.1.

Once the tip angle is calibrated, ^{3}He can be introduced to the measurement cell and the T_1 measurement may proceed. The measurement process first tips the atoms, measures

the magnetic field oscillatory response, takes the Fast Fourier transform (FFT) of the data, integrates the FFT, and compares a series of these values over time. Only the relative magnetization between successive measurements needs to be calculated from the results, so the absolute magnetization is not needed. The details of this process are discussed in the section 3.5.2.

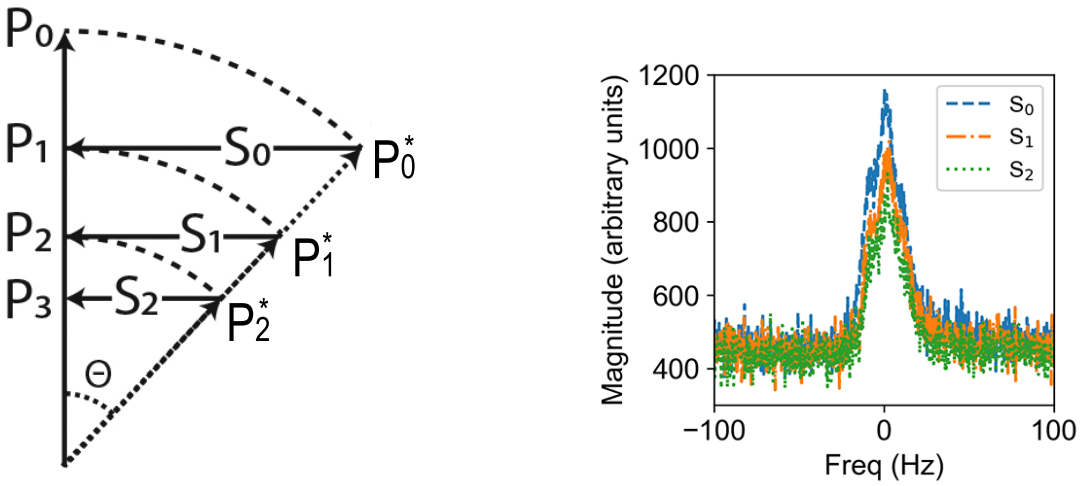
The results of the measurements are given in section 3.5.3.

3.5.1 Calibrating Tip Angle

This section describes the process of calibrating the tip angle on the system. The tip angle is calculated by $\theta = \frac{1}{2}\gamma \ |\overrightarrow{B_1}(t)| \ t$ (Eq. 3.25) where θ is the tip angle, γ is the gyromagnetic ratio, $\overrightarrow{B_1}(t)$ is the applied transverse NMR pulse, and t is the time over which the NMR pulse is applied.

The gyromagnetic ratio of ^{3}He is a known physical constant, $\gamma_{^3He} = 3.243 \ kHz/G$. The NMR pulse in this case is defined by $\overrightarrow{B_1}(t) = A \ sin(\omega_L \ t) \ \hat{i}$ where $\hat{i}$ is perpendicular to the magnetic holding field $\overrightarrow{B_0}$, and A and ω_L are defined in the TNMR program. Also note that in these studies, the orientation of the area of the pick up coils were facing the $\hat{j}$ direction, such that $\hat{i} \perp \hat{j}$.

When the NMR pulse is applied to the sample, the spin states in the polarized gas tilt. To illustrate repeated tips, see Fig. 3.13a. In the figure, the initial polarization P_0 is aligned with the magnetic holding field. Then an NMR pulse is applied transversely, as described in section 3.4. The magnetic moments are then rotated by and angle θ to P_0^*. Picking up the transverse oscillating signal with a conducting coil, gives a signal of magnitude $S_0 = P_0 \ sin(\theta)$. Once the system relaxes in a time $t \gg T_2$ and realigns with the holding field, the total polarization left is $P_1 = P_0 \ cos(\theta)$. Applying another tip with the same angle, gives a smaller signal $S_1 = P_1 \ sin(\theta)$. Repeating this process continuously reduces the magnitude of the available polarization. Sequentially, each pulse gives



(a) **(b)**

Figure 3.13: *NMR Tipping Technique Described Theoretically and Expressed As Data From a Measurement. (a) When Tipping the Magnetic Moments of a Sample With Initial Polarization P_0. The Transverse Magnitude After the Tip S_0 Is Then Measured by the NMR Pick up Coils. This Figure Was Originally Drawn by Austin Reid. (b) FFT of Data Collected While Calibrating Tip Angle Showing Results of Tipping. The Plot Is Centered Around the NMR Frequency ω_l.*

$$\begin{aligned} S_0 &= P_0\ sin(\theta) & P_1 &= P_0\ cos(\theta) \\ S_1 &= P_1\ sin(\theta) & P_2 &= P_1\ cos(\theta) \\ &\vdots & &\vdots \\ S_n &= P_n\ sin(\theta) & P_n &= P_0\ cos^n(\theta) \end{aligned} \tag{3.28}$$

where n is the number of pulses which have been applied.

The applied tip angle must be understood because the tip process results in some depolarization of the ensemble of atoms and this is taken into account when calculating T_1 in later measurements, as it results in some amount of the depolarization which is being measured. It is also ideal to select a tip angle which is small enough that as many tips as possible can be applied, therefore increasing the total number of measurements which can be performed. The tip angle also must be large enough that a signal can be detected.

When calibrating the tip angle, the pulses must be delivered in quick succession, so that the time between pulses is significantly shorter than T_1. This ensures the depolarization from T_1 does not influence the calibration significantly. We expected T_1 to be a few 100's of seconds long, so the tipping process was repeated every 2 seconds.

The time dependent response when a tip occurs is the type shown in Fig. 3.10. When the FFT of this signal is taken, plots such as that shown in Fig. 3.13b are generated. The FFT can be taken inside the TNMR program before exporting the data. Fig. 3.13b shows a series of successive signals. I wrote a C++11 code to calculate the tip angle. The code is found in App. C.4.

The code integrates the region beneath the curve. The user may define the region which will be integrated by defining if they would like to use the full width at half maximum or some other ratio of the maximum to background value. Using a larger portion of the region under the curve can result in lowering the variance of the measurement. The first integral in a series of measurements is defined as S_0. Any later integral in the series is S_n.

Once the integrals are taken, it is possible to calculate the angle to which the atoms were tipped by solving Eq. 3.28. Solving it for θ we find the function

$$\theta = acos\left(\sqrt[n]{S_n/S_0}\right) \tag{3.29}$$

For each measurement, a series of θ_k values are calculated where k is the index of the measurement and $1 \leq k \leq n$. Once these values were calculated, the mean and standard deviation of each set were taken. The technique for the analysis of the data is found in App. C.3.

To calibrate the system, a cell labeled *Kelley2* was borrowed from H. Gao's Duke physics group. This is a closed SEOP cell coated with Rb. The ^{3}He inside was polarized and it was placed into a setup which used the same NMR coils, holding field coils, and gradiometer used for the room temperature measurements. In the first tip angle calibration tests, the voltage across the NMR coils was varied. The tip angle was then calculated using Eq. 3.29.

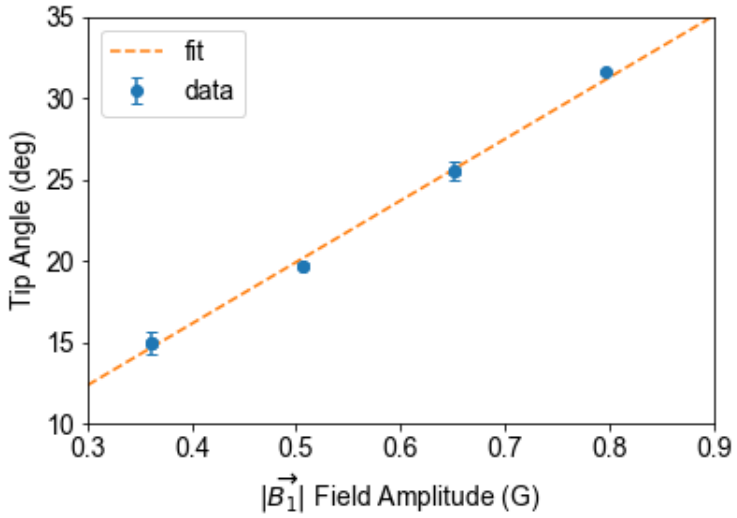


Figure 3.14: *Calibration of Tip Angle As a Function of Magnetic Field Strength.*

A COMSOL simulation was setup to estimate the magnetic field produced by the coils. COMSOL Multiphysics is a finite mesh analysis software [79]. Specifics about COMSOL are discussed in more detail in section 4.2. The voltage put into the coils and the impedance of the coils were used as inputs into the COMSOL model and the magnetic field strength $|\overrightarrow{B_1}|_{max}$ produced by the NMR coils was calculated using Eq. 3.25. This value for $|\overrightarrow{B_1}|_{max}$ was then used to estimate the tipping angle prior to the measurements. As you can see from Eq. 3.29, the measured tipping angle was not dependent upon this estimate in COMSOL.

Fig. 3.14 shows the results of eight measurements performed in this setup, two sets of measurements were performed at each magnetic field strength. The plot follows $\theta = \frac{1}{2}\gamma\ |\overrightarrow{B_1}(t)|\ t$ (Eq. 3.25) fairly well. The data was fit to a linear function using SciPy, an open-source software for python. Specifically, "curve_fit" from the "optimize" package was used. The fit returns a slope of $b = 37.8 \pm 0.9\ deg/G^{-1}$, which empirically is the product of the gyromagnetic ratio of ^{3}He and the time over which the NMR pulse was applied, $\gamma_{^3He} \times\ t$. In these measurements, the NMR pulse duration was $t = 210\ \mu s$. This time is set in the TNMR program with time resolution of $\sim$ 1 ns. By taking $b/t = 3140 \pm 71.6\ Hz/G$, we expect see the gryomagnetic ratio of ^{3}He. This value has previously been mentioned to

have an accepted value of 3.243 kHz/G. Agreement between the measured and accepted values, verifies the reliability of the calibration.

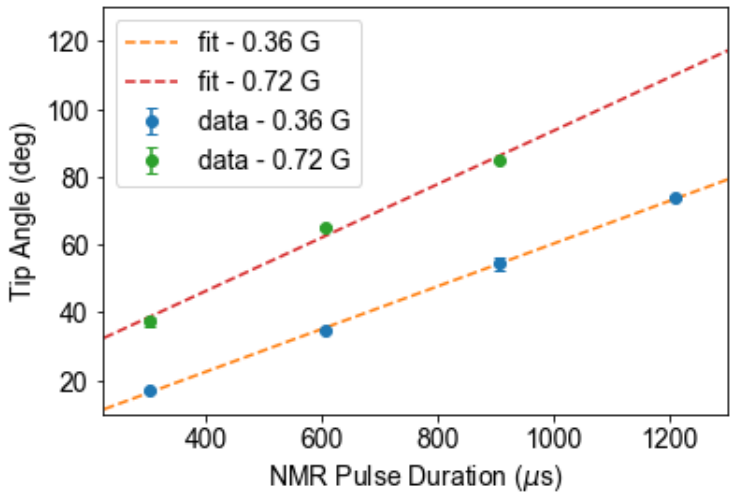


Figure 3.15: *Results of Measurments of Tip Angle As a Function of NMR Pulse Duration.*

A second calibration was performed that varied the NMR pulse duration. In these measurements, magnetic field strengths of 0.35 G and 0.44 G were applied. The NMR pulse duration was set to 302, 604, 906, and 1210 μs for the 0.35 G measurements, and 302, 604, and 906 μs for the 0.44 G measurements. Fig. 3.15 shows the results of these measurements and linear fits to the data. Again, these data should be following $\theta = \frac{1}{2}\gamma \, |\overrightarrow{B_1}(t)| \, t$ (Eq. 3.25) closely. Since the independent variable is time t, we expect the slope of the line to be $\gamma \, |\overrightarrow{B_1}|$. The slopes for the two curves are $b_{0.36\ G} = 63.0 \pm 1.0\ deg/ms$ and $b_{0.44\ G} = 78.8 \pm 7.4\ deg/ms$ for the lower and upper fits, respectively. We could then attempt to calculate the gyromagnetic ratio of ^{3}He from these slopes by $b/|\overrightarrow{B_1}|$. The calculated gyromagnetic ratios are $3125.1 \pm 51.5\ Hz/G$ and $3162.6 \pm 298.0\ Hz/G$. These are again reasonably consistent with the accepted value of 3243 Hz/G.

3.5.2 Calculation of the Longitudinal Relaxation Rate T_1

This section outlines a derivation of the depolarization of a polarized ensemble of particles. The time constant of the derived exponential equation is referred to as the *Longitudinal*

Relaxation Rate or T_1. The derivation of the equation is treated for a system with particles having magnetic moment $|\overrightarrow{\mu}| > 0$ because this is the usual treatment. Note, however, that for ^{3}He and neutrons, the orientation of their magnetic moments are anti-parallel to their spin. Mathematically, this means $\overrightarrow{\mu} < 0$. The section then goes on to discuss the technique used to measure T_1 in our system.

We start with an ensemble of particles where each particle has a magnetic moment $\overrightarrow{\mu}$. These particles are placed in a magnetic holding field $\overrightarrow{B}$. We now have a macroscopic ensemble of particles with two energy states [70], a state where the magnetic moments are aligned with the magnetic holding field and a state where the magnetic moments are anti-aligned with the magnetic holding field. Let's call these two states, N_- and N_+, respectively. The energy of each state can be calculated by $U = -\overrightarrow{\mu} \cdot \overrightarrow{B}$. Hence, when $|\overrightarrow{\mu}| > 0$ and $\overrightarrow{\mu}$ is aligned with $\overrightarrow{B}$, the energy $U < 0$. As with all conditions, the magnetic moments in the ensemble will eventually tend toward the lower energy state. These states are commonly referenced with the "-" and "+" subscripts to express the total energy in that state, where "-" refers to the lower energy state and "+" refers to the higher energy state.

For ^{3}He and neutrons, the magnitude of the magnetic moment is negative. For their moments, the aligned state is the higher energy state and the anti-aligned state is the lower energy state. The argument will continue however.

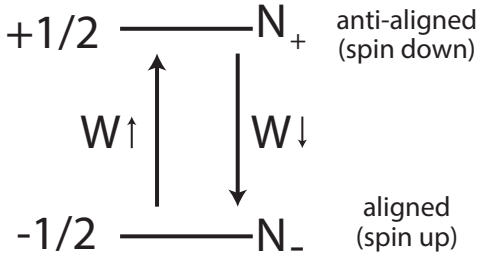


Figure 3.16: *Energy Levels in Two State Fermion System for ^{3}He.*

As in *Principles of Magnetic Resonance* by Slichter [70], let's call the probability per second of a transition from the aligned state to the anti-aligned state $W_{(-)\to(+)} = W\uparrow$ and the transition from the anti-aligned state to the aligned state $W_{(+)\to(-)} = W\downarrow$. See Fig.

3.16 for a graphic model of this system. Depending upon the conditions, $W\uparrow$ may or may not equal $W\downarrow$. For example, when the system is inside a SEOP setup, $W\uparrow > \ W\downarrow$, but when the system is left to rest and return to thermal equilibrium, $W\downarrow > \ W\uparrow$. Here we are particularly interested in the rate at which the system relaxes naturally.

Let's define two convenient variables $N = N_+ + N_-$ being the total number of atoms and $n = N_+ - N_-$ being the difference in the number of atoms in each state. Using these two definitions, we can define the number of atoms in the anti-aligned state as $N_+ = \frac{1}{2}(N+n)$ and the number of atoms in the aligned state to be $N_- = \frac{1}{2}(N-n)$. The rate per second at which the moments depolarize is the rate of transition out of the N_- state. Namely,

$$\frac{dN_-}{dt} = N_+ \ W\downarrow - \ N_- \ W\uparrow \tag{3.30}$$

This equation can be manipulated into a less obvious but useful form using the variables mentioned in the previous paragraph. In the following equation, we have a differential equation for the time dependent difference in the number of atoms in each state.

$$\frac{dn}{dt} = \frac{n_0 - n}{T_1} \tag{3.31}$$

where

$$n_0 = N\left(\frac{W\uparrow - W\downarrow}{W\uparrow + W\downarrow}\right) \qquad\qquad \frac{1}{T_1} = W\uparrow + W\downarrow \tag{3.32}$$

This form is useful because it helps to characterize how quickly the system will return to thermally equilibrium. Taking this one step further, we can solve the differential equation

$$n(t) = n_0 + A \ exp(-\ t/T_1) \tag{3.33}$$

where T_1 is the longitudinal relaxation rate, n_0 is the population at thermal equilibrium, t is time, and A is a constant.

It is called the longitudinal relaxation rate because it is related to the rate at which relaxation occurs in the longitudinal direction (alignment with magnetic holding field). It is also called the spin-lattice relaxation time because it is related to the rate at which the spin transfers energy to the surrounding environment (lattice). This relaxation time is influenced by the time constants for the relaxation rate on the wall T_{wall}, interactions between ^{3}He atoms $T_{^3He:^3He}$, and magnetic gradients throughout the measurement volume T_{grad} [1]. Together they form a total longitudinal relaxation rate

$$\frac{1}{T_1} = \frac{1}{T_{wall}} + \frac{1}{T_{^3He:^3He}} + \frac{1}{T_{grad}} \tag{3.34}$$

We need not be concerned too much with the gradient relaxation T_{grad} because the gradients in the measurement cell have been made sufficiently small.

The relaxation rate due to ^{3}He:^{3}He interactions is important because the mean free path of the atoms is short. We can get an estimate of the mean free path from the following equation [77].

$$\lambda = \frac{1}{4\sqrt{2}\,(N/V)\,r^2} \tag{3.35}$$

where N is the number of atoms in the measurement cell, V is the volume of the cell, and r is the radius of a ^{3}He atom. For the low temperature and room temperature measurements, $N_{cold} \approx 2 \times 10^{21}$ and $N_{warm} \approx 2 \times 10^{20}$, respectively. For both sets of measurements $V = 16.4 \times 10^{-6}\ m^3$ and $r = 31\ pm$ [80].

The mean free path for the low temperature and room temperature situations are $\lambda_{cold} \approx 5 \times 10^{-6}\ m$ and $\lambda_{warm} \approx 5 \times 10^{-7}\ m$. The average velocities of the atoms in the low and room temperature setups are $v_{cold} \approx 170\ m/s$ and $v_{warm} \approx 1500\ m/s$, respectively. This means the atoms collide with each other about $3 \times 10^7\ s^{-1}$ and $3 \times 10^9\ s^{-1}$ for the low and room temperature scenarios, respectively.

As described in Eq. 3.33, the relaxation is exponential. We can also drop the constant offset n_0 from that equation because it will not be measurable. The equation can then be written in terms of polarization as

$$P(t) = P_0 \; exp(-t/T_1) \tag{3.36}$$

where P_0 is the initial polarization of the sample.

As the technique described in section 3.5.1 outlines, a series of measurements are performed in succession but this time with a longer delay between measurements. Let us label a particular measurement in the sequence as k. Let us also call the duration between measurements to be t_0. When taking into account the depolarization both from the longitudinal relaxation rate and the tipping process, a new set of equations, similar to those shown in Eq. 3.28, emerge. Namely,

$$\begin{aligned}
S_0 &= P_0 \; sin(\theta) & P_1 &= P_0 \; cos(\theta) \; e^{\,-\,t_0/T_1} \\
S_1 &= P_1 \; sin(\theta) & P_2 &= P_1 \; cos(\theta) \; e^{\,-\,t_0/T_1} \\
&\vdots & &\vdots \\
S_k &= P_k \; sin(\theta) & P_k &= P_0 \; cos^k(\theta) \; e^{\,-\,k\;t_0/T_1}
\end{aligned} \tag{3.37}$$

For a visual depiction of this idea, please see Fig. 3.13a.

Let's consolidate those equations slightly to focus on the relationship between a signal received during some measurement S_k and the initial signal S_0.

$$\begin{aligned}
S_k &= (P_k) \;\; sin(\theta) \\
&= \left(P_0 \; cos^k(\theta) \; e^{\,-\,k\;t_0/T_1}\right) \;\; sin(\theta) \\
&= P_0 \; sin(\theta) \; cos^k(\theta) \; e^{\,-\,k\;t_0/T_1} \\
&= S_0 \; cos^k(\theta) \; e^{\,-\,k\;t_0/T_1}
\end{aligned} \tag{3.38}$$

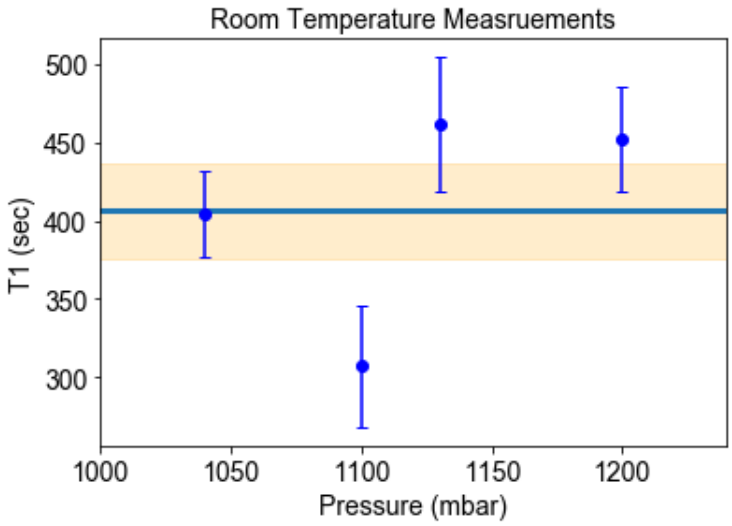


Figure 3.17: *The Results of the Room Temperature Measurements Are Shown. These Data Points Are Also Reported in Table C.1.*

We can now isolate the T_1 time constant for any particular measurement. Repeating the calculation on each measurement then allows for better statistics. We find

$$T_1 = \frac{n\ t_0}{ln\left(S_0/S_k\ cos^k(\theta)\right)} \tag{3.39}$$

and we are ready to perform the measurement and calculation.

3.5.3 Room Temperature Results

This section discusses the results of the room temperature measurement. The results were consistent with those found previously by C. Swank [1] and slightly less but still on the same order of magnitude as those measurements performed by Q. Ye [52].

The following input parameters were used to control the NMR pulse and sequence

I found that for this cell $T_1 = 407.48 \pm 34.11$ seconds. The results of the four individual measurements are reported in Fig. 3.17.

The pressure in the SEOP polarization cell decreased each time polarized ^{3}He was taken from it. When filling the transport cell, the ^{3}He flow is controlled by a valve opened by hand. It was therefore very difficult to always match the pressure on each filling. For this

Table 3.1: *Parameters Used in Room Temperature T_1 Measurements.*

Parameter	Value
Tip angle	25.48 ± 1.48^0
Frequency	32.8 kHz
Pulse time length	302 μs
Time between NMR pulses	32 s

reason, the pressure is plotted as the independent variable, though the T_1 does not appear to be strongly correlated to pressure in this regime.

These values and their mean are on the same order of magnitude as previous measurements at room temperature [1, 52]. In both the previous measurements mentioned, the T_1 was able to be measured at both room temperature and below 2 K. In each of those case, the T_1 increased by a factor of 2 - 3 times when the cell was cooled to below 2 K and filled with superfluid ^{4}He, as will be the case in the SNS-nEDM experiment. This leads to the conclusion that this type of dTPB-dPS coated cell will have a ^{3}He T_1 of $900 - 1200$ seconds at low temperature.

The present neutron bottle lifetime is measured to be 877 ± 0.7 (stat) $+0.4/-0.2$ (sys) seconds [81]. Since the T_1 measured here for ^{3}He is on that order or larger, this demonstrates that the coating technique was successfully applied and is further evidence that this technique may allow holding polarized ^{3}He to be held for timelines similar to or longer than the possible holding time of the neutron. This technique is therefore helpful for the PULSTAR-SOS and SNS-nEDM measurements.

The reader may also be interested to know that since the work discussed here has completed, a special machine for applying the glue has been purchased and setup at NC State University. It has been used to glue a number of measurement cells at this point. In the near future, one of these cells will be installed in the PULSTAR-SOS cryostat and tested with neutrons and ^{3}He at the same time, similar to the SNS-nEDM experiment. One

of these cells is shown in Fig. 2.1. The larger cell results in less depolarization as a result of wall bounces.

3.6 SQUID Overview and Motivation

The PULSTAR Apparatus and SNS-nEDM experiments both intend to use Superconducting QUantum Interference Devices (SQUIDs) to measure oscillating magnetic fields generated by the precessing spins of polarized ^{3}He. SQUIDs are extremely sensitive, being able to measure magnetic field strengths as small as 1 fT. In each of the aforementioned experiments, the concentration of ^{3}He will be fairly small resulting in small flux through any coil used to detect the signal. Calculations by Y. Kim and S. Clayton [82] have shown that even the small fields expected to be generated by ^{3}He in these future experiments will be measurable using a system of SQUIDs.

It is therefore necessary to develop an understanding of how to work with SQUIDs and the necessary electronics which control and read from them. For this reason, I installed a SQUID system in the same experimental apparatus used in the earlier sections of this chapter to develop familiarity with how SQUID systems operate.

It is suspected that the NMR tipping pulse which will manipulate the ^{3}He spins could flood the SQUID with excessive flux. It is possible that this could cause the SQUIDs to essentially be off-line for a short time, decreasing the duration measurements can be performed and restricting access to T_2 data. A device called a cryoswitch, can be used to interrupt the signal between the SQUID loop and pick up coils. A cryoswitch is a heat switch. Some details and simulations about cryoswitch operation will also be discussed in this section.

3.6.1 SQUID Principles of Operation

A SQUID operates on the phenomena of Josephson tunneling and flux quantization [74]. Magnetic flux through a superconducting loop is quantized into units of the flux quantum $\Phi_0 = h/2e \approx 2.07 \times 10^{-15}\ Wb = 2.07 \times 10^{-7}\ G\ cm^2$, where $h = 2\pi\hbar$ is the Planck constant

and e is the electronic charge. This arises from the single-valued nature of the Cooper pair's wave function when going once around a superconducting loop. The wave function can be expressed as

$$\Psi(\overrightarrow{r}, t) = |\Psi(\overrightarrow{r}, t)|\ exp[i\psi(\overrightarrow{r}, t)] \tag{3.40}$$

When a superconducting loop is free from applied fields and currents, the phase of the Cooper pairs throughout the superconductor all have the same value. In the presence of a magnetic flux through the loop, the phase changes by $2\pi n$ around the loop, where n is the number of enclosed flux quanta.

A Josephson junction is created by connecting two superconductors (S) across a thin insulating layer (I), SIS. In schematics, the Josephson junction is labeled with an 'X' as shown in Fig. 3.18. For low temperature SQUIDs, it is common for the superconducting sections of the loop to be made of thin, poly crystalline films of Nb ($\approx$ 10s of nm in width). For high temperature SQUIDs, the superconducting material most commonly used today is Yttrium Barium Copper Oxide (YBCO) [74] which has a critical temperature around 93 K [83] and therefore, can be cooled using liquid nitrogen.

To elicit the desired behavior, a bias current I_b is made to flow across the SQUID. Initially, increasing the bias current does not change the voltage across the Josephson junctions. When the bias current reaches the critical current I_{c1}, a voltage difference across the junctions begins to appear and exhibits an asymptotic trend. Fig. 3.19, is a diagram of this behavior. As the the current is increased above this value, the Cooper pair flow across the junctions constitute a supercurrent.

The reader may notice that in Fig. 3.19, two critical currents are shown. Note that $I_{c1} > I_{c2}$. The current I_{c1} occurs when the flux through the SQUID loop is $n\ \Phi_0$ for some integer n. If the flux remains constant, continuing to increase the bias current will result in the voltage across the junctions to follow the upper curve. The current I_{c2} occurs when the flux through the SQUID loop is $(n+1/2)\ \Phi_0$. The technique for using the SQUID to detect

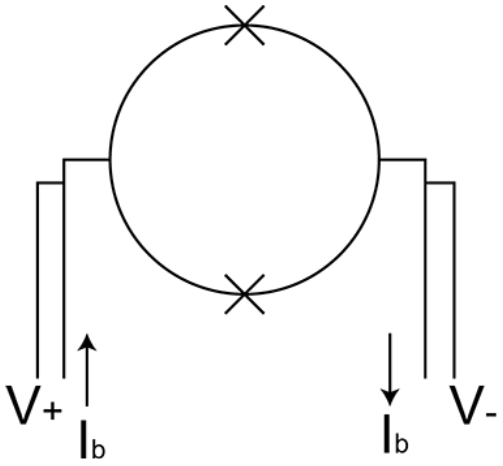


Figure 3.18: *Simple Schematic of SQUID. Josephson Junctions Are Marked With 'x'. I_b Is the Bias Current and 'V' Leads Are Where the Voltage Is Measured.*

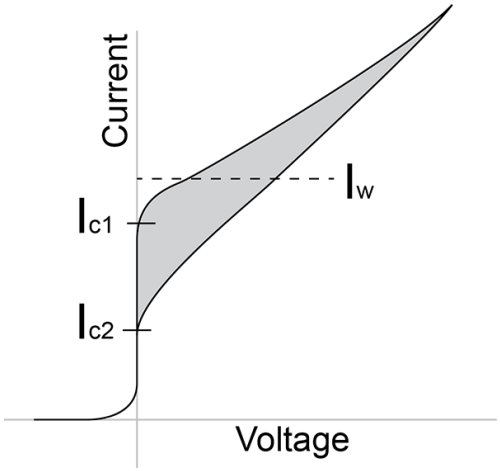


Figure 3.19: *Current Vs Voltage Curve Across Josephson Junctions. These Curves Are Used to Tune the SQUID for Operation.*

a signal requires increasing the current until it is slightly above I_{c1}, this is represented by a dashed line in the figure. Once this working current $I_b = I_w$ is reached, changes in the flux through the loop will cause measurable changes in the potential across the Josephson junctions. If the voltage starts on the upper curve and the flux through the loop changes, the voltage slides to the right along the dashed line to the lower curve then turns back toward the upper curve. Using leads as shown in Fig. 3.18 labeled by $V\pm$, one can use these voltage fluctuations to measure flux changes through the SQUID loop.

The dashed line in Fig. 3.19 is a partial representation of the relationship between the flux through the SQUID loop and the voltage measured across the Josephson junctions. As one may expect, the relationship between these phenomena is non-linear. Fig. 3.20 shows the relationship between the flux entering the SQUID loop and the voltage output. As the flux through the SQUID changes, it traces out some flux on the horizontal axis of this figure. The flux is then measured as a change in the voltage on the vertical axis of this plot.

The technique for tuning the SQUID and associated electronics for optimal operation is to arrange for small flux variations to be measured along a part of this curve with the maximum slope. That is, maximize $\delta V/\delta\Phi$. This is obtained in the linear regions of the

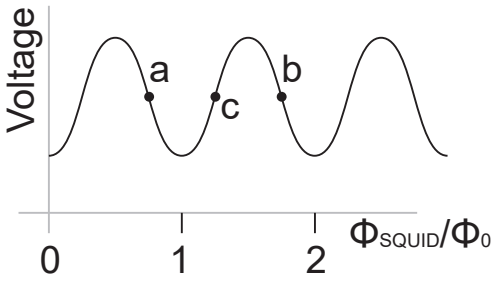


Figure 3.20: *Voltage Vs Flux Curve for DC SQUID. The Horizontal Units Are the Ratio of the Flux Through the SQUID Divided by the Flux Quantum.*

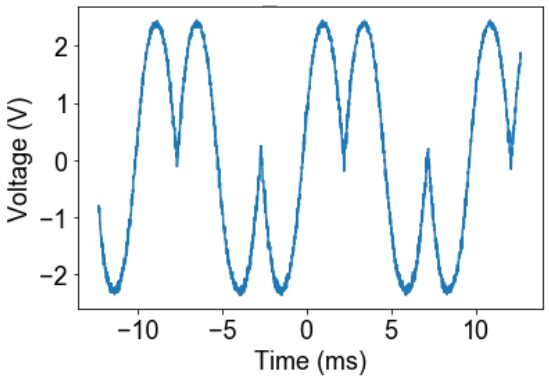


Figure 3.21: *Plot Measured on an Oscilloscope of Voltage Output While Tuning SQUID. During This Process, the Flux Entering the SQUID Sweeps Between Two Values, Such As the Dots Shown on Fig. 3.20*

curve shown in Fig. 3.20 where $\Phi \approx (2n+1)\ \Phi_0/4$ near the point c. Centering around this point is accomplished by modifying the current I_b from Fig. 3.19 so that the intersection of the dashed line and curve I_{c1} aligns with point a in Fig. 3.20. And so that the intersection of the dashed line from Fig. 3.19 aligns with the point b in Fig. 3.20.

The flux-to-voltage transfer coefficient, commonly called the *transfer coefficient*, is then maximized, $V_\Phi \equiv |\delta V/\delta\Phi|$. Consider applying a repeating *triangular* flux across the SQUID. In the time domain, this causes a linear sweeping back and forth across the horizontal axis of Fig. 3.20. When performing this operation, the voltage output will oscillate back and forth following the sine wave from point a to point b and back to point a. The result on an oscilloscope is shown in Fig. 3.21. When the flux through the SQUID loop is zero, the output rests at point c. When flux is slightly higher, it increases the output voltage, moving to the right of c. When the flux is slightly lower, it decreases the output voltage, moving to the left of c.

3.6.2 SQUIDs: A Practical Approach

When purchasing a SQUID from a manufacturer such as Star Cryogenics or Supracon, the SQUID comes on a chip. The chip has a number of other connectors and components.

The simple version of a SQUID has 6 solder pads and two input terminals. The solder pads are used in pairs for (a) controlling the bias current, (b) controlling a heater, and (c) setting up the flux modulation circuit. The input terminals are used to connect the chip to an external set of pick up coils. See Fig. 3.22 for a schematic of the design.

In this work, a Supracon CE2SBlue SQUID was used. For that reason, the parameters and examples discussed in this chapter will use values which come from that SQUID chip. The inductance of the SQUID loop is $L_S = 180\ pH$.

The input terminals are connected to a set of leads which are coupled to the SQUID loop. The terminals themselves have brass screws and washers with Nb pads. The leads and coupling loop are made of Nb. A set of pick up coils is attached to the terminals which closes the input circuit. When the pick up coils are exposed to an oscillating magnetic field, the current is carried to the loop which is coupled to the SQUID loop. Three important parameters are then needed, (a) input coil inductance $L_i = 420\ nH$, (b) input coil to SQUID mutual inductance $M = 8.1\ nH$, and (c) input coupling 0.26 $\mu A/\Phi_0$.

When connecting a pick up coil to a distant sensor, the inductance from the leads between the two may be significant. For a common twisted pair of wires, the added parasitic inductance is estimated to be 0.5 nH/mm due to leads [74]. As will be discussed later, the length of leads needed in this experiment was 40.6 cm, which gives a parasitic inductance $L_p = 203.2\ nH$. This is half the magnitude of the SQUID inductance and needs to be taken into account.

The bias current I_b was discussed in detail in section 3.6.1. In many of my tests, the bias current has had optimal values in the range $8\ \mu A < I_b < 25\ \mu A$.

When using a SQUID, excessive flux can sometimes become trapped in the SQUID loop. To expel this flux, the SQUID needs to be heated above it's superconducting temperature and allowed to cool again. The heating for our SQUIDs has usually required 100 ms while cooling lasts a few seconds. The use of an RF pulse to stimulate the rotation of the polarized ^{3}He can sometimes cause this flux trapping to occur. The heater requires 50 to 100 mA and

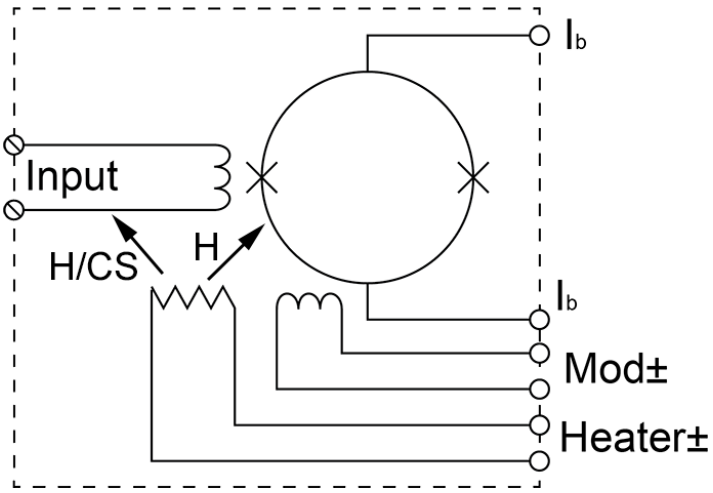


Figure 3.22: *Schematic of CE2SBlue SQUID Chip. The I_b Leads Are for the Bias Current Running Across the SQUID Loop, the* Mod *Leads Control the Modulation and Feedback, the* Heater *Leads Control a Resistor As Either a* Heater *or* Cryoswitch*, and the* Input *Circuit Connects to the Pick up Coils and Couples to the SQUID Loop. The* Heater *in the Schematic Is Drawn As a Resistor in a Usual Circuit Diagram. The* H *Label Shows That When Used As a* Heater*, Both the SQUID Loop and Input Circuit Are Heated. The* CS *Label Shows That When Used As a* Cryoswitch*, Only the Input Circuit Is Brought Above the Superconducting Temperature Threshold.*

usually will have a resistance in the range of 200 to 500 Ω. More details about a simulation I performed to understand this is found in section 3.6.4. Details about measurements I performed on cryoswitch resistance is found in section 3.6.5.

One way to work around this difficulty is to stop the excessive flux from reaching the SQUID loop in the first place. This can be accomplished by the use of a cryoswitch which is a heat switch that rapidly heats a section of the leads between the pick up coils and the SQUID loop. This may be an external chip placed in series with the pick up leads or may be a built-in switch, such as with the CE2SBlue. The cryoswitch in the CE2SBlue is the same as the heater. It is used by applying a current of 5 to 10 mA through the heater rather than the usual 50 to 100 mA. During testing, the cryoswitch was operated for ≈ 300 μ s. It could switch on and off in ≈ 5 ns.

One technique for SQUID operation is called the *Flux Locked* mode. When operated in this manner, (a) the SQUID response to applied flux is linearized, (b) it allows one to track flux changes of many flux quanta, and (c) it allows one to track flux changes of fractions

of a flux quantum. In this mode, the flux changes which are read out as the signal are amplified and fed back into the SQUID loop to cancel flux which had already entered it. The feedback circuit is contained in the Programmable Feedback Loop (PFL), described in more detail below. The feedback signal is fed in through the MOD± connections, shown in Fig. 3.22. For the CE2SBlue, the flux mod to SQUID mutual inductance is 80 pH and the flux mod coupling is 26 $\mu A/\Phi_0$.

When calculating the expected response from the SQUID, one must take into account each of the various inductances and couplings between the components of the system. This is because the transfer coefficient only gives one the flux into the SQUID loop. The inductances in the pick up coil circuit and the couplings between the input circuit and SQUID loop allow one to calculate the flux which had actually entered the pick up coils. The ratio of the flux entering the SQUID to the flux which entered the pick up coils is a geometric parameter called α [84]. The flux relationship can be written as follows

$$\Phi_{SQUID} = \frac{M}{L_S + L_p + L_i}\Phi_{pickup} = \alpha\ \Phi_{pickup} \tag{3.41}$$

where Φ_{SQUID} is the flux which enters the SQUID loop, Φ_{pickup} is the flux which entered the pick up coils, and the other parameters were defined previously. For those parameters defined previously $\alpha = 1.2\%$. The flux into the SQUID is often given in units of the flux quantum Φ_0 so it can easily be multiplied by the transfer coefficient V_Φ and converted to an expected output voltage.

To interact with the SQUID and setup control of it, a Programmable Feedback Loop (PFL) enclosure is used. The device we used was built by Star Cryo and called the PFL-100. This device contains the electronics for the flux modulation circuit and to read out from the SQUID. The flux mod circuit has an integrating capacitor and a feedback resistor which can be set to change the sensitivity of the system. While working with A. Matlashov at LANL, he suggested some modifications to the PFL which would assist in helping it to work more optimally in the range we intended to use it. He changed the values of the following

resistors 1 $M\Omega \rightarrow 121\ k\Omega$, 100 $k\Omega \rightarrow 60.4\ k\Omega$, 10 $k\Omega \rightarrow 30.1\ k\Omega$, and 1 $k\Omega \rightarrow 15\ k\Omega$. He changed the capacitors in the following manner 100 $nF \rightarrow 22\ nF$, 10 $nF \rightarrow 10\ nF$, and 1 $nF \rightarrow 4.7\ nF$,

The SQUID is controlled by the PCS100 SQUID Control Software provided by StarCryo through the PCI-1000 PC Interface device. The PCI-1000 unit is a piece of hardware which can be placed in an instrument rack and has 8 serial connections for PFL connections. From the PCI-1000, a test signal can be sent to the SQUID for tuning and the output from the SQUID can be fed to an oscilloscope or DAQ system. Fig. 3.24 has a diagram of the network of equipment components.

3.6.3 SQUID System Design and Construction

The SQUID was installed with a feedthrough at the top of the cryostat. A 1.5 m long SQUID cable from Star Cryo ran down the apparatus to the IVC. The SQUID cable has 5 twisted pairs of wire made of 36 AWG wire. Four twisted pairs were made of phosphor bronze (Ph Br) and one twisted pair was made of Cu. Four of the twisted pairs were used to interact with the SQUID. The Cu leads are used for the SQUID loop because the low electrical resistivity of Cu allows for more sensitive readout of the voltage across the loop. The Ph Br leads are used for (a) flux mod, (b) heater, and (c) cryoswitch. Inside the SQUID housing, the cryoswitch and heater leads are connected to the same heating element in the SQUID chip. They are separated externally allowing the ability to control the heating element as a heater using one device and a cryoswitch using another device. The bottom of the SQUID cable was heat sunk to the LHe bath at 4.2 K.

An enclosure was constructed from 0.5 mm thick sheet of Pb. The box has a Pb tube to allow the cryocable cold connector to be inserted into it and a long thin tube which the pick up coil leads can be slid through. The box is 55 (length) x 15 (width) x 12 (depth) mm. The Pb box is very weak and bends easily. A G10 breadboard is used to support the box. The box is soldered to the board in 6 places. A rectangular hole is cut to allow the Pb box to be in contact with the LHe bath. The SQUID is secured to the Pb box by GE

Varnish. After put into position, the SQUID was pressed to make the varnish layer as thin as possible.

The twisted pairs inside the SQUID cable are attached to a heat sink on the LHe bath. This stand is wrapped in GE Varnish and paper (allowed to set) then more varnish applied and the wires are wrapped around again. The final wrapping has about 3 full turns of wire in close contact with the heat sink. GE Varnish is used for thermal contact between the Pb box and LHe bath, and between the SQUID and Pb box. The heat sink has nylon washers between the cylinder and threads (M5). When the heat sink is screwed into place, it applies pressure to the varnish and Pb box increasing thermal contact. After the wires were wrapped around the heat sink, a layer of Pb was wrapped around the heat sink assembly to minimize noise from the breach in the side of the Pb box. The layer of Pb was soldered to the wall of the box to ensure grounding.

Inductance matching the SQUID to the pick up coils is the technique suggested in several reputable references [85, 58, 86]. The first-order gradiometer is composed of two magnetometers wound in opposing directions and displaced from each other on the same axis. One set of loops is called the "Signal Coil" and the other is the "Reference Coil". The signal coil picks up the desired signal and ambient noise. The second coil picks up ambient noise. The basic concept is that the coils will both pick up the same far field ambient magnetic field noise and because of their opposing windings, the noise will be canceled in analog.

The coils each had two turns Nb wire, Φ 0.076 mm, with a baseline of 1.2 inches and Φ 1.2 inches. Recall from Fig. 3.11, that the baseline is the separation between the coils on an axial first-order gradiometer. The pick up coils are wrapped in 90 nm gold coated foil to reduce high frequency noise. The gold side of the foil sheet is faced inward. The leads between the pick up coils and the SQUID are placed inside a Pb capillary. The capillary is grounded because it is in direct contact with the Pb box. The gold foil is then grounded because it is in contact with the Pb capillary and fastened tightly using dental floss.

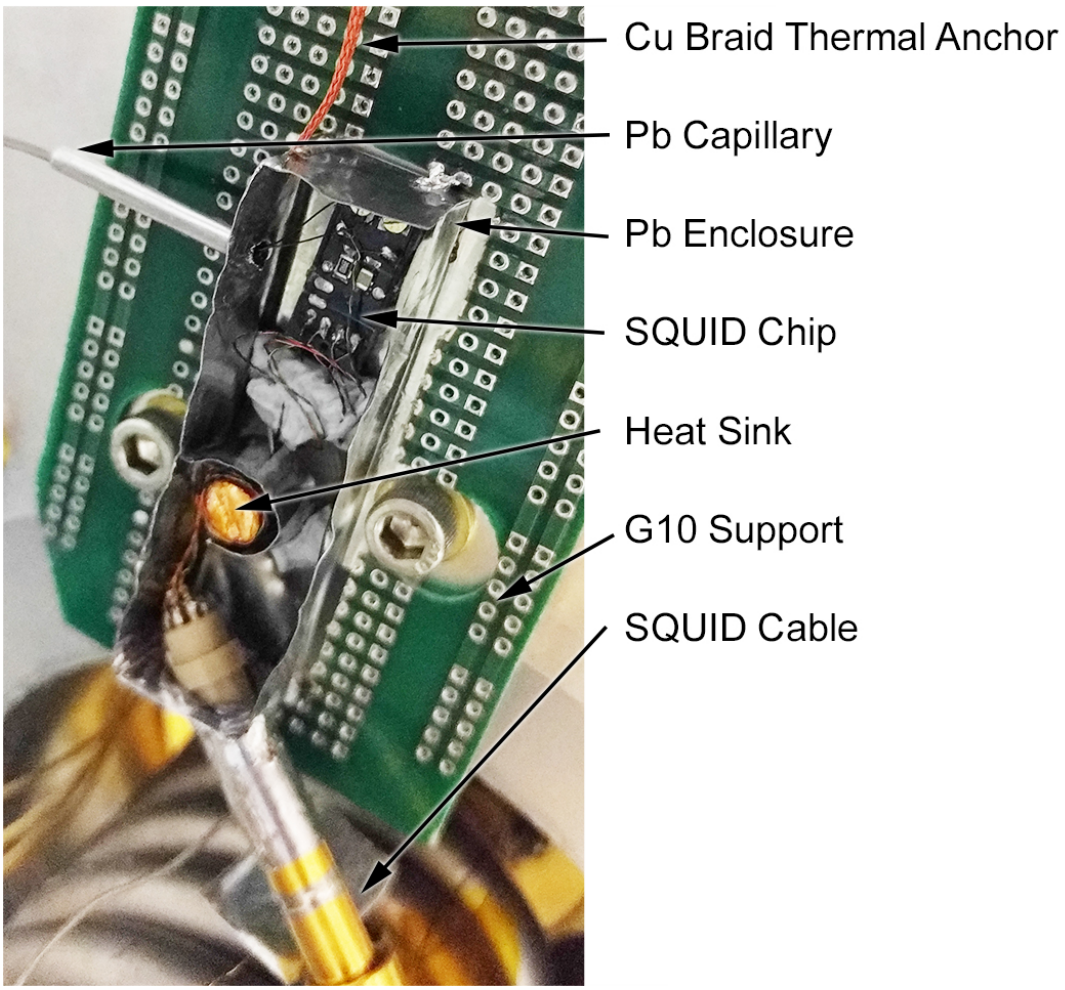


Figure 3.23: *Photo of SQUID Installation. In the Final State, the SQUID Is Placed Inside the Pb Enclosure and the Enclosure Is Soldered Shut With Another Sleet of Pb. This Assembly Is Attached to the LHe Bath.*

The Star Cryo PFL controls the heater by applying the necessary current. On the CE2SBlue, the heater can be used as a cryoswitch as well but requires a smaller current. A second connection to the heater was added by connecting to a separate twisted pair of wires running through the SQUID cable. This connection was made available by installing an enclosure which routed the used pairs from the PFL directly and allowed use of a BNC to connect to the additional twisted pair. This *Cryoswitch Port* enclosure was connected to the feedthrough and the PFL-100 connected to it. See Fig. 3.24 for a schematic of the electronics system.

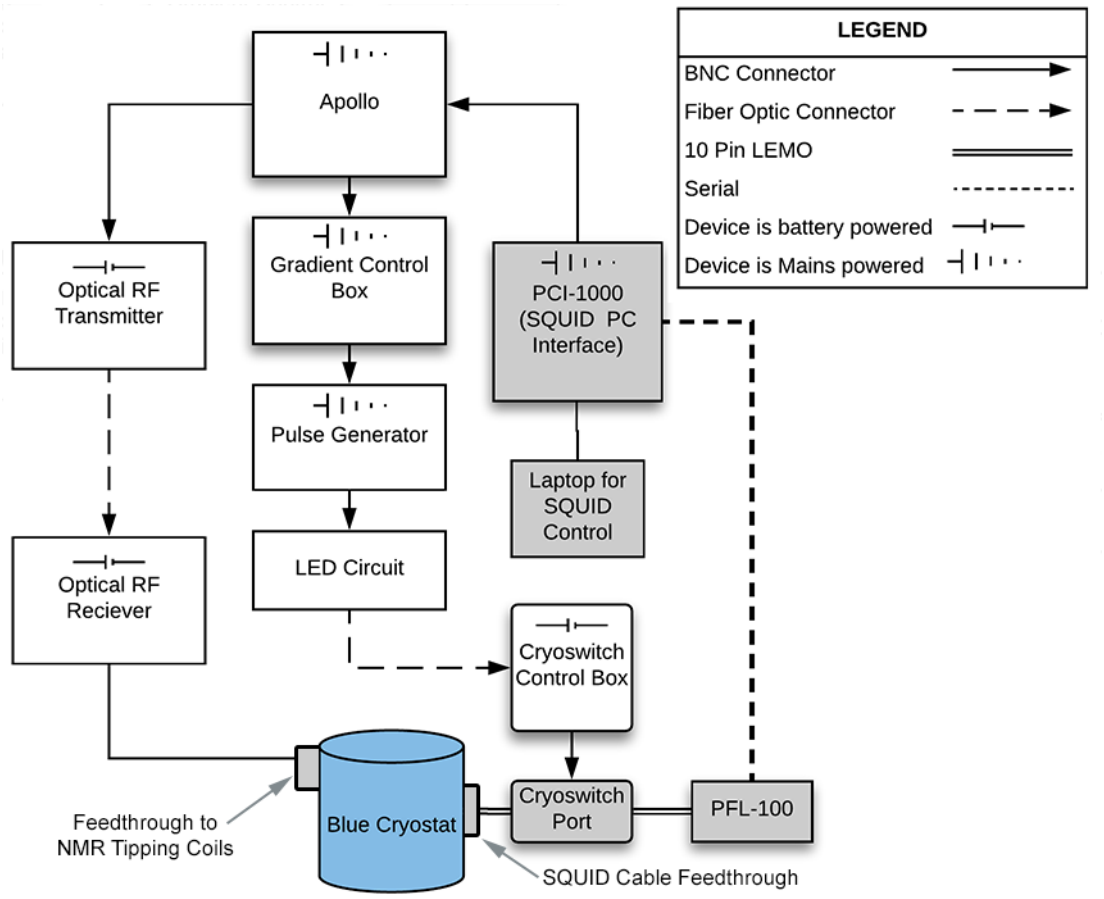


Figure 3.24: *Overview of Electronics Control Structure of Cryostat.*

I constructed the *Cryoswitch Control Box* to power the cryoswitch. The box is activated when light from an LED is fed through a fiber optic cable and delivered to a photodiode. The photodiode activates an NPN transistor which opens an electronic switch to feed power to the cryoswitch from a battery.

The PFL is controlled by the Star Cryo PCI-1000. This is an interface between the computer and the PFL. It is also the location from which data was taken from the SQUID and fed to the NMR computer for analysis.

3.6.4 Cryoswitch Simulation

As one additional check, a COMSOL model of the SQUID chip was created to attempt to calculate how heat is flowing through the chip. We weren't sure where the SQUID loop

was exactly within the chip and one task in creating the model was to identify the region of the SQUID Chip body which would be heated when delivering various amounts of power. Another task for this model was to identify heating due to the SQUID cable.

To recap: A cryoswitch is a device which interrupts the transfer of flux from the pick up coils to the SQUID loop. As was discussed in section 3.6.2, a part of the leads connecting the pick up coils and the SQUID loop are inside of the SQUID chip body and a part of the leads are outside the SQUID chip body. The part inside the SQUID chip are almost always Nb. The part outside the SQUID chip are usually superconducting, though sometimes non-superconducting leads are desirable if the the flux is going to be too large for the SQUID to process. In our applications, superconducting leads are desired and either niobium (Nb) or niobium-titanium (Nb-Ti) is used.

The cryoswitch is a heat switch that raises the temperature of the leads above their superconducting transition causing them to become resistive momentarily. The superconducting temperatures of Nb and Nb-Ti are 9.26 K [87] and about 10 K [88], respectively. The SQUID chip in our case is heat sunk to the atmospheric pressure LHe bath, which rests at 4.2 K.

The SQUID chip we decided to use for these tests was a Supracon CE2SBLue SQUID, which has an internal cryoswitch placed by the manufacturer during creation of the chip. The SQUID needs to be placed inside a Pb shield to eliminate environmental electromagnetic noise from overwhelming the SQUID loop. Because the SQUID chip is inside the Pb enclosure, a 0.5 mm Pb sheet is between the SQUID and the LHe bath.

The COMSOL simulation was created using the *heat transfer in solids* module to analyze heating and cooling of the SQUID chip. A surface representation of the model is shown in Fig. 3.25. The SQUID requires 6 leads to be controlled. At the time of the simulation, the cryocable, connecting the SQUID feedthrough to the SQUID had no thermal anchoring connector. The simulation was run expecting that it would be unrealistic to build one ourselves. In the end, I did end up manufacturing a heat sink. There is more discussion

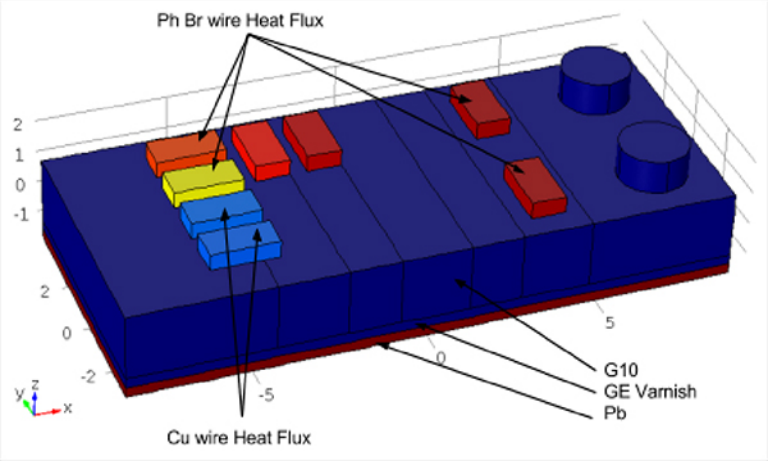


Figure 3.25: *Surface Representation of COMSOL Model of CE2SBlue SQUID Chip.*

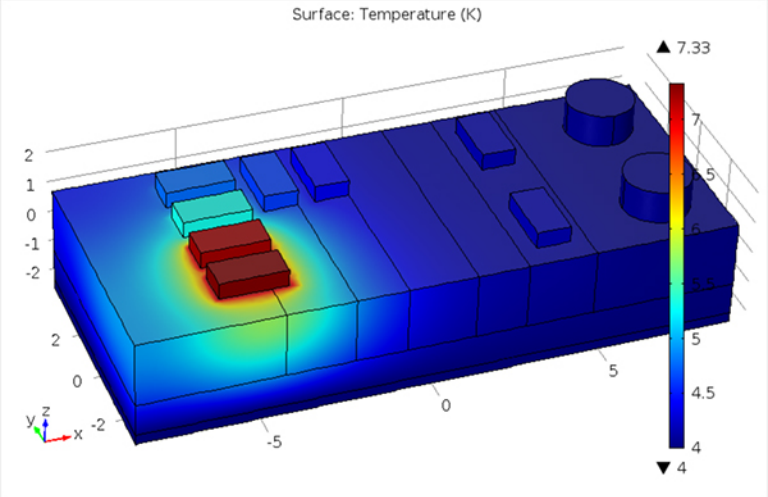
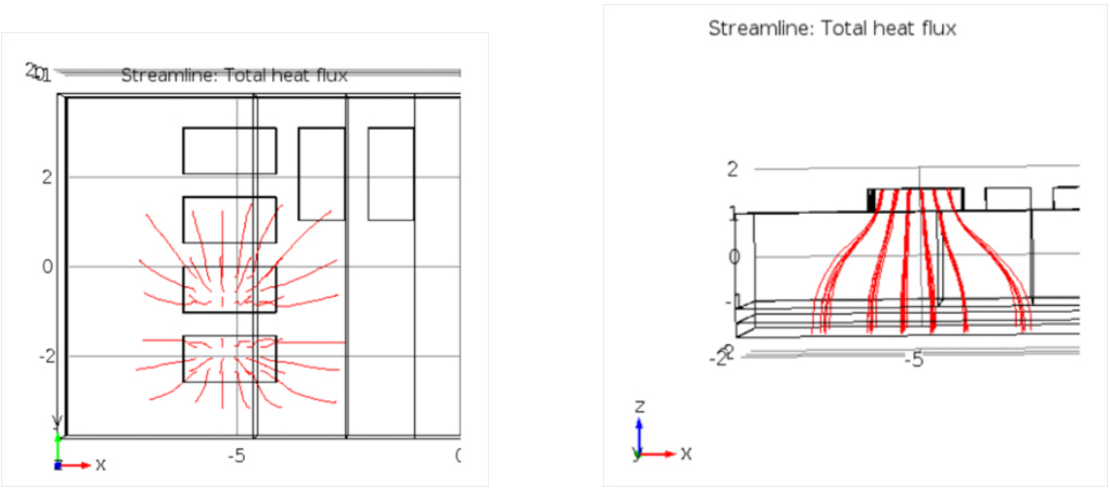


Figure 3.26: *Surface Temperature of COMSOL Model of CE2SBlue SQUID Chip With Wire Heat Loads From SQUID Cable.*

about this is section 3.6.3. For the simulation however, the leads were considered to be connected to room temperature at the feedthrough and the bottom of the model shown in Fig. 3.25 was connected directly to the LHe bath. All wire leads are 0.005 inches OD and have length 2 meters. Two wires are *copper* (Cu) and four wires are *phosphor bronze* (Ph Br). The thermal conductivity of Cu is orders of magnitude larger than Ph Br. The heat load from each wire was calculated using Eq. 4.4. The heat loads from the Cu and Ph Br wires are 1.03 mW and 32.7 μW, respectively.



(a) **(b)**

Figure 3.27: *Heat Flow Through SQUID Chip From Cu Leads of CE2SBlue Simulated In COMSOL.*

First, the model was used to estimate the temperature distribution across the chip. Fig. 3.26 shows the results of this simulation. It is evident that the Cu wires cause the greatest heat load into the chip. The SQUID loop must be below 5 K in order to operate. Experimental test with the SQUID in this configuration allowed the SQUID to operate properly, so one can deduce that the SQUID loop is closer to the right side of Fig. 3.26.

The streamline heat flow path through the chip can also be calculated by COMSOL. Figs. 3.27 show the path the heat takes through the chip from the warmer Cu leads to the wall of the LHe bath.

The next step was to install a resistor to act as the cryoswitch/heater. In the CE2SBlue SQUID, the heater and cryoswitch are the same unit and are controlled through the same leads. An internal cylindrical resistor with radius of 0.5 mm and length of 4 mm was added to the model between the heater solder pads. It has resistance 269 Ω. Fig. 3.28 shows the location of the resistor.

The manual for the SQUID states the heater requires 5 to 10 mA to operate as a switch and 50 to 100 mA to operate as a SQUID heater. In practice, I was able to progressively increase the current until it began to exhibit the expected cryoswitch behavior and found

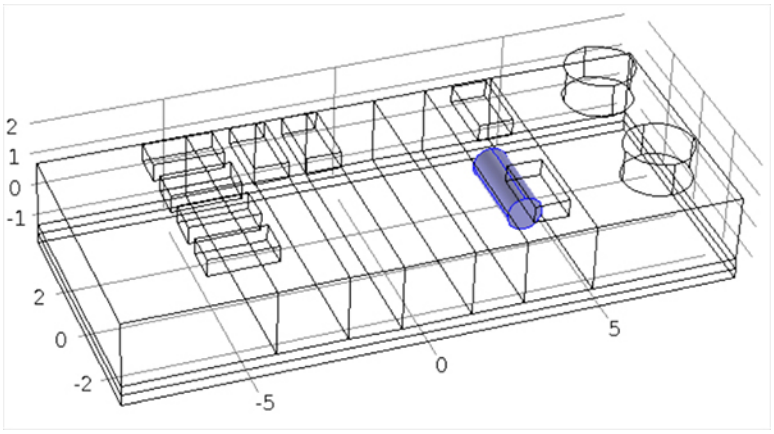


Figure 3.28: *Location of Resistor Placed in CE2SBluE COMSOL Model.*

that slightly above 5 mA, it would begin to activate. The measurement I performed is discussed in section 3.6.5.

A time dependent simulation was run which gave a 300 μs pulse to the resistor with 5, 10, and 50 mA currents. This was applied as a rectangular pulse with 5 μs transition time between zero and the maximum current. A number of points were selected between the resistor and the Cu leads to give an idea about how quickly cooling could progress under ideal conditions. The points were at the surface of the heater and 0.5, 2, and 4 mm away from the heater. Figs. 3.29 and 3.30 show the results of each of these simulations at each of the locations mentioned.

In Fig. 3.29, a set of three dimensional contour surfaces (aka *isosurfaces*) are shown. These are specific temperature surfaces distributed through the volume generated by heating the resistor.

Although, the 5 mA simulation only reaches a maximum temperature of 7.4 K and the superconducting transition of the Nb leads is 9.26 K, in practice the switch is still found to activate around this temperature. This gives us some idea about the accuracy of this modeling technique.

One valuable insight gained from these simulations are the rates at which the resistor allows the leads between the input circuit and SQUID loop to return to their supercon-

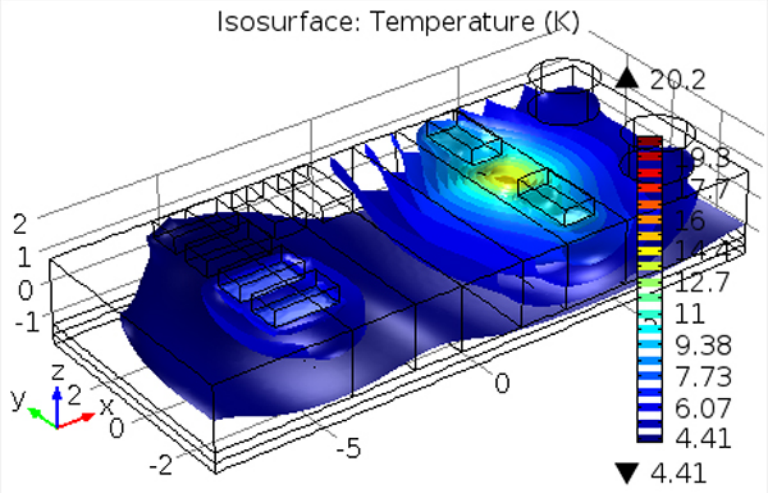
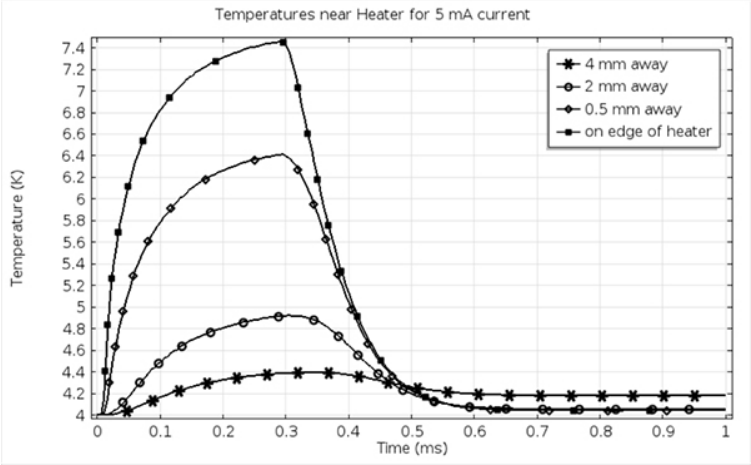


Figure 3.29: *Result of COMSOL Simulation Showing Region Warmed by Heating of Cryoswitch Using 10 mA Current.*

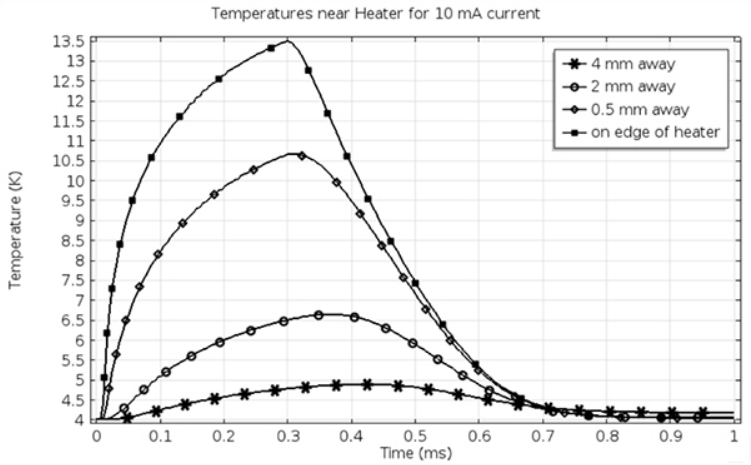
ducting state. For the 5 mA and 10 mA examples shown in Figs. 3.30, the chip stabilizes in about 300 and 400 μs, respectively. These results can be compared to Fig. 4.13 . In that figure, the large grid time units are 5 ms, meaning the single tick width of 1 ms is discernible by eye. Clearly, the SQUID begins to be influenced by the pick up coil flux in a time less than 1 ms. This is sufficiently fast for the purposes of the experiments performed in this thesis and the experiments to be performed in the PULSTAR-SOS and SNS-nEDM experiments.

At 50 mA, the chip takes a much longer time to stabilize. This is no problem because when the resistor is used as a heater, quick transitions between superconducting and non-superconducting states are not important.

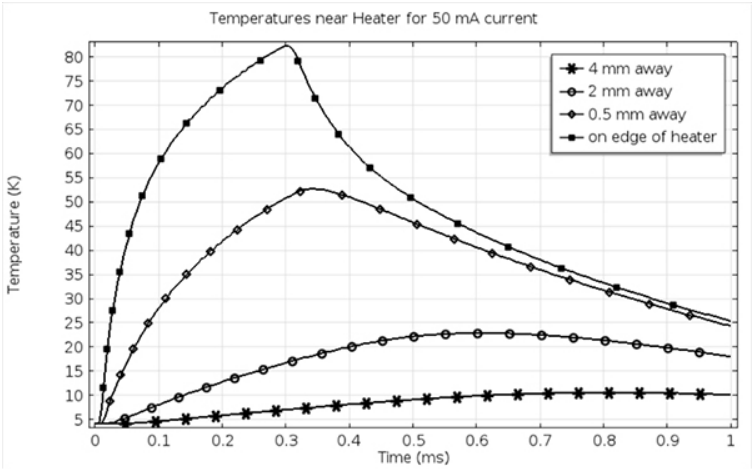
Attempts to measure the rate of transition into and out of the superconducting state were difficult to capture on the oscilloscope. We decided that the system was operating with faster transition time than would influence our experiments and thus no direct comparisons between these simulations and experimentation were conducted in earnest. Fig. 4.13 does show the output from a SQUID as the cryoswitch is activated and deactivated, though the temporal resolution is too large to compare to what we have discussed here.



(a) *5 mA applied to heater for 300 μs.*



(b) *10 mA applied to heater for 300 μs.*



(c) *50 mA applied to heater for 300 μs.*

Figure 3.30: *Time Dependent Results When Applying Current to Resistor Shown in Fig. 3.28.*

3.6.5 Cryoswitch Resistance Measurement

I performed testing on an external cryoswitch chip purchased from Supracon called the *SW1* switch. This is a simple cryoswitch chip designed to be activated with a 5 mA current, similarly to the CE2SBlue and made by the same manufacturer. It has two screw terminals (like a SQUID) for the input circuit and four solder pads which controlled the heat switch. Unlike a SQUID chip, the input circuit is a direct superconducting Nb trace which is thermally coupled to the switch heater. When used with a SQUID chip, the pick up coil leads are to be broken and connected to the screw terminals on the SW1 so that the pick up coils are in series with the SW1 input circuit. The four solder pads on the SW1 connected to two resistors inside the chip. Current could be applied to one or both of the resistors which heated the circuit inside the chip and disrupted the free flow of electrons through the superconducting input circuit and thus interrupt the signal from the pick up coils. The chip was connected to a current source by soldering leads onto the solder pads.

The resistance in the switch changes as the switch cools having 562 Ω and 450 Ω at 300 K and 4.2 K, respectively. The switch circuit was placed in series with a (a) potentiometer, (b) V = 3.2 V battery, and (c) ammeter. The input circuit (screw terminals) was connected to a low current resistance monitor, specifically a LakeShore Model 218 Temperature Monitor in *Cernox* setting.

The cryoswitch chip was placed inside a 60 L LHe dewar while the potentiometer was kept outside the dewar. The potentiometer resistance was slowly decreased allowing current I_{heater} to flow through the heat switch. The resistance through the input circuit was monitored to see how it responded.

The resistance in the input circuit as a function of the switch current is shown in Fig. 3.31. The resistance could be measured with resolution of 100 mΩ using a LakeShore Model 218 Temperature Monitor [89]. At 2.75 mA the resistance started to raise above 0 Ω. At 3.43 mA, the resistance had raised to 952 Ω. At 5.6 mA, the resistance had raised to 1.31 kΩ. Although this was not the exact cryoswitch which was used in the experiments here,

it gives one some impression about how the resistance in the input circuit changes when a cryoswitch is used to dissipate the signal.

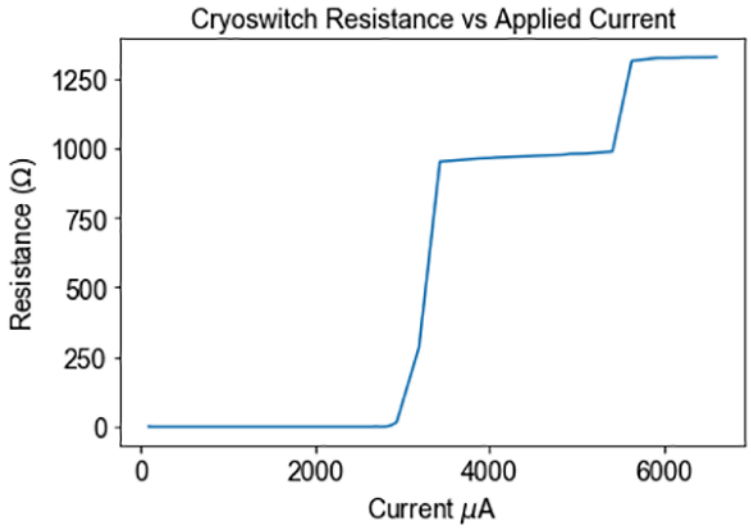


Figure 3.31: *Resistance in Supracon SW1 Cyroswitch Input Circuit As a Function of Applied Current.*

3.7 SQUID Measurements at 4 K

Measurements were taken with a Supracon CE2SBlue SQUID at 4 K. The purpose of these measurements were to understanding the electromagnetic environmental noise in the room and find ways to mitigate its influence on the SQUID signal if needed. The reason understanding the noise in this room is so important is that the PULSTAR-SOS apparatus, described in Ch. 4, will be setup and the SQUID system tested in the same room. We developed an understanding of the noise spectrum and found some ways to reduce it.

3.7.1 SQUID Experimental Setup

A cylindrical superconducting Pb shield was installed on the inside of the IVC. The shield was one single sheet of 3 mm thick Pb. While the IVC was immersed in LHe, the Pb was in a superconducting state and would not allow magnetic fields to penetrate it. This would reduce the environmental noise significantly. SQUID tests performed in a 60 L

storage dewar in the same room, without Pb shielding, resulted in enough noise that the SQUID was offline.

The shield was constructed from a single Pb sheet with the height of the IVC (15 inches) and a width of a few inches longer than the circumference of the IVC. It was wrapped fully around the interior circumference of the IVC. The top and bottom of the shield were left open. The magnetic holding field passed axially through top and bottom of the cylinder. The shield cancelled transverse magnetic fields, so the area of the pick up coils were orthogonal to the axis of the shield.

At the ends of the Pb sheet, where the Pb crossed back over itself to form a cylinder, it was wrapped in insulating tape to isolate each end from the other end. If the Pb ends had been able to contact each other, they would create a vertical cylindrical superconducting cylinder. If it were setup like that, it would be mathematically similar to a superconducting solenoid, which would cause a current to flow in response to changes magnetic flux through it. If that were the situation, changing the holding field strength would cause the field to be canceled inside the volume. This was not desired. Leaving the top and bottom open, and not allowing it to be a closed loop, prevented superconducting currents from canceling the field.

A laptop computer was attached to the PCI-1000 and directly controls the SQUID.

Nearly all electronics were powered through an isolation transformer. The isolation transformer is a 2.5 kW Topaz with 0.0005 pF. Early attempts to use the SQUID in the cryostat showed too much noise prior to the addition of the isolation transformer. Details about the reduction of noise in the SQUID after the addition of the isolation transformer was added are discussed in section 3.7.2.

The holding field coils were powered directly from the mains power in the building. A low pass filter was added to the holding field circuit at one point but showed little influence on SQUID performance and was removed after it was not found to be useful.

There were five temperature sensitive resistors positioned throughout the experimental

regions. They were measured using a PicoWatt AVS-47 Resistance Bridge and PreAmp. These resistors were positioned on the 1K Pot, Still, Sorb, Mixing Chamber, and inside the PEEK tube. The exact type of four of the resistors was unknown but their resistances with respect to temperature had previously been plotted and were available to us. The resistor inside of the PEEK tube was a Rox Ruthenium Oxide Resistor RX-102A from LakeShore Cryotronics.

3.7.2 Noise Spectrum

The largest challenge observed by most groups trying to implement the use of a SQUID system is figuring out how to deal with noise. During our discussions with other scientists, we found that many were simply unable to use them due to excessive background noise issues. When noise is dominating the system, the SQUID is observed to "hit the rails". This means the output sits at the maximum or minimum output potential and no change in the signal is observable. For the PCI-1000 unit, the rails are at ± 11 V.

To manage the noise, we found that all AC cables near the cryostat needed to be removed or intelligently positioned to minimize extraneous magnetic fields. The cables which needed to be close to the cryostat were lifted off the ground so that they approached radially at the height of the Pb shield.

The electronics rack which houses the NMR control system and telemetry units was open on three sides. Investigation into fully shielded racks discovered that an investment of $\sim$ \$10 - \$50,000 will be needed to fully shield the electronics. This option is under discussion for the PULSTAR SOS experiment. As a work around, the common technique of wrapping the sides of the rack with grounded aluminum foil was employed. This did help to reduce the noise in the system.

The cryostat itself was a series of 4 aluminum shields between the environment and the SQUID system. The cryostat exterior was grounded. An additional layer of grounded Cu fabric was wrapped around the exterior of the cryostat.

The NMR coils had previously been powered from the NMR control system through an RF amplifier which was connected to a feedthrough by a BNC cable. It was found that when the BNC was disconnected, the SQUID gave a visible output (not hitting the rails). When the BNC was connected to the cryostat, the system would hit the rails. So there was some noise issue arising from the mains power itself which interfered with the operation of the SQUID enough that it couldn't be used. We purchased a optical RF system to electronically decouple the NMR coils from the mains power. This was successful.

The optical RF system is a *PPM point2point Analog Fiber Optic System.* This system has two primary units, a transmitter and receiver. The transmitter unit can receive a signal through a BNC cable and sends it through a fiber optic cable. The receiver unit receives the signal from the fiber optic cable and outputs it through a BNC. Both the transmitter and receiver are battery powered by custom NiMH batteries. This allows for electronic isolation between active coils inside the IVC and the rest of the world. Using this setup, we were able to operate the SQUID. The transmitter was wrapped in grounded aluminum foil and the receiver was placed in a solid Faraday cage.

The Power Spectral Density (PSD) helps to demonstrate the amount of noise in a system. "The PSD approximates the amplitude of the signal within a 1 Hz bandwidth located at each frequency bin." [90]. Essentially, it resizes the bins to have a width of 1 Hz, so that the magnitude is held constant across any frequency range and thus different frequency ranges can be compared because each bin is essentially integrated over 1 Hz bandwidth.

The PSD was measured using a Stanford Research Model SR760 FFT Spectrum Analyzer. The flux entering the SQUID loop Φ_{SQUID} can be calculated by taking the spectrum output and dividing my the transfer coefficient V_Φ discussed in section 3.6.1. In this case, the PFL electronics were set to low sensitivity, which allows for a larger range of fluxes to be measured, and thus $V_\Phi = 0.28\ V/\Phi_0$. The flux entering the pickup coils Φ_{pickup} can then be calculated by multiplying the SQUID flux by α. So that $\Phi_{SQUID} = \alpha\ \Phi_{pickup}$ as shown in Eq. 3.41. Differentiating between the flux into the SQUID and flux into the pick up coils

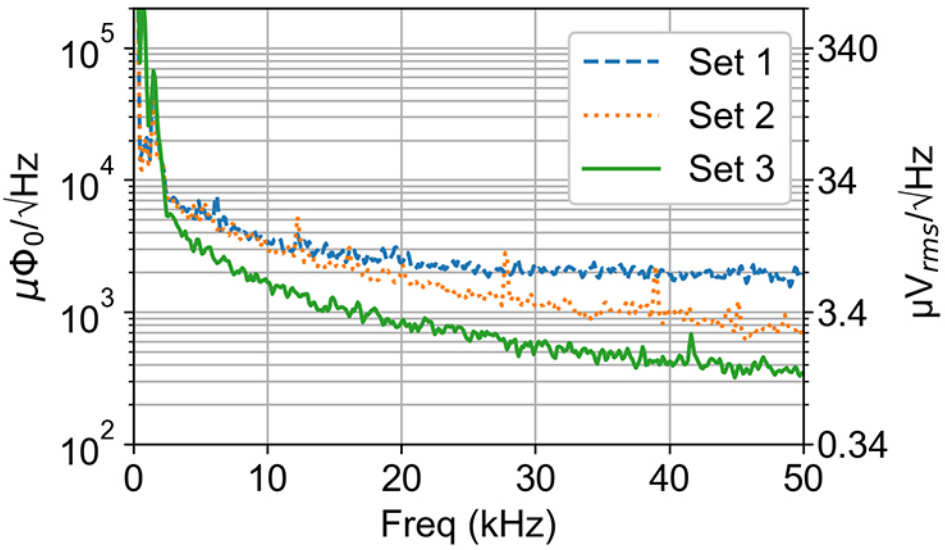


Figure 3.32: *PSD Flux Through the Pick up Coils Which Measure the Background Noise.*

is important to understand as they are useful for different types of characterizations of the system.

The three sets of data shown in Figs. 3.32, show decreases in the flux through the pick up coils as changes were made to the system shielding. The figure shows the background noise in the pick up coils. The shielding techniques mentioned need to be used or improved for implementation in both the PULSTAR SOS and SNS-nEDM experiments.

"Set 1" on the figure was the base stable configuration. To achieve this (a) the cryostat was wrapped in grounded Cu fabric, (b) leads from the power sources to the holding field coils were encased in grounded aluminum flex hoses, and (c) all AC power cables were removed or positioned radially and pointing directly at the Pb shield.

"Set 2" on the figure was achieved by unplugging both of the pumping stations from the wall, not simply turning them off.

"Set 3" on the figure was seen after (a) unplugging all electronics for the dilution refrigerator, (b) wrapping the electronics rack in aluminum foil, and (c) changing the SQUID laptop controller to be battery powered. This is the most obvious evidence that a closed electronics rack with fiber optic coupling to the NMR coils and the SQUID laptop is necessary.

Whether the noise is coming from the electronics and influencing the SQUID or the noise is entering directly into the electronic components themselves was unknown. Decoupling these systems was not reasonable in our lab conditions.

Prior to disassembling the experimental apparatus, the low frequency PSD was not recorded. It would have been quite useful to have a lower frequency bandwidth recorded because the PULSTAR-SOS experiment, discussed in Ch. 4, will be collecting NMR signals near 100 Hz.

It is still possible to estimate the background noise level and compare it to the expected signal in the PULSTAR-SOS experiment. If we anticipate the ability to reduce the background noise similarly to the reduction demonstrated by Fig. 3.32, we could expect the background noise to be roughly in the $10^{-3}\ \Phi_0/\sqrt{Hz}$ regime.

In the PULSTAR-SOS experiment the operational [^{3}He:^{4}He] concentration will be approximately 10^{-7}. A simulation was setup with the geometry of the experimental apparatus described in this chapter using a code written by S. Clayton at LANL. Some details about the simulation are discussed in App. D. The expected signal flux into the pick up coils is outlined in Fig. D.2. Using the values from the present experiment of ^{3}He polarization around 25% and a [^{3}He:^{4}He] concentration of about 10^{-7}, the figure shows that we would expect a signal around 1 Φ_0. This signal would then be about 1,000 times stronger than the anticipated background noise of $10^{-3}\ \Phi_0$ and therefore be measurable.

To the further benefit of such a measurement, the PULSTAR-SOS experiment will be using the MEOP polarization system, built by A. Reid, which was able to reach an absolute ^{3}He polarization greater than 80% [69]. As Fig. D.2 shows, this would increase the expected signal from the ^{3}He to something closer to 2 or 3 Φ_0.

3.8 Conclusions

The room temperature longitudinal relaxation time T_1 of the newly built dTPB-dPS coated measurement cell was measured and found to be of acceptable duration. This verifies the technique used to coat the cell and its usefulness for the construction of future cells.

The noise spectrum from the SQUID system was improved significantly and lessons were learned about improvements resulting from additional shielding around the cryostat and electronic systems. Future preparations for installation of SQUID systems in PULSTAR-SOS and SNS-nEDM will need to implement similar designs prior to building the systems.

Based on the background noise spectrum, the expected signal from polarized ^{3}He in the PULSTAR-SOS experiment have been calculated to exceed the background noise observed in the measurements reported in this chapter. This increases our confidence in our ability to measure the signals in that experiment and demonstrates that this was a useful exercise in learning important skills for moving forward with that experiment.

Chapter 4

SYSTEMATIC AND OPERATIONAL STUDIES APPARATUS

The PULSTAR Systematic and Operational Studies (PULSTAR-SOS) cryosat is intended to be a stepping stone on the way to developing the full scale SNS-nEDM experiment. The SNS-nEDM experiment will include the use of strong electric fields ($\sim$ 75 k cm^{-1}), ultra-cold neutrons (UCN), polarized ^{3}He, Superconducting QUantum Interference Devices (SQUIDs), and light collection using silicon photomultipliers (SiPM), among many other systems. The PULSTAR-SOS experiment will include all these systems except the large electric field. Additionally, the SNS-nEDM experiment will use two measurement cell simultaneously, while the PULSTAR-SOS experiment will only use one.

Two significant contributions are found in building this scaled down version of the experiment. First, it will be capable of housing a full sized measurement cell, the same ones used in the SNS-nEDM experiment. Therefore, systematic studies directly related to the SNS-nEDM experiment can be performed on this auxiliary apparatus using UCN and ^{3}He. Second, it will take around 1 or 2 weeks for a full cooling and warming cycle. The full scale SNS-nEDM cryostat will take 6 months for a single cooling and warming cycle. This saves significant time and resources for testing concepts for use or experimentation on systematics.

This chapter describes simulations and systems I worked on as part of the PULSTAR-SOS design. In section 4.1, an overview of the aspects of the system which are specific PULSTAR-SOS and different from the SNS-nEDM experiment are discussed. Some specific details and physics about the COMSOL simulation software used for my analyses are coverd in section 4.2.

I performed extensive analyses on three subsystems of the PULSTAR-SOS apparatus. These systems include a) an actuator arm, which opens and closes a valve on the side of the

measurement cell, and b) the neutron guide, which directs the neutrons from the outside of the cryostat to the measurement cell, and c) heat shields to separate the environment from the low temperature portions of the apparatus. Section 4.3 outlines the work and logic behind these system designs.

The PULSTAR-SOS magnetic field sensing will be performed with SQUIDs. The experiments discussed in Ch. 3 developed some of the techniques and knowledge needed to properly implement the use of SQUIDs in PULSTAR-SOS. Section 4.4 goes into details about design decisions and components in this experiment.

Section 4.5 offers a concise summary of the details reported in this chapter.

4.1 PULSTAR Measurement Overview

The PULSTAR cryostat will receive ultra-cold neutrons (UCN) from the PULSTAR nuclear reactor, located on the campus of NC State University. The device will have a dilution refrigerator and cryo-cooler installed. The dilution refrigerator will be used to bring the measurement cell to ~ 0.4 K. The cryo-cooler is a cryogen free heat pump which will take some of the heat load off of the LHe bath and thus save on LHe refilling cost and time. The outside of the cryostat has a diameter of 44 inches. The cryostat itself has a height of 82 inches. It is be mounted on a support structure which holds the cryostat high enough off the ground to allow the bottom of the heat shields to be dropped below it to allow work on the experimental region to occur. The final height of the system is greater than 15 ft.

A measurement cell, which is the same size and made of the same materials as those to be used in the SNS-nEDM, experiment will be installed. This cell has inner measurements of 3 inches by 4 inches by 40 cm. A photograph of the measurement cell to be used in the experiment can be seen in Fig. 2.1. See Fig. 4.3 for its location in the PULSTAR-SOS experiment. The inside of the cell will be coated with dTPB-dPS which will wavelength shift extreme ultra-violet (EUV) photons produced by the ^{3}He(n,p)^{3}H reaction to the visible spectrum as described in section 2.4. A series of fiber optic cables will be made into a flat

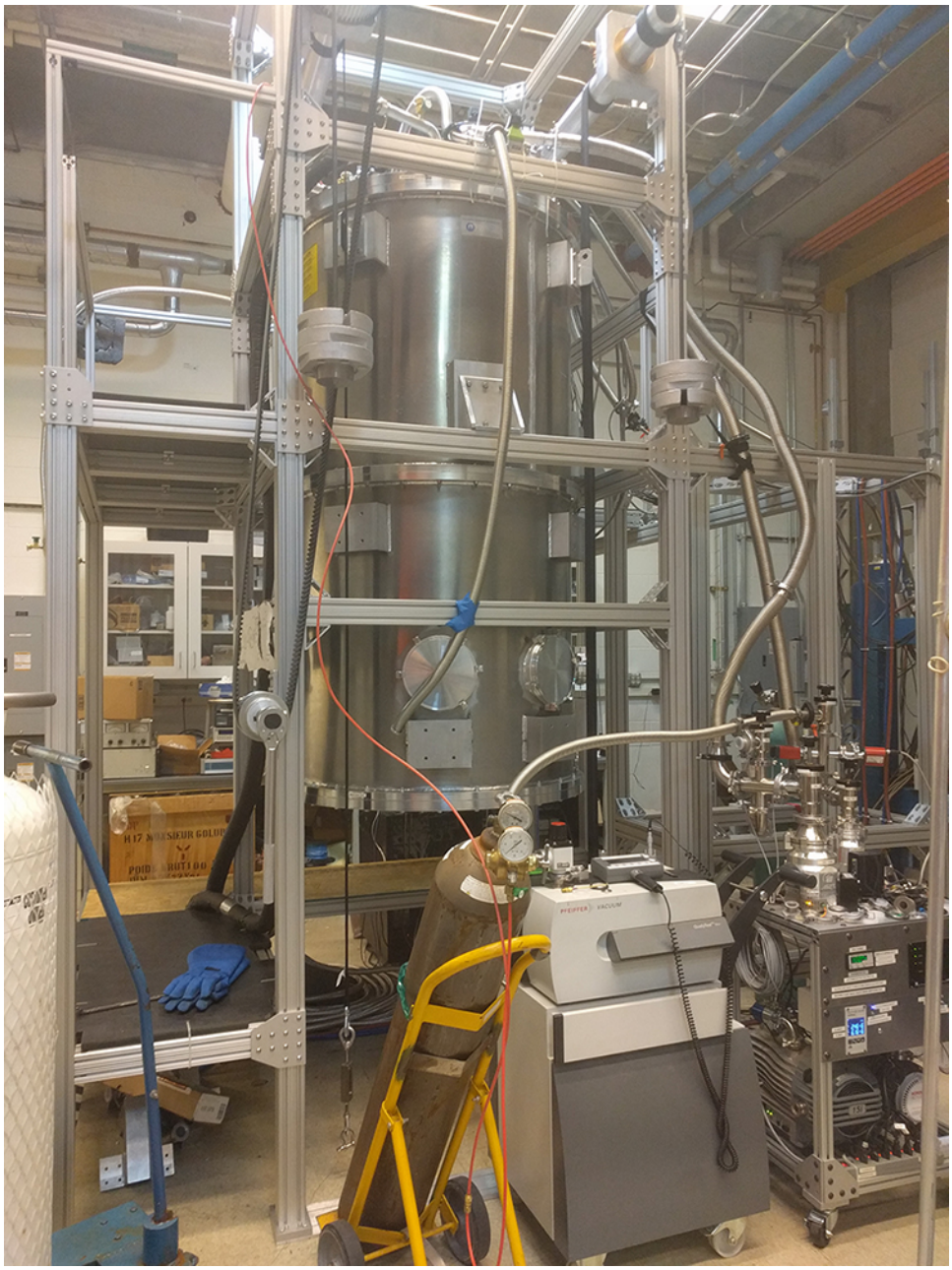


Figure 4.1: *Photo of PULSTAR-SOS Cryostat As Currently Assembled in TUNL.*

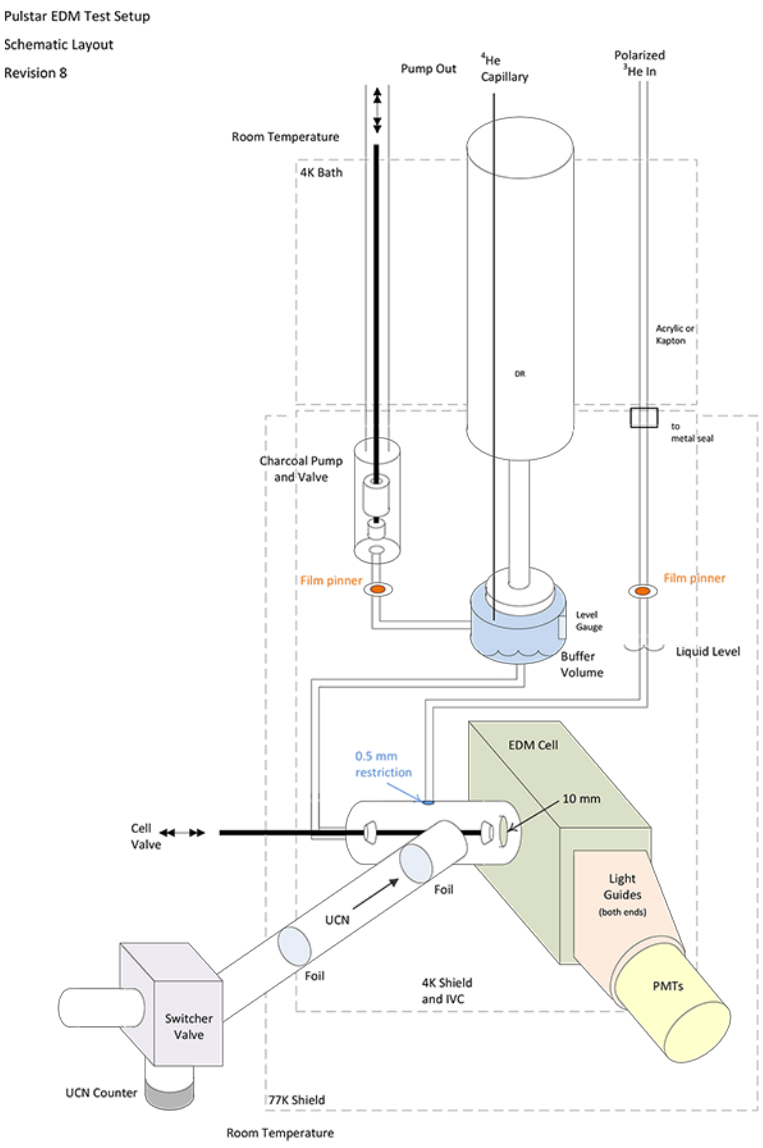


Figure 4.2: *Basic Schematic of Pulstar Cryostat Concept.*

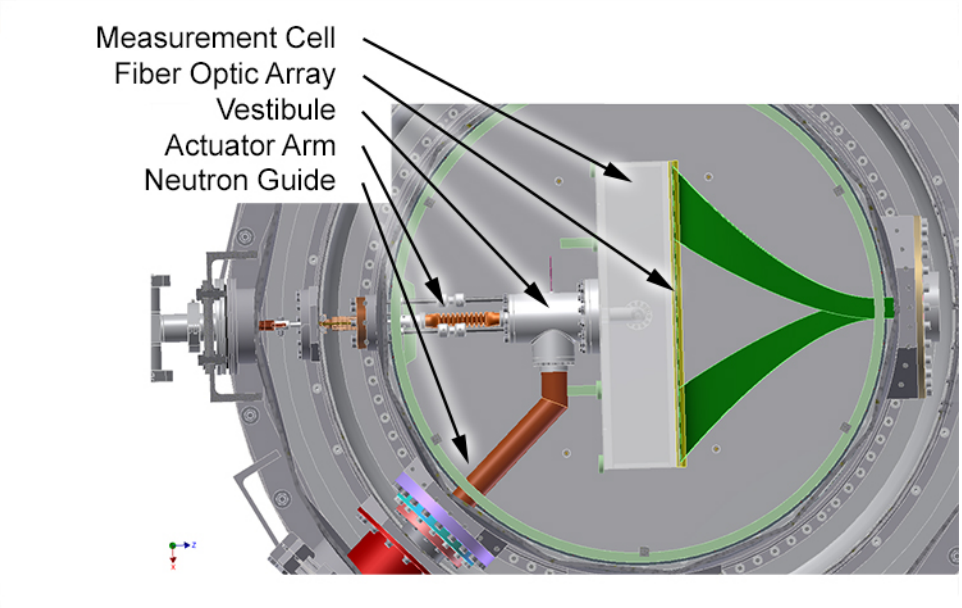


Figure 4.3: *Autodesk Inventor Model Created by Larry Bartoszek Showing IVC Internal Components for PULSTAR-SOS Experiment. This View Is From the Bottom of the Cryostat. The Measurement Cell Is Centrally Located in the IVC. The Green Fiber Optic Cable Array on the Right of the Figure Covers That Entire Side of the Measurement Cell. The Vestibule Has Ports for UCN, ^{3}He, and ^{4}He. Between the Vestibule and Measurement Cell Is a Φ 1 cm Hole With a Plug. The Plug Is Moved Into and Out of the Hole Via Operation of the Actuator Arm.*

surface covering one long side of the measurement cell. The cables will be ported to the side of the IVC volume and light will be sent to SiPMs for collection and analysis.

Attached to the other side of the measurement cell will be a vestibule. The vestibule has ports for ^{4}He, polarized ^{3}He, and UCN. Access to the vestibule is continuously open to each of these. The ^{4}He will be liquefied and cooled in a buffer volume attached to the bottom of the dilution refrigerator's mixing chamber. The ^{3}He will be polarized in a Meta Stability Optical Pumping (MEOP) system which lives on top of the cryostat [69].

Between the PULSTAR reactor and the cryostat will be placed an apparatus for converting the reactor neutrons to UCN [91]. This device couples a solid ortho-D_2 converter to two moderators. The first moderator is solid D_2O which thermalizes the reactor neutrons. A solid CH_4 puck then moderates the thermal neutrons to cold neutrons. These neutrons are then downscattered to UCN energies by the superfluid ^{4}He as described in section 2.2.

The neutron guide, which guides neutrons from the UCN source to the vestibule, has foil windows which will allow neutrons to enter the vestibule but will not allow ^{4}He or ^{3}He to exit it. The neutron guide is discussed in detail in section 4.3.2.

To allow access for atoms and neutrons from the vestibule into the measurement cell, a hole with Φ1 cm will be cut into the side of the measurement cell. An actuator will be used to open and close this hole using a plug. The actuator mechanical control system is outside the cryostat at room temperature. If the design had a mechanical actuator system inside the vestibule, magnetic and electronic components would need to be placed there. The design solution of using a room temperature mechanical actuator shifts the design challenge from one of low noise, non-magnetic, low temperature, mechanical actuation to one of managing heat flows into the vestibule. The challenge to be overcome is then one with a higher likelihood of effective implementation on the first try. Basically, the challenge is simply to moderate heat flow from room temperature into the measurement cell through the actuator arm. Section 4.3.1 outlines the design details of the actuator heat flow calculations and geometry.

Excluding the presence of an electric field, the majority of the physics for the PULSTAR-SOS experiment are consistent with those of the SNS-nEDM experiment. Refer to Ch. 2 to review details if interested.

4.2 COMSOL Simulations and Physics

The NCSU team needed to design the entire system for the PULSTAR-SOS experiment. I created simulations of the actuator arm, neutron guide, and heat shields to assist in the design of the SOS cryostat using COMSOL Multiphysics. COMSOL is a finite element mesh analysis software which uses partial differential equation solvers and is pre-programmed with many useful physics packages [79]. Initial designs of the systems were proposed by the group and modeled in Autodesk Inventor by L. Bartoszek (Bartoszek Engineering). I worked with E. Korobkina (NCSU Nuclear Engineering) and L. Bartoszek to find geometries and materials which allowed reasonable heat loads into the experimental region. This section

describes COMSOL and relevant physics simulated in COMSOL. These physical phenomena are also useful through following sections which include calculations.

COMSOL versions v4.3 to 5.0 were used with the "Heat Transfer in Solids" module. This module was used to calculate conductive and radiative heat loads. A description of the relevant physics for calculating conductive heat and radiative heat loads are found in sections 4.2.1 and 4.2.2, respectively. The volumes around the components being designed are in vacuum, therefore convective calculations were not necessary.

For these models, the material physics which are simulated by COMSOL take into account geometry, emissivity ϵ, and thermal conductivity $\kappa(T)$. When a time dependent simulation was needed, density and specific heat were incorporated. Due to the wide temperature range (0.4 K to 300 K) over which the components may be exposed, the dependence of each of these properties on temperature were included in the models. In many cases a time independent or "steady state" solution was sufficient to predict heat loads.

4.2.1 Conductivity

Starting with Ohm's Law from electricity and magnetism, we can build an intuitive understanding of how similar mathematical principles are applicable in the conduction of heat. Ohm's Law states

$$V = I\ R \tag{4.1}$$

where V is a voltage, I is an electrical current, and R is the resistance in the material to the flow of electrical current. In the case of thermal conductivity, the current is a heat current rather than an electrical current. Thus $I \rightarrow \dot{q}$.

The voltage from Ohm's Law expresses the boundary limits which drive the flow of current. In Ohm's Law, this is driven by a potential difference between two parts of a system which generates an electric field. When talking about heat loads, it is the energy stored in the material, expressed as temperature, which drives the current. All systems

are attempting to reach thermal equilibrium [92]. The high temperature materials are constantly giving energy to the lower temperature materials, meaning the heat flows from high temperature to low temperature. Thus $\Delta V \rightarrow \Delta T$.

Rather than focus on how well materials *resist* the flow of energy, as Ohm's Law does, let us focus on how well materials *allow* the flow of energy. The ease with which a material allows energy to flow is called its conductivity σ [77]. The reciprocal of conductivity is an intrinsic property called resistivity $\rho = 1/\sigma$. Let us consider a long cylinder with length L and cross sectional area A. We can reference the resistance R in Ohm's Law and relate it to the resistivity by $R = \rho\ L/A$. Bringing in the conductivity term, we can rewrite that as $R = L/(\sigma\ A)$. For heat processes, we want to use the thermal conductivity κ [92]. Note also that the thermal conductivity can be strongly temperature dependent, so we use $\kappa(T)$. We can replace the electrical conductivity in the last equation with $\kappa(T)$ and arrive at $R = L/(\kappa(T)\ A)$.

An additional benefit about conceptualizing the heat flow in relation to Ohm's Law and its resistance R is that the thermal resistances of materials can be mathematically treated in the same way that electrical resistances are treated. That is to say, the total resistance R_{total} of a series of thermal resistances is the sum of the individual resistances, $R_{total} = \sum R_i$, and the total resistance of a set of parallel resistances is the reciprocal of the sum of the inverses, $\frac{1}{R_{total}} = \sum \frac{1}{R_i}$, as one would think from the more familiar electrical resistance rules.

Let's now replace the variables from Ohm's Law and look at them in terms of thermal properties to develop an intuitive understanding of a derivation of the *Fourier Heat Conduction Law* [92]. First, let's start with Ohm's Law

$$I = \frac{\Delta V}{R} \tag{4.2}$$

Recall the replacements mentioned in the last few paragraphs

$$I \rightarrow \dot{q}, \qquad \Delta V \rightarrow \Delta T, \qquad R \rightarrow L/(\kappa(T)\ A)$$

Make the substitutions into Eq. 4.2

$$\begin{aligned} \dot{q} &= \frac{\Delta T}{L/(\kappa(T)\ A)} \\ \dot{q} &= \frac{A}{L}\ \kappa(T)\Delta T \end{aligned} \tag{4.3}$$

To make this more useful, we can take infinitesimal units of the temperature gradient from a high temperature surface T_{high} to a low temperature surface T_{low}, such that $\Delta T \rightarrow dT$. This lends itself naturally to becoming an integral and we have the *Fourier Heat Conduction Law* in integral form

$$\dot{q} = \frac{A}{L}\int_{T_{low}}^{T_{high}} \kappa(T)\ dT \tag{4.4}$$

where $\dot{q}$ is the heat load, A is the cross-sectional area, T_{high} and T_{low} are the temperatures of surfaces where heat may enter or leave the system, L is the length between the fixed temperature surfaces, and $\kappa(T)$ is the thermal conductivity of the material as a function of temperature.

Elements in the system may be as warm as room temperature (300 K) or as cold as the measurement cell (0.4 K). The thermal conductivity of many materials are temperature dependent. When performing simulations across this temperature range, it is necessary that the change in the thermal conductivity is taken into account. The book *Experimental Techniques for Low-Temperature* Experiments by J. W. Ekin [59] is a good resource for the values needed in this calculation.

4.2.2 Black-Body Radiation

As thermodynamics tells us, all energy is moving toward a state of equilibrium [92]. This is true even when the bodies are not in physical contact or touching each other. In this case, the energy is transmitted through the electromagnetic spectrum via photons.

Starting with the assumptions that atoms act as quantum mechanical harmonic oscillators, photons generated from those atoms radiate with specific energies. This model is

outlined in detail in *An Introduction to Thermal Physics* by D. V. Schroeder [92]. There, it is shown that the power per unit area emitted by a surface, based solely on its temperature is

$$\begin{aligned} power\ per\ unit\ area &= \frac{2\ \pi^5}{15}\frac{(kT)^4}{h^3c^2} \\ &= \sigma T^4 \end{aligned} \tag{4.5}$$

where k is the Boltzmann constant, T is the temperature of the material, h is the Planck constant, and c is the speed of light. The constant σ is called the *Stefan-Boltzmann constant.* This constant of proportionality has the value

$$\sigma = \ 5.67 \times 10^{-8}\ W\ m^{-2}\ K^{-4} \tag{4.6}$$

The situation is a little more complicated than Eq. 4.5 suggests. Particularly, we need to consider what happens when a surface is capable of reflecting or absorbing the photons which reach it. Here I am going to restrict the topic to solid materials only. First, think of a body which is purely black. For example, a material painted with Vantablack [93] which absorbs 99.965% of radiation in the visible spectrum, nearly all photons which reach its surface will be absorbed by it. Consider another surface which is a clean and reflective mirror, nearly all photons which reach this surface will be reflected by it. This gives rise to an adjustment factor which needs to be incorporated into Eq. 4.5 called the *emissivity.* The emissivity ε is the fraction of photons which are absorbed by the material. For the black material, nearly all photons are absorbed, so $\varepsilon \approx 1$. For the highly reflective material, nearly all photons are reflected, so $0 < \varepsilon \ll 1$. The emissivity can be multiplied as a constant.

In the case of all models created for our simulations, the surface area A of the geometry is well defined. Let's imagine two surfaces, which are at different temperatures and have the same surface area. We can write the difference in the power output or heat load from radiation between the higher temperature T_{high} to the lower temperature T_{low} surface as a modified version of Eq. 4.5. This takes the form

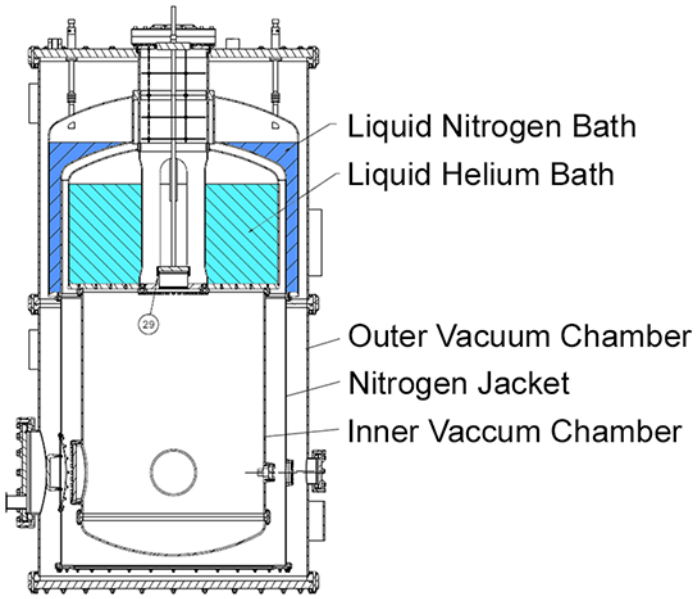


Figure 4.4: *Cutaway of PULSTAR Cryostat. The Measurement Cell, Shown in Fig. 4.3, Is Located Centrally in the Lower Section of the Inner Vacuum Chamber (IVC).*

$$\dot{q} = \sigma\varepsilon A(T_{high}^4 - T_{low}^4) \tag{4.7}$$

This is the radiation heat load and can be combined with the conductive heat load to perform calculations on the heat loads between components in the PULSTAR-SOS models.

4.3 COMSOL Simulation Models

The three systems investigated in this section are the actuator arm, neutron guide, and heat shields, found in sections 4.3.1, 4.3.2, and 4.3.3, respectively. Fig. 4.3 shows the relationship between these components inside the IVC. Fig. 4.4 offers a cutaway of the side of the cryostat, so that the various layers of heat shields are revealed. The measurement cell is located centrally in the IVC. The actuator arm and neutron guide penetrate each of the heat shields.

In the following simulations, each model was built and modified until a final solution allowing sufficiently low heat loads into the vestibule was found. The heat loads and temperatures of the connecting parts were then fed back into the other models to find the final

temperatures and heat loads from each individual component. The results of the simulations are reported in this section.

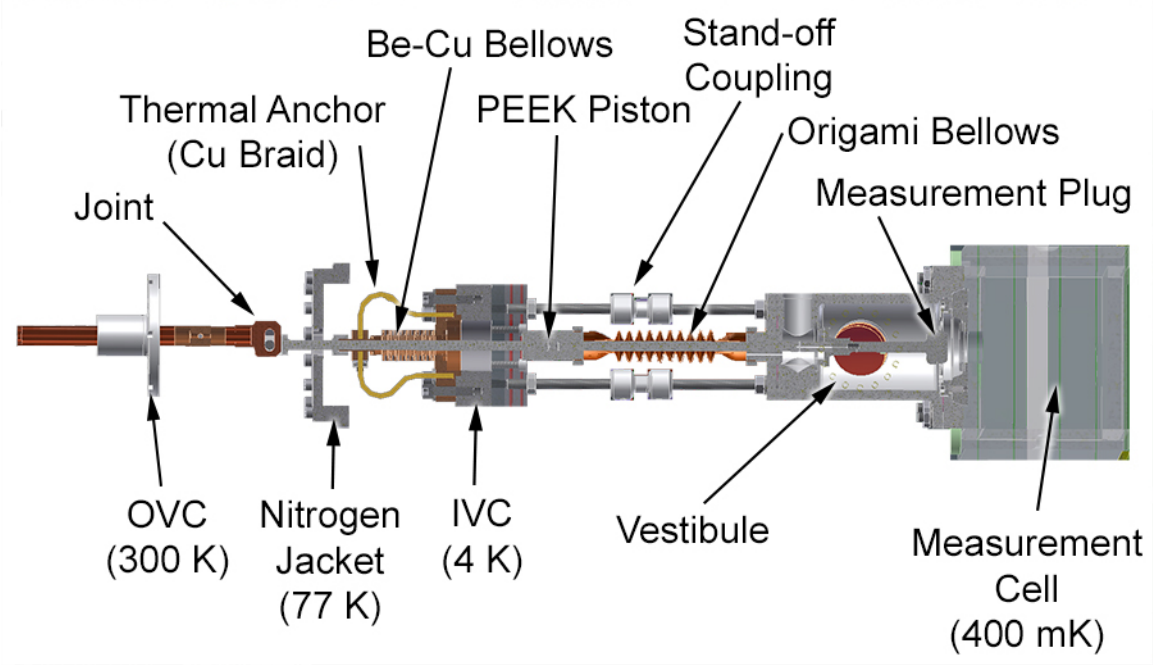


Figure 4.5: *Cross Section of Autodesk Inventor Actuator Arm Model. Lower Labels on the Model Mark General Components. Upper Labels Mark Specific Components Discussed in Detail in Section 4.3.1.*

4.3.1 Actuator Arm

The actuator arm is a component which is used to open and close the valve between the measurement cell and the vestibule. One end of the actuator arm is outside the cryostat at room temperature (300 K). The arm penetrates the Outer Vacuum Chamber (OVC), nitrogen jacket, IVC, and vestibule. It is then used to press a plug against the side of the measurement cell. The vestibule is continuously open to UCN and flooded with polarized ^{3}He when the measurement cell is to be filled. The plug is closed to contain a finite amount of UCN and polarized ^{3}He during the measurement cycle. Fig. 4.5 shows a cross section of the actuator arm assembly.

The travel of the valve is about 1 cm and must be carefully controlled to avoid improper seating and excessive force. It needs to be rigid enough to push and pull the valve open and closed. It also must provide the minimum heat load possible into the measurement cell, as temperature gradients inside the measurement cell may disrupt uniform distribution of the ^{3}He and UCN. Additionally, the OVC and IVC contain separate vacuum volumes. The actuator arm must operate consistently with the above stipulated conditions while penetrating and maintaining the vacuum.

The actuator arm and heat shields it is attached to are made of seven materials: Aluminum 6061-O, Copper 10100, Stainless Steel 304, PEEK, Copper, Beryllium-Copper, and Indium. The bibliography has a number of useful books and papers which cite thermal properties of these materials down to at least 4 K [59, 94, 95, 96, 97].

The left side of Fig. 4.5 is the OVC and at room temperature. There are 3.8 in between the OVC and nitrogen jacket. Following the Fourier Heat Conduction Law (Eq. 4.4), we see that minimizing the cross sectional area of the connection rod, decreases the heat load. The rod between the OVC and nitrogen jacket has thus been made into a tube with OD Φ 0.5 in and ID Φ 0.468 in. This gives a total cross sectional area of 0.024 in^2. This section of the actuator will be made of SS304 tube.

The section of the actuator which then penetrates the nitrogen jacket is made of PolyEther Ether Ketone (PEEK). The actuator will also be made with a slightly flexible joint between the SS tube and PEEK rod. All parts to the right of this joint (in Fig. 4.5) are cooled during operation causing thermal contractions of the internal components apparatus and raising them up by a few millimeters. This slightly flexible joint allows thermal contraction to occur without causing torque on either the OVC or nitrogen jacket flange. This joint will also reduce the surface contact area between the warm and cooler parts of the actuator in this region, again reducing the cross sectional area and reducing the total heat load.

After the full model was analyzed, we also found that moving the 77 K and 4 K connection points slightly further from the measurement cell helped to reduce the heat load

into the measurement cell. More will be mentioned shortly about the 4 K connection. To implement this idea, a small *top hat* flange was added to the assembly at this point.

The results of these ideas in the assembly is that a heat load of 50 mW will be put into the nitrogen jacket. Liquid nitrogen evaporates at a rate of 0.023 L/hr from 1 Watt of power input. We thus expect about 1.2 cc/hr of liquid nitrogen evaporation from this heat load. This is an extremely reasonable heat load for the evaporation of liquid nitrogen to mitigate.

The PEEK tube will penetrate the nitrogen jacket and is connected to a Cu piece. The Cu piece is the head of a set of Be-Cu bellows. The Cu head will be thermally anchored to the IVC flange using ~ 5 in of Cu braid. There will be two braids from the head to the flange. The use of braid in this manner is a common technique for thermal anchoring in cryogenic applications [59].

The Be-Cu bellows will have a thickness of ~ 0.006 in. The OD of the bellows will have $\sim \Phi$ 0.7 in and ID with $\sim \Phi$ 0.27 in. Thus, the cross sectional area is about 10^{-7} m^{-2}. The radial distance from the head to the end of the bellows will be ~ 1.3 in but because they are bellows, the actual length of material from the heat to the end of the bellows is actually closer to 14 inches = 35.6 cm.

The use of braids and bellows will then result in ~ 0.5 mW entering the wall of the IVC. LHe evaporates at a rate of 1.4 L/hr from 1 W of power and thus we estimate about 0.7 cc/hr evaporation. Recall as well, that a cryo-cooler will be able to take some of that heat load from the LHe bath, so we expect less evaporation. An image of the heat flow calculation made in COMSOL is shown in Fig. 4.6.

Some mechanical support for the vestibule is provided on the inside of the IVC flange by three PEEK support rods. The heat load from the warmer parts of the actuator arm put heat into this flange. The supports are attached to the flange and thus the previously discussed heat load has a direct influence on the heat load through the supports into the vestibule. The supports are made of threaded rod attached to the flange. The rods are

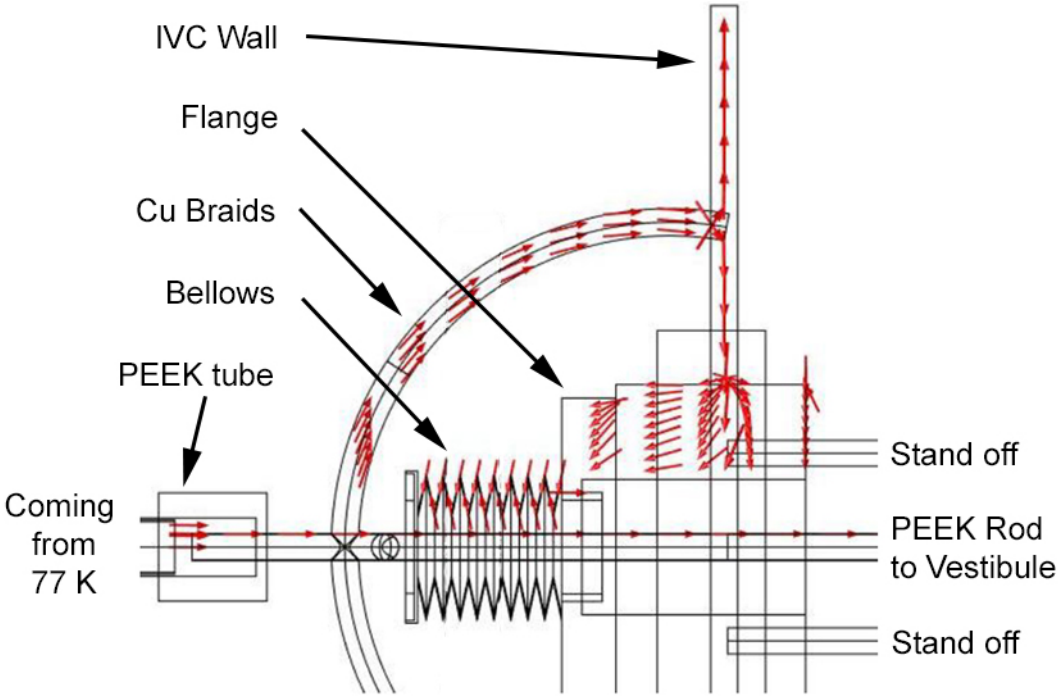


Figure 4.6: *Heat Flow Simulation in IVC Actuator Arm Flange Created in COMSOL. The Arrows Represent the Heat Flow Direction. The Size of the Arrows Is Normalized Due to the Many Orders of Magnitude Spanned by the Heat Flow Magnitude in Different Regions. The Left Side of the Image Comes From Room Temperature. The Curved Band Running Top to Bottom in the Middle of the Figure Represents the Cu Braids. The Large Volumes on the Right Are the IVC Flange. The Extremely Small Heat Flow Through the Bellows Is Observable Between the Braids and Flange.*

then attached to a stand-off coupling. On the vestibule side of the couplings, another threaded rod will be placed and attached to the couplings. The threaded rods are to be inserted into the coupling and a screw driven perpendicularly into the coupling gives mechanical anchoring. This technique of using a perpendicular screw to connect the rods to the couplings reduces the cross sectional area between the rods and the couplings. This reduces the heat flux through the couplings when compared to the thread on the rods being fully in contact with the coupling. The total heat flux from the supports into the vestibule are estimated to be about 20.4 μW.

The rod penetrating the IVC flange Be-Cu bellows is also made of PEEK. This PEEK rod travels a short distance into the IVC and then into the vestibule. On the other side of the piston are located a central PEEK rod acting as part of the actuator.

Near the vestibule, the PEEK rode mentioned in the previous paragraph is surrounded by a set of *origami bellows*. These bellows are a unique design created by Austin Reid (NCSU grad student) [69, 98]. The bellows are made from a Kapton tube mounted to a mandrel, heated, and compressed from the outside. A. Reid put much effort into investigating the mechanical properties of the bellows. The purpose of the origami bellows is to allow the volume they contain to be shared with the volume inside the vestibule and to allow motion of the actuator at very low temperatures. They have been demonstrated to be superfluid tight, while remaining flexible enough to be compressed and return to their original length. The origami bellows are glued onto the PEEK piston and vestibule with an exterior retaining ring.

Although the displacement volume between the *extended* and *collapsed* positions of the origami bellows was never measured directly, an estimate can be made. The bellows are made from a Φ 0.7 inches cylinder of Kapton and surround a Φ 0.25 inches rod. They will be compressed by 1 cm because that is the travel of the plug in the side of the measurement cell. The volume of a 1 cm long annulus with ID 0.25 inches and OD 0.7 inches has a volume of 2.17 cc. Since the distorted form of the bellows results in the volume being smaller, the displacement volume of the ^{4}He inside will be smaller as well.

The PEEK rod centrally located inside the origami bellows is the final piece which offers mechanical force to close the plug between the vestibule and measurement cell. The model predicts ~ 6.3 μW of heat to flow through this rod into the vestibule. The combination of the supports and the central PEEK rod thus impart ~ 26.7 μW into the vestibule while allowing a room temperature mechanical actuator to open and close the measurement cell.

4.3.2 Neutron Guide

The neutron guide transports ultra-cold neutrons (UCN) from the reactor into the measurement cell. This section describes details about the simulation and future construction of the guide from just outside the cryostat to the vestibule.

Fig. 4.7 shows a cross section of the neutron guide as seen from above. In the figure, the left side is room temperature and outside the cryostat. The right side of the figure is the measurement cell. Let's begin with a quick overview of the path the neutrons take. They enter the cryostat through a guide coming from the PULSTAR nuclear fission reactor. Upon entering the cryostat, they are guided by a series of Ti tubes. The Ti tubes end at the boundary to the IVC. The IVC flange will have a neutron permeable window. Once inside the flange, they enter a Kapton tube. The Kapton tube bends at 45^0 and approaches the vestibule. The path from the Kapton tube to the vestibule will have a neutron permeable window as well. At this point, the neutrons enter the vestibule and are ready to enter the measurement cell. The rest of this section will now discuss that sequence of components and their design principles in more detail.

As the neutrons approach the cryostat, they are first met with a top hat flange, with a length $\sim$ 9.5 inches and Φ 6 inches, which will be attached to the side of the OVC. The end of this flange is connected to a 4 inch long set of bellows. The inside of this volume will be under vacuum. The purpose in adding this additional volume to the vacuum is to allow additional length for conductive cooling of the material constructing this part of the apparatus.

Centrally located inside the top hat flange (in Fig. 4.7) are three orange colored tubes. These tubes will be made of copper coated titanium (Ti) and are intended to interact directly with the UCN. There are three Ti tubes which are not connected to each other. The tubes are supported by Ti springs wrapped all the way around them. The springs offer an extremely small cross sectional area minimizing conductive heat loads. The purpose in separating the three Ti tubes from each other is to minimize the heat load from room temperature into each of the heat shields. The result in separating them is that radiative heating is the primary source of heat from one to the next.

The Ti tubes are inside a series of stainless steel tubes. The stainless steel tubes are connected to each other by bellows. The bellows are placed at the end of each Ti tube to

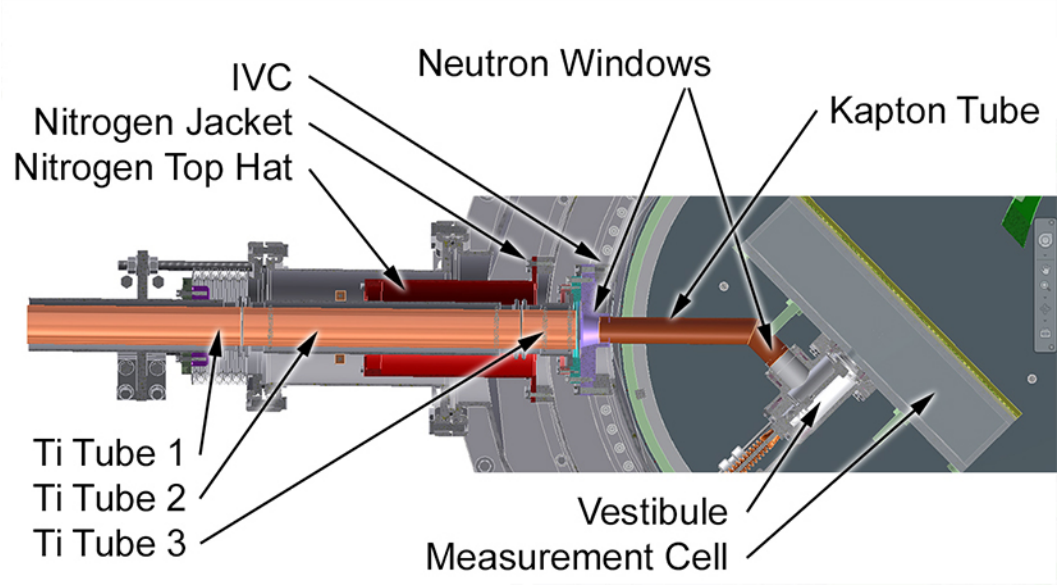
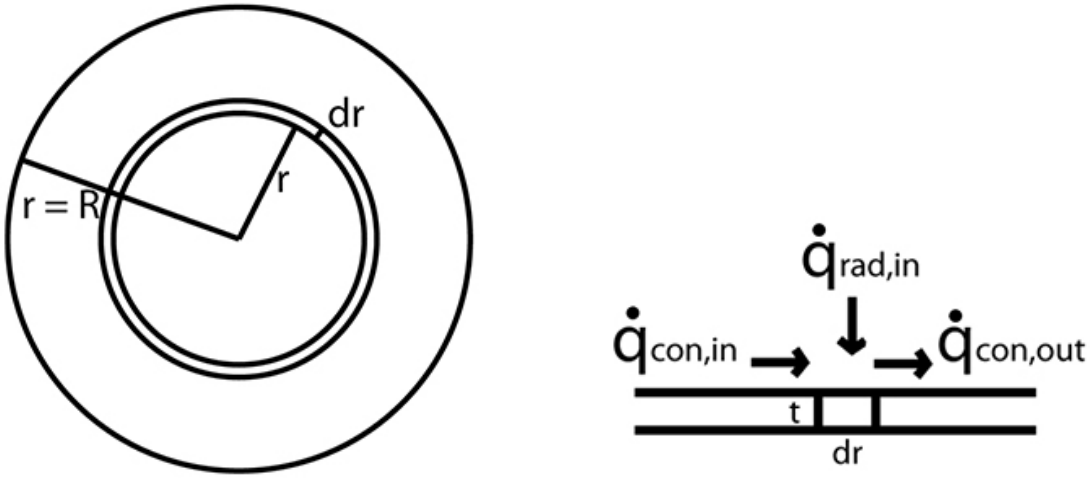


Figure 4.7: *Cross Section of Autodesk Inventor Neutron Guide Model.*

allow some flexibility as the internal components of the cryostat cool and thermally contract. The section of SS tube which is outside the cryostat at room temperature, is held at the end of the OVC top hat. Just inside the OVC top hat will be placed another top hat flange on the nitrogen jacket. This top hat is $\sim$ 8.8 inches long. A metal ring will be placed an inch further from the nitrogen jacket on the SS tubing with braid attachments from the SS to the top hat. This moves the effectively cooled region of the SS tubing even further from the IVC heat shield.

At the end of the last Ti tube will be a window. The window has three main purposes: (a) separate the vacuum inside the Kapton tube from the vacuum in the external neutron guide section, (b) act as a radiation barrier, and (c) allow neutrons to enter the next section of guide. The window will be $\sim$ 12 μm to 50 μm thick. The thickness has an influence on the temperature gradient on the window. However, it was found that the heat flux into the vestibule was not strongly dependent upon the temperature of the window. This may be due to the bend in the Kapton guide (inside IVC) which will be discussed below.

Although a COMSOL model simulating the window was performed, some insight into the physics can be gained through an analytical analysis of the radiative and conductive



(a) **(b)**

Figure 4.8: *Diagram of Geometry of Circular Neutron Window. (a) View of Window on Circular Face. (b) Cross Section of Window Showing Radiative Heat Load $\dot{q}_{rad,in}$, Conductive Heat Load From Warmer Middle Section of Window $\dot{q}_{con,in}$, and Conductive Heat Load $\dot{q}_{con,out}$ Leaving the Infinitesimal Volume in Question.*

heat loads. It was found that this analysis was qualitatively consistent with the temperature distribution found in the COMSOL simulation.

Begin by assuming our window has a circular profile with radius $R = 3.25$ cm and small thickness $t = 0.005$ cm, as shown in Figs. 4.8. We can assign two boundary conditions. The first is that there should be symmetry about the center and a maximum in the temperature at that point as shown in Eq. 4.8. Second, the temperature at the edge of the window should be the same temperature $T_{edge} = 4.2$ K as the support holding it, as shown in Eq. 4.9. In this case, a flange in the IVC wall is holding the window.

$$\left.\frac{dT}{dr}\right|_{r=0} = 0 \tag{4.8}$$

$$T(r = R) = T_{edge} \tag{4.9}$$

The heat transfer from radiative and conductive heat loads can be defined as follows

$$\dot{q}_{rad} = \sigma \epsilon A_1 (T_{rad}^{\ 4} - T_{edge}^{\ 4}) \tag{4.10}$$

$$\dot{q}_{con} = -\kappa A_2 \frac{dT}{dr} \tag{4.11}$$

where $\sigma = 5.67 \times 10^{-8}\ W\ m^{-2}\ K^{-4}$ is the *Stefan-Boltamann Constant*, $\epsilon = 0.04$ is the emissivity, $T_{rad} = 300\ K$ is the temperature of the incident radiation down the Ti tubes (assume high because it is actually varying along the tubes), κ is the thermal conductivity, $A_1 = 2\pi r\ dr$ is the area over which radiation is absorbed by the material, and $A_2 = 2\pi r\ t$ is the area over which heat conduction occurs for each infinitesimal slice of the cylinder.

To simplify the equations, we can take a closer look at the $T_{rad}^{\ 4} - T_{edge}^{\ 4}$ term. Note that $T_{rad} = 300$ K and $T_{edge} = 4$ K. Raising these two values to their fourth power, results in $T_{rad}^{\ 4} = 8.1 \times 10^{\ 9}$ K^4 and $T_{edge}^{\ 4} = 311$ K^4. We can therefore take $T_{rad}^{\ 4} - T_{edge}^{\ 4} \approx T_{rad}^4$.

From Fig. 4.8 and Eqs. 4.10 and 4.11 , a relationship between the heat loads describing the heat transfer in an infinitesimal section of the volume can be written.

$$\dot{q}_{con,out} = \dot{q}_{rad,in} + \dot{q}_{con,in} \tag{4.12}$$

$$-\kappa A_2 \frac{dT}{dr}(r + dr) = \sigma \epsilon A_1 T_{rad}^{\ 4} - \kappa A_2 \frac{dT}{dr}(r) \tag{4.13}$$

Rewriting this equation as a second order differential equation leads us to

$$\frac{d^2T}{dr^2} + \frac{1}{r}\frac{dT}{dr} - \frac{\sigma\ \epsilon\ T_{rad}^{\ 4}}{\kappa\ t} = 0 \tag{4.14}$$

The ansatz solution to this differential equation is $T(r) = Ar^2 + Br + C$. Implementing this ansatz and the boundary conditions from Eqs. 4.8 and 4.9, we find the coefficients to be

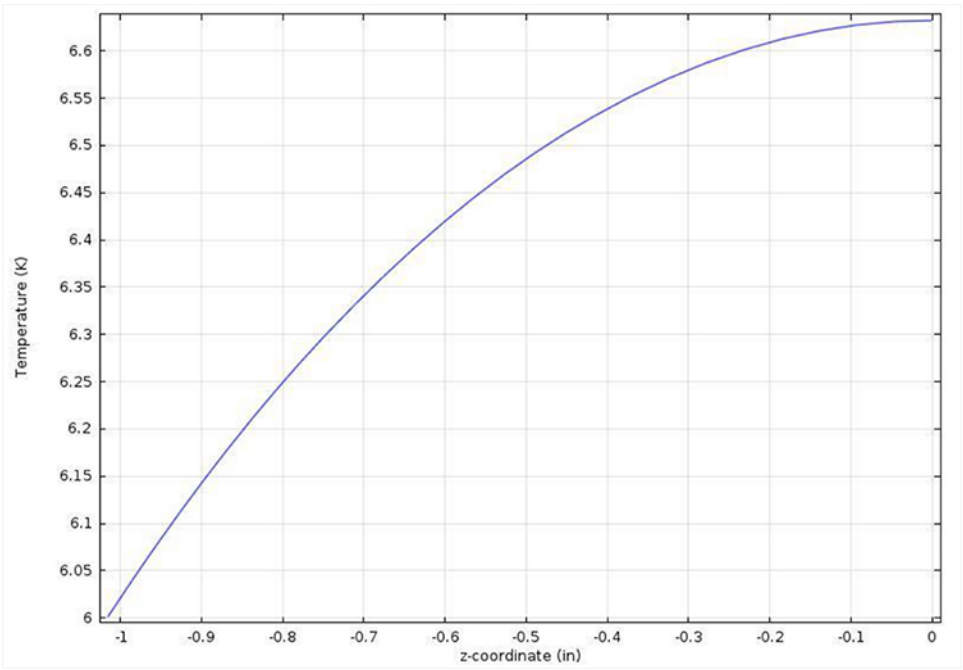


Figure 4.9: *Temperature Distribution on IVC Neutron Guide Window Simulated in COMSOL. Shown in Same Reference Frame As Eq. 4.18.*

$$A = -\frac{1}{4}\frac{\sigma\,\epsilon\,T_{rad}^{\,4}}{\kappa\,t} \tag{4.15}$$

$$B = 0 \tag{4.16}$$

$$C = T_{edge} + \frac{1}{4}\frac{\sigma\,\epsilon\,T_{rad}^{\,4}}{\kappa\,t}\,R^{\,2} \tag{4.17}$$

The full solution takes the form

$$T(r) = -\frac{1}{4}\frac{\sigma\,\epsilon\,T_{rad}^{\,4}}{\kappa\,t}(r^2 - R^{\,2}) + T_{edge} \tag{4.18}$$

This parabolic equation shows that there will be a maximum temperature at the center of the window where $r = 0$ and a minimum temperature of T_{edge} at the edge where $r = R$. This result is qualitatively consistent with the temperature profile calculated using COMSOL. The temperature distribution from the COMSOL model is shown in Fig. 4.9 .

After performing a series of studies on a variety of possible window materials, it became clear that Aluminized Mylar is the preferred material to use for the IVC window. This

material is made of a Mylar sheet with deposited Al on one surface. When ordering, the thickness of the Al layer is controllable. As the highest flux of radiant energy is coming from outside the IVC, the Al side of the window must be facing out. For this set of conditions, a series of simulations were performed using a variety of thicknesses for the Al1100 and Mylar layers. As the window temperatures have the largest influence on the temperature of the Kapton guide inside the IVC, it is necessary to understand its influence on the heat flux into the vestibule. Varying the thicknesses and monitoring the maximum temperature on the window, as well as the heat flux into the vestibule, Table 4.1 was generated.

Between the IVC flange window and the vestibule, there will be a tube of Kapton. Kapton is an excellent thermal insulator having thermal conductivity $\kappa < 0.1$ W m^{-1} K^{-1} for temperatures below 300 K. The Kapton tube is slightly bent in the middle because the neutron guide enters the cryostat at an angle of 45^0 to the measurement cell. The end of the Kapton tube will be glued directly onto the vestibule. Another window will be placed between the Kapton tube and the vestibule volume. The main purpose for this window is to keep the superfluid ^{4}He and polarized ^{3}He inside the vestibule while also allow UCN to enter.

With each of these concepts implemented, we predict the neutron guide will impart a heat flux into the vestibule of ~ 0.21 μW.

Table 4.1: *Maximum Window Temperatures Observed When Varying Window Layer Thicknesses for IVC Neutron Guide Window.*

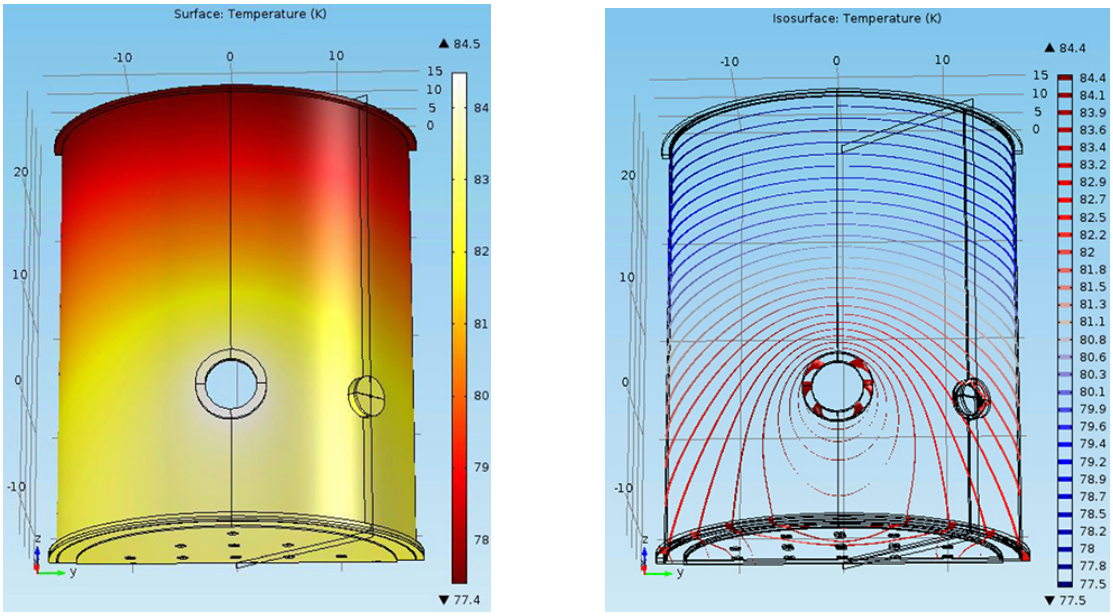
Window Thicknesses {Al1100, Mylar}	Window T_{max}	Heat flux into vestibule
12 μm {2, 10}	12.9 K	0.21037 μW
12 μm {4, 8}	10.1 K	0.21037 μW
25 μm {5, 20}	9.47 K	0.21015 μW
50 μm {5, 45}	9.53 K	0.21015 μW
50 μm {10, 40}	8.00 K	0.21007 μW

4.3.3 Heat Shields

Heat shields are the most basic and obvious necessity for a cryostat. The most exterior shield is only connected the the rest of the cryostat at the top and is referred to as the Outer Vacuum Chamber (OVC). It is expected to remain at around 300 Kelvin at all times. Within this volume is another shield known as the Nitrogen Jacket. The top of the nitrogen jacket has an annular volume in which liquid nitrogen sits. This can be seen in Fig. 4.4. The section of the shield which is below this bath sits in vacuum and is only conductively connected to the bath. Inside the nitrogen jacket is another volume which is known as the Inner Vacuum Chamber (IVC). The top of the IVC is thermally connected to the liquid helium bath at 4 K.

The walls of the heat shields are made of Al1100 and the flanges on the shields are made of Al6061. Due to the highly symmetric nature of the shields, each simulation modeled half of the full shield. Note that the nitrogen jacket is not vacuum tight. The vacuum inside the volume and the vacuum outside the volume are the same. The holes in the bottom of Fig. 4.10a indicate some locations where there are openings in jacket.

The nitrogen jacket and IVC are both wrapped in superinsulation. Superinsulation is often made of aluminum coated Mylar sheets with thickness < 1 μm. The evaporatively coated metal typically gives an emissivity coefficient around 0.06 [99], reflects radiative energy, and significantly reduces the radiative heat load onto the surface it covers. To ensure a realistic, and slightly over estimate of the heat loads, an emissivity of 0.1 was used in these simulations. The nitrogen jacket and IVC heat shields are wrapped in 10's of layers of superinsulation or Multilayer insulation (MLI) [59]. A convenient formula has been derived for calculating the heat load from shielding such as this which isn't actively cooled through conduction [100].



(a) **(b)**

Figure 4.10: *Temperature Plots of Nitrogen Jacket Simulations Made in COMSOL. The Central Port Shown in the Figures Is the Connection Point for the Neutron Guide and the Heat Load From It Was Applied at This Location. The Closed Port on the Right Side of the Figures Is the Location for the Actuator Arm and Its Heat Load Is Applied at That Location. The Top Surface of the Model Was Set to 77 K, As It Simulates Thermal Anchoring to the Liquid Nitrogen Bath. (a) Temperature Boundary Plot. (b) Temperature Contour Plot.*

$$\dot{q}_{si} = \frac{\dot{q}}{N+1} \tag{4.19}$$

where the subscript "si" stands for superinsulation, N is the number of layers of superinsulation, and an the un-insulated heat load was $\dot{q}$.

The influence of heat entering the shields from the neutron guide and actuator arm were of particular interest and were included in the heat shield simulations. As can be seen in Figs. 4.10 and 4.11, the temperatures on the heat shields are slightly above the temperatures of their respective cryogen baths as a result of these heat loads. Table 4.2 shows the heat loads from each of these parts into the heat shields and measurement cell.

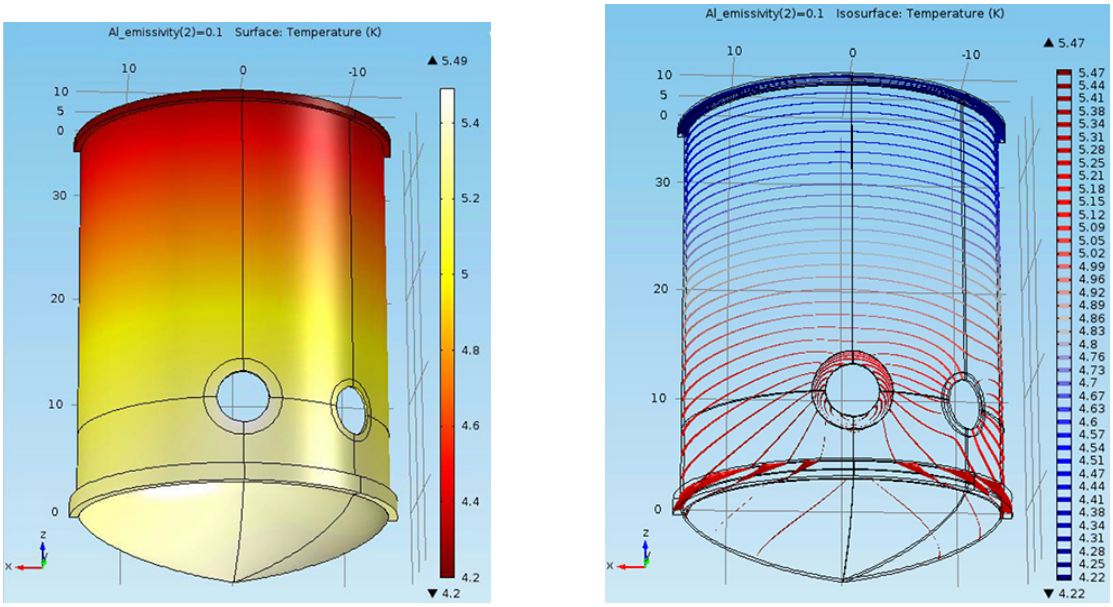
The analysis was carried out by setting the temperature of the boundary nearest the liquid cryogen bath to the appropriate temperature, 77 K for nitrogen jacket and 4.2 K for IVC. A radiative and conductive thermal analysis of the shield was performed. For

the nitrogen jacket, the entire outer surface was exposed to 300 K black-body radiation. The radiative heat load $\dot{q}$ into each surface was calculated. The radiative heat load physics were then removed from the simulation and a heat load $\dot{q}_{si}$ consistent with Eq. 4.19, using $N = 20$, was made incident on the exterior surface of the heat shield.

Table 4.2: *Heat Loads From Each Source Simulated in COMSOL and Fed Into the Appropriate Heat Shield Simulation. The Last Line of the Table Also Lists the Highest Temperature Simulated on Each Heat Shield.*

	Nitrogen Jacket	IVC	Vestibule
Heat load from neutron guide	14.7 W	0.193 W	0.21 μW
Heat load from actuator arm	50 mW	0.5 mW	27 μW
Total radiative heat load	3.45 W	0.25 W	-
Maximum Temperature on shield	84.5 K	5.37 K	-

Each of the heat loads listed in Table 4.2 represent energy which will (a) be dissipated by evaporation of a liquid cryogen, (b) be removed by the cryo-cooler, or (c) increase the temperature of some portion of the shield. For the nitrogen jacket, the energy will be dissipated by evaporation of liquid nitrogen. For liquid nitrogen, 1 W evaporates 0.023 L/hr. Thus with a heat load $\dot{q}_{NJ} \approx 18\ W$, we expect to evaporate at least 0.4 L/hr of liquid nitrogen. The energy entering the IVC heat shield will be dissipated both by the evaporation of LHe and a cryo-cooler. The cryo-cooler is placed in the top flange of the cryostat and hangs into the LHe main bath. The exact cooling power of the cryo-cooler is not yet known. LHe is known to evaporate at a rate of 1.4 L/hr from 1 W of heat input. Since the heat load $\dot{q}_{LHe} \approx 0.44\ W$, we would expect to evaporate about 0.6 L/hr of LHe. Initial testing with the cryostat, excluding all parts placed inside the IVC, have shown that the boil off rate is extremely slow when operating the cryo-cooler. At the present time, this is not a concern.



(a) **(b)**

Figure 4.11: *Temperature Plots of IVC Simulations Made in COMSOL With Radiation Incident on the Outer Surface. The Top Surface of the Model Was Set to 4.2 K, As It Simulates Thermal Anchoring to the Liquid Helium Bath. (a) Temperature Boundary Plot. (b) Temperature Contour Plot.*

4.4 SQUID System Design

The Superconducting QUantum Interferance Device (SQUID) system for the PULSTAR-SOS experiment includes all electronics and sensors for detection of rotating magnetic fields generated by ^{3}He. I have designed the majority of this system with the help of the rest of the NCSU team and some scientists from the LANL branch of the collaboration. This section describes the system in its current state of conception.

Section 4.4.1 begins by offering an overview of the entire system to give the reader the big picture. SQUIDs can be operated in a number of modes and controlled by using different numbers of leads. The functioning and possible control structures for the different modes are discussed in section 4.4.2.

The control and readout of SQUIDs utilize a number of room temperature electronic components. The components include a (a) PC Interface (PCI), which interacts with a Star Cryogenics program called PCS, (b) Programmable Feedback Loop (PFL), which interacts

directly with the SQUIDs through wire leads, and (c) additional electromagnetic shielding structures. The function of each of these components are outlined in section 4.4.3.

The low temperature SQUIDs (LTS) we will be using for these experiments need to be mounted somewhere within the IVC. Mounting locations for the components and how they are thermally anchored are important details when using them. Section 4.4.4, describes these details and offers some analysis of heat loads onto various parts of the cryostat and dilution refrigerator.

Although there are not many SQUID manufacturers in the world today, there are a few of them. Each manufacturer has a product line which includes SQUID sensors with different and specific properties. We have developed some experience in the operation of a few types of these SQUID options. The system is being designed with the intention that the specific sensing package which may be used in these experiments may be changed after the system is assembled, so that the same SQUID cabling can be used for different sensors. Section 4.4.5 outlines the options and reasons for them.

Adjacent to the measurement cell, an array of pick up coils or magnetometers will be placed to perform the sensing on the polarized ^{3}He. The first phase of testing the system will use a smaller measurement cell than the full sized version. The smaller cell will allow the team to test all components of the system, including the vestibule but take less time and ^{3}He resources to fully run through a measurement cycle. The pick up coil arrays are slightly different for the two cells. The arrays we are planning to use are explained in section 4.4.6.

Initial testing of the system will use just one SQUID to gather information on the background noise in the lab. If this single SQUID and pickup coil are operational as additional equipment is added to the cryostat, the team may be able to identify their contributions to the noise and plan accordingly to work around them. The second phase is to increase the number of SQUIDs to four. The final phase will include the use of eight SQUIDs.

4.4.1 Overview

This section provides and overview of the system from the outside in. It starts with the computer which will control the system and follows the control path inside the cryostat to the SQUIDs and pickups.

The system will be controlled by a computer which is optically connected to the Star Cryo PCI-1000 [101]. The output from the PCI-1000 will then be fed directly into the Apollo TNMR program. The PCI-1000 will control four to eight Star Cryo PFL-100 units. The array of PFL-100s will then be connected to a PFL Adapter Box which will be built by Star Cryo and connects four PFL-100s to a 26 pin cable. The cable will be connected to a 26 pin D-sub feedthrough.

The vacuum side of the feedthrough will be connected to four 10 lead SS shielded SQUID cables. The SQUID cables will have two heat sinks each, one for 4 K and one for the 1 K Pot. The cold side of the SQUID cables will be 10 pin LEMO connectors. These connector will attached directly to Nb housings for the SQUID chips made by Star Cryo.

The SQUIDs are then connected to leads which go to the pick up coils. The length of the pick up leads outside the Pb shield surrounding the experimental region will be placed inside of Pb capillary. The pick up coils will be placed near the measurement cell. Fig. 4.12 provides a schematic of this control structure.

4.4.2 SQUID and Cryoswitch Control Techniques

There are a number of ways to control and read out data from a SQUID chip [74]. This section describes some of these techniques as they relate to our specific experimental design. The reader may also wish to refer to section 3.6 for more details about SQUID operations. Additionally, specific information about how a cryoswitch operates in relationship to the SQUID chip is described.

A small number of leads is required for control of a SQUID chip. Each of the following connections require two leads. In its most basic configuration, the user must provide a bias

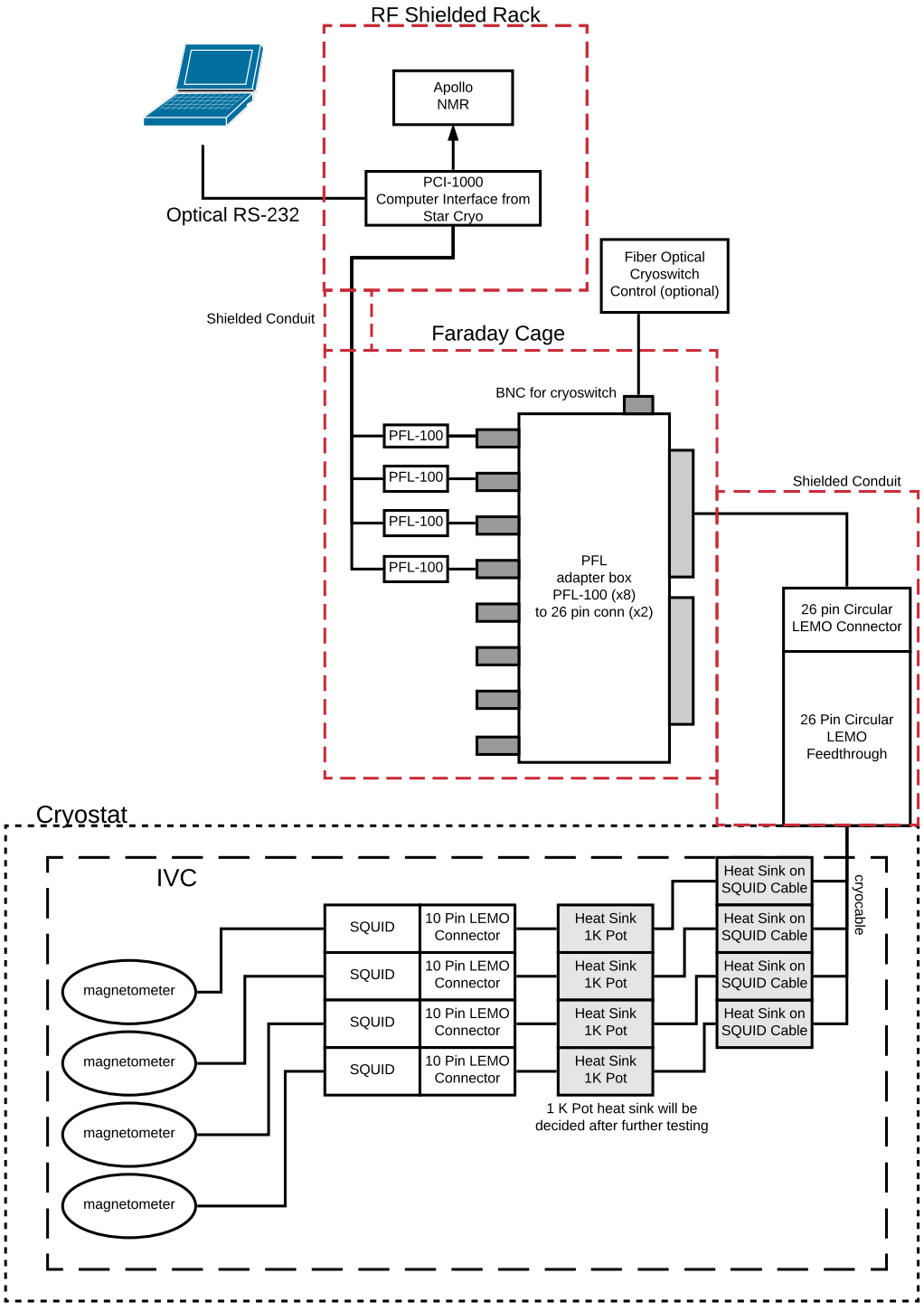


Figure 4.12: *Overview of SQUID System for SOS Experiment. This Is the Initial Setup with Four SQUIDs. It Will Be Possible to Include Eight SQUIDs Later.*

current I_b and a feedback (or MOD) current I_{fb}. Another very common set of leads which are used measure the voltage V across the SQUID near the SQUID chip, much like a four lead resistor.

It is likely that magnetic flux will become trapped in the SQUIDs at some points in the time, so a set of leads for heating H the device will also be needed. The heater will heat the SQUID chip to a temperature at which it is no longer superconducting. It is inoperable during this time until it is cooled back down below its superconducting threshold.

A common way to operate a SQUID is to have leads for I_b, I_{fb}, V, and H. This requires eight leads total per SQUID. When a number of SQUIDs are being controlled through a single cable, it is possible to couple control of all the heaters through a single set of leads. In this type of control structure, heating is applied to the entire set of SQUIDs simultaneously. This brings the total number of leads needed per SQUID to be six, plus two additional leads for the entire set. This technique will be referred to as the 8 lead technique.

A second operational technique is to pair the I_b and V leads to a single I-V group, so that four leads can be reduced to two. Again, in an array of SQUIDs, the heaters can be combined. For a system operated in this manner, the operation requires a total of four leads per SQUID for I-V, I_{fb}, and H. This technique will be referred to as the 6 lead technique. In a situation, where the number of available leads becomes restricted, this can be very useful.

In our apparatus it is possible that a cryoswitch will help to keep the SQUIDs operable immediately after an NMR tipping pulse is applied to the measurement cell. A cryoswitch is a heat switch designed to interrupt the signal from the pickup coils to the SQUID chip. Heating the cryoswitch does not cause the SQUID to exit its superconducting temperature regime but does cause the leads between the SQUID chip and pick up coils to become resistive. The switch can be controlled by applying a current I_{switch}. Please see Figs. 3.18 and 3.22 for schematics of a SQUID chips. The cryoswitch is activated while the NMR tipping pulse is applied to the measurement cell. The SQUID chip then does not *see* the

tipping pulse because the pick up coils are not coupled to it while the cryoswitch is active as a result of it becoming resistive as discussed in section 3.6.5.

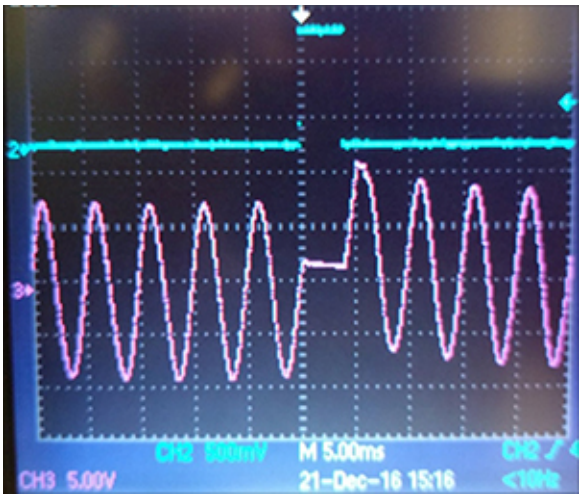


Figure 4.13: *Cryoswitch Operation. Top Trace Is Potential Across Cryoswitch. Bottom Trace Is Read Out From SQUID Electronics. The Offset Seen on the Right Side of the Flat Region in the Middle Is Discussed in the Text.*

It is likely that using a cryoswitch will help by allowing the SQUID to begin recording the polarized ^{3}He signal in the experiment quickly after the NMR tipping pulse is applied. This is because it is possible that the NMR tipping pulse may provide too much flux for the SQUID to handle, resulting in it hitting the rails and possibly requiring a heating cycle before it is back online.

Fig. 4.13 shows the output from the SQUID when the cryoswitch is activated. The SQUID was connected to a set of pick up coils with an excitation coil coupled to them. A sine wave was put into the excitation coil stimulating the pick up coils which then transferred the signal to the SQUID. The top trace is the potential across the cryoswitch. At $t = 0$ in the trace, a current was run through the cryoswitch for 4 ms. During this time, the flux going into the SQUID was interrupted. The bottom trace shows the read out from the SQUID electronics.

Notice that at $t = 0$, the flux into the SQUID stopped oscillating with the sine wave and began to decay slowly. Once the interruption was ceased, the SQUID began receiving

signals from the pick up coils again starting with the flux which remained in it at that time. That is, the amount of flux in the SQUID, when the cryoswitch was turned off, remains in the SQUID. When it starts to receive signals again from the pick up coils, it starts at that base line and adds or subtracts the new flux to the existing flux which was present.

We are working with Star Cryo to build our SQUID system. Star Cryo does not presently offer a SQUID chip with an on-board cryoswitch, though the technology has been successfully implemented by other manufacturers. They have already invested some R&D into the design. They will push forward with that design for implementation in the PULSTAR-SOS experiment. We are involved in funding and testing for the completion of that R&D to develop this technology.

4.4.3 Room Temperature Control Structure

This section describes the room temperature electronics needed to operate the SQUID system. These are the components outside of the cryostat. The electronics include a computer for SQUID control, a PC interface for data acquisition and interaction with SQUIDs, and programmable feedback loops. Electromagnetic shielding of these electronic components is also outlined.

The user interface for the system is the PCS program provided by Star Cryo installed on a computer. The computer will be optically connected to the Star Cryo PC Interface (PCI). The PCI-1000 is a piece of hardware capable of controlling up to eight SQUIDs simultaneously. The optical connection from the computer to the PCI can be made through a port powered RS-232 optical fiber converter such as the TCF-90 [102]. This allows for electronic isolation between the computer, which is outside RF shielding, and the rest of the system, which will be placed inside RF shielding.

The PCI and NMR control system will be housed inside an RF shielded rack. Output from the PCI will be fed directly into the Apollo. The NMR control system is designed to control and process Nuclear Magnetic Resonance (NMR) coils and systems. Controlling these devices inside the rack will be performed using fiber optic links to ensure electronic

isolation. A conduit will connect the rack to an enclosure housing other components of the SQUID system. The PCI controls the SQUIDs through Programmable Feedback Loops (PFL) via RS-232 or parallel port. One PFL can control one SQUID.

The PCI will be connected to an array of Star Cryo PFLs. The Star Cryo PFL-100 provides all room temperature electronics needed for direct interaction with a SQUID including the feedback resistor, integrator capacitor, amplifier, and lock-in detector [74].

The PFLs will be connected to a PFL adapter box custom built by Star Cryo. This box will support the operation of eight PFL units and thus eight SQUIDs. The PFLs will be grouped into two sets of four PFL units. Each set of PFLs will be ported through the box to a single 26 pin output. An additional BNC port will be included on the box in case an external cryoswitch control is needed, which can easily be activated via a fiber optic cable. See the middle of Fig. 4.12 for a schematic of this setup. If the new Star Cryo SQUIDs can be manufactured with on-board cryoswitches, it may be possible to control those using the same computer which controls the heater and the BNC may not be needed. It is there in case it is needed.

The cable between the PFL adapter box and the hermetically sealed feedthrough will be electromagnetically shielded by solid metal tubing with connection to a KF flange with an aluminum gasket [103]. The tubing may be made of Al bellows or some other solution might be found. It might be useful to increase the amount of shielding by wrapping the tube in Mu-metal or Metglas.

4.4.4 SQUID Mounting Location and Thermal Anchoring

This section describes where the SQUIDs will be mounted and where they may be thermally anchored. The mounting is designed to minimize the length of the leads between the SQUIDs and pick up coils to reduce inductance lost to the lead length. A mathematical analysis of the thermal anchoring is discussed with details about heat loads from SQUID heaters and cyroswitch operation.

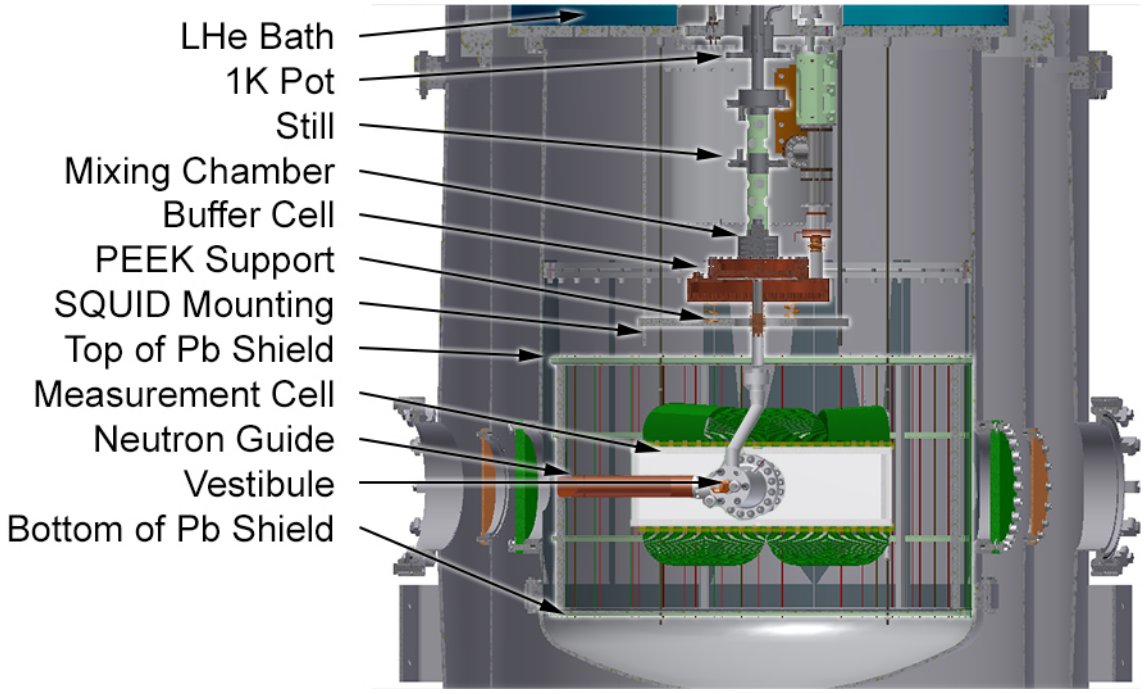


Figure 4.14: *Cutaway of Experimental Region in SOS Experiment. For Scale, the Outer Most Vacuum Chamber Has OD Φ 44 Inches. This Viewing Angle Faces Down the Length of the Actuator Arm.*

The feedthrough for a set of four SQUIDs is a 26 pin D-sub connector. This allows for six individual leads to each SQUID and two shared heater leads for all SQUIDs. Most of the leads are phosphor bronze (Ph Br). However, for each SQUID the leads used to read the potential across the SQUID chip are made of copper (Cu). These leads are used to read out the signal from the SQUID. This is important because the thermal conductivity of Cu is orders of magnitude larger than Ph Br. Meaning that even though the number of Ph Br wires is larger, the Cu wires will provide a larger heat load on cold components.

Table 4.3: *Heat Loads Through 36 AWG Wires and SS Braid for One Cryocable. For Each Cryocable, There Are Six Ph Br and Two Cu Leads. Lengths and Cross Sectional Areas of the Leads and Braid Are Discussed in This Section's Text. The Columns Labeled "wire" and "cryocable" Give the Heat Load Through a Single 36 AWG Wire and a Single Cryocable, Respectively.*

	Feedthrough to 4K Heat Sink			4K Heat Sink to 1K Pot		
		Heat Load			Heat Load	
Material	$\int_{4K}^{300K} \kappa\, dT$	Wire	Cryocable	$\int_{1.7K}^{4.2K} \kappa\, dT$	Wire	Cryocable
Ph Br	5.16 kW/m	44 μW	260 μW	22.4 W/m	1.2 nW	7.4 nW
Cu	162 kW/m	1.4 mW	2.8 mW	3 kW/m	170 nW	330 nW
SS Braid	3.06 kW/m	-	490 μW	0.645 W/m	-	36 nW
	Total per cryocable		**3.55 mW**	Total per cryocable		**370 nW**

Both sides of the feedthrough have a D-sub connector on them. A D-sub connector will be soldered to four SQUID cables so that it can be connected to the vacuum side of the feedthrough. A single SQUID cable consists of four twisted pairs of two wires which are surrounded by a Teflon jacket and stainless steel (SS) braid. The leads are 36 AWG wire with diameter of 0.005 $inches = 0.127\ mm$ giving a cross sectional area of $1.3 \times 10^{-8}\ m^2$ per lead. The SS braid is made of SS wires with diameter 0.06 mm arranged in groups of 6 wires in 14 groups surrounding the cable. The total cross sectional area of the SS shield is $2.4 \times 10^{-7}\ m^2$.

To calculate the thermal load from the SQUID cables, we need to use the conductive heat load equation (Eq. 4.4). The lengths from the feedthrough to the 4 K heat sink and from the 4 K heat sink to the 1K Pot are 1.5 and 0.23 meters, respectively. The heat sinks are 1 inch long cylinders with 1/4 inch diameter that can be heat sunk by clamping between two pieces of metal. The SQUID cable enters the IVC through a tube adjacent to the dilution refrigerator.

The calculated values for each section of the SQUID cables can be found in Table 4.3. The totals presented on the last line of the table are for a single SQUID cable. Each SQUID

cable will provide 3.55 mW of heat to the LHe bath. Recall that a cryo-cooler is also placed in the bath. Without the cryo-cooler, we would expect a single SQUID cable to boil off 5 cc per hour. We could then expect four SQUID cables to boil off 20 cc per hour or about 1/2 L per day and eight SQUID cables to boil off 1 L of LHe per day. This is manageable but with the cryo-cooler, we should get even better performance from the system.

If the 1 K Pot is used for thermal anchoring, the heat load into it would be 370 nW for a single SQUID cable. This is a continuous heat load into the 1K Pot. With four or eight SQUID cables, we then expect 1.5 or 3 μW of continuous heat into the volume for four or eight SQUIDs, respectively. Since the cooling power of the 1K Pot is on the order of $\approx$ 200 mW, this shouldn't be a problem but as mentioned previously there may be issues when heating the SQUIDs.

When heating four SQUIDs with a single pair of heating leads, the wires need to be arranged in a parallel-series combination. If two pairs of parallel connections are made then connect these two pairs in series, the resulting resistance is equal to the resistance of a single heater. This wiring needs to be made near the feedthrough, as below this location, the wires will be inside a manufactured SQUID cable and not accessible lower in the system.

The cold end of the SQUID cables are 10 pin LEMO connectors. These will connect to niobium (Nb) housings built by Star Cryo or Pb shields (as shown in Fig. 3.23). Nb is a superconductor below 9.26 K [87] and will shield the SQUID chip well from environmental noise.

Inside the housing, two options for connecting to the SQUIDs may be used. The team may choose to use Star Cryo printed circuit boards (PCB) with a step-up transformer or not to use the PCB. The PFL-100 is designed for a 25:1 step-up transformer coupling with the SQUID chip [101]. It can be set for either single or dual coupling options. When in single coupling configuration, a 25:1 transformer inside the PFL is used. When set for dual coupling, a 5:1 transformer is used inside the PFL and the circuit is expecting another 5:1 transformer to be outside the PFL. The additional 5:1 transformer is then housed on a Star

Cryo PCB near the SQUID. The PCB is at low temperature and thus adds less thermal noise to the system. A jumper in the PFL-100 devices needs to be set appropriately for the correct transformer coupling. Specific instructions for how to set this up are in the pcSQUID^{TM} User's Manual [101]. These options for the transformer coupling can be changed after full installation of the SQUID system.

A challenge which arises from using the PCB is that the current I and voltage V leads must be separated in the SQUID cable which leaves no additional wiring for leads to control a cryoswitch. This is described in section 4.4.2 as the 8 lead technique. We may find that using the 6 lead technique (also described in section 4.4.2) may be the best option however. For this reason, the PFL adapter box is designed for the ability to be rewired, so that the method desired can be utilized. No changes need to be made to the SQUID cable when changing control techniques, though some changes need to be made inside the PFL adapter box and the Nb housings, and these operations can be performed on a work bench.

All electronic systems have inherent noise due to many factors including thermal effects, SQUID systems are no exception. One way to reduce the thermal noise in the SQUID is to cool the SQUID as much as possible [74]. A challenge is that the SQUIDs will be heated periodically by activating the cryoswitch and powering the heater to expel trapped flux. Therefore, they need to be thermally anchored to the volume with the lowest temperature and which has enough cooling power to dissipate the introduced energy. The obvious choices for thermal anchoring are the LHe bath ($4\ K$), 1K pot ($1.8 - 2.0\ K$), still ($\sim 700\ mK$), and mixing chamber ($\sim$ 0.4 K). See Fig. 4.14 for a cutaway of the experimental region and labels indicating the locations of these components.

As is shown in the Fig. 4.14, the measurement cell is surrounded by an enclosed volume. The volume is cylindrical in shape with the symmetric axis vertical. The volume has a circular Pb shield to reduce environmental noise. A PEEK support plate will be placed a few inches below the buffer cell and above the Pb shield. The geometry of the support is not evident from the angle in the figure. It is supported by three rods hanging from the top

of the IVC, is pressed against the buffer cell via three springs, and has a roughly triangular shape when viewed from above. The SQUID packages may be mounted to this support directly above the Pb shield. In this location they will be as close to the pickup coils as possible, while keeping the measurement region insulated from distortions in the magnetic field which would be caused by the superconducting Nb housings of the SQUIDs.

First, let us analyze the energy which will be introduced during the heating processes. The resistance of the SQUID heater is $R \approx 300\ \Omega$. A current of $I_{heater} \approx 50 - 100\ mA$ is applied to activate the heater, resulting in delivering a power of

$$P_{heater} = I_{heater}^2\ R = (0.05\ A)^2\ (300\ \Omega) \approx 1\ W \tag{4.20}$$

Delivering this power for $t_{heater} = 0.1\ s$ gives a total energy to be dissipated of

$$E_{heater} = P_{heater}\ t_{heater} \approx 0.1\ J \tag{4.21}$$

per SQUID. This number can then be multiplied by the number of SQUIDs installed.

The cryoswitch will either use the same resistor or one of similar resistance but only require a current of $I_{switch} \approx 5\ mA$. The power delivered per SQUID for the cryoswitch is then

$$P_{switch} = I_{switch}^2\ R = 7.5\ mW \tag{4.22}$$

The measurements will be performed with a 100 Hz NMR pulse which will be applied for $t_{NMR} \approx 1\ s$. This is the duration over which the cryoswitch will need to be activated. Thus we have

$$E_{switch} = P_{switch}\ t_{NMR} = 7.5\ mJ \tag{4.23}$$

per SQUID. Again, scale by the number of installed SQUIDs.

The LHe bath has many of liters of LHe in it. The heat load which can be absorbed by the bath is very large compared to these calculated values.

In previous measurements from this dilution refrigerator, the cooling power of the still goes up to ~ 25 or 30 mW and the cooling power of the mixing chamber gets to ~ 4 mW. These values are highly temperature dependent [99]. However, at a glance, it is clear that the multiple Watts of cooling power needed to cool the SQUIDs is not available and would cause major disruptions to the operation of the dilution refrigerator's ability to operate smoothly. Therefore, the still and mixing chamber are not options for thermally anchoring the SQUIDs.

The 1K Pot sits at about $1.8 - 2.0$ K. The volume of one mole of LHe at these temperatures is $\sim$ 37 cc. The volume of our 1K Pot is $\sim$ 48 cc. The latent heat of vaporization for LHe is 80 J/mol at 1 K and 90 J/mol at 2.2 K [104]. We can just consider the energy dissipation for heating because it is larger and we expect a maximum of 0.1 $J/(80\ J/mol) = 0.00125\ mol$ to evaporate when heating a single SQUID. Theoretically, this does not pose an issue since the volume of LHe in the 1K Pot is much larger.

Using another analysis technique, we could consider that there will be some thermally conductive link between the 1 K Pot and the SQUID location, which is on the PEEK support plate. A set of four SQUIDs in Nb housings will be mounted together on a Cu support. The SQUID chips have *heat sink* solder pads on them which can be connected to that Cu support via Cu braids. The Cu support can then be thermally anchored to either the LHe bath or the 1 K Pot via Cu braids.

We can use Eq. 4.4, the *Fourier Heat Conduction Law*, to calculate the heat load onto either the LHe bath or the 1 K Pot. Assume the Cu support is connected to the 1 K Pot via a Cu braid which is made of 0.06 mm OD Cu wires with about 168 wires constructing the braid. The cross sectional area of such a braid is 4.75×10^{-7} m^2. The braid needs to have length L = 50 cm. We therefore have $A/L = 9.35 \times 10^{-7}$ m.

We aren't sure exactly how warm the SQUIDs become when heated but it is at least $T_{high} = 10$ K because that is higher than the superconducting transition temperature of the Nb SQUID loop and leads inside the chip. It could be as high as 20 K though, so I'll

include that here as well. The lower temperature limit T_{low} in the integral is either 4.2 K or 1.8 K for the LHe bath or the 1 K Pot, respectively. The thermal conductivity of Cu in this regime is variable depending upon the purity of the Cu, details can be found in *Experimental Techniques for Low-Temperature Measurements* by Ekin [59] in Appendix A3.1. For *electronics grade* or *ETP* Cu, the thermal conductivity $\kappa \approx 560$ W/(m K) near 4 K. For high purity Cu (99.999% Cu, aka *five nines*), $\kappa \approx 11{,}300$ W/(m K). Table 4.4 shows the results of this calculation.

Table 4.4: *Heat Loads Through Cu Braid from SQUID Mount to Heat Sink Location.*

	Braid Material			
	ETP Cu ($\kappa \approx 560$ W/(m K)		99.999% Cu ($\kappa \approx 11{,}300$ W/(m K))	
Heat Sink Location	$T_{high} = 10$ K	$T_{high} = 20$ K	$T_{high} = 10$ K	$T_{high} = 20$ K
LHe Bath	3.04 mW	8.27 mW	61.3 mW	167 mW
1 K Pot	4.29 mW	9.53 mW	86.6 mW	192 mW

The cooling power in the 1K Pot due to pumping is $\sim 200\ mW$, so it may be safe to thermally connect the SQUIDs here. However, we can see from Table 4.4 that it will not be necessary to use high purity Cu. The trouble with heating the 1 K Pot too much is that it can take a while for it to return to operating properly near its lowest temperature. To confirm that this won't be an issue while running the experiment, a heater will be attached to the 1K Pot to test if the system can handle this during a commissioning cool down of the cryostat in the near future.

4.4.5 SQUIDs in the SOS Experiment

This section describes SQUIDs which are being considered for use in the PULSTAR-SOS experiment. When the SQUID chip with integrated cryoswitch is developed by Star Cryo, these specs may change a bit.

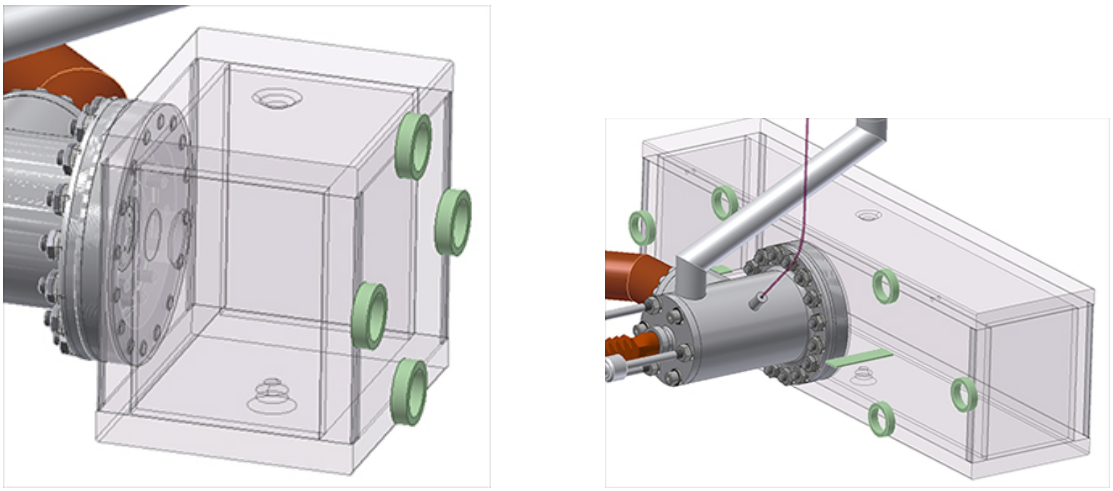
The type of SQUIDs which will be used in the experiment will be tested during commissioning. The design will use SQUID chips mounted in Nb housings. To attempt to be clear, the SQUID loop is manufactured inside a G10 board, this comes as a single *SQUID chip* with solder pads for connecting to the SQUID, feedback, and heater leads, and screw terminals for connecting to the pick up coil input circuit.

Initial testing will be performed using the CE2SBlue from Supracon. This is the type of SQUID which was used in Ch. 3. The same dilution refrigerator which was used for the studies in Ch. 3, is presently installed in the PULSTAR-SOS cryostat. During the transfer of the dilution refrigerator from the old cryostat to the new PULSTAR-SOS cryostat, the SQUID cabling from the previous experiment was left in place to allow testing of noise the SQUID senses early in the commissioning of the new cryostat. The CE2SBlue SQUID sensor has an integrated cryoswitch on-board, making it an optimal testing option.

Going forward, the focus will be on integrating Star Cryo SQUIDs into the system. The SQUIDs which have been discussed for future use are the SQ680 and SQ2800. The primary difference between these two types are the input inductance needed for proper coupling between the pick up coils and SQUID loop. The SQ680 is designed to operate with pick up coil input inductance around 680 nH and the SQ2800 is designed to operate with less than 2800 nH. Inductance in the pick up coil comes from both the leads and pick up coils themselves, as described in more detail in section 3.6.2. Being able to operate with a larger inductance means increasing the number of turns on each pick up loop, thus increasing the effective area and signal magnitude. This may or may not be beneficial depending upon the expected signal strength once all signal sources are present in the measurement cell.

Depending upon how the R&D with Star Cryo goes, we may have the option of a new type of SQUID which doesn't currently exist. Details about the development of a new SQUID with integrated cryoswitch can be found in section 4.4.2.

Initially, we had attempted to include the possibility of using pick up coils, either magnetometers or gradiometers, with *integrated SQUIDs*. Pick up coils which have *integrated*



(a) (b)

Figure 4.15: *Autodesk Inventor Models of Measurement Cells to Be Used in PULSTAR-SOS Experiment. This Model Was Created by L. Bartoszek. The Green Cylinders Are Positions Where Circular Pick Up Coils Will Be Placed. (a) Shows the Short Cell Which Will Be Used First for Intial Tests. (b) Shows the Full Sized Measurement Cell.*

SQUIDs have the SQUID printed directly onto the substrate holding the pick up coil. As the design developed, it was realized that sufficient cooling would need to be provided to these devices close to the measurement cell and a highly thermally conducting insulator, such as sapphire, would need to be used for thermally anchoring them to the top of the IVC at 4 K. Solid thermal anchoring is important because of the heat load when operating the heater or cryoswitches, as described in section 4.4.4. The challenge in using sapphire for this task is that the sapphire would need to be mounted to the top of the IVC, nearly 60 vertical cm from the measurement cell, and bent at some point to reach under sections of the dilution refrigerator and buffer cell, which is directly above the measurement cell. Additionally, another hole would need to be put into the Pb shield around the measurement region for the thermal anchor arm, allowing additional environmental electromagnetic noise to enter the measurement region. Due to these issues, this concept has been abandoned.

4.4.6 Pick Up Coil Arrays

This section describes details about the pick up coil arrays. The pick up coil arrays were designed by Steven Clayton at Los Alamos National Laboratory. He wrote a very useful Mathematica notebook to generate field calculations and plots. The combination of his efforts and those of the rest of the NCSU team have resulted in the design of the pick up coil arrays for the PULSTAR-SOS.

When discussing pick up coils for SQUIDs a few terms are commonly used. One might see *gradiometer* or *magnetometer* referred to in many texts. Gradiometers use two or more loops to cancel some aspects of environmental noise in analog. Often, changing magnetic fields which penetrate the array of loops are never picked up in the first place. A couple designs for first-order gradiometers are shown in Fig. 3.11 and a discussion about their operation is contained in that sections text, so that material will not be repeated here. It is possible to use more loops in more complex configurations for higher order gradiometers. If you are interested in this, I suggest you take a look at the *SQUID Handbook: Vol 1* by Clarke and Braginshi [74].

Another type of pick up coil which may be discussed is the *magnetometer*. A magnetometer is a single surface loop. It may have multiple turns but it is basically what one might think of when thinking of a most simple *pick up coil*. That isn't exactly true because some ingenious geometric tricks are sometimes used to build *pick up coils* but it is *basically* true.

The system has been designed to be able to use SQUIDs mounted in superconducting shields and pick up loops with leads fed through the top of the Pb shield surrounding the experimental region. The end of the SQUID cable will connect to a superconducting housing mounted onto the PEEK support directly above the Pb shield, see Fig. 4.14. From those enclosures to the top of the Pb shield, the leads for the pick up coils will be placed inside Pb capillary. Inside the Pb shield, the leads will not be protected by Pb capillary as this would distort the magnetic field in the measurement cell.

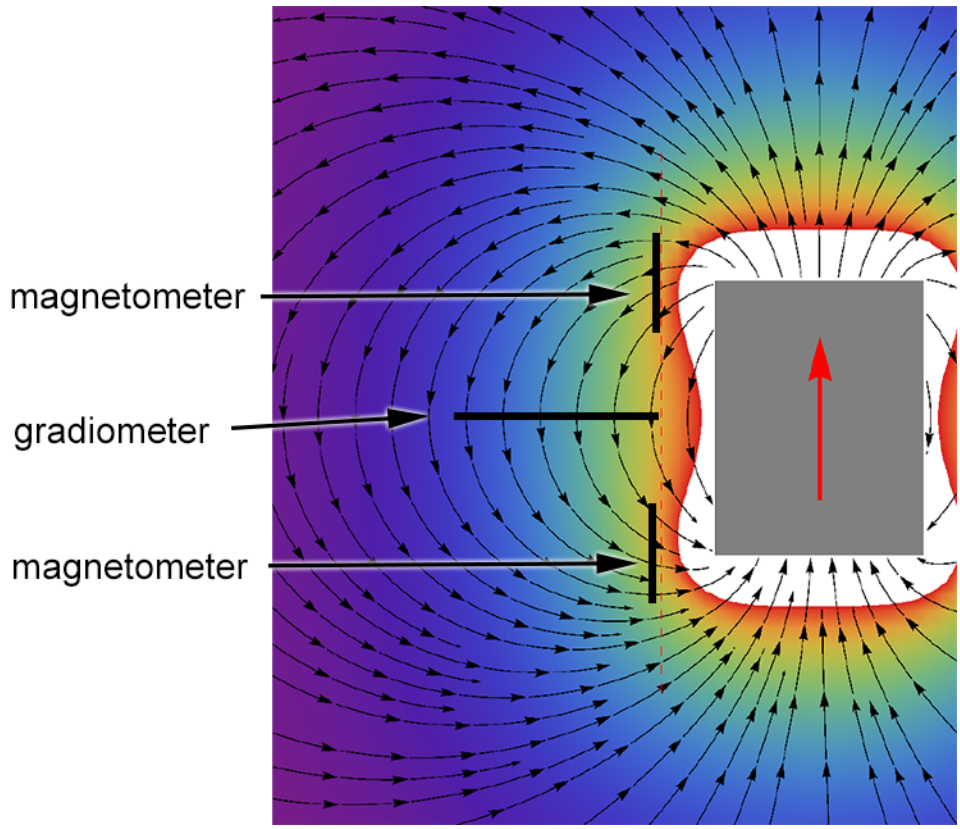


Figure 4.16: *Magnetic Field Generated by Oscillating Polarized ^{3}He Atoms. This View Is From the End of the Measurement Cell. The Magnetic Holding Field Runs Left to Right. The Atoms Will Precessing in the Plane Perpendicular to the Holding Field. The Planned Location of the Pick Up Coils Near the Top and Bottom of the Cell Are Shown As Well As the Possible Location of the Gradiometer. These Are Not Necessarily to Scale, As the Final Pick Up Coil Sizes Have Not Been Selected. This Image Was Taken From S. Clayton's Paper [2] and Generated Using the Mathematica Code Described in That Paper.*

The magnetic holding field is oriented along the axis of the vestibule. When the NMR tipping pulse is applied, the atoms will precess in the plane perpendicular to the holding field. Fig. 4.16 shows the magnetic field generated by the ^{3}He atoms as their spins precess past the vertical direction. Placing the pick up coils on the side of the measurement cell shown in the figure allows detection of the differential and quadrature fields generated by the atoms. The field from the spins will be out of phase between the top and bottom magnetometers. These magnetometers will each be connected to a single SQUID. The value in measuring each magnetometer individually rather than connecting them to each other to act as analog gradiometers is that more detailed processing can be performed digitally after

the measurements have been performed. The signals through any set of magnetometers can then be analyzed in relation to each other rather than be bound physically to a particular pair of pick up coils.

Some consideration was given to placing axial gradiometers on the top or bottom of the cell as well. This is also the *top* and *bottom* of the cell as seen in Fig. 4.16. This would be similar to the measurement technique used in section 3.5. The baseline of such a gradiometer would need to be on the order of the cell's vertical dimension, ≈ 10 cm. This was analyzed using the Mathematica code described. With such a baseline, the total field strength measured through the gradiometer would be ≈ 6 fT. With magnetometers on the side of the cell, as shown in the figure, the field at the magnetometers will be ≈ 8 fT with direct data from an pair of magnetometers we desire to analyze.

The measurement cell will be mounted on a support frame. When the larger cell is to be installed, the frame will first be attached to the fiber optic cables and measurement cell prior to installation into the cryostat. Once installed, the pick up coils will be mounted on a support on the side of the cell frame. In this setup, the pick up coils will not actually be touching the measurement cell but will instead be placed within a few mm of the outside wall of the cell.

As mentioned, a shorter measurement cell will be installed first for initial testing of many components of the apparatus. Each of the cell types are shown in Fig. 4.15. One side of the smaller cell will be completely covered by the vestibule and pick up coils will need to be mounted to the opposite side of the cell, see Fig. 4.15a. When the larger cell is installed, the side opposite the vestibule will be covered with fiber optic cables and thus the pick up coils will be mounted on the same side as the vestibule. That final setup will be the configuration shown in Fig. 4.15b.

4.5 Conclusions and Future Work

This chapter has described my work on the PULSTAR-SOS experiment design. The cryostat body has been delivered and construction of the majority of the support structure

for the first phase of commissioning has been completed at Duke University. Leak testing of the cryostat has been completed with liquid nitrogen and LHe in their respective baths, showing a leak rate of 5×10^{-9} mbar L s^{-1}. The OVC and IVC hold a vacuum of 10^{-6} mbar and 10^{-5} mbar, respectively.

The cryo-cooler has been installed and testing of the LHe and liquid nitrogen boil off showed no surprises. The dilution refrigerator has been installed and a cooling cycle will be performed soon with it. The 1K Pot already has a heater on it, so that heater will be used to test whether or not the energy needing to be dissipated from heating the SQUIDs and cryoswitches can be safely released through the 1K Pot.

The components described in section 4.3 have not yet been constructed. That section outlines how our designs will result in minimal heat loads into the measurement cell.

The SQUID system described in section 4.4 is being brought together piece by piece. In the meantime, the SQUID cable which is currently installed in the dilution refrigerator will be used to start SQUID noise background tests using a Supracon CE2SBlue SQUID. The PFL adapter box and feedthrough have been designed by Star Cryo and purchased by NCSU. We await their delivery for integration into the system.

Designs for the SQUID cabling for a set of four SQUIDs is well underway. We expect to determine final lengths of different parts of the cable in the coming months and will request a quote at that time. The heat sinks for the SQUID cabling have gone through a first draft of design but some refinements are needed. They will be ready by the time the SQUID cables arrive.

Presently the cryostat is constructed in the Triangle Universities Nuclear Laboratory (TUNL) on Duke campus. Testing of the dilution refrigerator, SQUID systems, ^{3}He polarization by MEOP, superfluid ^{4}He filling of the measurement cell, and actuator arm can all be conducted in it's presently location. Once these parts of the cryostat have been commissioned, the cryostat will be moved to the PULSTAR reactor. It will then be connected to the UCN source and be prepared for performing measurements on the ^{3}He(n,p)^{3}H reaction.

Chapter 5

LIQUID HELIUM SCINTILLATION

The ^{3}He(n,p)^{3}H reaction, which is central to the SNS-nEDM experiment, has a Q-value of 764 keV and results in oppositely directed reaction products with proton and triton energies E_p= 573 keV and E_{3H}=171 keV, respectively [42]. When immersed in liquid helium (LHe), these reaction products produce LHe scintillation in the extreme ultra-violet (EUV) [29]. The scintillation process, products, and equipment used for detection are of great interest. Scintillation experiments using α particles in superfluid ^{4}He across a range of electric field magnitudes and temperatures have shown a dependence of the scintillation products on electric field and temperature [105, 106]. The SNS-nEDM experiment will be using strong electric fields to assist in the detection of a possible electric dipole moment, in part, by detecting the scintillation products. Before attempting to detect scintillation from the neutron capture, it is prudent to test a process which is expected to generate the same response in the equipment without expending ^{3}He resources.

The scintillation process is theorized to be the result of energy being deposited into the ^{4}He atom causing (a) separation of an electron and its return to bonding, (b) production of helium ions (He^+), and (c) production of helium excimers (He_2^*) [107]. The captures and emissions cause a strong prompt pulse and after pulses of light. These processes are discussed in section 5.1.

We have conducted a series of experiments which observed the prompt and after pulse scintillation from a radioactive $^{241}_{95}$Am source while immersed in superfliud LHe and applying static electric fields at a range of magnitudes. The $^{241}_{95}$Am source produces 5.5 MeV α particles which result in a very pronounced signal. The experiments, which extended the research previously performed on α scintillation, were performed at Los Alamos National Laboratory (LANL). The theory and experimental procedures are outlined in section 5.2.

Section 5.3 discusses some experimental challenges which were encountered during the execution of the experiments. The analysis of the data resulting from the experiment is discussed in section 5.4 and the results derived are covered at the end of the chapter in section 5.5.

5.1 LHe Scintillation Theory

Since the 1950s much effort has been put into understanding the cause of LHe scintillation [108]. The present view is that as a charged particle makes its transit through the liquid, energy from the particle is deposited in helium atoms [105]. A portion of the energy ionizes helium atoms leaving electron-ion pairs and excited atoms along its path. The average energy needed to produce an electron-ion pair is defined by the W value, which is $W \sim 43\ eV$ for LHe.

After the electron is freed from its helium atom, the nearby helium atoms are pushed away from it as a result of Pauli exclusion. This is referred to as a *bubble* in the liquid. The positive He^+ ion, attracts nearby helium atoms and forms a *helium snowball*. Recombination of the bubbles and snowballs happens on the order of ~ 0.3 ns [107]. During the recombination or by direct interaction with the α, excited helium atoms He^* and molecules He_2^* called *excimers* are formed. The molecular species come in singlet and triplet states.

The radiative decay of the lowest-energy singlet state, $He_2\left(A^1\Sigma_u^+\right)$, occurs in less than 10 ns, emits a $\sim$ 16 eV EUV photon, and contributes to a large *prompt pulse* which is observed in the scintillation light (see Fig. 5.10). The triplet state, $He_2\left(a^3\Sigma_u^+\right)$ has a lifetime of $\sim$ 13 s [109]. In a high-excitation-density environment such as LHe, destruction of these excimers can occur within the first 100 ns through the Penning ionization process and contribute to a delayed (or *after pulse*) scintillation.

During the excitation process, slightly more than one third of the excited singlet helium atoms are promoted to states with principle quantum number of 3 or higher, while the rest will have $n = 2$ [105]. The atoms with $n \geq 3$ can then auto-ionize by the Hornbeck-Molnar process [110]

$$He^* + He \rightarrow He_2^* + e^- \tag{5.1}$$

As discussed in detail by Ito *et al* [105], Jaffe's columnar theory of recombination describes that the ionization track forms a dense plasma of positive and negative ions. The α deposits energy along a 0.27 mm long track which is 60 nm wide.

Jaffe's theory describes clouds of positive and negative ions which are pulled away from each other in the presence of an electric field. Recombination occurs at rates proportional to the product of the densities of these radially expanding clouds. The model was further refined by Kramers [111], who focused on the fact that the diffusivity of ions in a dense fluid is extremely small and the recombination would have a larger influence on the charge density's time dependence. Fitting to previously collected data, Kramers theory fits well to a cylindrical Gaussian charge distribution along a columnar track. In Ito *et al* [105], a thorough argument is offered which fits experimental observations to Kramers' theory of columnar recombination.

5.2 Overview of the Experiment

This section describes the execution of our experiment on the scintillation of LHe and the sources used in the experiments. The setup and design of the experiment is covered in section 5.2.1. The procedures used to conduct the experiment are outlined in section 5.2.2.

The experiment was designed to use two radioactive sources, $^{241}_{95}$Am and $^{113}_{50}$Sn, an alpha α and beta β source, respectively. The $^{113}_{50}$Sn source had been previously used in similar experiments by McKinsey *et al* [107]. In our experiment, the β signal was lost in the photomultiplier tube's dark counts. Thus, there is no analysis for the β signal to perform. The $^{241}_{95}$Am source produced 5.5 MeV α particles which were observed to cause scintillation in the LHe bath. Table 5.1, shows relevant properties of these two sources.

α induced scintillation had previously been explored in a varying electric field at cryogenic temperatures [105]. The previous work establishes a standard to which the team was

Table 5.1: *Radioactive Source Data*

Nuclide	Half-life	Type of decay	Particle		Photon		Rate[a]
			Energy (MeV)	Emission prob.	Energy (MeV)	Emission prob.	
$^{113}_{50}$Sn	0.315 y	EC	0.364 e^-	29%	0.392	65%	1370 Bq
			0.388 e^-	6%	In K x rays 97%		
$^{241}_{95}$Am	432.7 y	α	5.443	13%	0.060	36%	1250 Bq
			5.486	85%	Np L x rays 38%		

[a] Rate observed when sources were electroplated onto electrode in Aug 2017

able to compare its data to ensuring consistency. Consistency was found as the following sections will describe.

α induced scintillation in LHe also has a high ionization density. As shown in [105], a 5.5 MeV α particle deposits energy at a rate of 20 $keV/\mu m$ along a 0.27 mm long track. Making it practically a point source. Protons and tritons from the ^{3}He(n,p)^{3}H interaction also have demonstrated a high ionization density making it qualitatively similar to α induced scintillation.

Although the experiments we performed extend the general knowledge of LHe scintillation, they were also designed to develop the groundwork for further experimentation with β and neutron sources and their scintillation products in LHe. In both of these future experiments, an $^{241}_{95}$Am source will be used for calibration of the light collection system.

5.2.1 Experimental Setup

This section describes the experimental setup used. Here, information about the geometry and materials used will be described.

The device used was the medium scale high voltage test apparatus (MSHV). The system has a Leiden Cryogenics ^{3}He refrigerator set inside a cryostat with an outer vacuum chamber

(OVC), nitrogen jacket, and inner vacuum chamber (IVC). Previously, the ^{3}He refrigerator had been demonstrated to be capable of reaching temperatures below 0.6 K while attached to a 6 L volume of LHe.

The 6 L stainless steel volume, which can hold superfluid helium, is referred to as the central volume. The central volume was thermally connected to the bottom of the ^{3}He Pot. The central volume contained a high voltage (HV) electrode and a ground electrode placed with a 1 cm separation (see Fig. 5.3). The high voltage electrode was somewhat cylindrical (Φ 6 in) with rounded edges. The ground electrode was a metallic ring, with vertically aligned bars (Φ 0.079 in, center separation = 0.395 in) through its face.

The ^{241}Am radioactive source was electroplated to the center of the HV electrode (Φ 1 cm). This geometry allows roughly 2π steradians to be covered by the light collection system. Electroplating and measurements on the sources was performed in Aug 2017. At that time, the α source measured 1250 decays per second. The experiments reported here, were performed between January to April 2018.

There were two capillaries entering the central volume. One capillary was connected to the mensor gauge and a valve inside the LHe main bath, and ends at the bottom of the central volume. This capillary was thermally sunk to the 1 K Pot and the ^{3}He Pot. The capillary could be blocked by a needle valve. The other capillary starts at the top of the central volume and exits through the LHe bath. It can be blocked by a cryogenic valve made of Torlon built by collaborators at the University of Illinois Urbana-Champaign and is known as the the *UIUC Valve*. See Fig. 5.1 for a schematic of this part of the system.

The electrodes were enclosed by a sleeve of G-10 to prevent HV breakdown between the HV electrode and the central volume. As the central volume is filled, the LHe level was monitored by a superconducting level sensor for the first few inches. The top of the central volume had a capacitive level sensor which could monitor the last few inches of LHe. A Ruthenium Oxide (ROx) and LakeShore 670 Diode were located on the outside of the central volume to monitor the temperature. A ROx resistor was located inside the

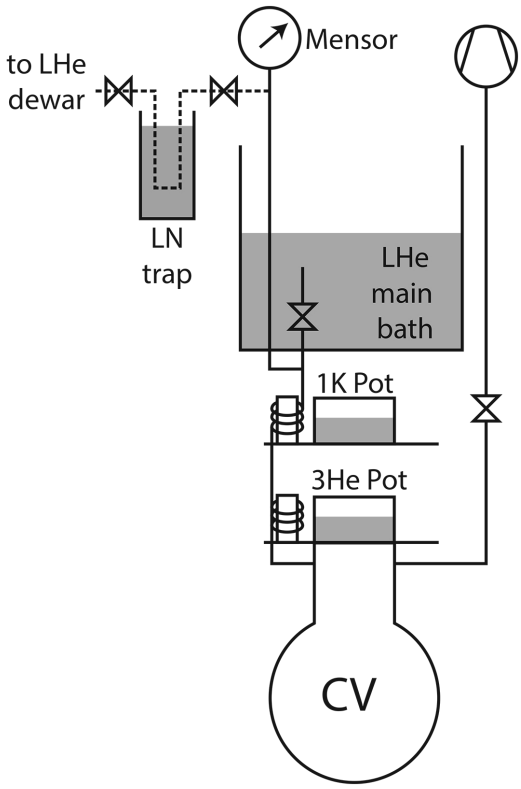


Figure 5.1: *Schematic of Central Volume and Important Plumbing Paths. During the Initial Run, the Dashed Line Was Not Present. This Was Added to Allow the Central Volume to Be Filled by Condensing Helium Gas From the Lhe Storage Dewar.*

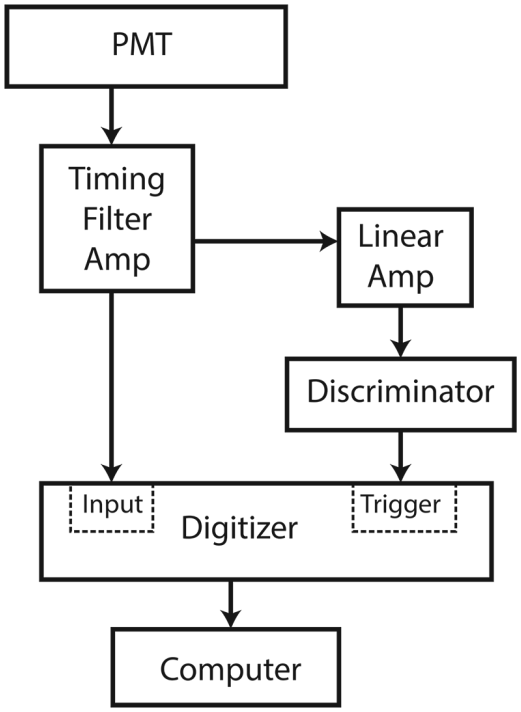


Figure 5.2: *Data Acquisition (DAQ) System. The Digitizer Was a Skutek DDC10 Digitizer.*

central volume as well. The central volume had been pressure tested to 8 bar and had a blow-out valve at that pressure. Therefore, the pressure on the surface of the liquid could be modified. A mensor gauge was connected to the outlet of the central volume to monitor the pressure inside the central volume.

Inside the ground electrode was a cylindrical PMMA plate whose surface (facing HV electrode) was coated with 125 mm thick layer of TetraPhenyl Butadiene (TPB). Here the EUV light is wavelength shifted to blue light. A bundle of fiber optic wires were pressed against the back side of the PMMA plate and trapped by a reflective plate. The fibers transport the blue light to the bottom of the central volume and through a sapphire window.

Outside the central volume and inside the IVC was a Hamamatsu R7725MOD photomultiplier tube (PMT) which had been modified to operate at cryogenic temperatures [112]. Although the PMT was hanging from the bottom of a flange on the central volume, effort was made to thermally isolate the PMT from the central volume by using long thin threaded rods. The PMT was thermally connected to the IVC body. It was also encased in a grounded aluminum shield to prevent arcing between the HV line (connecting to HV electrode) and the PMT.

There are two main reasons the arcing could cause significant issues. First, it is possible that a large current being delivered to some random place on the PMT could kill it. Second, in previous experiments [105], arcing had exposed the PMT to light flashes from the HV breakdown which decreased the PMT gain in a way which appeared to be permanent. The cable connecting to the HV feedthrough would also have a high voltage and the shield protected the PMT from this as well. If any of the HV components were exposed, it would produce an electric field between the component and any objects at other potentials (i.e. any surface inside the IVC). The grounded shield around the PMT would help to avoid allowing those electric fields to traverse the PMT body, which could cause decreased efficiency as the fields between the cathode, dynodes, and anode could be distorted.

The PMT resistor plate was removed and new plate was created by N. Phan (LANL post doc). The resistors were mounted on a circuit board, encased in Stycast 1266, and thermally anchored to the inside of the IVC. The board was then sandwiched between two Cu plates and thermal contact was made by applying vacuum grease. The 0.75 m leads between the resistor plate and the PMT were made of cryogenic wires from LakeShore. More details about the PMT temperature and heat loads are discussed in section 5.3.1.

The calculated efficiency of the light collection system was ∼7e-3 [113]. This value is a product of the (a) TPB conversion efficiency (100%), (b) light intercepted by the fiber optic cables (40%), (c) light capture by the fibers (10.8%), (d) light transmission (89%), (d) optical break (90%), and the (e) PMT quantum efficiency (20%). It had been previously

measured using a UV LED. This was enough for effective data collection. The measured rate of α scintillation detection was $\sim$400 Hz.

Once the light was collected by the PMT, the signal was sent through filters and discriminators, and to the data acquisition (DAQ) system (see Fig. 5.2). It used a SkuTek DDC10 Digitzer. The digitizer was rated for 100 MHz. However, due to (a) the number of data points which were to be collected for each signal and (b) downtime while transferring data to the DAQ computer, the rate was closer to 1 kHz.

This system was designed to be triggered in the discriminator by an oscillation in the PMT signal with a voltage larger than a certain threshold. Each specific data point it recorded was an Analog to Digital Conversion (ADC) Channel (proportional to the magnitude of the electromagnetic signal it received) and each data point collected was 10 ns in duration. Taking many of these points creates a 2D array for "ADC vs Time'. The total number of data points recorded for each trigger was 2048. An individual measured package of 2048 data points will be referred to as a *Waveform*. See Fig. 5.10 for an example of what our waveforms looked like. Each time the threshold was reached (and the system wasn't already recording), the system would save around 200 data points prior to the trigger event, equivalent to 2 μs. It would then record 1848 data points after the trigger, equivalent to about 18.48 μs. See section 5.4 for more details on data handling.

The minimum threshold set on the discriminator is referred to as the *cutoff threshold*. The cutoff threshold could be modified by adjusting a potentiometer. For example, if the potentiometer was set to have a voltage of 300 mV, it roughly correlated to a 0.5 PE cutoff threshold. Then all data with PEs larger than that would be collected. The dark counts have energies close to 1 PE.

When running the DAQ system, the r code (written by N. Phan) was set to collect a certain number of data points before ending the measurement cycle (i.e. it could be set to record 100,000 waveforms).

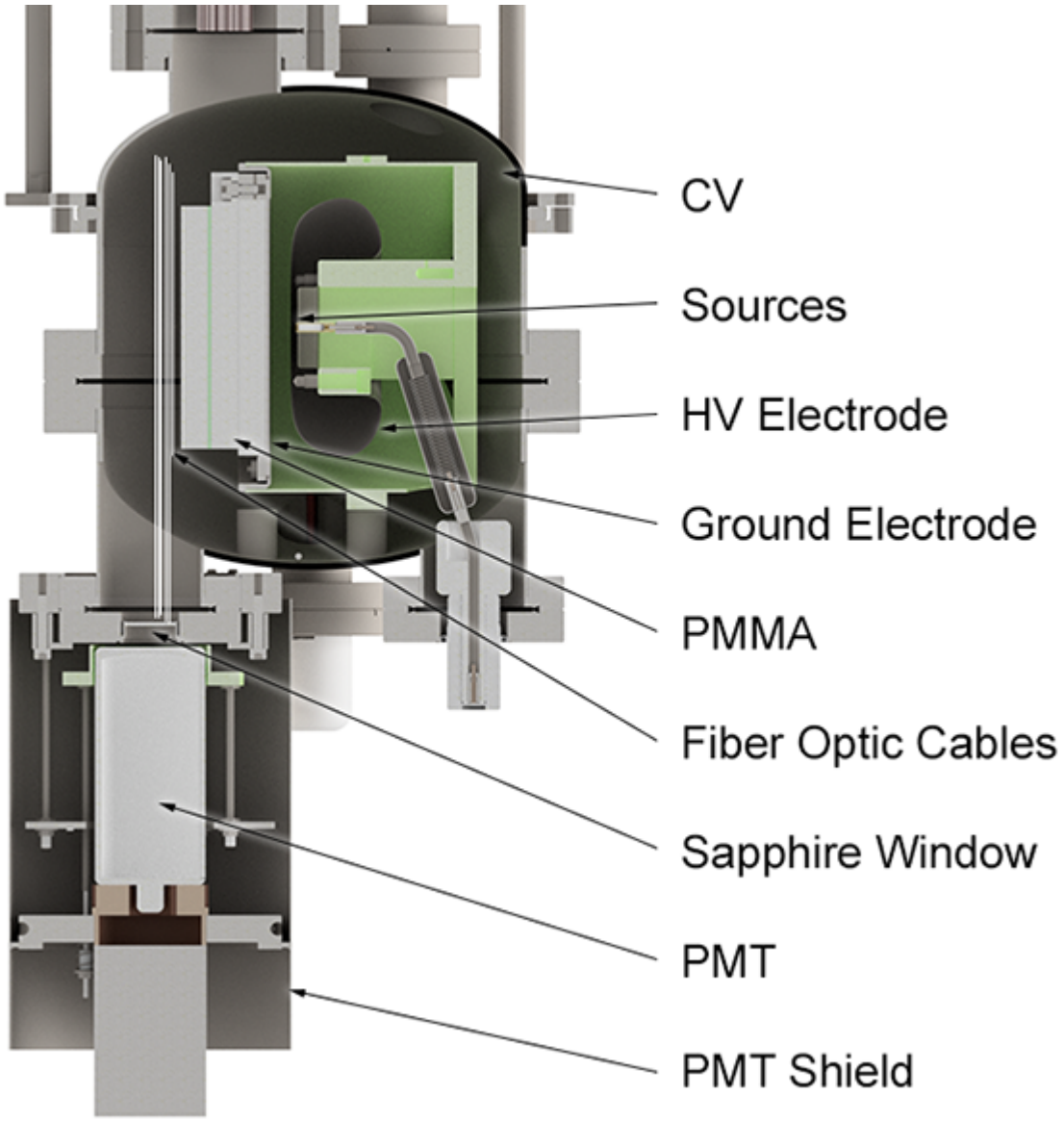


Figure 5.3: *Cutaway View of Central Volume From Autodesk Inventor Model Created by J. Ramsey (ORNL). All Components Shown Are Inside the IVC.*

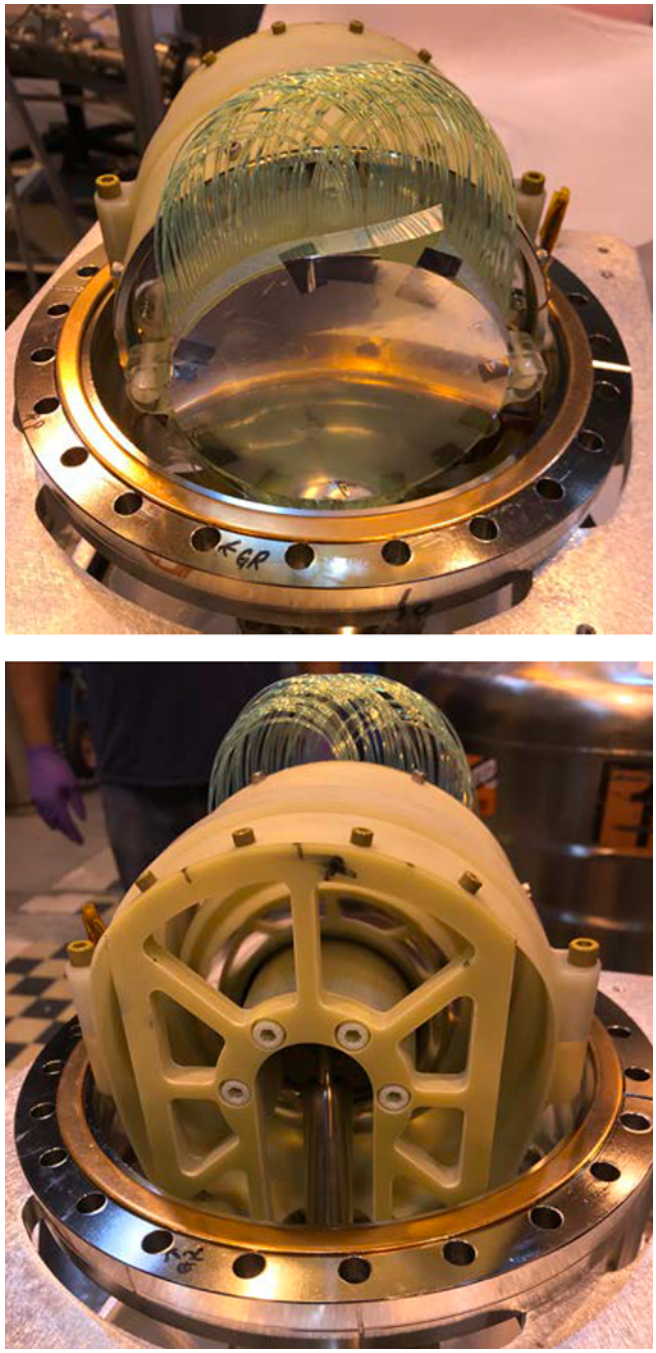


Figure 5.4: *Photographs of Electrode Support Held by Bottom of Central Volume. Top Image Shows Green Fiber Optic Cables. This Is a View From Left Side of Fig. 5.3. Bottom Image Shows Hv Connector and G-10 Support Structure. Viewing From Right Side of Fig. 5.3. Both Photos Taken by N. Phan.*

5.2.2 Experimental Procedure

The proposed series of experiments was started in Jan 2018. The technique used to cool the system was the common precooling technique using liquid nitrogen (LN), evacuation of all nitrogen, then add LHe.

When the bath started to collect LHe and the 1 K Pot reaches 4.2 K, pumping on the 1 K Pot could begin. The 1K Pot had an *always open* capillary and a *by-pass* valved capillary both fed from the main bath. The central volume would not be at 4.2 K yet, as it is a large volume with weak thermal connection to the bath.

With the 1 K Pot running, LHe from the LHe bath could start to be flowed into the central volume. While filling through this capillary, the liquid is delivered to the bottom of the central volume. The second capillary was connected at the central volume top and pumping on this line can cool the central volume more quickly than by evaporative cooling as reducing the pressure cools the helium gas and allows it to remove more heat as it exits the volume. After a few hours, the temperature of the central volume is low enough to begin collecting LHe. As the pressure in the central volume is lower than atmosphere, liquid can begin collecting at temperatures lower than 4.2 K.

Once the central volume was filled with LHe, the PMT could be turned on. The first data set could be collected then the potential on the HV electrode could be increased and data sets at higher electric field could be collected. During each data collection cycle, the system was set to record 10^5 triggers. Voltages from 0 kV to 35 kV were applied in increments of 5 kV generating the array of data.

5.3 Problems and Solutions

Three runs were performed to collect the data. Each run took the team about 1 week to complete. As expected, unexpected situations arose. These delightful surprises gave an opportunity for close analysis of the system's behavior.

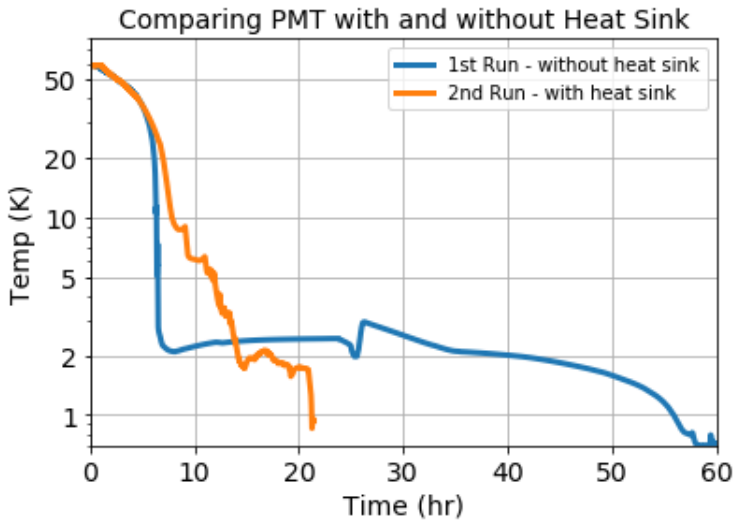


Figure 5.5: *Plot of Temperature Measured on Inside of Central Volume Using ROx Resistor. "1st Run" - the PMT Was Not Heat Sunk to IVC Causing a Heat Load of About 10 MW Into the Central Volume. "2nd Run" - the PMT Was Heat Sunk to 4 K on IVC Increasing the Cooling Power of the System.*

During the first run, the PMT was not properly heat sunk to the IVC. This resulted in the temperature of both the PMT and central volume to be larger than expected. In section 5.3.1, the thermometry data collected is compared to simulations of the system and demonstrate how effective good thermal sinking can be.

Throughout all runs, the system was plagued by issues with light collection. The plague was expressed to us by fewer PEs being collected than expected. Since that is the central theme of the experiment, this is obviously very interesting. When the HV electrode was electroplated, it had been electroplated with an α and a β source. The peak we expected to see from the β source was not near 12 PEs as expected but instead seemed to be at 1 PE overlapping the dark counts. Changes in technique were tried to identify the source of the light collection issues. Section 5.3.2 discusses some of the approaches used and the logic behind them.

5.3.1 PMT Heat Sink to IVC

During the first run in Jan 2018, issues arose with the central volume not cooling as quickly as desired. While revisiting the process of preparing the system, it was realized that the PMT had not been heat sunk to the IVC using a Cu braided wire as planned. This had resulted in a *hot* PMT trying to cool through weak thermal contacts with the central volume.

Nitrogen gas at a few hundred mbar is kept in the IVC while cooling the main bath with LN. This means the PMT was reliably known to be at 77 K or slightly below when attempts to cool it further were began. Before beginning to cool below 77 K, the nitrogen gas is pumped out to ensure it does not freeze. Helium gas cannot be added to the IVC while cooling to 4 K because the PMT amplification cavity is permeable to helium gas. Exposure to an environment saturated with helium gas causes irreparable contamination inside the amplification cavity of the PMT. Cooling the PMT must be performed using another gas or through conduction. Our plan was to use conduction.

Accordingly, the PMT was primarily being cooled by the weak thermal connection to the central volume. The central volume was expected to cool below 1 K in less than a day, it took more than 2 days to cool. At this time, the PMT did not have a thermometer on it and the closest one was inside the central volume. Fig 5.5 shows the temperature observed on the inside of the central volume by a ROx resistor during the first run and after the heat sink to the IVC was established on the following run.

To analyze the heat load from the PMT into the central volume, a COMSOL Multiphysics model was created with a geometry close to that of the actual system. Details were taken from observation and the three-dimensional .step models created by J. Ramsey (ORNL), see Fig. 5.6.

The least accurate aspect of the model is likely the internal composition of the PMT itself. Material provided from Hamamatsu were reviewed but these lack detailed schematics of the PMT internal construction. After working through a few models though, it is clear

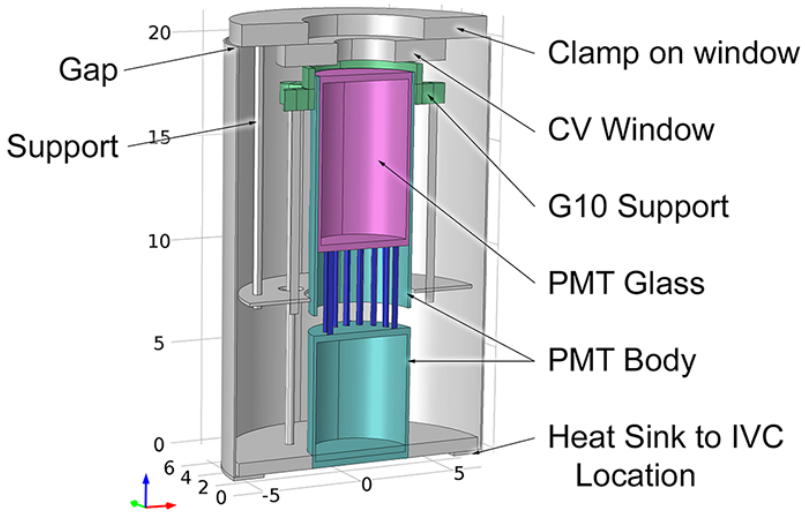


Figure 5.6: *Geometry Used in COMSOL Simulation. Axis Units Are Centimeters. Material Identification: Pink: Borosilicate Glass. Light Blue: Plastic Simulated With Epoxy Thermal Conductivity and Specific Heat in Middle of Plastics Range. Dark Blue: Copper Wires. Green: G-10. Grey: SS304.*

the primary heat source is the glass of the PMT. We do not know the wall thickness of the glass, it was placed in the model to have sidewall thickness of 1/8 inch and end cap thickness of 3/8 inch.

In Fig. 5.6, the top of the volume labeled "CV Window" is the flange on the central volume which has a sapphire window. The volume labeled "Clamp on Window" is a clamp which is a part of the PMT support structure. Thermal connection between these two parts is made by small screw clamps. Attached to the "Clamp on Window", are four "Support" rods. They are Φ 3/8 inch stainless steel threaded rods which connect to the plate in the middle of the assembly. The plate in the middle of the assembly is then connected to more rods of the same diameter which connect to the "G-10 Support". This G-10 piece is for alignment and to ensure the PMT viewing window does not get scratched during installation. It had weak thermal connection to the PMT. From the G-10 piece, long threaded rods extended down to the bottom plate. The bottom plate is squeezed onto the PMT and was thermally anchored to it. The underside of the bottom plate had two screws which were 180^0 apart. The heat sink to the IVC was connected to one of these screws.

Fig. 5.9 gives the reader a good feeling for the heat flow through the assembly. The outside of the assembly is surrounded by a metal shield for electrical insulation to ensure the leads to the HV electrode did not experience arcing with the PMT.

The G-10 support at the top of the PMT was not touching the bottom of the central volume at all, so the model includes no thermal connection at these locations. Likewise, the middle annulus was not connected directly to the PMT. The shield around the PMT was not touching the bottom of the central volume nor the middle annulus. There were 16 wires connecting the PMT to the lower electronics package, these were simulated with Cu material.

The entire geometry was set with an initial temperature of 77 K. Due to the high emissivity of all materials constructing the system and the low temperatures involved, back of the envelope calculations estimate the radiative heat load on the central volume would be minimal, so only conductive heating was considered in the COMSOL model.

The connection to the central volume was set with a certain temperature. This region is only the top surface of the "CV Window". The temperature here was set to 4 K in two of the studies and 2 K in two of the studies. It was set to 2 K because as Fig. 5.5 shows, the central volume was close to 2 K for almost 40 hrs.

A circular surface with Φ 3/8 inches on the bottom surface of the model acted as the heat sink on the bottom of the PMT shield to the IVC. In two studies, this was not set to a temperature for the purpose of studying the situation during the first run when the PMT was not thermally connected to the IVC. In two studies, this was set to 4 K, as if it were connected via a Cu braid to the inside of the IVC.

The simulation was set up as a time dependent solver with 30 min increments spanning 1 week.

The simulation predicted that the heat load on the central volume from the PMT was around 10 mW even after 60 hrs of cooling. This is an extremely large heat leak for the system. After the PMT was properly heat sunk to the IVC, at 4.2 K, the heat load was

predicted to be less than 0.1 mW after 24 hrs of cooling and would reach 26 μW after 60 hrs. The results of these simulations are shown in Fig. 5.7. Heat sinking the PMT on the second and successive runs alleviated the cooling issue.

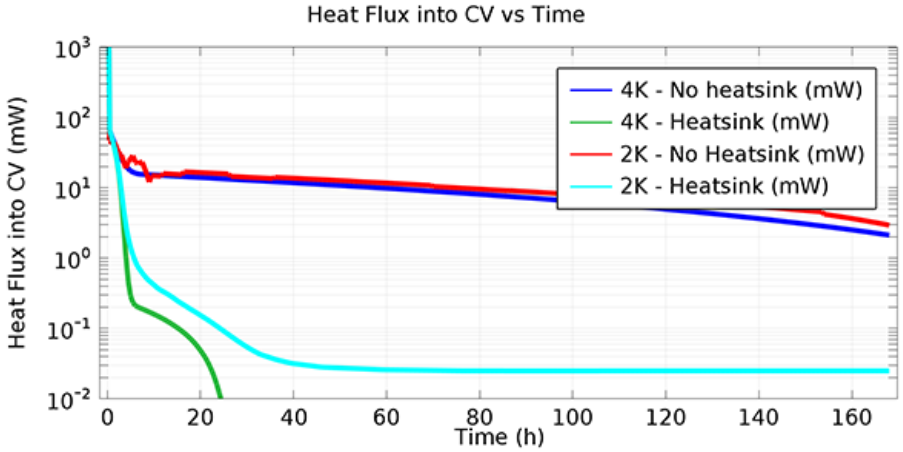


Figure 5.7: *Heat Load Into Central Volume From PMT As a Function of Time. The Temperature in the Beginning of the Names of the Plot Labels Refers to the Temperature of the Central Volume in the Model. The "no Heatsink" and "heatsink" Label Indicates Whether or Not the Bottom of the PMT Shield Was Thermally Connected to the IVC. The Thermal Connection to the IVC Was Always Set to 4 K.*

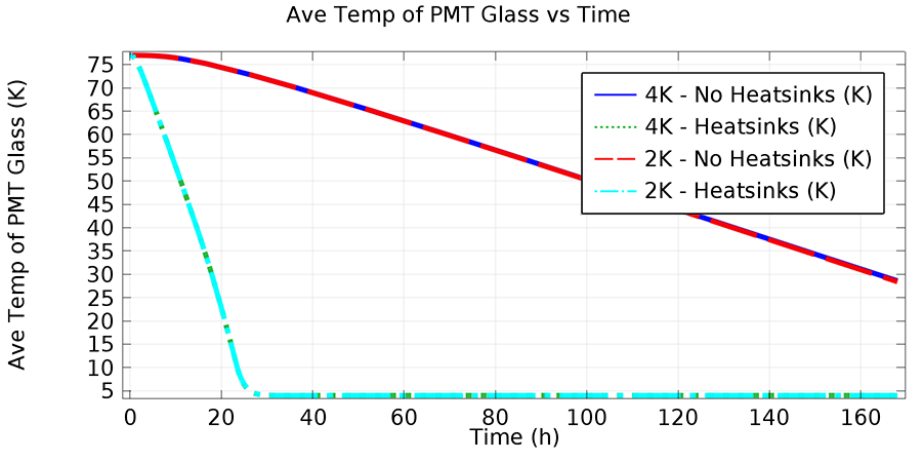


Figure 5.8: *Average Temperature of PMT Glass in COMSOL Simulation.*

The models also demonstrated that the glass volume of the PMT maintains the largest temperature during cooling. Fig. 5.8 shows the average temperature of the glass volume over time from the simulation. The average temperature was consistent for the models with no heat sinks and consistent for the models with heat sinks.

With hopes that the central volume could be cooled on a future run to 0.5 K, a stationary study was run. In this case, the central volume boundary was set to 0.5 K and the heat sink is connected to the bottom of the PMT was set to 4 K. The heat load into the central volume was calculated to be 30.8 μW. Fig. 5.9 shows the final temperatures simulated.

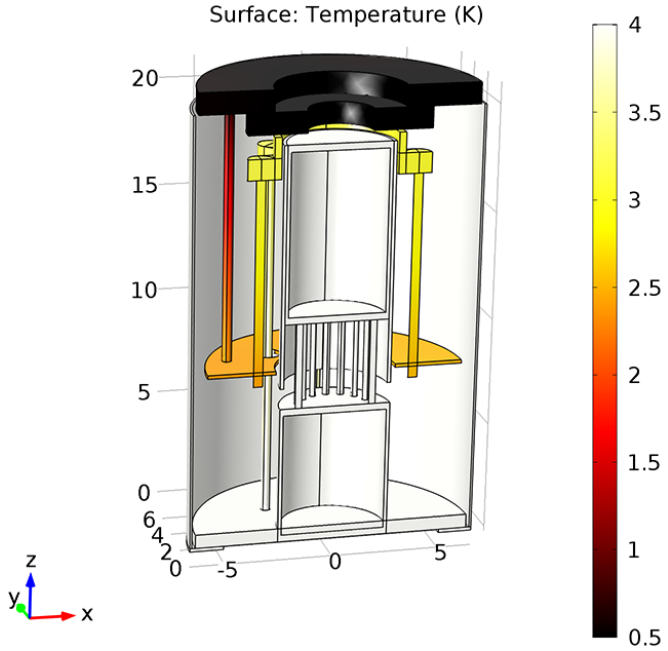


Figure 5.9: *Temperature Distribution on PMT and Support Structure in Stationary Simulation.*

5.3.2 Less Scintillation Light Than Expected

During the first run, we saw a smaller electric field dependence on the prompt pulse than that which had been observed in the Indiana Univ. experiments [105]. In those experiments, the reduction in the prompt scintillation was 15% when the electric field was changed from 0 to 45 kV/cm. During the first run, the reduction was observed to be around 5% when the field was increased to 35 kV/cm. This meant something in the experimental setup had

changed or some contamination had been introduced. A number of techniques were tried to discover the source of the issue.

Possible causes for the reduction in scintillation light could have been (a) problems with the sources, (b) incorrect spacing between the electrodes, (c) contamination in the central volume, and/or (d) issues with the TPB coating. Each of these issues were considered and investigated but a true resolution to problem was not found prior to the conclusion of my work on the project.

After the run, the assembly inside the central volume was removed (see Fig. 5.4). This assembly included both HV and ground electrodes, α and β sources, and the TPB coated PMMA plate. The radiation safety team at LANL has many devices for the detection of radiation. They came to the lab and took γ spectra on the sources. The spectra confirmed that the sources were in working order. The electrodes were expected to have a space of 1 cm between them. Inspection of the spacing confirmed that they were not displaced by a factor of 2 to 3 which would be necessary to explain the deviation from previous results.

The first idea for contamination in the central volume was that the LHe used to fill the central volume had condensed some H_2 from the atmosphere [114]. This could either have condensed onto the TPB coated surface or be small particles floating in the liquid. It was possible, the contamination could be absorbing the scintillation light. Takeyasu Ito (LANL) performed a calculation whereby he estimated that a layer of H_2 roughly 0.03 microns thick would be necessary to attenuate the light enough to cause the reduction observed. Based on calculations, 3 orders of magnitude more H_2 would have to have precipitated onto the TPB surface than was realistic and thus was not sufficient to be the cause. Therefore, impurities floating the liquid would be the next reasonable explanation.

If contamination were floating in the liquid, it would come from the LHe main bath or LHe dewar. As mentioned above, the LHe main bath was used to fill the central volume. A solution would be to condense purified helium gas into the central volume. Additional gas plumbing was added to the cryostat to allow helium gas to be taken from the vent port

on the LHe dewar. This source of helium gas is considered to be as pure as possible, as all other elements and molecules (except ^{3}He) are solids at 4.2 K. This means all other possible contaminants inside a LHe dewar should be solidified and either floating the LHe volume or resting on the bottom inside the dewar. The helium gas line was fed through a LN cold trap on its way to the central volume. While cooling the system, this gas was flowed continuously through the central volume to ensure all other contaminants were removed prior to beginning condensation.

Once the system was cooled, attempts to begin condensing liquid helium began. As mentioned, there were two capillaries allowing access into and out of the central volume. One of the capillaries is connected to the LHe bath and that one could not be used, as the LHe bath needed to be filled with LHe to provide sufficient cooling and may be a source of contamination. The gas then had to be pushed through the second capillary which was designed as an exhaust line and thus did not have effective thermal contact with the bath or other parts of the cryostat. The upper extension of the capillary did flow through the LHe bath but it was a straight tube. The most efficient technique discovered was to increase the pressure from the dewar to somewhere between 1100 to 1700 mbar. Eventually, the central volume was filled with condensed LHe but since the pressure was so much higher than the standard vapor pressure of LHe at 4.2 K, the initial temperature was as high as 6 K. During this time, the 1K Pot was operational and provided some cooling. This temperature is much too high for effective cooling from the ^{3}He Pot but since it was thermally connected to the central volume, adding some pressure, up to a few hundred mbar of ^{3}He in the circulation lines allowed enough thermal contact with the 1K Pot to accelerate cooling. As the system cooled, data was collected and similar results of a change of about 5 to 7% between 0 to 35 kV/cm were observed. This confirmed that contamination was not the issue.

While the central volume was opened, the TPB coating had been inspected visually using a UV light source. No visible scratches or blemishes could be observed. Barring all other options, this is the source of attentuation of the light which is most under scrutiny.

As the work to analyze different TPB coating techniques is still underway, the description of this effort will be outlined in section 5.6.

5.4 Data Analysis

Data was taken at a range of temperatures, vapor pressures, and voltages. Table E.1 shows the full list of the combinations which were tested. With a broad brush stroke, one could say that three data sets were collected: (a) 0.61 K - 2.42 K at 800 ± 70 mbar at 0 kV/cm, (b) 0.61 K at 750 and 28 mbar at 0-35 kV/cm, (c) 2.03 - 3.06 K at 1470 mbar at 0-35 kV/cm.

When operating the PMT, the cutoff voltage for the trigger needs to be set in the discriminator. For each temperature, the first measurement set the cutoff voltage to be 300 mV and included dark and β signals. This cutoff voltage roughly correlates to 0.5 PE. Following that, data was taken with the cutoff set to 1200 mV, ideally isolating only α scintillation. The 300 mV and 1200 mV threshold values will be referred to as *low threshold* and *high threshold*, respectively.

For most temperatures, 4 or 5 $\times$ 10^5 waveforms were collected at low threshold with the potential set to 0 kV. Also for most, a second set of high threshold measurements were performed with voltages set at 0, 5, 10, 15, 20, 25, 30, and 35 kV, in which 10^5 waveforms were collected at each potential. Since the distance between the electrodes was 1 cm, the electric field varied from 0 to 35 kV/cm. Attempts to increase the voltage further resulted in breakdown.

Each set of 10^5 waveforms for the low and high threshold data collection took 127.2 ± 2.7 secs and 252.9 ± 1.5 secs, respectively. Keeping the data collection periods short helped to avoid warming the PMT. Though some warming did occur as these 2 - 4 min periods were often repeated back to back for an hour at each temperature.

As mentioned, there were issues with light collection and we weren't able to distinguish between dark counts and β signals. The low threshold data was taken hoping that at some point an analysis technique could be found which may be able to differentiate between the

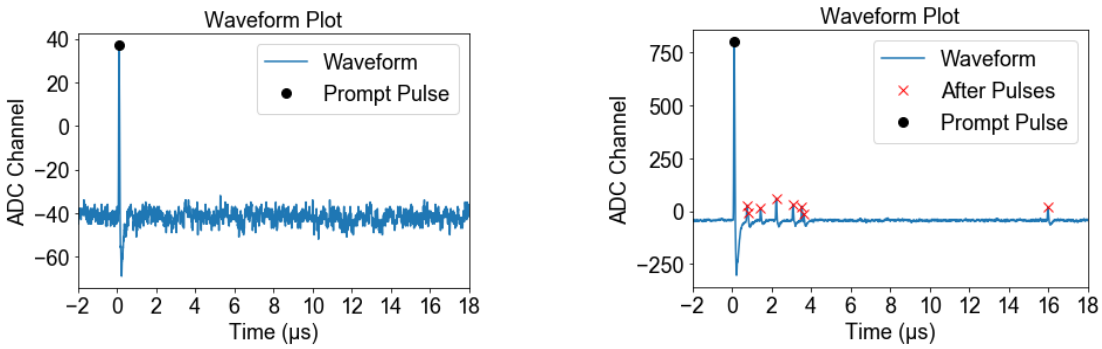


Figure 5.10: *Waveform Output Types. In These Waveforms, the Pedestal Offset Has Not Been Adjusted. However, All Analyzed Data Was Performed on Waveforms After the Pedestal Had Been Calculated and Added to the Waveforms. (a) Waveform Which Has No After Pulses and Thus Is From β or Dark Counts. (b) Waveform From α Scintillation Showing After Pulses Marked With Red X's.*

two. At this time, no such technique has been identified. Having collected the data while the system was in the desired state however, may still prove to be useful in the future and worth the extra 10 min of effort at each temperature.

Each trigger comes from one of three sources: (a) α scintillation, (b) β scintillation, or (c) dark counts (PMT noise). The α signals come with after pulses. The specifics of this behavior will be discussed later. The β and dark counts have low energy and no after pulses. It is therefore difficult to distinguish the difference between these types of counts. Common examples of each type are shown in Figs. 5.10.

Each data point is stored as two bytes, a 2^{15} signed integer. Each waveform has 2048 time points each spanning 10 ns. When the trigger activates, the hardware stores around 200 time points (2 ms) prior to the trigger. The mean of the values in this region (before the trigger) are taken as the pedestal of the PMT. The standard deviation of this region is taken as the standard deviation of the pedestal, σ_{ped}. This value is needed for the curve used to fit the data, see Eq. 5.3. It is sometimes expected that the pedestal will drift as the temperature or voltage is changed but this was not observed during these measurements. The values for the pedestal and σ_{ped} are shown in Fig. 5.11. The pedestal and σ_{ped} was calculated for each individual waveform and the offset was added to each point in the

waveform before the rest of the analysis was executed. A sample of the code I wrote to perform the analysis is included in App. E.2.

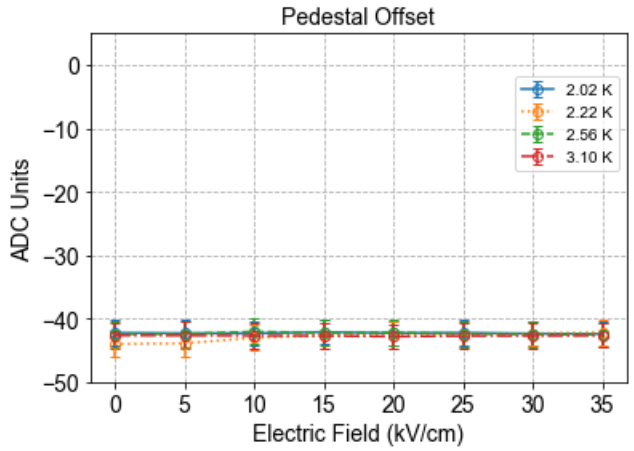


Figure 5.11: *Pedestal Offset and Standard Deviations Measured During 2.03 - 3.06 K Measurements. The Values Plotted Here Can Be Found in Table E.7*

The code checks for a second maximum value and compares its magnitude to the trigger. If the second maximum in a waveform is more than 1/2 the magnitude of the trigger pulse, the waveform is omitted. This ensures that α prompt pulses do not overlap and after pulses from two α events are not counted in the same group because the source of the after pulses would not be obvious.

For each data set, a single PE mean was calculated in terms of its ADC channel and used for the rest of that data set. This is because the single PE peak would drift. It was usually about 53 to 65 ADC units. Details about this computation will be discussed later.

If the trigger pulse had a magnitude greater than 150 ADC units, it is very likely that it came from an α scintillation and has after pulses. Take another look at Figs. 5.10 and specifically notice the magnitude of the trigger ADC channel. The waveforms which pass this cutoff are then analyzed for after pulses. Although not all triggers with magnitude greater than 150 ADC units come from α scintillation, it was reliable enough to fit the theoretical model. We found that even some after pulses had magnitude greater than 150 ADC.

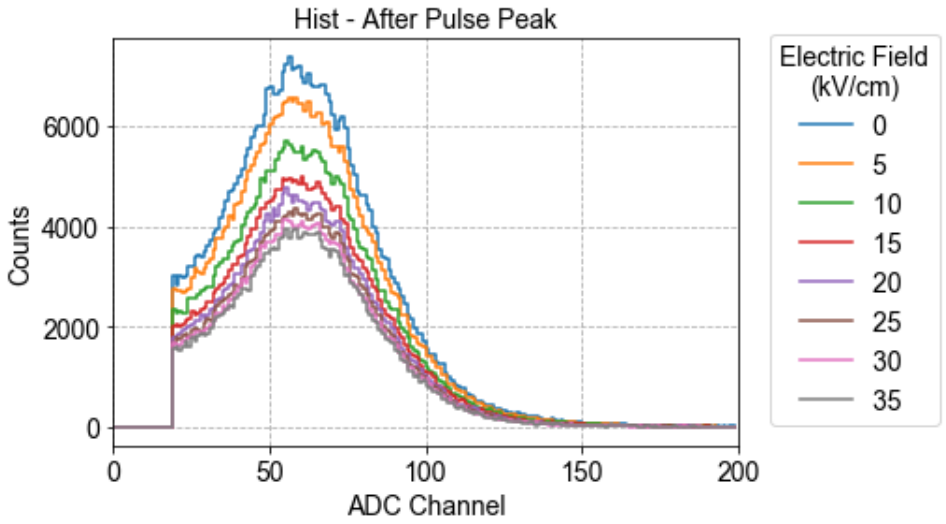


Figure 5.12: *Histogram of After Pulse Peak Values for 2.22 K Data Set. This Plot Clearly Shows the Dependence of the Number of After Pulses on Electric Field Strength. This Type of Trend Was Observable Across All Data Sets.*

After pulses with a magnitude above 20 ADC units were counted. Below this value, events may be included which appeared to be noise in the baseline signal. As shown in Table E.9, the 20 ADC unit cutoff equates to about 1/3 PEs. In the following paragraphs, the *Single PE* magnitude calculation will be discussed. The (a) total count for all after pulses at each voltage at each temperature, (b) mean number of after pulses and standard deviation in that number, and (c) the time after the trigger of each after pulse were recorded and are plotted in section 5.5.

Histograms of the after pulse magnitudes were then generated. Fig. 5.12 shows a sample of an after pulse magnitude histogram. The histogram was fit to the curve shown in Eq. 5.2. This equation is a convolution of a Poisson (to fit number of PEs) and Gaussian (to fit PMT response) [105]. Fig. 5.13 shows an example of a curve fit to the histogram. For the fit, the midpoint of each histogram bin is used. In each case, it was necessary to reduce the domain for which the fit was attempted or the fit would deviate at the extremes. The value of G taken from the fit is the single PE calibration magnitude at that temperature and electric field.

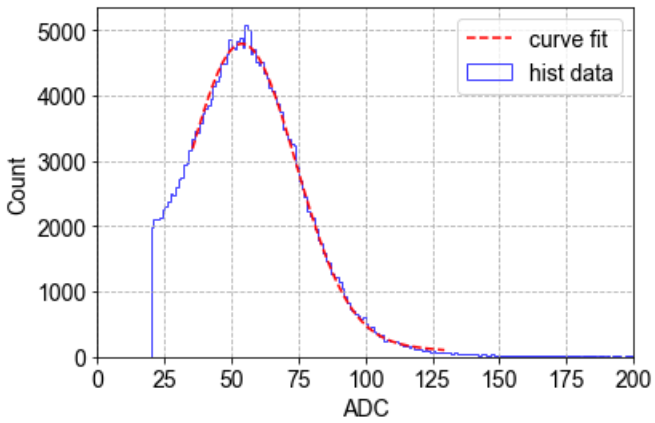


Figure 5.13: *Fit of Convoluted Poisson-gaussian to Histogram Data From Eq. 5.2. The Mean and Standard Deviation of the Fit Are Then Taken and Reported in the Results.*

$$f_{ADC}\,(x) = N \sum_{k=1}^{\infty} \frac{\mu^k\ e^{-\mu}}{k!} \frac{1}{\sqrt{2\pi\sigma_k^2}}\ exp\Big[-\frac{(x - G\ k)^2}{\sigma_k^2}\Big] \tag{5.2}$$

where N is the normalization constant, x corresponds to the ADC channel, μ fits the mean number of PE's, and G is the gain (ADC channel analogous to a *Single PE*). σ_k is defined as

$$\sigma_k = \sqrt{\sigma_{PMT}^2\ k + \sigma_{ped}^2} \tag{5.3}$$

When performing the analysis, it was found that setting $k_{max} = 15$ was sufficient to find convergence to within 0.000 1%, so it was kept constant throughout the fitting process.

When fitting to the Poisson-Gaussian distribution for the after pulse histogram, the curve was fit to N, μ, G, and σ_{PMT}. The values for σ_{ped} were taken from the pedestal calculations (mentioned earlier) and were fit for each voltage and each temperature maintaining consistency within the same fit data set.

A histogram of the trigger magnitudes was then generated and fit to the Poisson-Gaussian distribution. For this fit, the values of G and σ_{PMT} were taken from the single PE curve fit and σ_{ped} was taken from earlier calculations. For the prompt pulse, the curve was fit to μ and N. The value of N is not of interest here but usually was close to 10^6 $\pm$

10^4. The value of μ, is the mean number of PE's in the signal and a measured value being sought. Later, when the mean number of PEs is reported, it was taken from the fit value for μ.

5.5 Results

This section reports the results of the various experiments which were performed. The data sets are grouped into themes to assist in deciphering the data.

The first data set, reported in section 5.5.1, covers the largest temperature range. It starts at 0.61 K and goes to 2.42 K. During these measurements, no induced electric field was present.

The observations reported here show clear trends in the behavior of the scintillation. The findings were all consistent with previous observations and gave no unexpected results. For each of the data sets, I have plotted (a) total count for all after pulses at each voltage at each temperature, (b) mean number of after pulses and standard deviation in that number, and (c) the time after the trigger of each after pulse

5.5.1 Results For Temperature Range 0.61 K to 2.42 K

The data set with temperatures ranging from 0.61 to 2.42 K was conducted with no electric field. During the measurement process, the values between 0.86 and 1.93 K were taken as one data set while the system cooled. During the cooling, the vapor pressure was measured to be 888.25 ± 4.71 mbar. The values collected at 0.61 K and 2.42 K were taken separately and had pressures of 742.27 ± 0.24 mbar and 742.27 ± 0.93 mbar, respectively. At each temperature, 10^5 waverforms were collected.

The mean number of PE's ($\bar{N}_{PE}$) found across the temperature range is shown in Fig. 5.14. This data is consistent with the findings made in [105] (Fig. 9 in that paper), where $\bar{N}_{PE}$ is observed to increase for values above 1 K. In that publication however, values above the lambda point $T_\lambda \approx 2.2\ K$ point were not investigated. It is important to note that our team was not probing the temperature range closely enough to examine the behavior

around T_λ. Although the data spans that region, we will focus our attention here on the region below T_λ.

A few clear trends appear in the data presented in Fig. 5.14. First, there is a decrease in the prompt pulse intensity as the temperature drops from T_λ to lower temperatures. There is then a weak maximum above 1.5 K. Continuing to lower temperatures, we see a minimum slightly below 1 K.

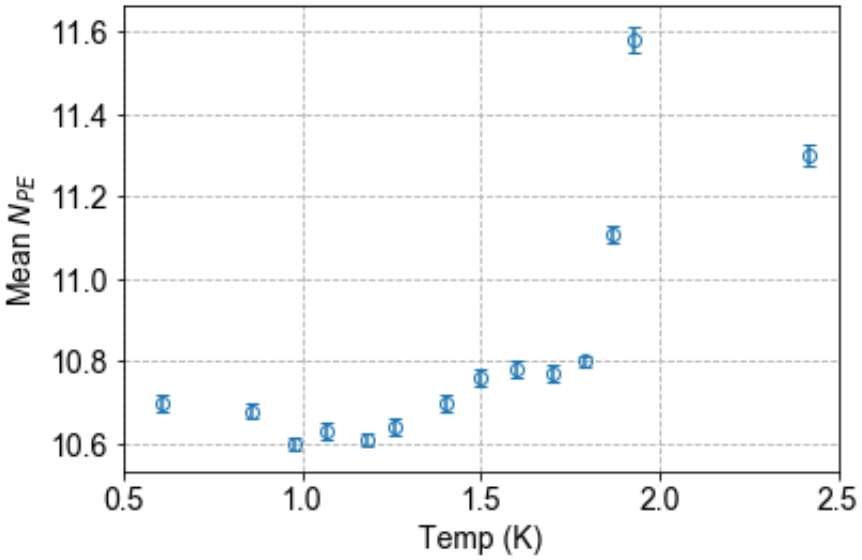


Figure 5.14: *Mean Number of PE's Observed in the Prompt Pulse Vs Temperature. The Values Recorded At .61 and 2.42 K Had Pressure ∼750 mbar. The Values Recorded in Between Had Pressure ∼890 mbar. A Table of This Data Can Be Found in Table E.3.*

The physical phenomena which allows the temperature to influence the prompt pulse intensity has not yet been resolved. Previous attempts to explain the behavior by Roberts *et al* [115, 106] followed a line of argument suggesting that at lower temperatures, the increased diffusion results in increased quenching. Quenching is the destruction of the singlet species in a nonradiative manner. As the α particles move through the liquid, they are down converted to excitations in the liquid helium volume, as described in section 5.1. As this occurs, the energy is transferred to phonons and rotons in the liquid and heats a column of liquid, a few tens of nanometers in radius, to about 2 K [116]. So the temperature of the α interaction region is independent of the bulk liquid temperature. Fig. 5.14 clearly shows

that the intensity of the prompt pulse is suppressed at a temperature slightly below 1 K. These results are consistent with previous findings.

The mean number of after pulses ($\bar{N}_{AP}$) observed during these experiments are reported in Fig. 5.15. The number of after pulses for each prompt pulse was counted generating an array of integers. The mean and standard deviation of this array are the reported values. This data set is consistent with the data found in [105] (Fig. 11 of that paper). An important difference to note between the present work and the previous investigation [105] is that the time intervals over which the data was recorded were 18 μs and 14 μs, respectively. The maximum $\bar{N}_{AP}$ observed in the present work was found at 1.61 K, while in the previous work, the maximum was somewhere in the range of 1.3 to 1.6 K.

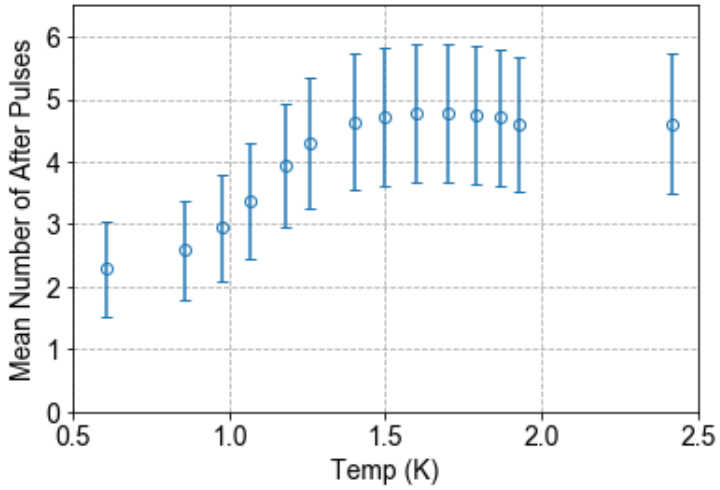


Figure 5.15: *Mean Number of After Pulses Observed Per Prompt Pulse. A Table of This Data Can Be Found in Table E.3.*

5.5.2 Results For Measurements at 0.61 K

With the system at 0.61 K, the vapor pressure inside the central volume was varied to analyze the influence of density on the scintillation process. The pressure was set to 28 and 750 mbar in each set of measurements. During the process, the electric field was also varied to analyze the influence of electric field on the scintillation processes.

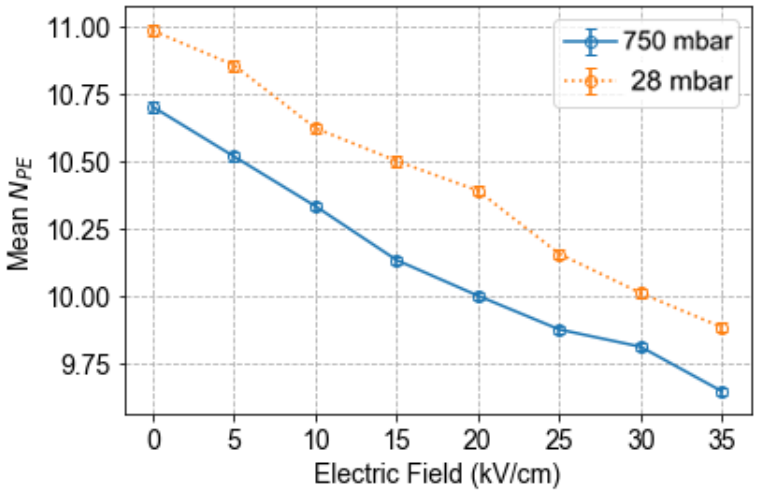


Figure 5.16: *Mean Number of Photoelectrons From 0.61 K Dataset at Range of Voltages. The Standard Deviation of Each Result Is Plotted Above but the Values Were so Small, They Are Difficult to See in the Figure. The Values Plotted Here Can Be Found in Table E.4.*

We observed that both data sets showed a linear decrease in the mean number of PEs N_{PE} as the electric field was increased. In the 28 mbar data set, N_{PE} was found to be consistently higher than that in the 750 mbar data set. Fig. 5.17 shows the results.

Liquid helium is highly compressible [117]. The density of the liquid increases as the vapor pressure is increased. As the density is increased the mobility of most particles is decreased. If this were a contributing factor to the recombination of the electron and ion pairs which produces the scintillation, one would expect an increase in the scintillation intensity at higher density because the electron may more easily tunnel to find its pairing ion. In Roberts *et al* [115], this behavior is observed when the pressure is higher than one bar. For example, at 1 K the density of the liquid is 145.2 kg/m^3 and 146.9 kg/m^3 at 0.1 mbar (standard vapor pressure) and 1000 mbar, respectively. This represents an increase in density of about 1.2%. Our results shows a decrease in N_{PE} of about 2.5% between these pressures. Our data is qualitatively consistent with Fig. 3 from Roberts [115] for pressures below 1 bar and temperatures below 1 K, where they also found that increasing the pressure, decreases in the intensity of the scintillation light.

The mean number of after pulses observed per prompt pulse event was found to be essentially equal for both data sets. The mean number of after pulses was found to decrease as the electric field magnitude was increased. These results are consistent with Fig. 12 from Ito *et al* [105].

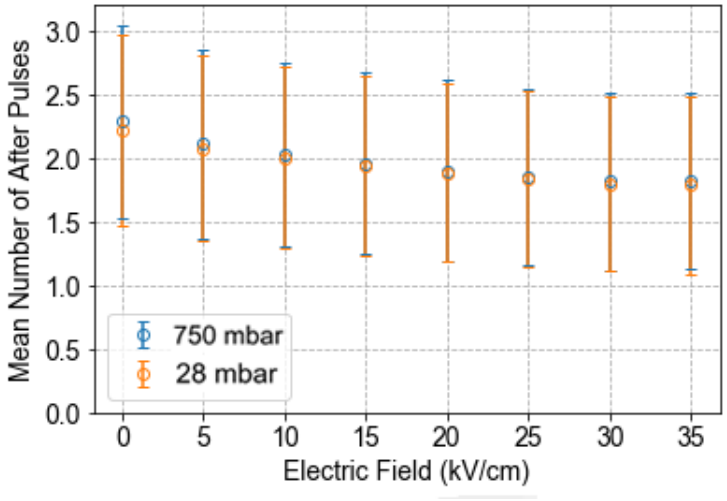


Figure 5.17: *Mean Number of After Pulses For 0.61 K Data Sets. At Each Electric Field Value, the Mean Number of After Pulses for the 28 mbar Data Set Is Slightly Smaller Than the 750 mbar Data Set, Though the Stand Deviations for Each Are Quite Large. The Values Plotted Here Can Be Found in Table E.4.*

5.5.3 Results For Temperatures Between 2.03 to 3.06 K Data

A series of measurements with electric fields between 0 to 35 kV/cm were performed at 2.03, 2.22, 2.56, and 3.06 K, again the number of PEs per prompt pulse and the number of after pulses per prompt pulse were investigated. The vapor pressure on the LHe volume was close to 1470 mbar for each of these measurements, though it varied slightly (see Table E.1 for more detail). This temperature range crosses T_λ, however we found that the data showed a linear decrease in the number of PEs as the electric field was increased above 5 kV/cm. The measurements also showed a non-linear decrease in the mean number of after pulses as the electric field was increased.

It may be worth noting that T_λ does decrease as the vapor pressure is increased [118]. The decrease in temperature is very slight however, being less than 1/2 K at slightly above

25 bar. Therefore, it is not worth discussing in detail in the context of the pressure in this experiment so close to 1 bar.

Previous measuments [105] demonstrated that for temperatures between 0.2 to 1.1 K, the prompt scintillation had little temperature dependence (see Fig. 10 in that paper). In the study reported in this section, it was found that some temperature dependence does exist between 2.03 to 3.06 K. The data revealed more PEs for the higher temperatures and fewer PEs for the lower temperatures.

At each temperature, the mean N_{PE} was observed to decrease by 6 to 7% between 0 - 35 kV/cm. The report from Ito *et al* [105], showed a decrease of about 12.5% at the lower temperatures across the same electric field range. Fig. 5.18 shows the prompt pulse data which was measured.

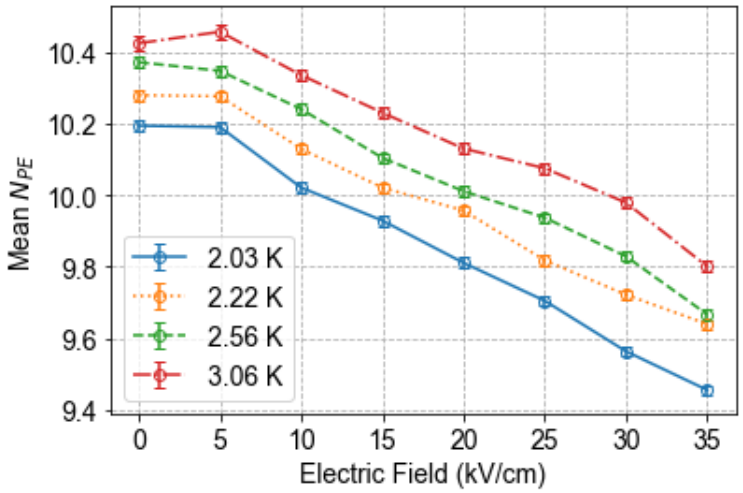


Figure 5.18: *Mean Number of PE's Observed in Prompt Pulse at Temperatures Between 2.03 to 3.06 K Vs Electric Field. The Values Plotted Here Are Also Found in Table E.5.*

The number of after pulses per prompt pulse however showed no temperature dependence in our investigation. The after pulse data was collected during the first 18 μs after the prompt pulse. The mean number of after pulses per prompt pulse is shown in Fig. 5.19. We found the number of after pulses to be independent of the temperature.

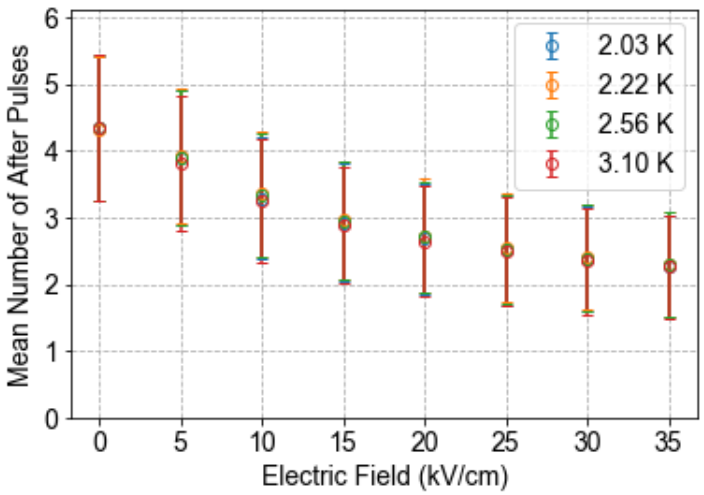


Figure 5.19: *Mean Number of After Pulses Observed Per Prompt Pulse at Temperatures Between 2.03 - 3.06 K Vs Electric Field.*

5.6 Conclusions and Future Work

In the research discussed in this chapter, we found that, for temperatures around T_λ, the number of PEs emitted by prompt pulse scintillation is temperature dependent. We found local maxima and minima at different regions between 0.61 to 2.42 K. However, the volume of LHe, where the interactions are occurring, is heated to about 2 K and thus are independent of the bulk liquid temperature. This leads to the hypothesis that the scintillation from both the prompt and after pulses are influenced by the expansion of the roton and phonon cloud, as discussed by Ito *et al* [105]. The results found here were consistent with previous findings and add further confidence to the theories discussed in section 5.1.

In all of the experiments conducted we found that the prompt pulse scintillation is basically linear in electric field strength. It was found that the pulse strength always decreased with increasing electric field. These measurements were again consistent with previous measurements and support the logic of Kramers' theory of columnar recombination, as again we found consistency with the data collected in Ito *et al* [105]. As our results fit so well to those theories, being strongly influenced by the electric field, further confidence has been

generated that the longer timeline for the after pulses are coming from triplet excimers interacting through the Penning ionization process.

As mentioned, there were issues with light collection in the system. Namely, calculations by T. Ito [113] expected to see around 59 mean PE's from the α scintillation actually resulted in observations of around 10 to 11 PE's. At the time of this writing, the primary culprit being investigated is the TPB coating.

Chapter 6

CONCLUSIONS AND FUTURE WORK

The search for an upper limit to the nEDM experiment to be conducted in the SNS facility at Oak Ridge National Laboratory is a significant undertaking which requires an understanding of subtle physical phenomena. The development of the experiment has resulted in many other research projects to broaden our understanding of those phenomena.

The SNS-nEDM experiment will use polarized ^{3}He in measurement cells coated with dTPB-dPS. The experiment will use SQUIDs to detect the NMR signals from the polarized ^{3}He. In Ch. 3, an experiment conducted on polarized ^{3}He in dTPB-dPS cells was discussed. Those finding, in conjunction with previous measurements [1, 52], suggest that the lifetime of the polarized ^{3}He will be sufficient for reliable use of both polarized ^{3}He and dTPB-dPS. In the SNS-nEDM experiment, the concentrations of polarized ^{3}He will be smaller than any of those conducted in this thesis or in the previous experiments. Thus further investigations into sensing the signal from lower concentration sources of polarized ^{3}He are needed. The PULSTAR-SOS experiment discussed in Ch. 4 is the next step in performing those measurements.

Using SQUIDs for sensing the polarized ^{3}He NMR signal has been demonstrated to be a realistic plan in Ch. 3. Those measurements found that the background noise in the apparatus used are low enough to allow sensing of the signal. The shielding planned for the PULSTAR-SOS experiment should be of higher quality than that used in the experiments performed and discussed in Ch. 3. The increased shielding includes better shielding for the electronics, optical controls for those electronics, and a nearly fully enclosed Pb shield around the experimental region in the new apparatus. Since the PULSTAR-SOS experiment will have many of the same parameters as the SNS-nEDM experiment (only excluding the electric field and a second measurement cell), invaluable data and techniques

for collecting data related to the SNS-nEDM will be collected in the near future, prior to the commissioning of the SNS-nEDM cryostat.

In Ch. 4, the designs and thermal models for the (a) *heat shields*, which compose the new cryostat, (b) *actuator arm*, used to open and close the plug on the PULSTAR-SOS experimental cell, and (c) *UCN guide*, which directs the neutrons from the outside of the reactor to the experimental cell, have all been discussed in detail. The heat shields for the cryostat have been delivered and are currently going through commissioning. In the coming months and years, the actuator arm and UCN guide will be built and commissioned as well.

The SQUID system for the PULSTAR-SOS experiment was outlined in Ch. 4. Many parts of that system have already been designed. Some parts of the system have already been purchased. The integration of SQUIDs in the experiment will require some iterations as the noise spectrum from pumps and equipment, which aren't currently on-site or installed, become part of the environmental electromagnetic noise in the locations the apparatus will be used. Presently, the cryostat is in the French Family Science Center in the Triangle Universities Nuclear Laboratory (TUNL) on Duke Campus in Durham NC. Once testing of the dilution refrigerator installation, addition of all components in the IVC (including the measurement cell), testing with the actuator arm and UCN guide, creation of superfluid helium-II, inclusion of the MEOP ^{3}He polarization system, and assembly and disassembly are completed, the cryostat will be moved to the PULSTAR reactor on NC State Campus in Raleigh NC. Once there, neutrons and polarized ^{3}He will occupy the measurement cell and direct R&D related to the SNS-nEDM experiment will be conducted.

When the interaction between neutrons and polarized ^{3}He produce superfluid helium-II scintillation in the measurement cell at the PULSTAR reactor, the efficiency of the fiber optic and PMT system will be thoroughly tested. Ch. 5 discussed experiments performed at Los Alamos National Laboratory (LANL) which investigated a similar scintillation mechanism. The geometry between the interaction region and PMT were different in the experiments discussed in this thesis but a reliable proof of concept was outlined. Some refinements

to the apparatus or technique are certainly needed. T. Ito continues that work at LANL with the assistance of post-docs and other scientists.

Significant contributions and R&D for the SNS-nEDM experiment are being conducted in the United States and Mexico. This vast effort lays the groundwork for performing a reliable measurement in the near future. The following is a list of universities, businesses, and national laboratories which have contributed to this effort.

(a) Arizona State University

(b) North Carolina State University

(c) Triangle Universities Nuclear Laboratory

(d) Duke University

(e) Los Alamos National Laboratory

(f) Bartoszek Engineering

(g) Oak Ridge National Laboratory

(h) North Carolina Central University

(i) University of Kentucky

(j) University of Virginia

(k) Universidad Nacional Autonóma de Mexico

(l) University of Illinois Urbana-Champaign

(m) Massachusetts Institute of Technology

(n) California Institute of Technology

(o) Mississippi State University

(p) University of Tennessee

(q) Simon Fraser University

(r) Tennessee Technological Institute

(s) Yale University

(t) Indiana University

(u) Brown University

(v) Harvard University

(w) Valparaiso University

REFERENCES

[1] Christopher M. Swank. *Thesis: An Investigation in the Dynamics of Polarized Helium-3 in Superfluid Helium-4 for the Spallation Neutron Source (SNS) neutron-electric-dipole-moment (nEDM) experiment.* 2012.

[2] Steven Clayton. Placement of SQUID pickup loops for the PULSTAR SOS apparatus. 2018.

[3] Paul A. M. Dirac. Quantised singularities in the electronmagnetic field. *Proceedings of the Royal Society A*, 133(821):60–72, 1931.

[4] Paul A. M. Dirac. Forms of relativistic dynamics. *Rev. Mod. Phys.*, 21(3):392–398, 1949.

[5] Paul A. M. Dirac. The theory of magnetic poles. *Phys. Rev*, 74(7):817–830, 1948.

[6] R. Golub and J. M. Pendlebury. The electric dipole moment of the neutron. *Contemporary Physics*, 13(6):519–558, 1972.

[7] E. M. Purcell and N. F. Ramsey. On the possibility of electric dipole moments for elementary particles and nuclei. *Phys. Rev*, 78(6):807, 1950.

[8] James Hammond Smith. *Thesis: A Search for a Permanent Electric Dipole Moment of the Neutron.* 1951.

[9] J. H. Smith, E. M. Purcell, and N. F. Ramsey. Experimental limit to the electric dipole moment of the neutron. *Phys. Rev*, 108:120, 1957.

[10] T. D. Lee and C. N. Yang. Question of parity conservation in weak interactions. *Phys. Rev*, 104(1):254–258, 1956.

[11] C. S. Wu, E. Ambler, R. W. Hayward, D. D. Hoppes, and R. P. Hudson. Experimental test of parity conservation in beta decay. *Phys. Rev*, 105(4):1413–1415, 1957.

[12] L. Landau. On the conservation laws for weak interactions. *Nuclear Physics*, 3:127–131, 1957.

[13] J. H. Christenson, J. W. Cronin, V. L. Fitch, and R. Turlay. Evidence for the 2π decay of the K_2^0 meson. *Physical Review Letters*, 13(4):138–140, 1964.

[14] K. Abe *et al*. Improved measurement of mixing-induced CP violation in the neutral B meson system. *Physical Review D*, 66(7):071102, 2002.

[15] B. Aubert *et al*. Measurement of the CP asymmetry amplitude $\sin 2\beta$ with B^0 mesons. *Physical Review Letters*, 89(20):201802, 2002.

[16] Gerhart Lüders. Proof of the TCP theorem. *Annals of Physics*, 2:1–15, 1957.

[17] Julian Schwinger. The theory of quantized fields. I*. *Phys. Rev*, 82(6):914–927, 1951.

[18] M. Kobayashi and T. Maskawa. CP-violation in the renormalizable theory of weak interaction. *Progress of Theoretical Physics*, 49(2):652–657, 1973.

[19] Max Tegmark. *Our Mathematical Universe*. Knopf, 2015.

[20] Planck Collaboration. Planck 2015 results. xiii. cosmological parameters. *arXiv:1502.01589v3*, 2016.

[21] D. J. Fixsen. The temperature of the cosmic microwave background. *arXiv:0911.1955v2*, 2009.

[22] Edwin Hubble. A relation between distance and radial velocity among extra-galactic nebulae. *Proceedings of the National Academy of Sciences of the United States of America*, 15(3):168–173, 1929.

[23] B. D. Fields, P. Molaro, and S. Sarka. Big-bang nucleosynthesis. *arXiv:1412.1408v1*, 2014.

[24] A. D. Sakharov. Violation of CP invariance, C asymmetry, and baryon asymmetry of the universe. *Soviet Physics Uspekhi*, 34(5):392–393, 1949.

[25] John Ellis, Mary K. Gaillard, D.V.Nanopoulos, and Serge Rudaz. A cosmological lower bound on the neutron electric dipole moment. *Phys. Lett. B*, 99(2):101–106, 1981.

[26] Konrad Kleinknecht. *Uncovering CP Violation*. Springer-Verlag Berlin Heidelberg, 2003.

[27] Yingchuan Li, Stefano Profumo, and Michael Ramsey-Musolf. Bino-driven electroweak baryogenesis with highly suppressed electric dipole moments. *Phys. Lett. B*, 673:95–100, 2009.

[28] V. Cirigliano, Yingchuan Li, S. ProfumoM, and J. Ramsey-Musolf. Mssm baryogenesis and electric dipole moments: an update on the phenomenology. *Journal of High Energy Physics*, 2, 2010.

[29] Robert Golub and Steve K. Lamoreaux. Neutron electric-dipole moment, ultracold neutrons and polarized ^{3}He. *Physics Reports*, 237(1):1–62, 1994.

[30] A. Baker *et al*. Improved experimental limit on the electric dipole moment of the neutron. *Phys. Rev. Lett.*, 97(13):131801, 2006.

[31] R. Alarcon *et al*. Conceptual design report for the neutron electric dipole moment project (nedm). *Project MIE#71RE for U.S. Department of Energy*, 2007.

[32] P. Schmidt-Wellenburg. The quest for an electric dipole moment of the neutron. *AIP Conference Proceedings.*, 1753:060002, 2016.

[33] John Wilks. *The Properties of Liquid and Solid Helium.* Oxford University Press, 1967.

[34] T. M. Ito *et al*. An apparatus for studying electrical breakdown in liquid helium at 0.4 K and testing electrode materials for the neutron electric dipole moment experiment at the spallation neutron source. *Rev. Sci. Instrum.*, 87:045113, 2016.

[35] A. Esler, J. C. Peng, S. K. Lamoreaux, C. Y. Liu, D. Chandler, D. Howell, and J. R. Torgerson. Dressed spin of helium-3. *arXiv:nucl-ex/0703029v1*, 2007.

[36] Home: Spallation neutron source. https://neutrons.ornl.gov/sns. Online; accessed 28 Feb 2019.

[37] Most powerful pulsed spallation neutron source. http://www.guinnessworldrecords.com/world-records/most-powerful-pulsed-spallation-neutron-source/. Online; accessed 28 Feb 2019.

[38] N. Fomin, G. L. Greene, R. R. Allen, V.Cianciolo, C.Crawford, T. M. Tito, P. R. Huffman, E. B. Iverson, R. Mahurin, and W. M. Snow. Fundamental neutron physics beamline at the spallation neutron source at ORNL. *Nuclear Instruments and Methods in Physics Research Section A*, 773:45–51, 2015.

[39] Kent Leung *et al*. The neutron electric dipole moment experiment at the spallation neutron source. *Unpublished Manuscript*, 2019.

[40] Brad Filippone. Overview of neutron properties. In *Neutron Summer School - NCSU*, 2018.

[41] R. Golub. On the storage of neutrons in superfluid 4He. *Phys. Lett. A*, 72(4):387–390, 1979.

[42] Glenn F. Knoll. *Radiation Detectibn and Measurement*. John Wiley & Sons, Inc., 1999.

[43] Vince Cianciolo. Light collection update. In *nEDM Collaboration Meeting - March*, 2018.

[44] R. Golub and J. M. Pendlebury. Super-thermal sources of ultra-cold neutrons. *Phys. Lett. A*, 53(2):133–135, 1975.

[45] Robert Golub, David J. Richardson, and Steve K. Lamoreaux. *Ultra-Cold Neutrons*. Adam Hilger, 1991.

[46] E. D. Commins. Berrys geometric phase and motional fields. 59(12):1077–108, 1991.

[47] J. M. Pendlebury *et al*. Geometric-phase-induced false electric dipole moment signals for particles in traps. 70, 2004.

[48] S. K. Lamoreaux and R. Golub. Detailed discussion of a linear electric field frequency shift induced in confined gases by a magnetic field gradient: Implications for neutron electric-dipole-moment experiments. 71(3):10, 2005.

[49] A. L. Barabanov, R. Golub, and S. K. Lamoreaux. Electric dipole moment searches: Effect of linear electric field frequency shifts induced in confined gases. *Phys. Rev. A*, 74(5):052115, 2006.

[50] A. L. Barabanov, R. Golub, and S. K Lamoreaux. Detailed discussion of a linear electric field frequency shift (important for next generation) electric dipole moment searches) induced in confined gases by a magnetic field gradient: Implications for electric dipole moment experiments (ii). 2005.

[51] Jacob Yoder. Measurement of wall relaxation times of polarized 3He in bulk liquid 4He for the neutron electric dipole moment experiment, 2010.

[52] Qiang Ye. *Thesis: ^{3}He Relaxation Time Measurements at Low Temperatures for the Neutron Electric Dipole Moment (nEDM) Experiment.* 2009.

[53] C. M. Swank, A. K. Petukhov, and R. Golub. Correlation functions for restricted brownian motion from the ballistic through to the diffusive regimes. *Phys. Lett. A*, 376(34):2319–2324, 2012.

[54] nEDM Collaboration. A new search for the neutron electric dipole moment: Funding pre-proposal. *The Department of Energy*, 2002.

[55] Slawomir Piatek. *Silicon Photomultiplier: Operation, Performance & Possible Applications.* Hamamatsu Photonics, 2018.

[56] W. M. Burton and B.A. Powell. Fluorescence of tetraphenyl-butadiene in the vacuum ultraviolet. *Appl. Opt.*, 12:87–89, 1973.

[57] Q. Ye, H. Gao, W. Zheng, D. Dutta, F. Dubose, R. Golub, P. Huffman, C. Swank, and E. Korobkina. Relaxation of spin-polarized ^{3}He in mixtures of ^{3}He and ^{4}He at about 330 mK. *Phys. Rev. A*, 80:023403, 2009.

[58] Steven M. Clayton. Flux through the SQUID gradiometer pickup loops. In *internal document for nEDM collaboration*, 2008.

[59] J. W. Ekin. *Experimental Techniques for Low-Temperature Measurements.* Oxford University Press, 2006.

[60] W. A. Fitzsimmons, L. L. Tankersley, and G. K. Walters. Nature of surface-induced nuclear-spin relaxation of gaseous He^3. *Phys. Rev*, 179:156–165, 1969.

[61] William Happer. Optical pumping. *Rev. Mod. Phys.*, 44:169, 1972.

[62] T.G. Walker and W. Happer. Spin-exchange optical pumping of noble gas nuclei. *Rev. Mod. Phys.*, 69:629–642, 1997.

[63] R. E. Jacob, S. W. Morgan, and B. Saam. ^{3}He spin exchange cells for magnetic resonance imaging. *J. Appl. Phys.*, 92:1588, 2002.

[64] Earl D. Babcock. *Thesis: Spin-Exchange Optical Pumping with Alkali-Metal Vapors.* 2005.

[65] S. Appelt, A. Ben-Amar Baranga, C. J. Erickson, M. V. Romalis, A. R. Young, and W. Happer. Theory of spin-exchange optical pumping of ^{3}He and ^{129}Xe. *Phys. Rev. A*, 58:1412, 1998.

[66] R. L. de Zafra. Optical pumping. *American Journal of Physics*, 28:646, 1960.

[67] David J. Griffiths. *Introduction to Quantum Mechanics.* Pearson Education, 2006.

[68] MS Albert, GD Cates, B Driehuys, W Happer, B Saam, CS Springer Jr, and A Wishnia. Biological magnetic resonance imaging using laser-polarized 129Xe. *Nature*, 370:199, 1994.

[69] Austin Randolph Reid. *Thesis: Helium-3 Polarization and Origami Folded Cryogenic Actuators and Metamaterials.* 2018.

[70] C. P. Slichter. *Principles of Magnetic Resonance. 3rd Edition.* Springer, 1996.

[71] J. J. Sakurai. *Modern Quantum Mechanics.* Addison-Wesley Publishing Company, Inc., 1994.

[72] P. J. Nacher, I. Shinkoda, P. Schleger, , and W. N. Hardy. Nuclear polarization enhancement by distillation of liquid ^{3}He-^{4}He solutions. *Phys. Rev. Lett.*, 67:839–842, 1991.

[73] Paul T. Callaghan. *Principles of Nuclear Magnetic Resonance Microscopy.* Oxford University Press, 1991.

[74] John Clarke and Alex I. Braginski. *The SQUID Handbook, Vol 1.* WILEY-VCH Verlag GmbH and Co. KGaA, 2004.

[75] P. J. Hore. *Nuclear Magnetic Resonance.* Oxford University Press, 1995.

[76] J L Flowers, B W Petley, and M G Richards. A measurement of the nuclear magnetic moment of the helium-3 atom in terms of that of the proton. *Metrologia*, 30(2):75–87, jan 1993.

[77] Randall D. Knight. *Physics for Scientists and Engineers: a Strategic Approach.* Pearson Education, Inc, 2004.

[78] Ajay M. Parikh. *Magnetic Resonance Imaging Techniques.* Elsevier Science Publishing Co., Inc, 1991.

[79] http://www.comsol.com.

[80] Flinn Scientific. Atomic sizes and radii chart. https://www.flinnsci.com/atomic-sizes-and-radii-chart/ap6897. Online; accessed 4 February 2019.

[81] R. W. Pattie Jr. *et al.* Measurement of the neutron lifetime using a magneto-gravitational trap and in situ detection. *Science Magnazine*, 360:627–632, 2018.

[82] Young Jin Kim and Steven M. Clayton. Tests of a SQUID-based ^{3}He co-magnetometer readout for a neutron edm experiment. *IEEE Transactions on Applied Superconductivity*, 25, 2015.

[83] Neeraj Khare. *Handbook of High-Temperature Superconductor Electronics.* CRC Press, 2003.

[84] Young Jin Kim and Steven M. Clayton. Development of a SQUID-based ^{3}He co-magnetometer readout for a neutron electric dipole moment experiment. *IEEE Transactions on Applied Superconductivity*, 23, 2013.

[85] Wangzhi Zheng. *Thesis: Experiments of Search for Neutron Electric Dipole Moment and Spin-Dependant Short-Range Force.* 2012.

[86] Robin Cantor. *StarCryo Model 550 Single Channel SQUID Controller: User's Manual.*

[87] B. T. Matthias, T. H. Geballe, and V. B. Compton. Superconductivity. *Rev. Mod. Phys.*, 35:1–22, 1963.

[88] Z. Charifoulline. Residual resistivity ratio (RRR) measurements of LHC superconducting NbTi cable strands. *IEEE Transactions on Applied Superconductivity*, 16(2):1188–1191, 2006.

[89] LakeShore. *User's Manual Model 218 Temperature Monitor: Revision 2.5.* Lake Shore Cryotronics, Inc., 2017.

[90] Stanford. *Model SR760 FFT Spectrum Analyzer Manual.* Standford Research Systems, 2018.

[91] E. Korobkina, B. W. Wehring, A. I. Hawari, A. R. Young, P. R. Huffman, R. Golub, Y. Xu, and G. Palmquist. An ultracold neutron source at the NC State University PULSTAR reactor. 579(1):530–533, 2007.

[92] Daniel V. Schroeder. *An Introduction to Thermal Physics.* Addison Wesley Longman, 199.

[93] https://en.wikipedia.org/wiki/Vantablack.

[94] J. M. Lockhart and J. C. Mester. Remanent magnetization of instrument materials for low magnetic field applications. *Czechoslovak Journal of Physics*, 46:2751–2752, 1996.

[95] E.D. Marquardt, J. P. Le, and R. Radebaugh. Cryogenic material properties database. *NIST, Boulder CO*, 2000.

[96] G. L. Salinger and J. C. Wheatley. Magnetic susceptibility of materials commonly used in the construction of cryogenic apparatus. *Rev. Sci. Instrum.*, 32:872, 1961.

[97] G. Ventura. Thermal expansion and thermal conductivity of torlon at low temperatures. *Cryogenics*, 39:481–484, 1999.

[98] Austin Reid, Frederic Lechenault, Sergio Rica, and Mokhtar Adda-Bedia. Geometry and design of origami bellows with tunable response. *Phys. Rev. E*, 95:137–146, 2017.

[99] Frank Pobell. *Matter and Methods at Low Temperatures. 3rd Ed.* Springer, 2007.

[100] B. A. Hands. *Cryogenic Engineering.* Academic Press, 1986.

[101] Robin Cantor. *pcSQUID^{TM} User's Manual.* 2018.

[102] https://www.moxa.com/product/TCF-90.htm. Online; accessed 10 October 2018.

[103] https://www.vacuum-shop.com/category/2072853/iso-kf-aluminum-edged-seal.html. Online; accessed 4 December 2018.

[104] Russell J. Donnelly and Carlo F. Barenghi. The observed properties of liquid helium at the saturated vapor pressure. *Journal of Physical and Chemical Reference Data*, 27:1217, 1998.

[105] T. M. Ito, S. M. Clayton, J. Ramsey, M. Karcz, C. Y. Liu, J. C. Long, T. G. Reddy, and G. M. Seidel. Effect of an electric field on superfluid helium scintillation produced by α-particle sources. *Phys. Rev. A*, 85:042718, 2012.

[106] Huey A. Roberts and Frank L. Hereford. Luminescence of helium it produced by weak α-particle sources. *Phys. Rev. A*, 7:284–291, 1973.

[107] D. N. McKinsey, C. R. Brome, S. N. Dzhosyuk, R. Golub, K. Habicht, P. R. Huffman, E. Korobkina, S. K. Lamoreaux, C. E. H. Mattoni, A. K. Thompson, L. Yang, , and J. M. Doyle. Time dependence of liquid-helium fluorescence. *Phys. Rev. A*, 67:062716, 2003.

[108] H. Fleishman, H. Einbinder, and C. S. Wu. Scintillations from liquid helium. *Rev. Sci. Instrum.*, 32:1130–, 1959.

[109] D. N. McKinsey, C. R. Brome, J. S. Butterworth, S. N. Dzhosyuk, P. R. Huffman, C. E. H. Mattoni, J. M. Doyle, R. Golub, , and K. Habicht. Radiative decay of the metastable $He_2(a^3\Sigma_u^+)$ molecule in liquid helium. *Phys. Rev. A*, 59:200, 1999.

[110] J. A. Hornbeck and J. P. Molnar. Mass spectrometric studies of molecular ions in the noble gases. *Phys. Rev*, 84:621, 1951.

[111] H. A. Kramers. On a modification of jaffe's theory of column-ionization. *Physica*, 18:665–675, 1952.

[112] H. O. Meyer. Dark rate of a photomultiplier at cryogenic temperatures. *arXiv:0805.0771*, 2008.

[113] T. Ito. Status of the experiment to measure the e-field dependence of lhe scintillation. In *nEDM - Internal Technical Committee meeting on Feb 14*, 2018.

[114] C. Jewell and P.V.E. McClintock. A note on the purity of liquid helium-4. *CRYOGENICS*, page 682, 1979.

[115] Huey A. Roberts, William D. Lee, and Frank L. Hereford. Scintillation of liquid helium under pressure. ii. $2 > t > 0.3\ ^0k$. *Phys. Rev. A*, 4:2380–2385, 1971.

[116] S. R. Bandler, S. M. Brouër, C. Enss, R. E. Lanou, H. J. Maris, T. More, F. S. Porter, , and G. M. Seidel. Angular distribution of rotons generated by alpha particles in superfluid helium: A possible tool for low energy particle detection. *Phys. Rev. Lett.*, 74:3169–3172, 1995.

[117] Steven W. Van Sciver. *Helium Cryogenics*. International Cryogenics Monograph Series, 2012.

[118] J. K. Hoffer, W. R. Gardner, C. G. Waterfield, and N. E. Phillips. Thermodynamic properties of ^{4}he. ii. the bcc phase and the p-t and v-t phase diagrams below 2 k. *Journal of Low Temperature Physics*, 23:63–102, 1976.

[119] O. V. Lounasmaa. *Experimental Principles and Methods Below 1K*. London: Academic Press, 1974.

[120] H. J. Pain. *The Physics of Vibrations and Waves*. John Wiley & Sons, Ltd., 2005.

[121] Thomas Gentile. A whole new angle on neutron spin analysis. 2013.

[122] John R. Taylor. *An Introduction to Error Analysis*. University Science Books, 1997.

[123] Thomas Gentile, Michael Hayden, and Michael Barlow. Comparison of metastability-exchange optical pumping sources. *J. Opt. Soc. Am. B*, 20:2068–2074, 2003.

[124] Thomas Gentile, Michael Hayden, and Michael Barlow. Time-dependent spin dressing using a ^{3}He atomic beam. *Phys. Rev. A*, 85:032124, 2012.

APPENDIX A

CALCULATION OF HEAT TRANSFER BETWEEN LIQUID HELIUM AND METAL SURFACES

This appendix describes relevant mathematics for calculating the efficiency of moving heat between two mediums. This is often referred to as the Kapitza resistance [119]. The following discussion is covered in *Matter and Methods at Low Temperatures* by F. Pobell [99] but a few more mathematical details are covered here. When cooling cells to be used with enclosed liquids, heat needs to be able to dissipate from the liquid to the container and be removed from the system. We can break the phenomena down into two parts. First, inefficiencies in heat transfer are considered through their wavelike properties in section A.1. Next, inefficiency of heat transfer from acoustic losses are considered in section A.2. The product of the two shows how inefficient the transfer of heat actually is. In the case of the experiments being discussed in this thesis, helium will need to cool through the cell wall as well as through the walls of a copper volume. Considered in detail here is the heat transfer from liquid helium into a copper surface.

A.1 Snell's Law

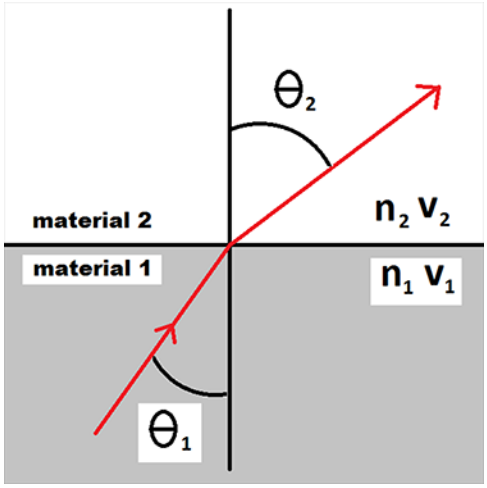


Figure A.1: *Graphic Depiction of Snell's Law. The Incident and Refracted Angles Are θ_1 and θ_2, Respectively. The Index of Refraction of Each Material Are n_1 and n_2. The Velocity of the Wave in Each Material Are v_1 and v_2.*

A useful technique for performing mathematical operations on a collection of particles is to model each particle as a three dimensional harmonic oscillator [92]. Expanding the model, we can say energy is stored in the oscillators and can be transferred to other particles.

Tracking the transfer of energy rather than the particles, results in a view similar to tracking sound or light waves, and follows Huygen's principle. In the case of thermal waves, we call the particles by the name "Phonon". A phonon obeys Bose-Einstein statistics and can be treated like any other wave.

When a wave transfers from one medium to another, its incident angle and outgoing (refracted) angle are not necessarily equal [77]. Fig. A.1 shows an incoming wave from the bottom which reaches the interface between two materials at an angle θ_1. The velocity that the wave can propagate through each material is different in this case. Here specifically, the incident and refracted wave velocities are v_1 and v_2, respectively. This change in velocity results in the direction of the wave, after passing the boundary, to be shifted slightly so that it is refracted at an angle θ_2. Snell's Law describes the relationships between the incident and refracted angles, and the wave velocities in each material.

$$\frac{Sin(\theta_1)}{Sin(\theta_2)} = \frac{v_1}{v_2} \tag{A.1}$$

We are particularly interested in the direction of the refracted angle because if $\theta_2 \geq \frac{\pi}{2}$, the phonon and thus the heat will not be transferred across the interface. Taking Eq. A.1 and solving for the transmission angle, we find

$$\theta_1 = Sin^{-1}\left(\frac{v_1}{v_2}\ Sin(\theta_2)\right) \tag{A.2}$$

When $\theta_2 \geq \frac{\pi}{2} = \theta_c$, it is called the *critical angle*. When the critical angle is reached $sin(\theta_1) = 1$. In our case, we are dealing with heat being in liquid helium and exiting to copper. It is useful to know that the velocity of sound in liquid helium and copper are $v_{He} = 240\ m/s$ and $v_{Cu} = 3995\ m/s$ because these are the velocities at which the phonons will also move. The critical angle for transmission of phonons from liquid helium to copper is

$$\begin{aligned}\theta_{c,\ He\to Cu} &= Sin^{-1}\left(\frac{v_{He}}{v_{Cu}}\right)\\ &= Sin^{-1}\left(\frac{240\ m/s}{3995\ m/s}\right)\\ &= 0.06\ rad\\ &= 3^0\end{aligned} \tag{A.3}$$

The angle θ_c must then be swept across a spherical surface to find the solid angle it subtends Ω_c and compare that to the solid angle from which phonons may approach $\Omega_{1/2} = 2\pi$. We may wish to call this region the critical cone [99]. The cross section is

$$\begin{aligned}f &= \frac{\Omega_c}{\Omega_{1/2}}\\ &= \frac{\int_0^{\theta_c} Sin(\theta)\ d\theta\ \int_0^{2\pi} d\phi}{\int_0^{\pi/2} Sin(\theta)\ d\theta\ \int_0^{2\pi} d\phi}\\ &= \frac{\frac{1}{2}\theta_c^2\ (2\pi)}{2\pi}\\ &= \frac{1}{2}\theta_c^2\\ &= \frac{1}{2}\left(\frac{v_{He}}{v_{Cu}}\right)^2\\ &\approx 1.8\times 10^{-3}\end{aligned} \tag{A.4}$$

Note that the small angle approximation $sin(x) \approx x$ has been used here.

A.2 Acoustic Impedance

Acoustic impedance is another important factor in considering the efficiency of heat to transfer out of the liquid helium [99]. Let us now use the quantum mechanical forms for wave reflection and propagation at a boundary. We can write the wavefunction in the liquid helium volume and the copper volume as follows

$$\Psi_{He}(r) = A\ e^{i\ k\ r} + B\ e^{-\ i\ k\ r}$$

$$\Psi_{Cu}(r) = C\ e^{i\ k'\ r}$$

Where Ψ_{He} and Ψ_{Cu} are the wavefunctions in the incident and reflected regions, respectively. The coefficients A, B, and C are the incident, reflected, and transmitted coefficients, respectively. The incident wave contains the entire amplitude of the wave and we can set $A = 1$. Centering the coordinate system around the boundary, such that $r = 0$ is the interface between the two mediums, we additionally have

$$\Psi_{He}(0) = \Psi_{Cu}(0) \tag{A.5}$$

Consistent with the usual quantum mechanical treatment of transmission and reflection of a wavefunction, the derivatives must also be equal.

$$\frac{Z_{He}}{k}\ \frac{\delta\Psi_{He}}{d\ r}\bigg|_{r=0} = \ \frac{Z_{Cu}}{k'}\ \frac{\delta\Psi_{Cu}}{d\ r}\bigg|_{r=0} \tag{A.6}$$

Where $Z_i = \rho_i\ v_i$ is the acoustic impedance, ρ is the density of the material, and v is the velocity of sound in the material. Into Eqs. A.5 and A.6, we can plug in boundary condition at the interface, namely at $r = 0$ to find

$$1 + B = C \tag{A.7}$$

$$\frac{Z_{He}}{k}(ik - ikB) = \frac{Z_{Cu}}{k'}ik'C \tag{A.8}$$

Solving Eq. A.8 for C and plugging it into Eq. A.7, we find the reflected wavefunction's amplitude [120]

$$B = \frac{Z_{He} - Z_{Cu}}{Z_{He} + Z_{Cu}} \tag{A.9}$$

The transmission coefficient is of more interest to us here however, as the objective of this exercise is to calculate the efficiency of transmitting phonons out of the liquid helium. From Eq. A.7, we can write

$$\begin{aligned} C &= B - 1 \\ &= \frac{-2Z_{Cu}}{Z_{He} + Z_{Cu}} \end{aligned} \tag{A.10}$$

However, this is a coefficient of a wavefunction. Squaring the coefficient gives the probability t of finding the wavefunction in a location or region [67]. Since the total probability of finding the wave on either side of the interface is 1 at all times, we see

$$\begin{aligned} t &\equiv 1 - B^2 \\ &= 1 - \left(\frac{Z_{He} - Z_{Cu}}{Z_{He} + Z_{Cu}} \right)^2 \\ &= \frac{(Z_{He} + Z_{Cu})^2 - (Z_{He} - Z_{Cu})^2}{(Z_{He} + Z_{cu})^2} \\ &= \frac{4\ Z_{He}\ Z_{Cu}}{(Z_{He} + ZCu)^2} \end{aligned} \tag{A.11}$$

To arrive at a reasonable approximation, note that $v_{Cu} \gg v_{He}$ and $\rho_{Cu} \gg \rho_{He}$. Specifically, $\rho_{He} = 0.145\ g/cm^3$ and $\rho_{Cu} = 8.98\ g/cm^3$. Which leads us to the observation that the impedance of the metal is larger than the impedance of the helium by many orders of magnitude, $Z_{Cu} \gg Z_{He}$. Hence,

$$\begin{aligned} t &\cong \frac{4Z_{He}}{Z_{Cu}} \\ &= 3.9 \times 10^{-3} \end{aligned} \tag{A.12}$$

A.3 Transmission

We can now take the products from the last two sections to find the total probability of transmission of a phonon when it arrives at the interface between a liquid helium volume and a copper wall.

$$\begin{aligned} f \cdot t &= (1.8 \times 10^{-3}) \cdot (3.9 \times 10^{-3}) \\ &\approx 10^{-5} \end{aligned} \tag{A.13}$$

APPENDIX B

SPIN EXCHANGE OPTICAL PUMPING (SEOP) CELL PRODUCTION

This appendix describes the process of manufacturing valved SEOP Rb coated cells for polarization of ^{3}He. Advise was given by and many thanks are given to B. Drieyhuys (Center for InVivo MIcroscopy at Duke Medical Center), Q. Ye (NIST), T. Gentile (NIST) and B. Saam (Univ. of Utah) for their help in guiding me to developing a workable system.

Selecting the best glass is very important to ensure optimal performance of SEOP cells. From a conversation with Prof Driehuys: In the 1990's a number of studies showed that wall relaxation of ^{3}He in glass cylinders was the largest relaxation parameter of issue at the time. It was discovered that using reblown glass spheres resolves a large part of this problem. It is expected that the Rb coating on the walls and increased uniformity in the interior glass surface decreases interaction between the (possibly) porous wall glass and the ^{3}He atoms.

The most ideal material for these cells at this time is GE180. This is a General Electric designed aluminosilicate glass which minimizes neutron absorption (not a problem for us but notable) by being boron-free and is known for its low helium permeability and resistance to alkali metals [121]. Unfortunately, it is also known for being very difficult to work with and fabrication issues are a problem even at NIST. For this reason we will be using Pyrex.

The SEOP bulbs attached to the manifold had a diameter of $\sim$2 inches and capillaries with a length of $\sim$ 7 inches. These are what is used as the polarization cells after the process is completed.

The manifold was cleaned thoroughly using the following sequence of steps

1. Flush with deionized water (x10)
2. Mix dishwashing soap with some deionized water and mix it around. Remove the foam from the top of the solution and flush the glassware with it. Rinse with fresh deionized water and repeat (x5)
3. Flush again with deionized water (x10)
4. Flush with Ethanol (x5)

The glass valves used on the open SEOP cells come with a number of different materials for the o-rings. Lightly greased Ethylene Propylene (E.P.) will be used for the seat o-ring because other materials have been found to depolarize ^{3}He more quickly [63]. The valves used were CG-975-01 from Chemglass Inc. These valves have one tip o-ring #007 and two body o-rings #009.

Fig. 2 in [63] shows the glass manifold design. The manifold was wrapped in ceramic fabric at the support locations to avoid glass to metal contact. After the manifold was hung, the cells are wrapped in heater tape, shown in Fig. B.1 . The surface should be as thoroughly covered as possible making small diameter circular heater tape desirable. If possible, an oven can also be built around the manifold. For an increased vacuum and cleanliness, the liquid nitrogen trap is of extreme importance.

The manifold has a vertical tube at one end called a *retort*. The retort is open only on the top. This is the location into which the cracked Rb ampule is placed. In some literature, it is suggested that the Rb ampule is set with a Pyrex coated magnet which is left sealed then broken once the system has sat for 2 days. We tried this type of ampule and found the breaking process arduous with no gains in T_1 of the final cell. Instead the technique used was to have N_2 continuously flowing through the manifold then break the Rb ampule in the gas flow near the mouth of the retort and place it upside down in the retort. It is also possible to use other non-reactive gases such as Ar for this task. The 1 g Rb ampule was broken in the N_2 flow, just outside of the retort and drop quickly in. The process should be completed in less than 1 sec because as soon as the Rb is exposed to air it will begin to oxidize. This process results in the loss of a small amount of Rb, as it reacts instantaneously with water vapor to become Rubidium Hydroxide mostly and other compounds of various Rb oxides. The layer is visible because it's color is slightly different than that of Rb (which should be as reflective as a mirror). RbOH forms a white solid powder. The N_2 flow was stopped as soon as the end of the retort is sealed.



Figure B.1: *Photo of Glass Manifold Wrapped in Heater Tape.*

With the Rb ampule inside and all exits sealed begin to pump the system down. We were able to pump the system down to 4.4×10^{-8} mbar overnight. While the system is pumping down, the heater tape is warmed to 400^0 C.

The next day, a short region of the heater tape was removed. The first small reservoir between the retort and the cells was baked using a methane torch for a few minutes. The torch was then used to heat the Rb ampule inside of the retort. The melting point of Rb is 39.30 ^{0}C or 102.74 ^{0}F. The melting point of Rubidium Oxide is > 500 ^{0}C. It takes a few minutes until the Rb breaks through the Rb_2O layer which builds up around the ampule. Movement of the Rb inside the ampule was noticeable before the liquid spilled out into the retort. During this stage, the torch is set to have a loose red or orange flame. It should not be the tight blue flame needed for melting the glass. The Rb will vaporize and start to coat surfaces inside the manifold which are cool enough for it to condense upon. The process of moving the Rb from the retort to the reservoir is a process of distillation and removes many impurities. Care must be taken to keep all sections of the retort hot enough to move the Rb into the reservoir. About 10-20% of the Rb may be left in the retort [63].

After the retort has been completely cleared of Rb, the system was allowed to cool for 5 - 10 min. It was allowed to cool long enough for the retort to be comfortably touched with the hand. Then the restriction is heated and supported by hand until the retort is removed. Since the pressure inside the manifold was so low, the glass easily collapses on itself.

The system was then left at 400 ^{0}C while being pumped for 1 to 5 days. It is up to the discretion of the user. Ideally, leaving it longer results in cleaner glass. We found the best results when leaving it for 5 days. The next day, the heat tape was turned off and allowed to cool. The heat tape around the next reservoir was removed and the Rb chased to that reservoir. The first reservoir was then removed. The Rb can then be chased into the first polarization cell. Enough Rb should be left in the reservoir to ensure the second cell can be filled as well. Once the first cell has a drop or two of Rb in it ($\sim$ 0.1 - 0.3 g of Rb), the cell can be removed. The Rb is then chased into the second cell and it is removed as well.

The cells were then filled, through the valve, with ultra high purity N_2 to a pressure slightly higher than one bar. With the N_2 in the cell, they were wrapped in heat tape again and heated to 200 ^{0}C. They were left overnight at this temperature.

At this point, they are ready to be evacuated, then filled with ^{3}He, and be tested. The most optimal option, was to fill them with polarized ^{3}He and use an NMR setup to test the T_1. If the $T_1 < 15\ hrs$ they will not polarize ^{3}He and the process must be repeated. If polarized ^{3}He is not available, they may be filled with un-polarized ^{3}He and one can attempt to polarize the ^{3}He in them. This may, of course, not polarize the ^{3}He and just show that their T_1 is too short.

APPENDIX C

ROOM TEMPERATURE T_1 DETAILS

C.1 Calculationn of Longitudinal Rexlation Rate

In section 3.5.2, some math was skipped in the definition of terms for Eq. 3.31. This section describes those steps in a bit more detail.

The general basis of this argument can be found in *Principles of Magnetic Resonance* by Slichter [70]. First, let us define

$$N = N_+ + N_- \tag{C.1}$$

$$n = N_+ - N_- \tag{C.2}$$

Where N is the total number of atoms and n is the difference in the number of atoms in each state. We can use these equations to write equations for the number of atoms in the anti-aligned state $N_+ = \frac{1}{2}(N + n)$ and the number of atoms in the aligned state $N_- = \frac{1}{2}(N - n)$.

We wish to develop a characterization for how quickly the transitions between the states occur dn/dt and eventually how quickly they stabilize. Taking the derivative, we find

$$\frac{dn}{dt} = \frac{dN_+}{dt} - \frac{dN_-}{dt} \tag{C.3}$$

The derivative of the number of atoms in the aligned state is giving in Eq. 3.30. That equation is repeated below with the complimentary equation for the derivative of the number of atoms in the anti-aligned state.

$$\frac{dN_+}{dt} = N_- W \uparrow - N_+ W \downarrow \tag{C.4}$$

$$\frac{dN_-}{dt} = N_+ W \downarrow - N_- W \uparrow \tag{C.5}$$

Now returning to Eq. C.3 and substituting Eqs. C.4 and C.5 into it, we have

$$\frac{dn}{dt} = \frac{dN_+}{dt} - \frac{dN_-}{dt} \tag{C.6}$$

$$= (N_- W \uparrow - N_+ W \downarrow) - (N_+ W \downarrow - N_- W \uparrow) \tag{C.7}$$

$$= 2\ (N_- W \uparrow - N_+ W \downarrow) \tag{C.8}$$

Plugging in the definitions for N_+ and N_-

$$\frac{dn}{dt} = 2\ \left[\frac{1}{2}(N-n)W \uparrow - \frac{1}{2}(N+n)W \downarrow)\right] \tag{C.9}$$

$$= (N-n)\ W \uparrow - (N+n)\ W \downarrow \tag{C.10}$$

$$= N\ (W \uparrow - W \downarrow) - n\ (W \uparrow + W \downarrow) \tag{C.11}$$

$$= (W \uparrow + W \downarrow)\ \left[N\ \left(\frac{W \uparrow - W \downarrow}{W \uparrow + W \downarrow}\right) - n\right] \tag{C.12}$$

Eq. C.12, was manipulated intentionally to lead the reader to see two definable terms. They are

$$n_0 = N\ \left(\frac{W \uparrow - W \downarrow}{W \uparrow + W \downarrow}\right) \tag{C.13}$$

$$\frac{1}{T_1} = W \uparrow + W \downarrow \tag{C.14}$$

Where n_0 is the population difference at thermal equilibrium and T_1 is the characteristic time constant for approach the equilibrium state. This allows us to conveniently write Eq. C.12 (also written as Eq. 3.31),

$$\frac{dn}{dt} = \frac{n_0 - n}{T_1} \tag{C.15}$$

C.2 Table of Room Temperature Results

Table C.1: *Measured T_1 Values for Measurement Cell at Room Temperature As Reported in Section 3.5.3.*

Measurement Number	Data Set Number	T1 ± Stdev (sec)	Cell Pressure (mbar)
1	101_02	461.59 ± 85.57	1130
2	102_01	404.54 ± 55.08	1040
3	104_01	452.35 ± 66.26	1200
4	105_01	307.10 ± 77.67	1100
mean		407.48 ± 34.11	

C.3 Tip Angle and T_1 Data Analysis

This section outlines how data analysis was handled for the room temperature data reported in section 3.5.2. The mathematics of this section is primarily gathered from John Taylor's *An Introduction to Error Analysis* [122].

Given a set of measured values $(x_0, x_1, \ldots x_n)$, the arithmetic mean of the set can be calculated by

$$\bar{x} = \frac{1}{N}\sum_{i=1}^{N} x_i \tag{C.16}$$

where N is the number of values in the set and x_i is a member of the set.

The standard deviation of the mean can be calculated by

$$\sigma = \sqrt{\frac{1}{N}\sum_{i=1}^{N}(x_i - \bar{x})^2} \tag{C.17}$$

The technique of using the weighted mean was employed to increase the accuracy of the reported values. The purpose of the weighted mean is to honor the spirit of the arithmetic mean, except each point does not contribute equally to the final mean or standard deviation. Data points with smaller standard deviation are allowed to influence the final mean and

final standard deviation more. While the influence of data points with larger standard deviation are heavily suppressed in their ability to influence the final values. A back of the envelope validation of this technique is in that if the data points have equal weights (same standard deviation) then the arithmetic mean is reclaimed.

The weight for each particular value is defined as

$$w_k = \frac{1}{\sigma_k^2} \tag{C.18}$$

The mean of the set is then calculated as

$$\bar{x} = \frac{\sum_{k=1}^{N} w_k \; x_k}{\sum_{k=1}^{N} w_k} \tag{C.19}$$

As commonly used, the variance of a standard deviation is σ^2. The variance of the weighted mean is

$$\sigma^2 = \frac{1}{\sum_{k=1}^{N} \sigma_k^{-2}} \tag{C.20}$$

When the weighted mean is applied to experimental data, there is often some error in the variance of each individual data point. It is common for the variance to be under estimated as it is difficult to take into account all possible sources of error. To handle this situation the variance is replaced by

$$\sigma^2 \to \sigma^2 \; \chi_\nu^2 \tag{C.21}$$

where χ_ν^2 is χ^2 divided by the number of degrees of freedom (dof). The dof is this case is $N - 1$. The weighted variance is then

$$\sigma^2 = \frac{1}{\sum_{k=1}^{N} \sigma_k^{-2}} \times \frac{1}{N-1} \sum_{i=1}^{N} \frac{(x_i - \bar{x})^2}{\sigma_i^2} \tag{C.22}$$

The benefit then is that values with larger standard deviation are given less influence over the final reported value.

C.4 Tipping Angle and T1 Measurement Code

The following C++ code takes the TNMR output and can be set to calculate the tipping angle or T1 from a complete dataset. Lines 1 to 81 are basic file setup and simple math functions. Lines 83 to 413 deal with processing arrays of data once they are taken from the source files and placed into arrays in the RAM. Lines 415 to 516 control interactions between the highest level functions and the previous lines. Lines 518 to 646 calculate the T_1 or the tipping angle for a set of data, this is perhaps the highest level mathematical operation in the code. Lines 648 to 796 interact with the command .txt file, and checks for the appropriate file structure for data output and creates it if it is not found. Lines 798 to 831 are the Main() function and controls the user interface.

```
1  #include <iostream>
   #include <fstream>
   #include <iomanip>
   #include <stdio.h>
   #include <string.h>
6  #include <vector>
   #include <cstdlib>
   #include <sys/stat.h>
   #include <math.h>
   #include <direct.h>
11 #include <windows.h>
   #include <string>
   using namespace std;

   #define PI 3.14159265
16
   ////////////////////////////////////////
   // created by: Adam Dipert            //
   // started: Mar 23, 2015              //
   // for Geometric Phase Simluation     //
21 // to calculate the                   //
   // tipping angle                      //
   // and T1                             //
   // of 3He atoms during use of TNMR    //
   ////////////////////////////////////////
26 //NOTE: Put read file name in CommandFile.txt


   bool fileExists(const std::string& filename)
   {
31     struct stat buf;
       if (stat(filename.c_str(), &buf) != -1)
       {
           return true;
       }
36     return false;
   }

   bool dirExists(const std::string& dirName_in)
```

```
    {
41      // check if a directory exists by the given name
        DWORD ftyp = GetFileAttributesA(dirName_in.c_str());
        if (ftyp == INVALID_FILE_ATTRIBUTES)
            return false;  //something is wrong with your path!

46      if (ftyp & FILE_ATTRIBUTE_DIRECTORY)
            return true;   // this is a directory!

      return false;    // this is not a directory!
    }
51
    double nthroot(double number, int root)
    {
        // calculate the nth root of the input double
         double result = pow(number,1.0/root);
56       return result;
    }

    int rms_stdev(std::vector<double> data, double (&rms), double (&stdev))
    {
61      // calculate the standard deviation rms of the input array
         vector<double>::size_type data_size; data_size = data.size();
        cout<<"\nIN RMS_STDEV\n-----------------------------------"<<"\n\ndata
            size = "<<data_size;

         for(int i = 0; i < data_size; i++)
66       {
             rms = rms + data.at(i)*data.at(i);
           cout<<"\nrms "<<sqrt(rms)<<" data "<<data.at(i);
         }

71       rms = nthroot( rms / data_size , 2 );

         for(int i = 0; i < data_size; i++)
         {
             stdev = stdev + (data.at(i) - rms)*(data.at(i) - rms);
76       }

        stdev = nthroot( stdev / (data_size - 1) , 2);

        return 0;
81  }

    int populate_vector (char *filename, std::vector<double> (&real_vector),
         std::vector<double> (&Img_vector), std::vector<double> (&Freq_vector),
         int (&Points_1D), double (&swing), int (&TNMR_2D_num))
        //reads first data set
    {
86      // populates a vector array with data values and returns
         double real, Img, Freq;
         char holder[80];
         Points_1D = 0;

91       ifstream data_file (filename); //Open actual data file

        if(data_file.is_open())
         {
             cout<<"\n\n Data File is OPEN \n\n";
96           char key[] = "Ending", chHz[] = "Hz";

             do { //decide if data file has 2D_Points = 1 or not
```

```
            data_file>>holder;
        } while (strcmp(key,holder) != 0); //search for word "Ending" in
            TNMR File

        //collect 1D_Points
        data_file>>holder; data_file>>Points_1D;

        //checks for data files with only one data set
        for(int i=1; i<=3; i++)
        {
         data_file>>holder;
            if(strcmp(holder,chHz) == 0){TNMR_2D_num = 1;}
        }

        //if data file has more than one data set, this if-statement finds
            the number of 2D points
        if(TNMR_2D_num != 1)// if 2D_Points != 1, then find number of 2
            D_Points
        {
            for(int i=1; i<=3; i++){data_file>>holder;}
            data_file>>TNMR_2D_num;
            for(int i=1; i<=3; i++){data_file>>holder;}
        }

        //Collect Data Points in Vector
        data_file>>real; data_file>>Img; data_file>>swing;
        real_vector.push_back(real); Img_vector.push_back(Img); Freq_vector
            .push_back(swing);
        for(int i = 1; i<=Points_1D-1; i++)
        {
            data_file>>real; data_file>>Img; data_file>>Freq;
            real_vector.push_back(real); Img_vector.push_back(Img);
                Freq_vector.push_back(Freq);
        }

      data_file.close();
    }
    else{cout<<"\n\n DATA FILE IS NOT OPEN\n\n";cin>>holder;cin.ignore();
        cout<<"\n";}

  return 0;
}

int average_noise(std::vector<double> real_vector_noise, double (&
    real_noise_average) )
{
    //averages noise over central 150 values
    int averaging_size = 150;  //change this value if you would like to use
        a larger size
    real_noise_average = 0.0;
    vector<double>::size_type real_vector_size;
    real_vector_size = real_vector_noise.size();

  for(int i = (real_vector_size/2 - averaging_size/2); i< (
      real_vector_size/2 + averaging_size/2); i++ )
    {
        real_noise_average = real_noise_average + real_vector_noise.at(i);
    }
    real_noise_average = real_noise_average / averaging_size;

  return 0;
}
```

```
int subtract_noise(std::vector<double> (&signal_vector), std::vector<double
    > signal_vector_noise, int Points_1D)
{
   // subtracts noise from vector array of data
156     double signal_noise_average;
        average_noise(signal_vector_noise,signal_noise_average);

   for(int i = 0; i<Points_1D; i++)
    {
161         signal_vector.at(i) = signal_vector.at(i) - signal_vector_noise.at(
                i);
    }

   cout<<"++++++++++ subtract vectors ran ++++++++++++\n";

166    return 0;
}

int Average_data (char *filename, char *average_filename, std::vector<
    double> (&real_vector), std::vector<double> (&Img_vector), std::vector<
    double> (&Freq_vector), int Points_1D, int averaging_num, double swing,
     double frequency, std::vector<double> (&realVectorAve),std::vector<
    double> (&ImgVectorAve),std::vector<double> (&FreqVectorAve))
{
171     // to use this function you must have already populated the vectors
            with the valyes you would like to average
        double real = 0.0, Img = 0.0, Freq = 0.0;
        int i_iterator = 0;
        char holder;

176     for(int i = 0; i<= Points_1D-1; i++)
        {
            real=real+real_vector.at(i); Img=Img+Img_vector.at(i);
            if((i+1)%averaging_num == 0)
            {
181             realVectorAve.push_back(real/averaging_num); real = 0;
                ImgVectorAve.push_back(Img/averaging_num); Img = 0;
                FreqVectorAve.push_back(swing-2*swing/Points_1D*(averaging_num
                    /2+averaging_num*i_iterator)); Freq = 0;
                i_iterator++;
            }
186     }

        strcpy( average_filename, filename);
        average_filename[strlen(average_filename)-4] = '\0';
       cout<<"\n\n +-+-+-+ average_filename "<<average_filename;
191     strcat(average_filename, "_AVE.txt");

        ofstream Write_Ave_File (average_filename);
        if(Write_Ave_File.is_open())
        {
196         cout<<"\n\n *** WRITE FILE IS OPEN *** \n\n";
            Write_Ave_File<<"Freq: "<<frequency<<" bin_size: "<<averaging_num<<
                " number_of_entries: "<<i_iterator<<"\nReal Img Hz\n";
            for(int i = 0; i<= i_iterator-1; i++)
            {
                Write_Ave_File<<realVectorAve.at(i)<<" "<< ImgVectorAve.at(i)<<
                    " "<<FreqVectorAve.at(i)<<"\n";
201         }
            Write_Ave_File.close();
        }
```

```
        else{cout<<"\n\nWRITE AVE FILE IS NOT OPEN\n\n";cin>>holder;cin.ignore
            ();cout<<"\n";}
        Write_Ave_File.close();
206     return 0;
    }

    int find_max_and_FDHM(char *filename, int (&maximum_real_freq_index),double
         Partial_Max_Percentage, int (&FWHM_index_low), int (&FWHM_index_high),
         int Points_1D, std::vector<double> realVectorAve,std::vector<double>
        ImgVectorAve,std::vector<double> FreqVectorAve, int scan_range_start)
    {
211     // find the maximum value in the vector array and calculate the full
            width at half max (FWHM)
        int j = 0, k, frequency, Img1, Img2, real1, real2, Switch=0;

        //scans to frequency = 100; finds index "j"
        do{
216         j++;
            frequency = FreqVectorAve.at(j);
        }while(frequency>scan_range_start);

        //find index of imaginary zero crossing near origin
221     k = j;
        //looks at img averaged vector and scans until it equals zero.  Finds
            index 'j'.  This is the maximum real index also.
        do{
            Img1 = ImgVectorAve.at(k);
            k++;
226         Img2 = ImgVectorAve.at(k);
            if((Img1<=0) && (Img2>0)){cout<<"\n pos to neg crossing at "<<
                FreqVectorAve.at(k)<<"\n"; Switch = 1;}
            if((Img1>=0) && (Img2<0)){cout<<"\n neg to pos crossing at "<<
                FreqVectorAve.at(k)<<"\n"; Switch = 1;}
        }while(Switch == 0);

231     maximum_real_freq_index = k;
        int Real_Max = realVectorAve.at(k), Real_Max_Partial = Real_Max*
            Partial_Max_Percentage;
        j = k; //'j' set to real maximum index
        cout<<"\n\nAveraged Freq Max Index is "<<k<<"\nAveraged Img is Zero at
            Freq "<<FreqVectorAve.at(k)
            <<"\nReal Vector Max is "<<realVectorAve.at(k)
236         <<"\nreal max partial is "<<Real_Max_Partial;

        Switch=0;

        // find low end of signal to integrate
241     do{
            real1 = realVectorAve.at(k) - Real_Max_Partial;
            k++;
            real2 = realVectorAve.at(k) - Real_Max_Partial;
          //cout<<"\n\(k, real1, real2\) = \("<<k<<", "<<real1<<", "<<real2
              <<"\)";
246         if( real1 == 0 ){real1 == 1;}
            if( real2 == 0 ){real2 = real2 - 1 ;}
            if( (real1<=0) && (real2>=0)){cout<<"\n(1) partial max is at freq "
                <<FreqVectorAve.at(k)<<"\n"; Switch = 1;}
            if( (real1>=0) && (real2<0)){cout<<"\n(2) partial max is at freq "
                <<FreqVectorAve.at(k)<<"\n"; Switch = 1;}
        }while(Switch == 0);
251
        FWHM_index_low = k;  Switch = 0;
```

```
        cout<<"\n\nAverage FDHM index low is "<<k<<"\nAverage FDHM low Freq
            Value is "<<FreqVectorAve.at(k)
           <<"\nReal FDHM value is "<<realVectorAve.at(k);

256      // find high end of signal to integrate
         do{
             real1 = realVectorAve.at(j) - Real_Max_Partial;
             j--;
             real2 = realVectorAve.at(j) - Real_Max_Partial;
261
             if( real1 == 0 ){real1 = real1 - 1;}
             if( real2 == 0 ){real2 == 1;}
             if( (real1 <=0) && (real2 >0)){cout<<"\n(1) partial max is at freq "
                <<FreqVectorAve.at(j)<<"\n"; Switch = 1;}
             if( (real1 >=0) && (real2 <0)){cout<<"\n(2) partial max is at freq "
                <<FreqVectorAve.at(j)<<"\n"; Switch = 1;}
266      }while(Switch == 0);
         FWHM_index_high = j;

        cout<<"\n\nAverage FDHM index high is "<<j<<"\nAverage FDHM high Freq
            Value is "<<FreqVectorAve.at(j)<<"\nReal FDHM value is "<<
            realVectorAve.at(j);

271      return 0;
    }

    int analyze_noise_find_max_FDHM(char *read_file_name, char *noise_file_name
        , int (&Points_1D), double (&swing), int averaging_num, double
        frequency, int (&FWHM_index_low), int (&FWHM_index_high), int (&
        maximum_real_freq_index), int (&real_sum),double Partial_Max_Percentage
        , int (&TNMR_2D_num), std::vector<double> (&realVectorNoise),std::
        vector<double> (&ImgVectorNoise), std::vector<double> (&FreqVectorNoise
        ), int scan_range_start)
    {
276     // analyze the noise in relation to FWHM
         int empty_2D;
         std::vector<double> realVector, ImgVector, FreqVector,
                             realVectorAve, ImgVectorAve, FreqVectorAve;
         char average_file_name[80];
281
         populate_vector(read_file_name,realVector,ImgVector,FreqVector,
             Points_1D,swing,TNMR_2D_num);
        cout<<"\n\n1D data points "<<Points_1D<<"\n\n";

        populate_vector(noise_file_name,realVectorNoise,ImgVectorNoise,
            FreqVectorNoise,Points_1D,swing,empty_2D);
286      subtract_noise(realVector,realVectorNoise,Points_1D);

         Average_data(read_file_name,average_file_name,realVector,ImgVector,
             FreqVector,Points_1D,averaging_num,swing,frequency, realVectorAve,
             ImgVectorAve,FreqVectorAve);
         find_max_and_FDHM(average_file_name,maximum_real_freq_index,
             Partial_Max_Percentage,FWHM_index_low,FWHM_index_high,Points_1D,
             realVectorAve,ImgVectorAve,FreqVectorAve,scan_range_start);

291     //adjust from averaged indices to actual indices
         FWHM_index_low = (FWHM_index_low) * averaging_num + averaging_num/2;
         FWHM_index_high = (FWHM_index_high) * averaging_num + averaging_num/2;
         maximum_real_freq_index = (maximum_real_freq_index) * averaging_num +
             averaging_num/2;

296      return 0;
```

```
}

int integrate_signal_in_partial_region(std::vector<double> (&
    signal_strength), std::vector<double> realVector, std::vector<double>
    ImgVector, std::vector<double> FreqVector, int FWHM_index_range, int
    Points_2D_index)
{
   // integrate signal within user defined partial maximum, may be FWHM if
       user defines 0.5
    double real_double_sum = 0.0;

    for(int i=1; i<(FWHM_index_range) ; i++)
    {
        real_double_sum = real_double_sum + realVector.at(i+
            FWHM_index_range*Points_2D_index)*(FreqVector.at(i-1+
            FWHM_index_range*Points_2D_index)-FreqVector.at(i+
            FWHM_index_range*Points_2D_index));
    }
    signal_strength.push_back(real_double_sum);

    return 0;
}

int Tipping_Angle(char *read_file_name, double Partial_Max_Percentage, std
    ::vector<double> signal_strength, int F1_Amp, int larger_than_90)
{
   // calculate the tipping angle and return value
    char record_angles_file_name[] = "record\\RECORD_DATA.txt";

   ofstream record_angles_file (record_angles_file_name, ios::app);
    if (record_angles_file.is_open())
    {
        cout<<"\n\nRECORD DATA FILE IS OPEN\n\n";
        vector<double>::size_type signal_strength_size;
            signal_strength_size = signal_strength.size();
        if(signal_strength_size > 1)
        {
         cout<<"\n -- in if --"
            <<"\nsignal strength size = "<<signal_strength_size;
            record_angles_file<<"\n"<<read_file_name<<" "<<
                Partial_Max_Percentage<<" "<<F1_Amp<<" ";
            std::vector<double> angle;
            double standard_deviation = 0.0 , rms = 0.0 ;

            for(int i = 1; i < signal_strength_size; i++)
            {
            cout<<"\nsignal strength\("<<i<<"\) "<<signal_strength.at(i);

            if(larger_than_90 == 0)
                {
                    angle.push_back( acos( nthroot( ( signal_strength.at(i)
                        / signal_strength.at(0) ) , i ) ) * 180.0 / PI);
                }

                if(larger_than_90 == 1)
                {
                    angle.push_back( 180.0 - acos( nthroot( (
                        signal_strength.at(i) / signal_strength.at(0) ) , i
                        ) ) * 180.0 / PI);
                }

            cout<<"\nangle\("<<i-1<<"\) = "<<angle.at(i-1);
```

```
346                 }

                cout<<"\nNEXT";
                    rms_stdev(angle,rms,standard_deviation);
                cout<<"\nrms "<<rms<<"\nstdev "<<standard_deviation;
351
                for(int i = 1; i < signal_strength_size; i++)
                    {
                        record_angles_file<<angle.at(i-1)<<" ";
                    }
356                 record_angles_file<<" "<<rms<<" "<<standard_deviation;
               }
               record_angles_file.close();
        }
        else{cout<<"\n\n ------- RECORD ANGLE FILE IS NOT OPEN ------- \n\n";}
361
        return 0;
    }

    int integrated_vectors_write_file(char *signal_strength_name, char *
        checking_vectors_original)
366 {
       // write integrated values to log file
        int number_of_lines, k = 0;
        char signal_strength_record[100];
        std::vector<double> holder_vector;
371     double holder;

        strcpy(signal_strength_record,signal_strength_name);
        signal_strength_record[strlen(signal_strength_record)-4] = '\0';
        strcat(signal_strength_record, "_integrated_values.txt");
376
        ifstream checking_vectors (checking_vectors_original);
        if( checking_vectors.is_open())
        {
            checking_vectors>>number_of_lines;
381
            while( !checking_vectors.eof() )
            {
                checking_vectors>>holder;
                holder_vector.push_back(holder);
386             k++;
            }
            checking_vectors.close();
        }
        else{cout<<"\n\n------------------------CHECKING VECTORS FILE CANNOT BE
            READ--------------------\n\n";}
391
        ofstream record_integrated_signal (signal_strength_record);
        if ( record_integrated_signal.is_open() )
        {
             for(int i = 0; i<3*(number_of_lines-1); i++)
396         {
                record_integrated_signal<<holder_vector.at(i)<<" "<<
                    holder_vector.at(i+1)<<" "<<holder_vector.at(i+2);

                for(int j = 1; j<=(k/number_of_lines/3); j++)
                {
401                 record_integrated_signal<<" "<<holder_vector.at((3*j)*(
                        number_of_lines-1)+i+1)<<" "<<holder_vector.at((3*j)*(
                        number_of_lines-1)+i+2);
                }
```

```
                record_integrated_signal<<"\n";
                i++; i++;
406         }
            record_integrated_signal.close();
        }
        else{cout<<"\n\n----------------------------Record Signal File is NOT OPEN
            ----------------------";}

411
        return 0;
    }

    int analyze_dataset_2D(char *read_file_name, char *signal_strength_name,
        std::vector<double> (&signal_strength), int FWHM_index_low, int
        FWHM_index_high, int maximum_real_freq_index, int real_sum, double
        Partial_Max_Percentage, int Points_2D, double frequency, int Points_1D,
         std::vector<double> realVectorNoise, std::vector<double>
        ImgVectorNoise, std::vector<double> FreqVectorNoise, int F1_Amp, int (&
        larger_than_90))
416 {
       // analyze data set across multiple measurements in same file
        char holder[200];
        double real, Img, Freq, realNoiseAve, ImgNoiseAve;
        std::vector<double> realVector, ImgVector, FreqVector;
421
        average_noise(realVectorNoise,realNoiseAve);
        average_noise(ImgVectorNoise,ImgNoiseAve);
        vector<double>::size_type real_vector_size;
        vector<double>::size_type Img_vector_size;
426     vector<double>::size_type Freq_vector_size;

       std::vector<double> Checking_Vectors; //temp file for holding data for
           specific vectors integrated
       vector<double>::size_type Checking_Vectors_Size;

431     ifstream read_file (read_file_name);
        if(read_file.is_open())
        {
            cout<<"\n\n read file in analyze dataset 2D is OPEN \n\n";
            for(int i=0; i<4; i++){read_file.getline(holder,200);}
436
            //RUN ANALYSIS OF DATA
            for(int i = 0; i<Points_2D; i++)
            {
                for(int j = 0; j<Points_1D; j++)
441             {
                    read_file>>real; read_file>>Img; read_file>>Freq;
                    if( (j>FWHM_index_high) && (j<FWHM_index_low) )
                    {
                        if(real>0)
446                     {
                            realVector.push_back(real-realNoiseAve);
                            ImgVector.push_back(Img-ImgNoiseAve);
                            Checking_Vectors.push_back(real-realNoiseAve);
                            Checking_Vectors.push_back(Img-ImgNoiseAve);
451                     }
                        if(real<0)
                        {
                            realVector.push_back(-real+realNoiseAve);
                            ImgVector.push_back(-Img+ImgNoiseAve);
456                         Checking_Vectors.push_back(-real+realNoiseAve);
```

```
                        Checking_Vectors.push_back(-Img+ImgNoiseAve);
                        larger_than_90 = 1;
                    }
                    FreqVector.push_back(Freq);
461                 Checking_Vectors.push_back(Freq);
                }
            }
        real_vector_size = realVector.size(); Img_vector_size = ImgVector.
            size(); Freq_vector_size = FreqVector.size();
        Checking_Vectors_Size = Checking_Vectors.size();
466     cout<<"\n\n++++++++++++++++++++++++++++++++++++++++++++++++\n"
            <<real_vector_size<<" "<<Img_vector_size<<" "<<Freq_vector_size
                <<"\n";
        }
        read_file.close();
    }
471 else{cout<<"\n\n read file in analyze dataset 2D is NOT OPEN \n\n";}

    cout<<"\nChecking Vector Size = "<<Checking_Vectors_Size;
    char checking_vectors_filename[] = "record\\Checking_Vectors.txt";
    ofstream checking_file (checking_vectors_filename);
476 if(checking_file.is_open())
    {
        checking_file<<FWHM_index_low-FWHM_index_high<<"\n";
        for(int k = 1; k <= Checking_Vectors_Size; k++)
        {
481         checking_file<<Checking_Vectors.at(k-1)<<" ";
            if( k%3 == 0){checking_file<<"\n";}
        }
        checking_file.close();
    }
486 else{cout<<"\n\n----------------------CHECKING VECTORS FILE IS NOT OPEN
        ----------\n";}

    int Points_1D_size = real_vector_size/Points_2D;
    cout<<"\nPoints_1D_size "<<Points_1D_size;
    for(int Points_2D_index = 0; Points_2D_index<Points_2D; Points_2D_index
        ++)
491 {
        integrate_signal_in_partial_region(signal_strength,realVector,
            ImgVector,FreqVector, real_vector_size/Points_2D,
            Points_2D_index);
    }

    bool check_file = fileExists(signal_strength_name);
496
    ofstream write_file_signal_strength (signal_strength_name, ios::app);
    if(write_file_signal_strength.is_open())
    {
        cout<<"\n++++++++ Signal record file is open ++++++++++ \n";
501     for(int i = 0; i < Points_2D; i++)
        {
            if(!check_file){write_file_signal_strength<<"file frequency
                max_integral_frequency min_integral_frequency
                max_real_intensity min_real_intensity partial_max Point_2D
                integral";}
            check_file = 'true';
            write_file_signal_strength<<"\n"<<read_file_name<<" "<<
                frequency<<" "<<FreqVector.at(0)<<" "<<FreqVector.at(
                FWHM_index_low-FWHM_index_high)<<" "<<realVector.at(0)<<" "
                <<realVector.at(FWHM_index_low-FWHM_index_high)<<" "<<
                Partial_Max_Percentage<<" "<<i+1<<" "<<signal_strength.at(i
```

```
                    );
506             }
                write_file_signal_strength.close();
        }
        else{cout<<"\n---------- Signal Strength Write File is NOT OPEN
            ---------- \n";}

511     //compose checking_vectors.txt file into easy spreadsheet readable
            format

        integrated_vectors_write_file(signal_strength_name,
            checking_vectors_filename);

        return 0;
516 }

    int T1_measurement(int F1_Amp, int t_between_num, char *t_between_unit, std
        ::vector<double> signal_strength, char *read_file_name)
    {
       // calculate T1 from measurement
521
        char holder_char[80], angle_char[80], next_line[] = "\n";
        int read_F1_Amp, stop = 1;    double angle, stdev;
        std::vector<double> relaxation_time_vector;
        vector<double>::size_type signal_strength_vector_size;
            signal_strength_vector_size = signal_strength.size();
526
        //read tip angle from file
        ifstream read_angle_file ("record\\record_data_official_angle.txt");
        if(read_angle_file.is_open())
        {
531         cout<<"\n\n ++++ T1 read angle file open ++++";
            if(t_between_unit[0] == 'm'){t_between_num = t_between_num * 60;}
          cout<<"\n\nnumber of seconds "<<t_between_num;

            read_angle_file>>holder_char>>holder_char>>holder_char;
536
            do
            {
                read_angle_file>>read_F1_Amp>>angle>>stdev;
             cout<<"\nread F1Amp, angle, stdev = "<<", "<<read_F1_Amp<<", "<<
                 angle<<", "<<stdev;
541         }while( read_F1_Amp != F1_Amp );


          cout<<"\nF1 Amp: "<<F1_Amp<<"\nangle: "<<angle<<"\nstdev: "<<stdev<<"
              \n";

546         for(int i = 0; i < signal_strength_vector_size - 1; i++)
            {
                relaxation_time_vector.push_back( (i+1) * t_between_num / log(
                    signal_strength.at(0) * pow( cos(angle * PI / 180), i+1) /
                    signal_strength.at(i+1) )  );
             cout<<"\ni = "<<i
                <<"\nsignal strength at 0: "<<signal_strength.at(0)
551             <<"\nsignal strength at point: "<<signal_strength.at(i+1)
                <<"\nCos to the n: "<<pow( cos(angle * PI / 180), i+1)
                <<"\nLog: "<<log(signal_strength.at(0) * pow( cos(angle * PI /
                    180), i+1) / signal_strength.at(i+1) )
                <<"\nrelaxation time: "<<relaxation_time_vector.at(i)<<"\n";
            }
556         read_angle_file.close();
```

```
        }
        else{cout<<"\n\n ---- T1 read file is NOT OPEN ----";}

        ofstream write_angle_file ("record\\record_data_T1.txt", ios::app);
561     if(write_angle_file.is_open())
        {
            double rms, standard_dev;
            write_angle_file<<"\n"<<read_file_name<<" "<<angle<<" "<<stdev<<" "
                ;
            for(int i = 0; i < (signal_strength_vector_size - 1); i++)
566         {
                write_angle_file<<relaxation_time_vector.at(i)<<" ";
            }
            rms_stdev(relaxation_time_vector,rms,standard_dev);
            write_angle_file<<rms<<" "<<standard_dev;
571
            write_angle_file.close();
        }
        else{cout<<"\n\n ---- write angle file is NOT OPEN ----";}

576     return 0;
    }


    int Analysis(int selection)
581 {
        // perform general analysis based on user preference

        char read_file_name[80], data_file_name[80], noise_file_name[80],
            signal_strength_name[80], choice[1], t_between_unit[1];
        //read_file_name is the full name (with extension) and location of the
            file
586     //data_file_name is the 6 digit code specificying the run number
        int TNMR_2D_num = 0, averaging_num = 1, Points_1D = 1,
            maximum_real_freq_index, FWHM_index_low, FWHM_index_high, real_sum =
             0, Points_2D_index = 0, scan_range_start = 0, choiceNUM = 0, F1_Amp
            , t_between_num, larger_than_90 = 0;
        //number of 2D points in TNMR, number of values averaged for final
            output, SW +/- in TNMR
        double Partial_Max_Percentage, frequency, swing = 0.0;
        std::vector<double> realVectorNoise, ImgVectorNoise, FreqVectorNoise,
            signal_strength;
591
        if (selection == 1)
        {
           cout << "\n\nWould you like to calculate for a range of partial
               maximums?\nN or Y\n";
           cin >> choice; cin.ignore();
596        char choiceNO[] = "N";
           if (strcmp(choice, choiceNO)) { choiceNUM = 7; }//runs for multiple
               integration values
           else { choiceNUM = 2; }//runs one integration value
        }
        else { choiceNUM = 2; }//runs one integration value
601
        read_command_file(read_file_name, noise_file_name, signal_strength_name,
             averaging_num, scan_range_start, Partial_Max_Percentage);
        strcpy(data_file_name, read_file_name);
        read_record_txt(data_file_name, frequency, t_between_unit, F1_Amp,
            t_between_num);

606     int first_time = 1, number_of_points_to_analyze = 1;;
```

```
    do {
        analyze_noise_find_max_FDHM(read_file_name, noise_file_name,
            Points_1D, swing, averaging_num, frequency, FWHM_index_low,
            FWHM_index_high, maximum_real_freq_index, real_sum,
            Partial_Max_Percentage, TNMR_2D_num, realVectorNoise,
            ImgVectorNoise, FreqVectorNoise, scan_range_start);
        cout << "\n\nFWHM_index_high " << FWHM_index_high
611         << "\nmax real index " << maximum_real_freq_index
            << "\nFWHM_index_low " << FWHM_index_low
            << "\n2D Points " << TNMR_2D_num;

        int leave_loop = 0;
616     if (first_time == 1)
        {
            do {
                cout << "\n\nThe file has " << TNMR_2D_num - 1 << " data points
                     for analysis."
                    << "\nWould you like to run all points?"
621                 << "\nif yes, enter 1"
                    << "\nif no, enter the number of values you would like to
                        analyze:\n";
                cin >> number_of_points_to_analyze;
                cin.ignore();

626             if (number_of_points_to_analyze > TNMR_2D_num) { cout << "\n\
                    nWARNING: You must enter a number less than or equal to "
                    << TNMR_2D_num - 1; }
                if (number_of_points_to_analyze <= TNMR_2D_num) { leave_loop =
                    1; }
            } while (leave_loop == 0);
        }
        if (number_of_points_to_analyze != 1) { TNMR_2D_num =
            number_of_points_to_analyze + 1; }
631     first_time++;

        analyze_dataset_2D(read_file_name, signal_strength_name,
            signal_strength, FWHM_index_low, FWHM_index_high,
            maximum_real_freq_index, real_sum, Partial_Max_Percentage,
            TNMR_2D_num, frequency, Points_1D, realVectorNoise,
            ImgVectorNoise, FreqVectorNoise, F1_Amp, larger_than_90);
        if (selection == 1)
        {
636         Tipping_Angle(read_file_name, Partial_Max_Percentage,
                signal_strength, F1_Amp, larger_than_90);
            signal_strength.clear();
        }
        Partial_Max_Percentage = Partial_Max_Percentage + 0.1;
        choiceNUM--;
641 } while (choiceNUM > 1);

    if (selection == 2) { T1_measurement(F1_Amp, t_between_num,
        t_between_unit, signal_strength, read_file_name); }

    return 0;
646 }

int read_command_file(char *read_file_name, char * noise_file_name, char *
    signal_strength_name, int (&averaging_num), int (&scan_range_start),
    double (&Partial_Max_Percentage))
{
    // read command file
```

```
651
        char holder[80];

       ifstream Command_File ("CommandFile.txt");
        //Read in parameters
656     if(Command_File.is_open())
        {
            cout<<"\n\nCommand file is OPEN\n\n";

            Command_File>>read_file_name;Command_File>>read_file_name;
661         Command_File>>noise_file_name;Command_File>>noise_file_name;
            Command_File>>holder;Command_File>>signal_strength_name;
            Command_File>>holder;Command_File>>averaging_num;
            Command_File>>holder;Command_File>>scan_range_start;
            Command_File>>holder;Command_File>>Partial_Max_Percentage;
666
            Command_File.close();
        }
        else{cout<<"\n\n COMMAND FILE IS NOT OPEN\n\n";cin>>holder;cin.ignore()
            ;cout<<"\n";}

671     return 0;
    }

    int read_record_txt(char *data_file_name, double (& frequency), char *
        t_between_unit, int (&F1_Amp), int (&t_between_num))
    {
676    // read previously recorded data to calculate averages

        char record_file_name[] = "record\\RECORD.txt", holder[80];
        ifstream RECORD_FILE (record_file_name);
        if(RECORD_FILE.is_open())
681     {
            cout<<"\n+++++++ RECORD FILE IS OPEN +++++++";
            for(int i = 0; i < 6; i++)
            {
                data_file_name[i] = data_file_name[i+5];
686         }
            data_file_name[6] = '\0';

            do
            {
691             RECORD_FILE>>holder;
                if(RECORD_FILE.eof()){cout<<"\n\n---------- data record is not
                    found in RECORD.TXT file ----------\n\nplease exit and check
                     RECORD.TXT";cin>>holder;cin.ignore();}

            }while(strcmp(data_file_name,holder) != 0);

696         RECORD_FILE>>holder;
            RECORD_FILE>>frequency;
            RECORD_FILE>>F1_Amp;
            RECORD_FILE>>t_between_num;
            RECORD_FILE>>t_between_unit;
701
            RECORD_FILE.close();
        }
        else{cout<<"\n\n------- RECORD FILE IS NOT OPEN -------";}
        cout<<"\n";
706     return 0;
    }
```

```
int setup_file_structure()
{
    // setup file structure
    // create "data" directory
    cout<<"\n...checking if \"data\" directory exists.....\n";
    if(dirExists("data")) {cout<<".....\"data\" directory exists
        .....\n";}
    else
    {
        mkdir("data");
        cout<<".....\"data\" directory has been created.....\n";
    }

    // create "record" directory
    cout<<"\n...checking if \"record\" directory exists.....\n";
    if(dirExists("record")) {cout<<".....\"record\" directory exists
        .....\n";}
    else
    {
        mkdir("record");
        cout<<".....\"record\" directory has been created.....\n";
    }

    // create "command file"
    cout<<"\n...checking if command file exists.....\n";
    if(fileExists("CommandFile.txt")) {cout<<".....command file exists
        .....\n";}
    else
    {
        ofstream commandFileName;
        commandFileName.open("CommandFile.txt");
        commandFileName<<"filename: \n"
                       <<"Noise_filename: \n"
                       <<"Signal_Strength_filename: data\\078
                           _Signal_Strength_01.txt\n"
                       <<"averaging_number_of_values(odd_number): 11\n"
                       <<"scan_range_start: 50\n"
                       <<"Partial_Max_Percentage: 0.40\n";
        commandFileName.close();
        cout<<".....command file has been created.....\n";
    }

    // create "RECORD file"
    cout<<"\n...checking if RECORD file exists.....\n";
    if(fileExists("record\\RECORD.txt")) {cout<<".....RECORD file exists
        .....\n";}
    else
    {
        ofstream RECORDFileName;
        RECORDFileName.open("record\\RECORD.txt");
        RECORDFileName<<"Name_of_file Coil_Type Frequency F1_Amp
            Time_between_measurements Time_Unit 2D_points tau Cell Purpose\
            n";
        RECORDFileName.close();
        cout<<".....RECORD file has been created.....\n"
            ;
    }

    // create "RECORD data file"
    cout<<"\n...checking if RECORD_DATA file exists.....\n";
    if(fileExists("record\\RECORD_DATA.txt")) {cout<<".....RECORD_DATA file
         exists.....\n";}
```

```
        else
        {
            ofstream RECORDFileName;
            RECORDFileName.open("record\\RECORD_DATA.txt");
766         RECORDFileName<<"File partial F1_Amp data(...) rms stdev\n";
            RECORDFileName.close();
            cout<<".....RECORD_DATA file has been created.....\n"
                ;
        }

771     // create record_data_official_angle
        cout<<"\n...checking if official angle file exists.....\n";
        if(fileExists("record\\record_data_official_angle.txt")) {cout<<".....
            official angle file exists.....\n";}
        else
        {
776         ofstream RECORDFileName;
            RECORDFileName.open("record\\record_data_official_angle.txt");
            RECORDFileName<<"F1AMP angle stdev\n";
            RECORDFileName.close();
            cout<<".....official angle file has been created.....\n";
781     }

        // create record_data_T1 file
        cout<<"\n...checking if record_data_T1 file exists.....\n";
        if(fileExists("record\\record_data_T1.txt")) {cout<<".....
            record_data_T1 file exists.....\n";}
786     else
        {
            ofstream RECORDFileName;
            RECORDFileName.open("record\\record_data_T1.txt");
            RECORDFileName<<"File tip_angle tip_angle_stdev T1_data(...) rms
                stdev\n";
791         RECORDFileName.close();
            cout<<".....record_data_T1 file has been created.....\n";
        }

        return 0;
796 }

    int main()
    {
        int choice;
801     cout<<"\nMake sure you are in the folder with \"CommandFile.txt\" and
            the file you would"
            <<"like to analyze. Press any key to continue.\n\n";

        do{
            cout<<"\n\n~~~~~~~~~~~~~~~~~~~~~~~~~~~~~~~~~~~~~~~~~~~~\n"
806             <<"What would you like to do?\n"
                <<"1. Calculate the Tipping Angle\n"
                <<"2. Calculate T1\n"
                <<"3. Setup file structure\n"
                <<"4. exit\n\n";
811         cin>>choice;
            cin.ignore();
            cout<<"\n";

            switch(choice)
816         {
                case 1: // Tipping angle calculation
                    Analysis(1);
```

```
                cout<<"\n";
            break;
821         case 2: // Calculate T1
                Analysis(2);
                cout<<"\n";
            break;
            case 3:
826             setup_file_structure();
                cout<<"\n";
            break;
        }
        }while(choice != 4);
831 }
```

APPENDIX D

EXPECTED SQUID OUTPUT

This appendix describes the calculation of the expected SQUID flux from a range of ^{3}He absolute polarization and ^{3}He:^{4}He concentrations. When performing SEOP polarization, the common absolute polarization will be up to about 40% [63]. When performing MEOP polarization, the absolute polarization can reach 80% [123]. While atomic beam sources, such as that planned for the SNS-nEDM experiment, the polarization can be as high as 95% [124]. Note that these calculations are performed using the specific geometry for gradiometers and the specific values for the CE2SBlue SQUID as discussed in Ch. 3.

D.1 Flux Into Gradiometer From Polarized Source

The simulation was generated by using Steven Clayton's Mathematica code with parameters fit to our system. The code allows the user to determine the concentration of ^{3}He as the parameter [^{3}He:^{4}He], which for the lower end in our case should be around 10^{-6} or 10^{-7}. This value is defined in terms of number of atoms per m^3, so it can be setup to allow for easy calculation in a vacuum. The code allows the user to determine the polarization fraction of the ^{3}He. It also allows the user to determine the geometry of the sample volume and pickup coils.

An image output of the model is shown in Fig. D.1 . The yellow region is the region containing polarized ^{3}He atoms and the blue disks represent the signal and reference coils on the gradiometer. The signal coil is the one closer to the yellow region. The dimensions used in the model are given in Table D.1.

Table D.1: *Parameters Put Into Simulation Discussed in This Appendix.*

Parameter	Value
Sample side wall	25 mm
X locations of near side of coil	22.49 mm
Gradiometer Radius	15.24 mm
Gradiometer Baseline	24 mm

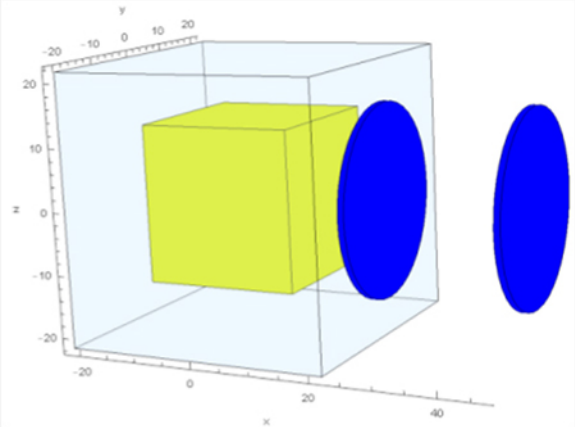


Figure D.1: *Geometry Used in Mathematica Simulation. Dimensions Are mm.*

In our system we do not expect 100% polarization from the SEOP or MEOP. Table D.2 and Fig. D.2 show the expected flux through the gradiometer from the sample volume for a range of concentrations and the fraction of ^{3}He which was polarized during the SEOP or MEOP process.

Table D.2: *Flux Through Gradiometer in Units of* Φ_0 *for Various Concentrations and Fractions of Polarization.*

	Ratio of [^{3}He:^{4}He] Atoms			
Fraction of ^{3}He Polarized	10^{-4}	10^{-5}	10^{-6}	10^{-7}
10 %	319.0	31.90	3.190	0.3190
20 %	637.9	63.79	6.379	0.6379
30 %	956.9	95.69	9.569	0.9569
40 %	1276	127.6	12.76	1.276
50 %	1595	159.5	15.95	1.595
60 %	1914	191.4	19.14	1.914
70 %	2233	223.3	22.33	2.233
80 %	2552	255.2	25.52	2.552

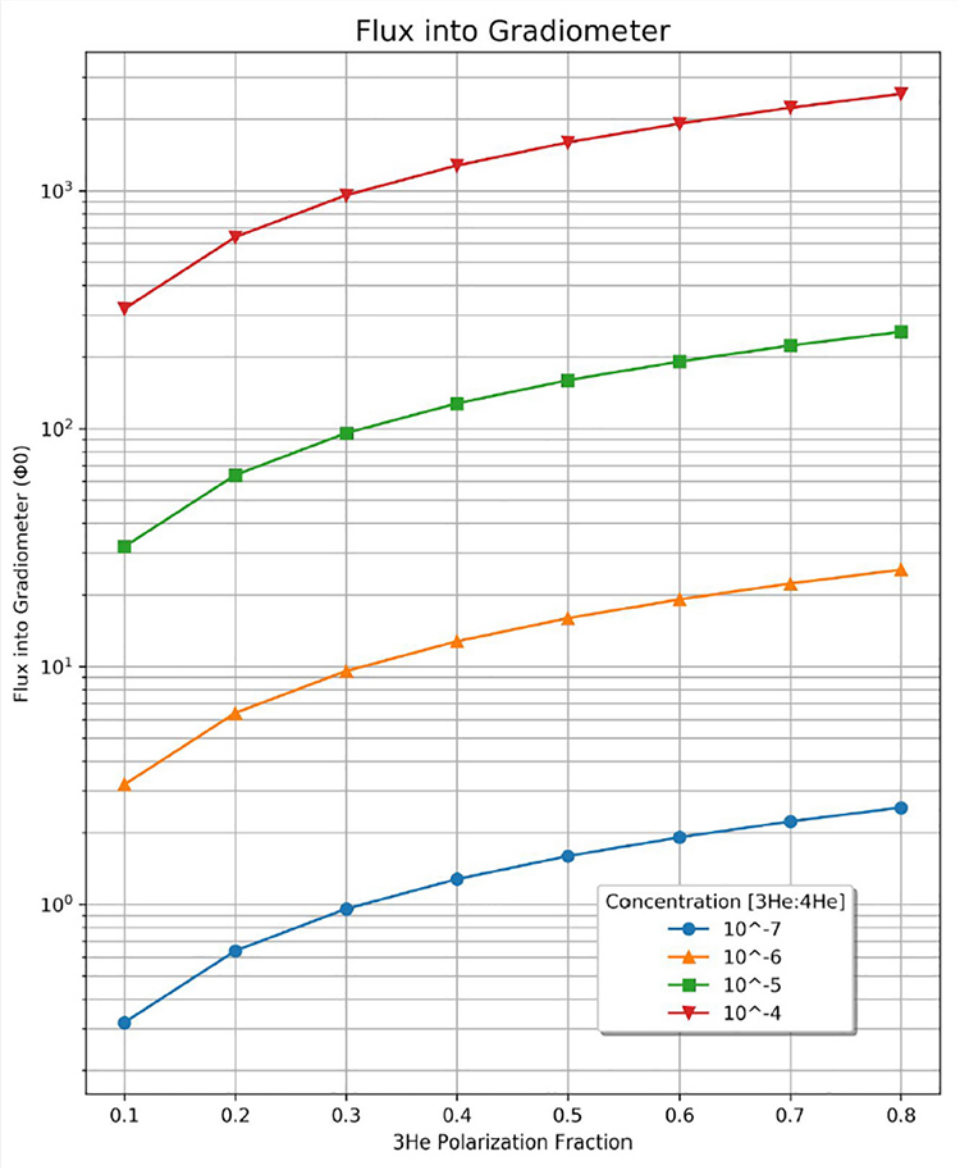


Figure D.2: *Flux Through Gradiometer in Units of* Φ_0. *This Is the Same Data As Table D.2.*

APPENDIX E

LIQUID HELIUM SCINTILLATION DATA AND CODE

E.1 Results - LHe Scintillation Data Tables

E.1.1 General Outline of Data Sets

This subsection gives a general overview of some important parameters when the data sets were taken. No single plot encompasses the values given here. It is intended as a quick reference for comparisons between the conditions for the various data sets.

Table E.1: *Outline of Data Sets Collected at LANL.*

Temp[a]	Voltage	Pressure[b]	PMT Cutoff
0.61 K[c]	0 - 35 kV	742.27 ± 0.24 mbar	1200 mV
	0 - 35 kV	28.50 ± 0.08 mbar	1200 mV
0.86 - 1.93 K[d]	0 kV	888.25 ± 4.71 mbar	1200 mV
2.03 ± 0.01 K	0 kV	1479.00 ± 0.08 mbar	300 mV
	0-35 kV	1479.21 ± 0.08 mbar	1200 mV
2.22 ± 0.01 K	0 kV	1439.33 ± 0.12 mbar	300 mV
	0-35 kV	1439.29 ± 0.88 mbar	1200 mV
2.42 ± 0.01 K	0 kV	755.64 ± 0.93 mbar	300 mV
	0-35 kV	755.64 ± 0.93 mbar	1200 mV
2.56 ± 0.01 K	0 kV	1435.54 ± 0.12 mbar	300 mV
	0-35 kV	1435.31 ± 0.65 mbar	1200 mV
3.06 ± 0.01 K	0 kV	1427.14 ± 15.33 mbar	300 mV
	0-35 kV	1432.63 ± 5.81 mbar	1200 mV

[a] Temperatures measured using ROx sensor inside of CV unless otherwise noted

[b] Pressures measured using Mensor Gauage

[c] This temperature was recorded from the PicoWatt Resistance Bridge and a standard devation was not taken

[d] The range of temperatures cited here can be found in Table E.2

Table E.2: *Measured Temperatures for Temperature Dependent Data Set With No Electric Field. These Values Were Measured Using a ROx Resistor Inside of the Central Volume.*

Reported Temp	Recorded Temp ± StDev
0.86 K	0.863 8 ± 0.003 7 K
0.98 K	0.976 5 ± 0.004 5 K
1.07 K	1.072 5 ± 0.003 5 K
1.18 K	1.182 4 ± 0.002 7 K
1.26 K	1.260 7 ± 0.002 2 K
1.40 K	1.398 6 ± 0.001 6 K
1.50 K	1.500 6 ± 0.001 3 K
1.60 K	1.597 1 ± 0.001 4 K
1.70 K	1.702 0 ± 0.001 2 K
1.79 K	1.791 4 ± 0.000 9 K
1.87 K	1.870 7 ± 0.000 9 K
1.93 K	1.932 1 ± 0.000 7 K

E.1.2 Results Data Table For 0.61 K to 2.42 K

Table E.3: *Mean Number of Photoelectrons (PE's) and Mean Number of After Pulses Per Prompt Pulse Vs Temperature. More Details About These Results Discussed in Section 5.5.1.*

Temperature	PEs in Prompt Pulse	After Pulses Per Prompt
0.61 K	10.70 ± 0.04	2.29 ± 1.52
0.86 K	10.68 ± 0.04	2.58 ± 1.60
0.98 K	10.60 ± 0.03	2.94 ± 1.72
1.07 K	10.63 ± 0.04	3.37 ± 1.85
1.18 K	10.61 ± 0.03	3.94 ± 2.00
1.26 K	10.64 ± 0.04	4.29 ± 2.10
1.40 K	10.70 ± 0.04	4.64 ± 2.18
1.50 K	10.76 ± 0.04	4.72 ± 2.19
1.60 K	10.78 ± 0.04	4.78 ± 2.23
1.70 K	10.77 ± 0.04	4.77 ± 2.20
1.79 K	10.80 ± 0.03	4.75 ± 2.21
1.87 K	11.11 ± 0.04	4.71 ± 2.19
1.93 K	11.58 ± 0.06	4.60 ± 2.17
2.42 K	11.30 ± 0.05	4.61 ± 2.25

E.1.3 Results Data Table For 0.61 K

Table E.4: *Mean Number of Photoelectrons (PE's) and Mean Number of After Pulses Per Prompt Pulse Vs Voltage at Two Pressures. More Details About These Results Discussed in Section 5.5.2.*

	PEs in Prompt Pulse		After Pulses Per Prompt	
Electric Field	28 mbar	750 mbar	28 mbar	750 mbar
0 kV/cm	10.98 ± 0.04	10.70 ± 0.04	2.23 ± 2.30	2.29 ± 2.32
5 kV/cm	10.86 ± 0.04	10.52 ± 0.03	2.38 ± 1.46	2.31 ± 2.30
10 kV/cm	10.62 ± 0.04	10.33 ± 0.03	2.30 ± 1.43	2.32 ± 1.45
15 kV/cm	10.50 ± 0.04	10.13 ± 0.03	2.34 ± 1.41	2.36 ± 1.43
20 kV/cm	10.39 ± 0.03	10.00 ± 0.02	1.89 ± 1.41	2.30 ± 1.42
25 kV/cm	10.16 ± 0.03	9.88 ± 0.03	1.83 ± 1.38	1.86 ± 1.38
30 kV/cm	10.01 ± 0.03	9.81 ± 0.03	1.79 ± 1.37	1.81 ± 1.39
35 kV/cm	9.88 ± 0.03	9.65 ± 0.03	1.79 ± 1.39	1.82 ± 1.40

E.1.4 Results Data Tables For 2.03 to 3.06 K

Table E.5: *Mean Number of PEs Vs Voltage Between 2.03 to 3.06 K.*

	Temperature (K)			
Electric Field	2.02 K	2.22 K	2.56 K	3.10 K
0 kV/cm	10.19 ± 0.03	10.28 ± 0.03	10.37 ± 0.03	10.42 ± 0.04
5 kV/cm	10.19 ± 0.03	10.28 ± 0.03	10.35 ± 0.03	10.46 ± 0.04
10 kV/cm	10.02 ± 0.03	10.13 ± 0.03	10.24 ± 0.03	10.34 ± 0.04
15 kV/cm	9.93 ± 0.03	10.02 ± 0.03	10.10 ± 0.03	10.23 ± 0.03
20 kV/cm	9.81 ± 0.03	9.96 ± 0.03	10.01 ± 0.03	10.13 ± 0.03
25 kV/cm	9.71 ± 0.03	9.82 ± 0.03	9.94 ± 0.03	10.07 ± 0.03
30 kV/cm	9.56 ± 0.02	9.72 ± 0.03	9.83 ± 0.03	9.98 ± 0.03
35 kV/cm	9.46 ± 0.03	9.64 ± 0.03	9.67 ± 0.03	9.80 ± 0.03

Table E.6: *Num of After Pulses*

	Temperature (K)			
Electric Field	2.02 K	2.22 K	2.56 K	3.10 K
0 kV/cm	4.33 ± 2.16	4.33 ± 2.17	4.34 ± 2.17	4.34 ± 2.17
5 kV/cm	3.89 ± 2.03	3.92 ± 2.03	3.89 ± 2.03	3.81 ± 2.02
10 kV/cm	3.29 ± 1.85	3.35 ± 1.89	3.33 ± 1.87	3.26 ± 1.85
15 kV/cm	2.92 ± 1.75	2.96 ± 1.76	2.95 ± 1.76	2.88 ± 1.74
20 kV/cm	2.67 ± 1.66	2.72 ± 1.71	2.70 ± 1.68	2.65 ± 1.66
25 kV/cm	2.51 ± 1.64	2.54 ± 1.62	2.52 ± 1.64	2.48 ± 1.62
30 kV/cm	2.37 ± 1.56	2.41 ± 1.59	2.39 ± 1.60	2.34 ± 1.59
35 kV/cm	2.27 ± 1.54	2.30 ± 1.55	2.29 ± 1.56	2.25 ± 1.54

Table E.7: *Pedestal Offset*

	Temperature (K)			
Electric Field	2.02 K	2.22 K	2.56 K	3.10 K
0 kV/cm	-42.24 ± 4.20	-44.01 ± 4.01	-42.48 ± 3.95	-42.66 ± 4.13
5 kV/cm	-42.31 ± 4.22	-43.91 ± 3.99	-42.41 ± 4.08	-42.67 ± 4.24
10 kV/cm	-42.32 ± 4.00	-43.02 ± 4.07	-42.05 ± 4.10	-42.70 ± 3.91
15 kV/cm	-42.13 ± 3.84	-42.66 ± 4.01	-42.24 ± 4.07	-42.72 ± 4.04
20 kV/cm	-42.27 ± 3.88	-42.63 ± 4.14	-42.19 ± 3.91	-42.83 ± 3.97
25 kV/cm	-42.23 ± 4.04	-42.49 ± 3.90	-42.40 ± 4.08	-42.73 ± 3.94
30 kV/cm	-42.37 ± 3.87	-42.35 ± 3.97	-42.49 ± 4.10	-42.72 ± 4.01
35 kV/cm	-42.43 ± 3.95	-42.16 ± 3.92	-42.56 ± 3.92	-42.67 ± 3.87

Table E.8: *Sigma PMT Calibration*

	Temperature (K)			
Electric Field	2.02 K	2.22 K	2.56 K	3.10 K
0 kV/cm	31.13	32.15	33.12	35.55
5 kV/cm	31.35	31.98	32.94	35.20
10 kV/cm	31.20	31.73	32.98	35.26
15 kV/cm	30.95	31.88	32.70	35.12
20 kV/cm	31.11	31.60	32.52	34.97
25 kV/cm	30.91	31.55	32.70	34.67
30 kV/cm	30.61	31.41	32.49	34.74
35 kV/cm	30.72	31.62	32.31	34.67

Table E.9: *Single PE Calibration*

	Temperature (K)			
Electric Field	2.02 K	2.22 K	2.56 K	3.10 K
0 kV/cm	58.19	59.71	61.26	65.27
5 kV/cm	58.31	59.66	61.34	65.00
10 kV/cm	58.46	59.96	61.48	65.23
15 kV/cm	58.59	60.06	61.68	65.27
20 kV/cm	58.59	60.09	61.81	65.15
25 kV/cm	58.68	60.22	61.67	65.18
30 kV/cm	58.82	60.16	61.73	65.02
35 kV/cm	58.87	60.32	61.87	65.18

Table E.10: *Total Number of After Pulses Counted Per Voltage (in thousands).*

	Temperature (K)			
Electric Field	2.02 K	2.22 K	2.56 K	3.10 K
0 kV/cm	415.49	415.63	420.09	422.25
5 kV/cm	374.09	376.63	376.99	371.23
10 kV/cm	316.71	322.18	322.55	317.84
15 kV/cm	281.71	285.21	285.48	281.27
20 kV/cm	257.93	262.04	261.77	258.19
25 kV/cm	242.38	245.22	244.04	242.15
30 kV/cm	228.46	232.11	231.57	228.67
35 kV/cm	219.00	221.53	221.84	220.17

E.2 LHe Scintillation Code

This section of the appendix contains the code which was used to process the ADC data discussed in Ch. 5. The code requires at least two files. The first file, presented in section

E.2.1, is a .txt command file which gives various directions to the larger code. The second file, present in section E.2.2, is a Python code which takes the binary data and processes it into data sets. Throughout the process, different sets of data had common themes or common parameters. The code was modified for different types of data. Although about three variations on the code exist, this code, which only processed the lowest temperature data, is provided as an example of how the best fit functions were implemented.

The Python code found in section E.2.2 essentially has two major sections. Lines 10 to 705 are a set of defined functions which are used to process the data. Lines 706 to the end of the code are the actual processing commands for the data.

E.2.1 Command File

```
Data File Directory: D:\nEDM\Scillation LANL\runs\0.61K\

data_length_to_process: 100000
number of bins: 200

Do you want to process low energy: Yes
If not, what value to use for single PE: 23.26

List of Low Energy Files

List of alpha data files
Jan-28-MSHV-Am241-Sn113-scint-1700V-TTL-50ns-50ns-0kV-0.70K-run1_binary.bin
Jan-28-MSHV-Am241-Sn113-scint-1700V-TTL-50ns-50ns-5kV-0.70K-run1_binary.bin
Jan-28-MSHV-Am241-Sn113-scint-1700V-TTL-50ns-50ns-10kV-0.70K-run1_binary.
    bin
Jan-28-MSHV-Am241-Sn113-scint-1700V-TTL-50ns-50ns-15kV-0.70K-run1_binary.
    bin
Jan-28-MSHV-Am241-Sn113-scint-1700V-TTL-50ns-50ns-20kV-0.70K-run1_binary.
    bin
Jan-28-MSHV-Am241-Sn113-scint-1700V-TTL-50ns-50ns-25kV-0.70K-run1_binary.
    bin
Jan-28-MSHV-Am241-Sn113-scint-1700V-TTL-50ns-50ns-30kV-0.70K-run1_binary.
    bin
Jan-28-MSHV-Am241-Sn113-scint-1700V-TTL-50ns-50ns-35kV-0.70K-run1_binary.
    bin
```

E.2.2 LANL Data Analysis Code

```
from matplotlib import pyplot as plt
import numpy as np
import math
import statistics as stat
import peakutils
import datetime
from math import pi
import os
```

```
#-------------------------------------------------
# ------     get time  --
#-------------------------------------------------

def get_now():
    return datetime.datetime.now()

#-------------------------------------------------
# ------  check if folder exists and if not create it  ----
#-------------------------------------------------

def folder_check_and_create(folder_path):
    if not os.path.exists(folder_path):
        os.mkdir(folder_path)

#-------------------------------------------------
# --------  log that stores to file   -------
#-------------------------------------------------

def logging(file_name, num_data_points, num_alphas, mean_ap_per_alpha,
    stdev_ap_per_alpha, run_time, ped_mean, ped_stdev, notes):
    #string = str(get_now())
    string = get_now().strftime('%Y/%m/%d_%H:%M')
    string += ' %s' % file_name
    string += ' %d' % num_data_points
    string += ' %d' % num_alphas
    string += ' %0.2f' % mean_ap_per_alpha
    string += ' %0.2f' % stdev_ap_per_alpha
    string += ' %0.2f' % ped_mean
    string += ' %0.2f' % ped_stdev
    string += ' %s' % str(run_time)[:-7]
    string += ' %s ' % notes

    save_to_file_name = 'D:\\nEDM\\Scillation LANL\\runs\\logging\\
        python_log.txt'
    f = open(save_to_file_name, 'a+')
    f.write('\n%s' % string)
    f.close()

#-------------------------------------------------
# ----  read command file  --------
#-------------------------------------------------

def read_command_file(command_file_name = "Command_File_To_Process_Data_02.
    txt"):
    print('reading command file: %s' % command_file_name)
    with open(command_file_name, 'r') as f:
        content = f.readlines()
    # you may also want to remove whitespace characters like `\n` at the
        end of each line
    content = [x.strip() for x in content]

    calculate_low_energy_max = False
    yes_calculate_low_energy = False
    in_lines_of_low_energy_files = False
    in_lines_of_alpha_files = False

    low_energy_files = []
    alpha_files = []

    single_PE_max = 0
```

```
        #print('\n')
        for line in content:
            # get list of single_PE files
71          if in_lines_of_low_energy_files and yes_calculate_low_energy and
                line not in '\n':
                low_energy_files.append(line)
            if in_lines_of_low_energy_files and yes_calculate_low_energy and
                line in '\n':
                in_lines_of_low_energy_files = False

76          # get list of alpha data files
            if in_lines_of_alpha_files and line not in '\n':
                alpha_files.append(line)
            if in_lines_of_alpha_files and line in '\n':
                in_lines_of_alpha_files = False
81
            # get file base directory
            if 'Data File Directory:' in line:
                file_path_dir = line[21:]
                #print('data file dir: %s' % file_path_dir)
86
            # get data length to process
            if 'data_length_to_process:' in line:
                data_length_to_process = int(line[24:])
                #print("data_length_to_process: %d" % data_length_to_process)
91
            # get number of bins
            if "number of bins:" in line:
                number_of_bins = int(line[15:])
                #print('sorting into %d bins' % number_of_bins)
96
            # trigger calculate single PE max
            if 'Do you want to process low energy' in line:
                if 'Yes' in line:
                    #print('\nGoing to calculate single PE data...')
101                 calculate_low_energy_max = True

            # trigger start recording single PE file names
            if calculate_low_energy_max:
                if 'List of Low Energy Files' in line and
                    calculate_low_energy_max:
106                 yes_calculate_low_energy = True
            if yes_calculate_low_energy and 'List of Low Energy Files' in line:
                in_lines_of_low_energy_files = True

            # trigger start recording alpha file names
111         if 'List of alpha data files' in line:
                in_lines_of_alpha_files = True

        # get value for single_PE
        if not calculate_low_energy_max:
116         for line in content:
                if 'If not, what value to use for single PE:' in line:
                    single_PE_max = float(line[41:])
                    #print(single_PE_max)
        f.close()
121
        return file_path_dir, low_energy_files, alpha_files, single_PE_max,
            data_length_to_process, number_of_bins

    #-----------------------------------------
```

```
# ------    process data into histogram arrays  -------
#-----------------------------------------------------

def process_data_02(file_path_dir, file_names, data_length_to_process,
    Voltages = list(range(0,40,5)), space_for_checking = 10,
    save_to_different_arrays = False, save_folder_dir = ''):
    trigger_hist_data = []
    ap_hist_data = []
    ap_per_waveform = []
    ap_peak_time = []

    pedestal_mean = 0
    pedestal_stdev = 0
    pedestal_statistics = [] # [0]: mean, [1]: stdev

    for k in range(len(file_names)):
        print('...%s ... %s' % (str(get_now())[10:16], file_names[k]))

        raw_data_array = []
        current_pedestal_mean = 0
        current_pedestal_var = 0

        with open(file_path_dir + file_names[k], 'rb') as f:
            while True:
                chunk = f.read(4096)
                if not chunk:
                    break
                raw_data_array.append(chunk)

        if save_to_different_arrays:
            this_dataset_hist = []
            this_ap_data = []
            this_ap_per_waveform = []
            this_ap_peak_time = []

        # deals with each waveform individually
        for j in range(data_length_to_process):
            current_trace = []
            # gets each waveform point value
            for i in range(0,4096,2):
                int1 = raw_data_array[j][i].to_bytes(1, byteorder = 'little
                    ')
                int2 = raw_data_array[j][i+1].to_bytes(1, byteorder = '
                    little')
                signed_value = int.from_bytes(int1+int2, byteorder = '
                    little', signed=True)
                current_trace.append(signed_value)

            # get trigger data for histogram
            current_max = max(current_trace[150:250])
            current_max_index = current_trace[150:250].index(current_max)
                +150 # restricting domain and adding 150 avoids waveforms
                with two peaks at the same height

            # check for second peak
            second_max = max(current_trace[:current_max_index-
                space_for_checking] + current_trace[current_max_index+
                space_for_checking:])

            # calculate mean and standard deviation for PMT pedestal before
                 trigger peak
```

```
176             current_ped_mean = stat.mean(current_trace[0:current_max_index
                    -20])
                current_ped_var = stat.variance(current_trace[0:
                    current_max_index-20])
                current_max -= current_ped_mean

                # add first maximum to data collection for histogram
181             if save_to_different_arrays:
                    current_pedestal_mean += current_ped_mean
                    current_pedestal_var += current_ped_var

                    this_dataset_hist.append(current_max)
186
                else:
                    pedestal_mean += current_ped_mean
                    pedestal_stdev += current_ped_var

191                 trigger_hist_data.append(current_max)

                # only pass waveforms to after pulse processing which only have
                     one primary signal and
                # are triggered at the beginning
                if current_max*0.5 > second_max and current_max_index > 150 and
                     current_max > 150:
196
                    #print(current_max_index)
                    #print('ped mean: %0.2f' % current_ped_mean)
                    #print('ped var: %0.2f' % current_ped_var)

201                 # find values of after pulses
                    current_trace = np.array(current_trace)
                    ap_peak_indices = peakutils.indexes(current_trace[
                        current_max_index+5:],
                                                        thres=0.5,
                                                        min_dist=5)
206
                    # make sure ap_peak_indices are the same as original trace
                        indices
                    ap_peak_indices = [x+current_max_index+5 for x in
                        ap_peak_indices]
                    #print(ap_peak_indices)

211                 ap_peaks = []
                    ap_peak_indices_final = []
                    for x in ap_peak_indices:
                        # trim data after peakutils to make sure low values are
                             not counted
                        if current_trace[x] > (current_ped_mean+20):
216                         ap_peaks.append(current_trace[x] - current_ped_mean
                                )
                            ap_peak_indices_final.append(x)

                    #print(ap_peak_indices_final)
                    #print(ap_peaks)
221
                    if save_to_different_arrays:
                        this_ap_data.extend(ap_peaks)
                        this_ap_per_waveform.append(len(ap_peaks))
                        this_ap_peak_time.extend([x-current_max_index for x in
                            ap_peak_indices_final])
226                 else:
                        ap_hist_data.extend(ap_peaks)
```

```
                        ap_per_waveform.append(len(ap_peaks))
                        ap_peak_time.extend([x-current_max_index for x in
                            ap_peak_indices_final])

        # after processing for one whole voltage dataset is complete
        if save_to_different_arrays:
            trigger_hist_data.append(this_dataset_hist)

            ap_hist_data.append(this_ap_data)
            ap_per_waveform.append(this_ap_per_waveform)
            ap_peak_time.append(this_ap_peak_time)

            current_pedestal_mean = current_pedestal_mean/
                data_length_to_process
            current_pedestal_stdev = math.sqrt(current_pedestal_var/
                data_length_to_process)
            pedestal_statistics.append([current_pedestal_mean,
                current_pedestal_stdev])

    # after all data has been processed
    if save_to_different_arrays:
        cumulative_ap_per_waveform = []
        [cumulative_ap_per_waveform.extend(data) for data in
            ap_per_waveform]
        ap_mean_per_waveform = stat.mean(cumulative_ap_per_waveform)
        ap_stdev_per_waveform = stat.stdev(cumulative_ap_per_waveform)

        num_waveforms_with_ap = sum([len(dataset) for dataset in
            ap_per_waveform])

        ap_statistics = []
        for ap_set in ap_per_waveform:
            ap_statistics.append([stat.mean(ap_set), math.sqrt(stat.
                variance(ap_set))])

        folder_check_and_create(file_path_dir + save_folder_dir)
        plot_statistics(Voltages, ap_statistics, data_box_first_line='vol (
            kV)  ap mean   ap stdev', x_label='Electric Field (kV/cm)',
            y_label='Mean Num of after pulses', plot_title='Mean Num of
            After Pulses per Waveform vs Electric Field',
            file_path_and_name=file_path_dir + save_folder_dir+'\\Num of
            After Pulses', save_file=True)
    # ++++++++++ PLOT AP_PER_WAVEFORM +++++++

    else:
        pedestal_mean = pedestal_mean/(len(file_names)*
            data_length_to_process)
        pedestal_stdev = math.sqrt(pedestal_stdev/ (len(file_names)*
            data_length_to_process -1 ) )
        print('final ped mean: %0.2f' % pedestal_mean)
        print('final ped stdev: %0.2f' % pedestal_stdev)
        pedestal_statistics = [pedestal_mean, pedestal_stdev]

        ap_mean_per_waveform = stat.mean(ap_per_waveform)
        ap_stdev_per_waveform = stat.stdev(ap_per_waveform)
        num_waveforms_with_ap = len(ap_per_waveform)

    print('%d waveforms out of %d total had after pulses' % (
        num_waveforms_with_ap, len(file_names)*data_length_to_process))
    print('there were %0.2f after pulses +- %0.2f per alpha' % (
        ap_mean_per_waveform, ap_stdev_per_waveform))
```

```
        # empty memory of waveforms
        del raw_data_array

        return trigger_hist_data, ap_hist_data, num_waveforms_with_ap,
            ap_mean_per_waveform, ap_stdev_per_waveform, ap_peak_time,
            pedestal_statistics

    #-----------------------------------------------
    # ---- fit data to Poisson Gaussian distribtion ------
    #-----------------------------------------------

    #Gaussian function
    def gauss_function(x, a, x0, sigma):
        return a*np.exp(-(x-x0)**2/(2*sigma**2))

    def fit_to_poisson_gauss_02(n, bins, file_path_dir,
                                general_data_package, voltage, type_name,
                                hist_data, hist_max_value, num_bins,
                                N0 = 10000000,
                                mu0 = 0.5,
                                G0 = 40,
                                sigmaPMT0 = 30, # simga PMT
                                sigmaPED = 3,
                                x_start = 30,
                                x_end = 100,
                                mu_min = 0,
                                mu_max = 2,
                                mu_num = 1,
                                do_print = False, font_size=14, save_folder_dir
                                    = ''):
        # This function takes data from the histogram and the actual dataset to
            operate

        plt.rcParams.update({'errorbar.capsize': 3})
        plt.rcParams['font.family'] = 'sans-serif'
        plt.rcParams['font.sans-serif'] = ['Arial']

        # program
        from scipy.optimize import curve_fit

        x = bins[x_start:x_end] + (bins[1]-bins[0])/2
        y=n[x_start:x_end]

        plt.plot(x,y,'ok', mfc='None', label='fit region') #Overplot the dots
        plt.show()

        # setup trigger for signal types
        is_single_PE = False
        is_alpha = False
        if type_name.find('single') == 0:
            is_single_PE = True
            print('fitting for single PE')
        elif type_name.find('alpha') == 0:
            is_alpha = True
            print('fitting for alpha peak')
        else:
            print('---------- YOU DID NOT LABEL THE type_name APPROPRIATELY (
                PLEASE USE \'single\' or \'alpha\')')
            return

        for mu_i in np.linspace(mu_min,mu_max,mu_num):
            print('\nmu_i is %0.2f: ' % mu_i)
```

```
331         #do the fit!
            try:
                if is_single_PE:
                    popt, pcov = curve_fit(poisson_gauss_function, x, y, p0 = [
                        N0, mu_i, G0, sigmaPMT0])
                if is_alpha:
336                 popt, pcov = curve_fit(poisson_gauss_function, x, y, p0 = [
                        N0, mu_i])

                #error = [np.abs(pcov[i][i]**2) for i in range(len(popt))]
                error = [np.abs(pcov[i][i]**0.5) for i in range(len(popt))]

341             print(popt)
                print('error: %0.2E' % error[1])

                if error[0] > 0:
                    print('PG - error is greater than zero')
346                 fit_data = poisson_gauss_function(x, *popt)
                    fit_peak_index = peakutils.indexes(fit_data)
                    print('PG - fit peak indices')
                    print(fit_peak_index)
                    if len(fit_peak_index) > 1:
351                     print('PG - .. in index if')
                        #continue
                        all_peaks = [fit_data[i] for i in fit_peak_index]
                        print(all_peaks)
                        list_index = all_peaks.index(max(all_peaks))
356                     print('PG - max value of %d at pos %d' % (max(all_peaks
                            ), list_index))
                        print(x[fit_peak_index[list_index]])
                        fit_peak_max = max(all_peaks)
                        fit_peak_ADC = x[fit_peak_index[list_index]]
                    else:
361                     fit_peak_max = fit_data[fit_peak_index[0]]
                        fit_peak_ADC = x[fit_peak_index[0]]
                    print('PG - maximum at %0.2f' % fit_peak_ADC)
                    single_PE_peak = fit_peak_ADC

366                 if is_alpha:
                        print('PG - trying Gaussian Function fit')
                        popt_gau, pcov_gau = curve_fit(gauss_function, x, y, p0
                            = [1900, fit_peak_ADC, 200])
                        print('PG - Gaussian Fit Values\nmag: %d\tpeak: %0.2f\
                            tstdev: %0.2f' % (popt_gau[0], popt_gau[1],
                            popt_gau[2]))
                        print('PG - general_data_package[0]: %d' %
                            general_data_package[0])
371                     mu_error = popt_gau[2]/math.sqrt(general_data_package
                            [0])
                        print('PG - mu_error: %0.2f' % mu_error)

                # Calculate stdev
                #stdev_of_mean = math.sqrt(sum([(n[i]-fit_peak_max)**2 for i in
                    range(len(y))])/sum(y))
376
                # CREATE PLOT
                fig, ax = plt.subplots()
                print('PG - set plots')

381             # these are matplotlib.patch.Patch properties
                props = dict(boxstyle='round', facecolor='white', alpha=1.0)
                # create text lines to go on plot
```

```
                text_in_right_box = 'N (est): %d' % N0
                text_in_right_box += '\nmu (est): %0.2f' % mu_i
386             if type_name.find('single') >=0:
                    text_in_right_box += '\nG (est): %d' % G0
                    text_in_right_box += '\n$\sigma_{PMT}$ (est): %0.2f' %
                        sigmaPMT0

                print('PG - text1')
391             text_in_right_box += '\n\n                  min    max'
                text_in_right_box +=   '\nbin num: %d  %d' % (x_start, x_end)
                text_in_right_box +=   '\nADC cha: %d  %d' % (bins[x_start],
                    bins[x_end])
                text_in_right_box += '\ntotal number of bins: %d' % (num_bins)

396             print('PG - text2')
                text_in_right_box += '\n\nN (fit): %0.3E +- %0.3E' % (popt[0],
                    error[0])
               #text_in_right_box += '\nmu (fit): %0.3f +- %0.3f' % (popt[1],
                    mu_error)

                if is_single_PE:
401                 text_in_right_box += '\nmu (fit): %0.3f +- %0.3f' % (popt
                        [1], error[1])
                    text_in_right_box += '\nG (fit): %0.2f +- %0.3E' % (popt
                        [2], error[2])
                    text_in_right_box += '\n$\sigma_{PMT}$ (fit): %0.2f +- %0.3
                        E' % (popt[3], error[3])
                if is_alpha:
                    #text_in_right_box += '\nmu (fit): %0.3f +- %0.3f' % (popt
                        [1], mu_error)
406                 text_in_right_box += '\nmu (fit): %0.3f +- %0.3f' % (popt
                        [1], error[1])
                    text_in_right_box += '\nG: %0.2f' % G0
                    text_in_right_box += '\n$\sigma_{PMT}$: %0.2f' % sigmaPMT0
                text_in_right_box += '\nk$_{max}$: 15'
                text_in_right_box += '\n$\sigma_{ped}$: %0.2f' % sigmaPED
411             text_in_right_box += '\n%d total points for %0.2f K' % (sum(n),
                     voltage)

                right_box = ax.text(1.1, 1.0, text_in_right_box, transform=ax.
                    transAxes, fontsize=14, verticalalignment='top', bbox =
                    props)
                print('PG - text3')

416             title = ax.set_title(type_name + ' peak at %0.2f K' % voltage,
                    fontsize=font_size)
                ax.set_xlabel('ADC Channel', fontsize=font_size)
                ax.set_ylabel('Count', fontsize=font_size)
                ax.tick_params(axis='both', which='major', labelsize=font_size)
                ax.set_xlim(0,hist_max_value)
421             ax.set_xticks(list(range(0,hist_max_value+1,int(hist_max_value
                    /8))))
                ax.grid(True, linestyle = '--')
                print('PG - create text box')

               #plot the fit results
426             plt.plot(x,poisson_gauss_function(x, *popt), 'r--', label='
                    curve fit')
                print('PG - make PG plt')
                plt.hist(hist_data, num_bins, facecolor='green', alpha=0.75,
                    log=False, histtype='step', range=(0,hist_max_value), label
                    ="hist data", lw=1, color='b')
```

```
                print('PG - plot histogram')
                plt.legend(fontsize=font_size)

                specific_name = 'curve_fit_%s_%0.2f_K.png' % (type_name,
                    voltage)
                save_name = file_path_dir + save_folder_dir + '\\' +
                    specific_name
                print(save_name)
                plt.savefig(save_name, bbox_extra_artists=(right_box, title),
                    bbox_inches='tight')
                print('saved fig')

                if do_print:
                    plt.show()
                    print(popt)
                    print([np.abs(pcov[i][i]**2) for i in range(len(popt))])

                if is_single_PE:
                    return popt[2], popt[3] # fit_peak (fit), sigmaPMT (fit)
                if is_alpha:
                    #return popt[1], mu_error, popt[0] # mu(fit) , mu error (
                        fit), N (fit)
                    return popt[1], error[1], popt[0] # mu(fit) , mu error (fit
                        ), N (fit)
            except:
                print('mu_i = %d did not work' % mu_i)


#-------------------------------------------
# -----  make histogram plots -----
#-------------------------------------------

def hist_plot_02(data, hist_max, num_bins, xlabel, ylabel, ymax, file_name,
    file_path_dir, save_name, specific_title, general_data_package, save=
    False, islog=True, save_to_different_arrays = False, voltages = [],
    islogx = False, font_size=14, save_folder_dir=''):

    # unpack general_data_package
    data_length_to_process, pedestal_statistics, num_waveforms_with_ap,
        ap_mean_per_waveform, ap_stdev_per_waveform = general_data_package

    plt.rcParams.update({'errorbar.capsize': 3})
    plt.rcParams['font.family'] = 'sans-serif'
    plt.rcParams['font.sans-serif'] = ['Arial']

    ax = plt.subplot()
    if not save_to_different_arrays:
        n, bins, patches = plt.hist(data, num_bins, facecolor='green',
            alpha=0.75, log=islog, histtype='step', range=(0,hist_max))
    else:
        n = []
        bins = []

        for i in range(len(data)):
            n_curr, bins_curr, patches_curr = plt.hist(data[i], num_bins,
                facecolor='green', alpha=0.75, log=islog, histtype='step',
                range=(0,hist_max), label='%0.2f K' % voltages[i])
            n.append(n_curr)
            bins.append(bins_curr)
    ax.legend( loc=(1.08,-0.15), fontsize=font_size)

    ax.set_xlabel(xlabel, fontsize=font_size)
```

```
        ax.set_ylabel(ylabel, fontsize=font_size)
        ax.set_ylim(1,ymax)
        ax.set_xlim(0,hist_max)
        ax.tick_params(axis='both', which='major', labelsize=font_size)
        ax.set_xticks(list(range(0,hist_max+1,int(hist_max/8))))
        ax.grid(True, linestyle = '--')

        title = ax.set_title(file_name[0] + '\n' + specific_title, fontsize=
            font_size)

        # these are matplotlib.patch.Patch properties
        props = dict(boxstyle='round', facecolor='white', alpha=1.0)
        # create text lines to go on plot
        text_in_right_box = 'number of waveforms: %d' % (len(file_name)*
            data_length_to_process)
        if not save_to_different_arrays:
            text_in_right_box += '\ndata points included: %d' % len(data)
        else:
            text_in_right_box += '\ndata points included: %d' % sum([len(data[i
                ]) for i in range(len(data))])
        text_in_right_box += '\nbin width: %0.2f' % (hist_max/num_bins)
        text_in_right_box += '\nnumber of bins: %d' % num_bins
        text_in_right_box += '\n%d waveforms out of %d total had after pulses'
            % (num_waveforms_with_ap, len(file_name)*data_length_to_process)

        right_box = ax.text(1.5, 0.9, text_in_right_box, transform=ax.transAxes
            , fontsize=14, verticalalignment='top', bbox = props)

        if save:
            plt.savefig(file_path_dir + save_folder_dir + '\\' + save_name,
                bbox_extra_artists=(title, right_box), bbox_inches='tight')
            print('saved %s' % specific_title)
            print('--- to: %s' % (file_path_dir + save_folder_dir + '\\' +
                save_name))
            hist_data_to_text_file(bins, n, file_path_dir + save_folder_dir + '
                \\', save_name)
        plt.show()

        del ax
        return n, bins


    #-----------------------------------------------
    #-----------------------------------------------
    # ------  save histogram data to txt file  -----
    #-----------------------------------------------
    #-----------------------------------------------

    def hist_data_to_text_file(bin_data, n_data, file_path_dir, file_name):
        print('(1/2)...start to save \'%s\' to txt file' % file_name)

        # create string to save to file
        vol_str = ''
        for volt in Voltages:
            vol_str += '\t%0.2f' % volt

        hist_data_str = 'bin' + vol_str
        for i in range(len(n_data[0])):
            hist_data_str += '\n%d' % bin_data[0][i]
            for j in range(len(Voltages)):
                hist_data_str += '\t%d' % n_data[j][i]
```

```
        #print(hist_data_str)
        # save string to file
        f = open(file_path_dir + file_name + '.txt', 'w+')
        f.write(hist_data_str)
        f.close()

        print('(2/2)...\'%s\' saved to txt file' % file_name)

        del hist_data_str, vol_str

    #-----------------------------------------------
    # ------  read histogram data from txt file ------
    #-----------------------------------------------

    def read_hist_txt_file(file_path_dir, file_name, do_you_want_to_see_plot =
        False, save_folder_dir=''):
        # open file and start reading data to content
        full_file_path = file_path_dir + save_folder_dir+ '\\' + file_name + '.
            txt'
        with open(full_file_path) as f:
            content = f.readlines()
        content = [x.strip() for x in content]

        # get voltages data from first line
        content1 = [x for x in content[0].split('\t')]
        Volts = content1[1:len(content1)]
        Volts = [int(i) for i in Volts]

        # get histogram data and bins
        hist_data_by_row = []
        bins = []
        for i in range(1,len(content)):
            content2 = [x for x in content[i].split('\t')]
            bins.append(int(content2[0]))
            data_content = [int(x) for x in content2[1:len(content2)]]
            hist_data_by_row.append(data_content)

        f.close()

        # sort data into proper datasets
        hist_data = [[hist_data_by_row[i][j] for i in range(len(
            hist_data_by_row))] for j in range(len(Volts))]

        if do_you_want_to_see_plot:
            for i in range(len(Volts)):
                plt.plot(bins, hist_data[i], label='%0.2f K' % Volts[i])
            plt.title('Plot of \'%s\'' % file_name)
            plt.legend()
            plt.show()

        return hist_data, bins, Volts
        del content, content1, Volts, hist_data, bins, content2, data_content,
            hist_data_by_row, data_holder

    #-----------------------------------------------
    # ----  plot and save statistical data  ------
    #-----------------------------------------------

    def plot_statistics(voltages, plot_data, data_box_first_line='', x_label=''
        , y_label='', plot_title='',
                        file_path_and_name='', save_file=False, additional_info
                            = [], font_size=14):
```

```
        plt.rcParams.update({'errorbar.capsize': 3})
        plt.rcParams['font.family'] = 'sans-serif'
591     plt.rcParams['font.sans-serif'] = ['Arial']

        y_data = [plot_data[i][0] for i in range(len(plot_data))]

        ax =plt.subplot()
596     ax.set_xlabel(x_label, fontsize=font_size)
        ax.set_ylabel(y_label, fontsize=font_size)
        Title = ax.set_title(plot_title, fontsize=font_size)
        plt.grid(True, linestyle='--')
        ax.tick_params(axis='both', which='major', labelsize=font_size)
601
        plt.errorbar(voltages, y_data,
                     yerr=[plot_data[i][1]/2 for i in range(len(plot_data))],
                     fmt='o-', ecolor='r', color='r',
                     mfc='none', markersize='4')
606
        # these are matplotlib.patch.Patch properties
        props = dict(boxstyle='round', facecolor='white', alpha=1.0)
        # create text lines to go on plot
        text_in_right_box = data_box_first_line
611     for i in range(len(voltages)):
            text_in_right_box += '\n    %0.2f          %0.2f          %0.4f' % (
                voltages[i], plot_data[i][0], plot_data[i][1])
        if len(additional_info) > 0:
            text_in_right_box += '\n'
            for line in additional_info:
616             text_in_right_box += line

        right_box = ax.text(1.1, 1.0, text_in_right_box, transform=ax.transAxes
            , fontsize=14, verticalalignment='top', bbox = props)

        if save_file:
621         plt.savefig(file_path_and_name, bbox_extra_artists=(right_box,
                Title), bbox_inches='tight')
            print('saved \'%s\' plot to: %s' % (plot_title, file_path_and_name)
                )

            # save figure data to text file
            save_fig_data_as_txt(voltages, [plot_data[i][0] for i in range(len(
                plot_data))], file_path_and_name, x_label, y_label, stdev = [
                plot_data[i][1] for i in range(len(plot_data))])
626
    #-----------------------------------------
    # ----  plot and save  data  ----
    #-----------------------------------------
    def plot_func(x, y, plot_title = '', x_label='', y_label='',
        file_path_and_name='', save_file=False, font_size=14):
631     plt.rcParams.update({'errorbar.capsize': 3})
        plt.rcParams['font.family'] = 'sans-serif'
        plt.rcParams['font.sans-serif'] = ['Arial']

        ax = plt.subplot()
636     plt.plot(x, y, color='b')
        plt.plot(x,y, 'ob')

        ax.set_xlabel(x_label, fontsize=font_size)
        ax.set_ylabel(y_label, fontsize=font_size)
641     Title = ax.set_title(plot_title, fontsize=font_size)
        ax.tick_params(axis='both', which='major', labelsize=font_size)
        ax.grid(True, linestyle = '--')
```

```
        if save_file:
646         plt.savefig(file_path_and_name, bbox_extra_artists=(Title, ),
                bbox_inches='tight')
            save_fig_data_as_txt(x, y, file_path_and_name, x_label, y_label)
            print('saved %s to: %s' % (plot_title, file_path_and_name))
        plt.show()

651 #-------------------------------------------------
    #-----  plot total counts vs voltage   -----
    #-------------------------------------------------

    def plot_sum_of_data(x, y, y_scale, x_label, y_label, text_title,
        file_path_dir, file_name, font_size=14, save_folder_dir=''):
656     plt.rcParams.update({'errorbar.capsize': 3})
        plt.rcParams['font.family'] = 'sans-serif'
        plt.rcParams['font.sans-serif'] = ['Arial']

        counts_per_group = [sum(dataset)/y_scale for dataset in y]
661
        ax = plt.subplot()

        plt.plot(x, counts_per_group, 'ok')
        plt.plot(x, counts_per_group)
666
        ax.set_xlabel(x_label, fontsize=font_size)
        ax.set_ylabel(y_label, fontsize=font_size)
        title = ax.set_title(text_title, fontsize=font_size)
        ax.tick_params(axis='both', which='major', labelsize=font_size)
671     ax.grid(True, linestyle = '--')

        file_path_and_name = file_path_dir + save_folder_dir + '\\' + file_name
        plt.savefig(file_path_and_name, bbox_extra_artists=(title, ),
            bbox_inches='tight')
        plt.show()
676
        # save figure data to text file
        save_fig_data_as_txt(x, counts_per_group, file_path_and_name, x_label,
            y_label)

    #-------------------------------------------------
681 #-----  save plot data  -----
    #-------------------------------------------------

    def save_fig_data_as_txt(x, y, file_path_and_name, x_label, y_label, stdev
        =[]):
        f = open(file_path_and_name + '.txt', 'w+')
686     write_text = '%s\t%s' % (x_label, y_label)
        for i in range(len(x)):
            write_text += '\n%0.2f\t%0.3f' % (x[i], y[i])
            if len(stdev) > 0:
                write_text += '\t%0.4f' % stdev[i]
691     f.write(write_text)
        f.close()
        plt.show()

    #-------------------------------------------------
696 #-------------------------------------------------
    #----- run code  -----
    #-------------------------------------------------
    #-------------------------------------------------
```

```
run_data_processing = True

#from functions_for_waveform_data import *

#-------------------------------------------------
# ------ start data processing  ------
#-------------------------------------------------

start_time = get_now()
print('started at: %s' % str(start_time))
Voltages = list(range(0,40,5))
print('\nusing voltages:')
print(Voltages)

if run_data_processing:
    #-------------------------------------------------
    # ---- read command file for file names  -----
    #-------------------------------------------------
    print('\nREADING COMMAND FILE')
    command_File_Name = "Command_File_To_Process_Data_08_0.61K_run2.txt"
    save_dir_name = 'images_run2'
    add_notes = '0.61K_data_run2'
    file_path_dir, low_energy_files, alpha_files, single_PE_max,
        data_length_to_process, number_of_bins = read_command_file(
        command_file_name = command_File_Name)
    print('data length to process: %d' % data_length_to_process)

    #-------------------------------------------------
    # ------ process alpha files into histogram arrays  -----
    #-------------------------------------------------

    print('\nPROCESSING VOLTAGE DATA')
    save_files = True
    trigger_hist_data, ap_hist_data, num_waveforms_with_ap,
        ap_mean_per_waveform, ap_stdev_per_waveform, ap_peak_time,
        pedestal_statistics = process_data_02(file_path_dir, alpha_files,
        data_length_to_process, Voltages, save_to_different_arrays=True,
        save_folder_dir=save_dir_name)

    # plot and save pedestal statistics
    plot_statistics(Voltages, pedestal_statistics, data_box_first_line='vol
        (kV)  ped mean  ped stdev', x_label='Electric Field (kV/cm)',
        y_label='ADC Units', plot_title='Pedestal Offset vs Electric Field'
        , file_path_and_name=file_path_dir + save_dir_name + '\\Pedestal
        Offset', save_file=save_files)

    #-------------------------------------------------
    # ----  packages for all histograms  -----
    #-------------------------------------------------

    print('\nGENERATING GENERAL DATA FOR ALL HISTOGRAMS')
    general_data_package = [data_length_to_process, pedestal_statistics,
        num_waveforms_with_ap, ap_mean_per_waveform, ap_stdev_per_waveform]

#-------------------------------------------------
#-------------------------------------------------
# ------  the histogram of the trigger data  -----
#-------------------------------------------------
#-------------------------------------------------

print('\nSTARTING HISTOGRAM OF TRIGGER DATA')
trigger_hist_max_value = 2000
```

```
    n_trig, bins_trig = hist_plot_02(trigger_hist_data, trigger_hist_max_value,
         number_of_bins, 'ADC Channel', 'Counts', 3000, alpha_files,
        file_path_dir, 'Hist - Trigger Data', 'Trigger ADC Channel',
        general_data_package, save = save_files, save_to_different_arrays =
        True, voltages = Voltages, save_folder_dir=save_dir_name)

    #-------------------------------------------
    # ---- the histogram of the after pulse data    -----
    #-------------------------------------------

    print('\nSTARTING HISTOGRAM OF AFTER PULSE DATA')
    ap_hist_max_value = 200
    n_ap, bins_ap = hist_plot_02(ap_hist_data, ap_hist_max_value,
        number_of_bins, 'ADC Channel', 'Counts', 20000, alpha_files,
        file_path_dir, 'Hist - After Pulse Peak', 'After Pulse Peak Data',
        general_data_package, save = save_files, save_to_different_arrays =
        True, voltages = Voltages, save_folder_dir=save_dir_name)

    #-------------------------------------------
    # ----  the histogram of the after pulse time -----
    #-------------------------------------------
    print('\nSTARTING HISTOGRAM OF AFTER PULSE TIME DATA')
    ap_time_max = 2048
    bin_width = 2**3
    n_ap_time, bins_ap_time = hist_plot_02(ap_peak_time, ap_time_max, int(
        ap_time_max/bin_width), 'ADC Time (x10 = ns)', 'Counts', 18000,
        alpha_files, file_path_dir, 'Hist - After Pulse Time', 'After Pulse
        Timing', general_data_package, save = save_files, islog=False,
        save_to_different_arrays = True, voltages = Voltages, save_folder_dir=
        save_dir_name)

    notes = 'all_histograms_analyzed'+add_notes
    logging(alpha_files[0], len(alpha_files)*data_length_to_process,
        num_waveforms_with_ap, ap_mean_per_waveform, ap_stdev_per_waveform,
        get_now()-start_time, stat.mean([pedestal_statistics[i][0] for i in
        range(len(pedestal_statistics))] ), stat.mean([pedestal_statistics[i
        ][1] for i in range(len(pedestal_statistics))] ), notes)


    #-------------------------------------------
    #-------------------------------------------
    # --  fit after pulse to Poisson Gaussian Distribution for single PE -----
    #-------------------------------------------
    #-------------------------------------------

    print('\n\n----------------------STARTING FIT ANALYSIS----------------------\n'
        )
    single_PE_peak_array = []
    sigmaPMT_array = []
    ap_bins_in = len(bins_ap[0])-1

    for i in range(len(Voltages)):
        def poisson_gauss_function(x, N, mu, G, sigmaPMT, k=15, sigmaPED=
            pedestal_statistics[i][1]):
            final_array = []
            for j in x:
                current_value=0
                for i in range(1,k+1):
                    current_value += ((mu**i * math.exp(-mu) )/math.factorial(i
                        ) ) * (1/math.sqrt(2*pi*(sigmaPMT**2*i+sigmaPED**2))) *
                         math.exp(-(j-G*i)**2 / (sigmaPMT**2*i+sigmaPED**2))
                final_array.append(N*current_value)
```

```
            return final_array


796         print('\nSTARTING SINGLE PE CALCULATION for %0.1f K...' % Voltages[i])
            single_PE_peak, sigmaPMT = fit_to_poisson_gauss_02(n_ap[i], bins_ap[i],
                 file_path_dir, general_data_package, Voltages[i], 'single PE',
                ap_hist_data[i], ap_hist_max_value, ap_bins_in, N0 = 10000000, mu0
                = 0.5, G0 = 58, sigmaPMT0 = 30, sigmaPED = pedestal_statistics[i
                ][1], x_start = 35, x_end = 130, mu_min = 0, mu_max = 0.2, mu_num =
                 11, do_print = True, save_folder_dir=save_dir_name)
            single_PE_peak_array.append(single_PE_peak)
            sigmaPMT_array.append(sigmaPMT)

801     # plot single PE data vs voltage
        plot_func(Voltages, single_PE_peak_array, plot_title='Single PE Calibration
             vs Electric Field', x_label='Electric Field (kV/cm)',
                  y_label='ADC Channel (G)', file_path_and_name=file_path_dir+
                      save_dir_name+'\\Single PE Calibration', save_file=save_files
                      )

        # plot sigma PMT data vs voltage
806     plot_func(Voltages, sigmaPMT_array, plot_title='$\sigma_{PMT}$ Calibration
            vs Electric Field', x_label='Electric Field (kV/cm)',
                  y_label='Sigma PMT', file_path_and_name=file_path_dir+
                      save_dir_name+'\\Sigma PMT Calibration', save_file=save_files
                      )

        # plot cumulative data for number of after pulses vs voltage
        plot_sum_of_data(Voltages, n_ap, 10**3, 'Electric Field (kV/cm)', 'Total
            number of After Pulses Recorded (x$10^3$)', 'Total After Pulses Counted
             vs Voltage', file_path_dir, 'After Pules per Voltage')
811
        # log previous calculations
        notes = 'fit_for_single_PE_complete'+add_notes
        logging(alpha_files[0], len(alpha_files)*data_length_to_process,
            num_waveforms_with_ap, ap_mean_per_waveform, ap_stdev_per_waveform,
            get_now()-start_time, stat.mean([pedestal_statistics[i][0] for i in
            range(len(pedestal_statistics))] ), stat.mean([pedestal_statistics[i
            ][1] for i in range(len(pedestal_statistics))] ), notes)

816
        #-----------------------------------------------
        # fit alpha to Poisson Gaussian Distribution for mean PE vs Voltage
        #-----------------------------------------------

821     # parameters to modify for following function
        fit_alpha_bin_start = 35
        fit_alpha_bin_end = 80

        # arrays for collecting data from following function
826     mu_fit_array = []
        N_fit_array = []
        num_bins_trig = len(bins_trig[0])-1

        for i in range(len(Voltages)):
831         def poisson_gauss_function(x, N, mu, G=single_PE_peak_array[i],
                sigmaPMT=sigmaPMT_array[i], k=15, sigmaPED=pedestal_statistics[i
                ][1]):
                final_array = []
                for j in x:
                    current_value=0
                    for i in range(1,k+1):
```

```
                    current_value += ((mu**i * math.exp(-mu) )/math.factorial(i
                        ) ) * (1/math.sqrt(2*pi*(sigmaPMT**2*i+sigmaPED**2))) *
                         math.exp(-(j-G*i)**2 / (sigmaPMT**2*i+sigmaPED**2))
                final_array.append(N*current_value)
            return final_array

        print('\nSTARTING ALPHA PE CALCULATION for %0.1f K...' % Voltages[i])
        mu_fit, mu_stdev, N_fit = fit_to_poisson_gauss_02(n_trig[i], bins_trig[
            i], file_path_dir, general_data_package, Voltages[i], 'alpha',
            trigger_hist_data[i], trigger_hist_max_value, num_bins_trig, N0 =
            10000000, mu0 = 0.5, G0 = single_PE_peak_array[i], sigmaPMT0 =
            sigmaPMT_array[i], sigmaPED = pedestal_statistics[i][1], x_start =
            fit_alpha_bin_start, x_end = fit_alpha_bin_end, mu_min = 8, mu_max
            = 12, mu_num = 8, do_print = True, save_folder_dir=save_dir_name)
        mu_fit_array.append([mu_fit, mu_stdev])
        N_fit_array.append(N_fit)
    print('\nmu_fit_array')
    print(mu_fit_array)
    print('\n')

    #-----------------------------------------
    # ----- make plot of num PEs vs Voltage -----
    #-----------------------------------------

    [print('%0.2f K -> %0.2f ADC +- %.02f' % (Voltages[i], mu_fit_array[i][0],
        mu_fit_array[i][1])) for i in range(len(Voltages))]

    NPE_percent_change=((mu_fit_array[0][0]-mu_fit_array[len(mu_fit_array)
        -1][0])/mu_fit_array[0][0]*100  )
    NPE_text = '\ndrop by %0.2f percent' %  NPE_percent_change
    print(NPE_text)

    # plot and save pedestal statistics
    plot_statistics(Voltages, mu_fit_array, data_box_first_line='vol (kV)    mu
         fit      mu stdev', x_label='Electric Field (kV/cm)', y_label='Mean
        $N_{PE}$', plot_title='Mean $N_{PE}$ vs Electric Field',
        file_path_and_name=file_path_dir + save_dir_name + '\\Mean Number of
        PEs vs Voltage', save_file=save_files, additional_info = [NPE_text])

    #-----------------------------------------
    #-----------------------------------------
    # ----  log time and other details  -------
    #-----------------------------------------
    #-----------------------------------------
    end_time = get_now()
    print('\nended at: %s' % str(end_time))
    total_time = end_time - start_time
    print('it took %s to complete %d data points' % (str(total_time)[:-4],
        data_length_to_process))
    notes = 'alpha_fit_to_dist'+add_notes
    logging(alpha_files[0], len(alpha_files)*data_length_to_process,
        num_waveforms_with_ap, ap_mean_per_waveform, ap_stdev_per_waveform,
        get_now()-start_time, stat.mean([pedestal_statistics[i][0] for i in
        range(len(pedestal_statistics))] ), stat.mean([pedestal_statistics[i
        ][1] for i in range(len(pedestal_statistics))] ), notes)
```